UNIVERSITY OF SOUTHAMPTON

Studies of Fluidics, Linear and Nonlinear Phenomena in Polariton Microcavities

by

Pasquale Cilibrizzi

A thesis submitted in partial fulfillment for the degree of Doctor of Philosophy

in the

Faculty of Physical Sciences and Engineering

School of Physics and Astronomy

September 2015

UNIVERSITY OF SOUTHAMPTON

Abstract

Faculty of Physical Sciences and Engineering
School of Physics and Astronomy

Doctor of Philosophy

by Pasquale Cilibrizzi

Exciton-polaritons are half-light half-matter bosonic quasiparticles formed by the strong coupling between quantum well excitons and the photonic mode of a planar semiconductor microcavity. By increasing the polariton population above a threshold density, polaritons can macroscopically occupy the ground state of the dispersion and form a non-equilibrium Bose-Einstein condensate.

This thesis addresses some of the fundamental concepts studied in polariton microcavities, such as dark solitons, polariton spin textures and condensation, by concentrating on the linear and nonlinear nature of these effects.

In the first part, the formation of dark solitons is studied by investigating the propagation and scattering of polaritons in a planar microcavity in the linear regime. The propagation of the polariton wave across an extended defect creates phase and intensity patterns with identical qualitative features previously attributed to dark and half-dark solitons of polaritons. By combining both experimental evidence and theoretical analysis, all the experimental observations supporting the formation of dark solitons in polariton microcavities are questioned. Since they are observed with negligible nonlinearity (i.e., polariton-polariton interaction), they are not sufficient to identify dark and half-dark solitons. A condition based on the healing length of the condensate is proposed as a new criterion to identify dark solitons in polariton microcavities.

In the second part, the spin dynamics of polariton condensates is investigated in the non-linear emission regime, by studying the spatial, angular, energy and transient dynamics of the polariton emission. In a radially expanding condensate, polaritons with opposite spin arrange themselves in geometrically ordered spin textures and propagate over hundreds of microns in the plane of the microcavity. Depending on the polarization of the excitation pump different spin textures are observed. Moreover, a polariton "spin whirl" namely a spin texture that rotates in the plane of the microcavity on picosecond scale is reported for the first time.

Finally, the condensation of polaritons in a strain compensated microcavity is investigated. Signatures of polariton condensation, according to the current understanding of polariton condensates, are experimentally observed, including the observation of a second threshold which marks the transition from the strong to the weak-coupling regime.

Contents

List of Figures

List of Tables

Declaration of Authorship

I, PASQUALE CILIBRIZZI, declare that this thesis titled, 'Studies of Fluidics, Linear and Nonlinear Phenomena in Polariton Microcavities' and the work presented in it are my own. I confirm that:

- This work was done wholly or mainly while in candidature for a research degree at this University.
- Where any part of this thesis has previously been submitted for a degree or any other qualification at this University or any other institution, this has been clearly stated.
- Where I have consulted the published work of others, this is always clearly attributed.
- Where I have quoted from the work of others, the source is always given. With the exception of such quotations, this thesis is entirely my own work.
- I have acknowledged all main source s of help.
- Where the thesis is based on work done by myself jointly with others, I have made clear exactly what was done by others and what I have contributed myself.
- The data presented in this work have been published previously in Ref.[31] (Chapter 5), Ref. [32] (Chapter 6) and Ref. [33] (Chapter 4, section 4.4.3 and Chapter 8).

Signed: _____

Date: _____

Acknowledgements

I had left home with a suitcase full of hopes and fears. Each choice, for better or for worse, it is always followed by both. Many things I've lost, many other I've missed, completely swallowed by the PhD life. However, if I look back I could not be happier for this choice. Here in Southampton I have grown a lot, both as a person and as a scientist.

For this, the first big thank you goes to Pavlos that gave me the possibility to work in this high challenge research environment. Every day, in the dark of the lab I have learned a lot. As a supervisor, he encouraged and supported me, particularly during the most obscure moments.

Thanks to my tutors, Elena and Hamid. I consider myself very lucky to have had the opportunity to share part of this journey with them. Elena, as brilliant PhD student, initiated me into all those mysteries of the polaritons world. Hamid, as experienced and talented postdoc, introduced me into the fine art of "pushing buttons" in the lab, which is "what make a researcher an experimentalist!" If I've learned a lot, it is also thanks to them. Thanks also to Alexis, for his support when things did not run so smoothly.

As a PhD candidate, I was also particularly lucky to have the chance to collaborate with top researchers in the field of polaritons. In primis, Prof. Wolfgang Langbein. The work on the linear wave dynamics (Chapter 5) and condensation in strain compensated microcavity (Chapter 8) are also the result of his inestimable contribution. Thanks to Tomas Ostatnicky, Tim Liew and Helgi Sigurdsson that performed the simulations reported in this thesis and always found time to discuss and share precious ideas with me. Thanks also to Ivan Shelykh for his contribution on the spin whirls work (Chapter 7), and to Pavlos Savvidis, Sven Höfling and Wolfgang Langbein for providing the microcavity samples studied in this thesis. I also owe big thanks to the European Commission for giving me the opportunity to receive a Marie Curie Fellowship for the first two years of my PhD and to the UK Engineering and Physical Sciences Research Council (EPSRC) for funding my last years.

Thanks to the mad scientists that compose the Hybrid Photonics group. To Mael and Nico for the long nights in search of gold and stars, to the "old chaps" of the group, Junis, Chunyong, Christos, Stefano and Peppe as well as the young fellows Peri, Giacomo, Matteo and Tao. Thanks a lot to Natanino for having been a sensational DJ and a temerarious sommelier in foreign lands and a friend in Soton. Thanks to Tom, Justin and Colin for fighting every day with the helium liquefier and giving me the possibility to run the experiments (lucky enough we didn't have to use the vise!).

It would have been much harder to face difficulties and dark periods without those people that have shared part of this journey with me, outside the lab, under the dark English clouds. For this I am thankful to the friends I've met during my first year in

Soton, Maty, Angeles, Ania, Amandine, Lorena, Alexia and Eva, and to the ones that entered my life lately, Francesco&Marta for their extraordinary Matriciana, Valentina, Lucia and Francesca for their amazing way to be so easy-going friends. You rock Sis!
A super special thanks goes to Caro, for deciding to share this crazy period with me and being always by my side, in spite of the ocean!
Lastly, the biggest thank you goes to my family, my Mam, my Dad, my Grandma, my Brother and my Sister. While I was "wandering off from the straight path", trying to find my way, they had always encouraged and gave me unconditional support, every day since the beginning. Despite the distance, the time and the uncertainty of the future, they had always been there. When you are sailing the open sea, it is always nice to know that there are things that never changes. I also owe a great thanks to my Bro, to share his experience with me and, most of all, to my Sis, whose faithful support during this long journey was invaluable. This thesis is dedicated to her, who never stopped believing in this dream with me. *"Not all those who wander are lost !"* (J.R.R. Tolkien).

Publications

- Linear Wave Dynamics Explains Observations Attributed to Dark Solitons in a Polariton Quantum Fluid.
  P. Cilibrizzi, H. Ohadi, T. Ostatnicky, A. Askitopoulos, W. Langbein and P. Lagoudakis - Physical Review Letters **113**, 103901 (2014).

  Fig.1 of this paper has been selected for the cover of Physical Review Letters **113**, N. 10 (2014).

- Reply to the comment on Linear Wave Dynamics Explains Observations Attributed to Dark Solitons in a Polariton Quantum Fluid.
  P. Cilibrizzi, H. Ohadi, T. Ostatnicky, A. Askitopoulos, W. Langbein and P. Lagoudakis - Accepted in Physical Review Letters.

- The Non-linear Optical Spin Hall Effect and Long-Range Spin Transport in Polariton Lasers.
  E. Kammann, T.C.H. Liew, H. Ohadi, P. Cilibrizzi, P. Tsotsis, Z. Hatzopoulos, P. G. Savvidis, A. V. Kavokin and P.G. Lagoudakis - Physical Review Letters **109**, 036404 (2012).

  Highlighted in Nature Photonics **6**, 637 (2012).

- Spin textures in polariton microcavities.
  P. Cilibrizzi, H. Sigurdsson, T.C.H. Liew, H. Ohadi, I. A. Shelykh, S. Höfling and P. Lagoudakis - In preparation.

- Polariton Spin Whirls.
  P. Cilibrizzi, H. Sigurdsson, T.C.H. Liew, H. Ohadi, S. Wilkinson, A. Askitopoulos, I. A. Shelykh, and P. Lagoudakis - Submitted (under review).

- Polariton Condensation in a Strain-compensated Planar Microcavity with InGaAs Quantum Wells.
  P. Cilibrizzi, A. Askitopoulos, M. Silva, F. Bastiman, E. Clarke, J.M. Zajac, W. Langbein and P.G. Lagoudakis - Applied Physics Letters **105**, 191118 (2014).

"It is questions with no answers that set the limit of human possibilities, describe the boundaries of human existence."

Milan Kundera,
The Unbearable Lightness of Being

To my sister, my brother
and my family.

Abbreviations

QED	**Q**uantum **E**lectrodynamics
GaAs	**Ga**llium **A**rsenide
DBR	**D**istributed **B**ragg **R**eflector
QW	**Q**unatum **W**ell
BEC	**B**ose **E**instein **C**ondensation
VCSEL	**V**ertical **C**avity **S**urface **E**mitting **L**aser
CdTe	**C**admium **Te**lluride
LPB	**L**ower **P**olariton **B**runch
UPB	**U**pper **P**olariton **B**runch
GPE	**G**ross **P**itaevskii **E**quation
CCD	**C**harge **C**oupled **D**evice
AOM	**A**cousto **O**ptical **M**odulator
TE/TM	**T**ransverse **E**lectric / **T**ransverse **M**agnetic

Chapter 1

Introduction

The physics of light-matter interaction, in its modern understanding as interaction between photons (i.e., quanta of light) and particles, started in 1900 when Max Planck, in his famous postulate, revealed one of the most fundamental principles of nature, remained obscure until then: electromagnetic energy is emitted or absorbed in discrete "bundles" (or quanta) of energy. In other words, the energy is quantized. In 1905, Einstein used the concept of energy quantization to formulate the photoelectric effect [34] and, in 1917, to theoretically predict the stimulated emission of radiation [35]. Since then, the study of light-matter interaction has played a fundamental role in pushing forward our understanding of the quantum world and has brought invaluable technological discoveries that have completely revolutionized our daily life. First among many, the laser which takes advantage of the stimulated emission process to emit a coherent, monochromatic, unidirectional and highly intense beam.

A turning point in the modern research of light-matter interactions, was the realization that the strongest effects are observed when both light (i.e. photons) and matter (i.e. atoms or excitons) are confined in microscopic or nanoscopic structures. An example of these nanostructures are the semiconductor microcavities studied in this thesis.
The central object of studies in microcavities is the exciton-polariton, a half-light half-matter bosonic quasiparticle that exhibits interesting physical properties and play a key role in the investigation of several fascinating effects, such as Bose Einstein condensation (BEC) and superfluidity, which could open the way to the creation of novel light sources

and optical logic elements. The research activities gravitating around polariton microcavities belong to this scenario at the crossroads of quantum electrodynamics (QED), optoelectronics and nanotechnology.

1.1 From strong coupling to Bose-Einstein condensate

For long time cavity QED has been studied prevalently in atomic physics. However, in the last decades, the continuous and rapid improvement of crystal growth techniques, such as metal-organic chemical vapor deposition and molecular beam epitaxy (see Appendix A), has made possible the realization of cavities with less and less losses (i.e., higher photon lifetime), allowing the investigation of coupling effects between light and matter, also in solid state systems. The first observation of strong coupling in semiconductor microcavities goes back to 1992 and it was realized by Weisbuch and coworkers [7], who observed the appearance of two minima in the reflectivity spectra (Rabi splitting) of a GaAs/GaAlAs based microcavity [36]. This observation, which corresponds to the solid state analogue of the Rabi splitting in the atomic case, marks the start of a new era for the semiconductor microcavity. QED effects, so far exclusive of the atomic systems, begin to be investigated also in solid state systems.

A semiconductor microcavity consists of a *cavity*, sandwiched between two highly reflective mirrors, called *distributed Bragg reflectors* (DBRs) and one or more sets of *quantum wells* (QWs) present within the cavity. By placing the QWs at the positions where the cavity mode has an antinode, the coupling between the photons confined into the cavity, and the excitons confined into the quantum well, can be increased beyond their respective decay rates and the regime of strong coupling can be observed. In this regime, the new eigenstates are not the photon and the exciton modes anymore but a superposition of the two, namely *exciton-polaritons* which combine the properties of both excitons and photons. In particular, they inherit a very light effective mass ($\sim 10^{-4} - 10^{-5}$ smaller than the free electron mass) from their photonic part and their tendency to interact with each other from their excitonic part. Moreover, like their constituents (i.e., the exciton and the photons), polaritons microcavity are *bosons* (Chapter 2).

The light effective mass together with their bosonic nature makes polaritons a potential candidate for the observation of BEC at temperatures several orders of magnitude

higher than the atomic case. This follows from the fact that, the critical temperature at which a gas of non-interacting bosons undergoes BEC, is inversely proportional to their mass (see equation 3.6). On the basis of this considerations, Imamoglu and coworkers proposed, in 1996, the realization of a "polariton laser"[37]. In the initial proposal the polariton laser was thought to operate by taking advantage of the bosonic nature of polaritons and the coherent properties of BEC. Being bosons, polaritons can macroscopically occupy a single state and form a condensate that spontaneously emits a coherent and monochromatic light, due to the tunneling of photons from the cavity through the Bragg mirrors [38]. The polariton lasing and the main differences with a standard vertical cavity surface emitting lasers (VCSEL) is discussed further in section 2.6.

This proposal was immediately followed by an extensive research and many features of polariton condensation and lasing were successfully reported. In particular, the nonlinear behavior of the polariton emission in power dependent measurements [39, 40] and the stimulated scattering of polaritons, resulting in a polariton parametric amplification [41], were both observed. These observations confirmed the macroscopic occupation of the same state by polaritons and their bosonic character. However, since these features are common to both polariton lasing and BEC, a sufficient evidence of BEC was still missing.

In 2006, Kasprzak and coworkers reported for the first time the formation of a polariton BEC in the lowest energy state of the polariton dispersion, together with the appearance of long range order in a CdTe microcavity at 5K [11]. Later, condensation at room temperature under optical excitation was reported in GaN [42] and more recently in ZnO [43] and organic systems [44, 45]. These results, however, divided the polariton community. The question of whether these observations correspond to polariton lasing or BEC remains unresolved and it is still a matter of debate [46–48] (see section 3.2.2). The main argument against polariton BEC is the fact that, contrarily to conventional BECs, polariton condensates never reach thermal equilibrium, due to the finite lifetime of polaritons, which is shorter than their relaxation time. As a consequence, the polariton condensate is a *nonequilibrium* condensate, and its steady-state results from a dynamical balance of pumping and losses [49]. On the basis of above, in this thesis the term *"polariton condensate"* will be used as a broader term to encompass both polariton BEC and polariton lasing. In III-V materials, polariton condensation and lasing

have been reported in MCs with GaAs QWs under optical pumping [10, 50, 51]. The implementation of electrically injected polariton condensates has also been reported in GaAs [52] and recently in GaN at room temperature [53].

Despite the controversy, many works followed the first observation of polariton BEC [11], mainly focused toward the observation of other phenomena that were strongly related to BEC in the case of atomic condensates [54]. Phase transitions in atomic BECs are associated with symmetry breaking and the appearance of topological defects, such as quantized vortices and dark solitons. In the case of quantum fluids, the appearance of quantized vortices in a rotating condensate marks the transition to the superfluid regime [55, 56]. In the last decade, a great effort has been put in the research of topological defects also in polariton condensates. The experimental observation of BEC [11] and superfluidity [57, 58] of exciton-polaritons, has sparked interest in the quantum-hydrodynamic properties of polariton fluids. In particular, the nucleation of quantized vortex [59–61], vortex-antivortex pairs [62] and dark solitons in the wake of an obstacle (i.e. defect) [18–22] has been claimed recently. Here, the source of nonlinearity essential for the formation of such a solitary wave has been identified in the mainly repulsive polariton-polariton interactions [18–22].

Although theoretical models based on Gross-Pitaevskii equation support the formation of vortices in polariton condensates, it is well know that their observation alone is not a sufficient evidence for BEC and superfluidity [59]. Vortices, appearing as fork-like dislocations, are present also in linear optical systems [63, 64]. In the case of dark-solitons, on the other hand, the observation of dark notches in the intensity profiles together with a π shift in the phase were used as sufficient signatures for dark and half-dark solitons in polariton microcavities [18–22]. In the work claiming the first observation of dark soliton in polariton condensate [18] it is stated, for example, that *"An unambiguous characteristic of solitons in BECs is the phase jump across the soliton"*, suggesting that other features are not necessary to support the claim. The theoretical framework of the Gross-Pitaevskii equation admits soliton solutions [65] and supports the appearance of dark notches and π phase shift in polariton condensate [17]. However, *are these features really sufficient to claim the observation of dark soliton in a polariton condensate?*

In Chapter 5, we address this question by providing both experimental evidence and

theoretical analysis that question all the claims of dark-solitons [18–21] and half-dark solitons [22] previously reported in polariton microcavity literature.

1.2 The spin-optronics dream

Since the very beginning, semiconductor microcavities have represented a model system for a wide range of fundamental [66] and applied studies [67, 68] focused on the spin properties of exciton-polaritons. Polaritons in strongly coupled semiconductor microcavities, in fact, possess highly interesting spin dynamics. The spin of a polariton is directly connected with the polarization of the light absorbed or emitted by the microcavity (see section 2.7) enabling the use of polaritons in polarization sensitive devices [69–71], also known in the polariton community as "spin-optronic" devices. Being neutrally charged, polaritons allow, in principle, to solve some of the main problems deriving from the use of charged particles (i.e., electrons) in conventional spintronic devices, such as dephasing of the electron flow due to Coulomb scattering and different speed of electron flows [72]. In contrast, polaritons due to their long range coherence [73] are potentially able to transport spin over macroscopic distances, with minimal scattering and minimal loss of spin information. In this regards, the manipulation and control of polariton propagation and their polarization is therefore a fundamental step toward the realization of such optical spin devices.

In Chapter 6 and Chapter 7 the spin dynamics of polariton condensates is addressed. In particular, the spin transport properties of a radially expanding polariton condensate is experimentally and theoretically demonstrated.

1.3 Outline

This thesis focuses on the study of fluidics, linear and non-linear phenomena in polariton microcavities and consists of seven chapters, this introduction and a chapter of conclusion (Chapter 9), where the entire experimental work is summarized. The seven chapters, consist of two theoretical chapters where the physics of exciton-polariton (Chapter 2) and polariton quantum fluids (Chapter 3) is reviewed together with the state of art in polariton microcavities. In particular:

In Chapter 2, an overview of the physics behind microcavity polaritons is presented. Starting from the concept of quasiparticle in semiconductors, the theory of the confinement of photons in a planar cavity and excitons in a quantum well is discussed. In the second part of the chapter, the fundamental properties of exciton-polaritons, including their spin and polariton lasing, are reviewed.

In Chapter 3, the physics of Bose Einstein condensates (BECs), quantum fluids and dark solitons is presented. The main theories and breakthrough discoveries in atomic condensates, which have inspired several works in semiconductor microcavities, are discussed and compared with the equivalent observations reported in polariton condensates. In particular, in section 3.2.2 the main differences between atomic and polariton BEC are discussed.

In Chapter 4, the experimental setups, methods and microcavities samples used throughout this thesis are described.

The remaining four chapters represent the experimental work conducted during the period of PhD candidature. In particular:

Chapter 5 represents a study of the formation of dark soliton in polariton microcavity. In section 5.1.1, the unusual properties of polariton dark solitons, with respect to the atomic case, are highlighted. By combining both experimental evidence and theoretical analysis, all the experimental observations supporting the formation of dark solitons [18–21] and half-solitons [22] in polariton microcavities is questioned. At the end, a condition based on the healing length of the condensate is proposed as a new criterion to identify dark solitons in polariton microcavities.

Chapter 6 and Chapter 7 of this thesis are dedicated to the study of the spin dynamics in polariton condensates. In Chapter 6, it will be shown how polaritons with different spin, arrange themselves in geometrically ordered spin textures, which propagate over hundreds of microns in the plane of the microcavity. Depending on the polarization of the excitation pump different spin textures are observed. In Chapter 7, on the other hand, the dynamical evolution of the spin textures will be studied. It will be shown that, under specific experimental conditions, it is possible to create spiralling spin textures, which rotate in the plane of the microcavity on a picosecond scale. We call these spin textures *"polariton spin whirls"*.

Finally, in Chapter 8 the condensation of polaritons in a new generation of samples is presented. The sample in question is a strain compensated planar microcavity with embedded InGaAs quantum wells, characterized by a reduced cross-hatch disorder density (see section 4.4.3). The features supporting polariton lasing and condensation, according to the current understanding and knowledge of polariton condensates, are experimentally observed. In particular, the observation of a second threshold, which marks the onset of photon lasing, proposed as an additional criterion to distinguish between polariton and photon lasing [74] is also reported. This work represents the first demonstration of polariton condensation in a InGaAs QWs microcavity under non resonant excitation.

Chapter 2

Exciton-polaritons in semiconductor microcavities

In this chapter, the physics behind microcavity polaritons is presented. The chapter starts from the concepts of quasiparticle in semiconductors (section 2.1) and continues by discussing the theory of the confinement of excitons in a quantum well (section 2.2) and photons in a planar cavity (section 2.3). In the second part of the chapter (section 2.4), the fundamental properties of exciton-polaritons will be reviewed. A description of two distinct regimes occurring in polariton microcavities, i.e., strong (section 2.4.2) and weak (section 2.4.4) coupling regime, together with the excitation and relaxation mechanism of polaritons (section 2.5) is illustrated. Finally, in the last part of the chapter, the polariton laser operation mechanism (section 2.6) and the spin properties of polaritons (section 2.7) will be discussed.

2.1 Semiconductor quasiparticles

2.1.1 Band structure in semiconductors

Crystals can be considered as solids composed by many atoms assembled together in a regular periodic structure (i.e., lattice). According to the Bloch's theorem [75], the eigenfunctions of electrons in such crystal can be written as a plane wave modulated by

a periodic function:

$$\psi_{n\mathbf{k}}(\mathbf{r}) = e^{i\mathbf{k}\cdot\mathbf{r}} u_{n\mathbf{k}}(\mathbf{r}) \tag{2.1}$$

where n is the index of the band, $\mathbf{k}$ an effective wave vector and $u_{n\mathbf{k}}(\mathbf{r})$ the periodic function with the periodicity of the lattice. Contrarily to the free electron wave vector, $\mathbf{k}$ is not proportional to the electronic momentum and the quantity $\hbar\mathbf{k}$ do not represents the momentum of the electron in the lattice. This is due to translational symmetry of the space and in particular to the fact that the $\psi_{n\mathbf{k}}$ is not an eigenstate of the momentum operator [75]. For this reason the quantity $\hbar\mathbf{k}$ is usually called "quasi-momentum" (or crystal momentum).

The quasi-momentum assumes non identical values only inside well defined regions of the reciprocal space. These regions, known as Brillouin zones, correspond to the primitive cells of the reciprocal lattice and can be determined from the periodicity in real space. It can be shown that the solutions found in the first Brillouin zone fully characterize the Bloch states in all the other regions of the crystal. It is common, therefore, to consider only the first Brillouin zone for the calculations. By substituting the Bloch wavefunction 2.1 into the Schrödinger equation for an electron propagating in a crystal, one can calculate the band structure of the particular lattice material, which corresponds to calculate the energy eigenvalues and eigenstates as a function of the quasi-momentum $\hbar\mathbf{k}$ and the band index n.

The electronic and optical properties of solids are in general determined by the occupation of the bands. In the case of insulators and semiconductors, electrons can occupy only specific bands of energy, while they are forbidden from others. In particular, the highest occupied and the lowest unoccupied bands, called respectively valence (E_v) and conduction (E_c) bands, are separated by a forbidden region where no allowed energy states for electrons exist [75]. This region, corresponding to the energy difference between the top of the valence band and the bottom of the conduction band ($E_g = E_c - E_v$) is known as band- or energy-gap (E_g). Depending on the absolute value E_g, a more quantitative distinction between insulators (i.e., dielectrics) and semiconductor can be drawn. A semiconductor, in fact, can be thought as an insulator with a small band-gap. Usually, if E_g is less than $3-4\ eV$, the conduction band has non-negligible population at elevated temperatures, and this type of crystal is called semiconductor [3]. On the other hand, materials with wider band gaps ($E_g > 4\ eV$) are considered insulators.

In Fig. 2.1 the band structure and the energy gap for the case of Gallium Arsenide (GaAs) are shown. Like many other III-V semiconductors, GaAs is characterized by a zincblende structure with a cubic symmetry. In this case, the dispersion relation at the center of the Brillouin zone ($\mathbf{k} = 0$) can be approximated by a quadratic equation and an effective mass (m_{eff}) for the electron in the crystal can be calculated:

$$\frac{1}{m_{eff}} = \frac{1}{\hbar^2}\frac{d^2E}{dk^2} \tag{2.2}$$

From equation 2.2 follows that the electron effective mass is related to the curvature of the band E(k). Large curvatures of E(k) (i.e., large second derivative) correspond to smaller effective mass. In the case of GaAs shown in Fig. 2.1, the highest occupied valence band (Γ_8) and the lowest unoccupied conduction band (Γ_6) have both small effective mass [76]. In general, in zincblende semiconductors, the valence band split into three sub-bands referred to as the heavy hole, light-hole and spin-off bands [77]. The first two, usually are approximated by two parabolic bands with different curvatures (i.e., the wider one is the heavy hole band while the narrower one is the light-hole band) and are degenerate in bulk crystals. However, this degeneracy is lifted by strain, external fields or, as we will discuss in section section 2.2.2 inside the quantum wells due to confinement effects.

Finally, it is possible to notice that in the case of GaAs band structure of Fig.2.1, the conduction band minimum occurs at the same k value as the valence band maximum. For this reason, GaAs together with CdTe, GaN, ZnO, is called *direct-gap* semiconductor. On the other hand, crystals where the smallest band separation between E_c and E_v is not vertical in k-space (i.e., do not occur at the same k value), like for example Si and Ge, are considered *indirect-gap* semiconductors. The difference between the two semiconductors has many consequences in their optical processes. In particular, in indirect semiconductor the transition of an electron from the valence band to the conduction band can happen only if an acoustical phonon take part to the process (i.e. phonon assisted transition), due to the wave vector conservation requirements.

2.1.2 What is a quasiparticle?

It is common in solid state physics to approximate a many-body problem of interacting particles with a much simpler one, by considering a small number of *quasiparticles* which

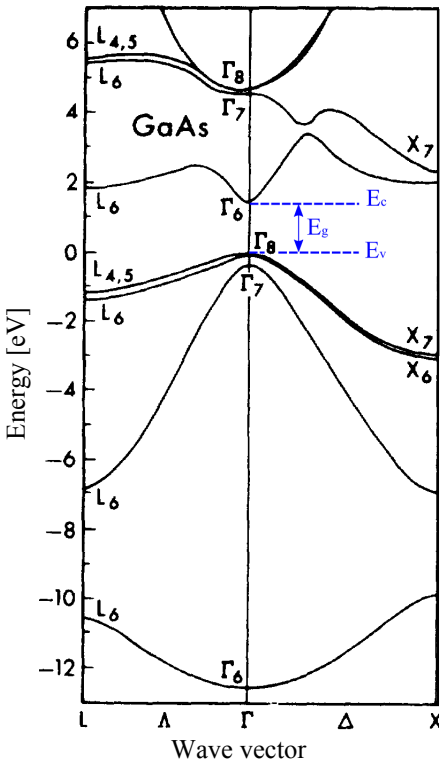

FIGURE 2.1: The band structure of the bulk GaAs in the reduced zone scheme, where the wave vector k are restricted to the first Brillouin zone. L, Γ and X represent high symmetry points of the Brillouin zone. In particular, the center of the Brilloiun zone is always denoted by Γ and corresponds to $k = 0$ [1]. Λ and Δ correspond to high symmetry lines connecting these points. In particular, $\overline{\Gamma\Delta X}$ and $\overline{\Gamma\Lambda L}$ corresponds to the crystallographic direction [100] and [111] of the first Brilloiun zone [1]. The maximum of the valence band E_v, the minimum of the conduction band E_c and the energy gap E_g are indicated in blue. The zero is set at the top of the valence band (E_v). Figure adapted from Ref.[2].

only weakly interact with each other. These quasiparticles are described as elementary excitations of the system consisting of a number of real particles [3].

This approach, formulated for the first time by L. Landau to explain the physical properties of ^3He [78, 79], it has been extensively applied in the case of solid state physics to describe the properties of crystals constituted by a large amount of atoms. In fact, to describe in full detail the motion of an electron trough a semiconductor, one should consider the many-body interactions that the electron in the conduction band will experience with all the positive nuclei composing the lattice and all the other electrons present in the system. Instead of considering all the possible interactions, it is common approach to treat the whole crystal as an isolated system in the ground state and electrons in the conduction band as elementary excitations of the crystal. Thus, in the case of semiconductors, the ground state corresponds to the state with filled valence

band and empty conduction band. When an electron is excited from the valence band to the conduction band, a quasiparticle or an elementary excitation is created. This elementary excitation is essentially the electron *quasiparticle* which, contrarily to the elementary particles, like for examples quarks, can only exists inside the solid.

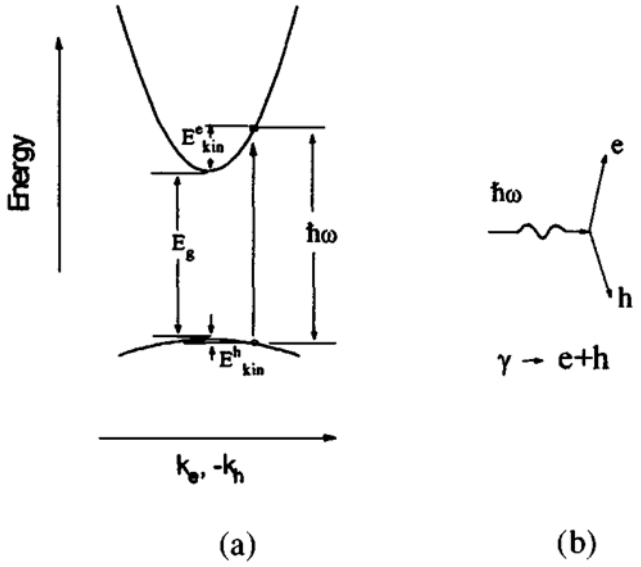

FIGURE 2.2: The process of absorption of a photon resulting in a creation of a one electron-hole pair described by the dispersion bands (a) and Feynman (b) diagrams. In a) the absorption of a photon is shown as a vertical transition of an electron, from the valence band to the conduction band, with simultaneous conservation of energy and momentum. In (b) the same process is treated as a conversion of a photon into an electron hole pair [3].

Electrons in the conduction band are not the only elementary excitations in semiconductor. Another example is represented by a *hole*, which is a quasiparticle relevant to an ensemble of electrons in the valence band from which one electron is removed [3]. A hole is usually created during optical excitation of a semiconductor. In fact, when the energy of an incident photon ($\hbar\omega$) is large enough to exceed the energy gap (i.e., $\hbar\omega > E_g$), an electron with charge -e is excited from the the valence band into the conduction band, with simultaneous creation of a vacancy in the valence band. This vacancy in the valence band is called hole and can be treated as a quasiparticle with opposite charge +e with respect to the electron. The process just described, corresponding to the absorption of a photon, is shown in Fig. 2.2 (a) for the case of a direct-gap semiconductor. Since the momentum of the photon is orders of magnitude smaller than that of the quasiparticles (i.e., electrons and holes), there is no change of momentum and the optical transition is

essentially vertical with the energy and momentum conservation [3]

$$\begin{aligned} \hbar\omega &= E_g + E_{ekin} + E_{hkin} \\ \hbar\mathbf{k} &= \hbar\mathbf{k}_e + \hbar\mathbf{k}_h. \end{aligned} \tag{2.3}$$

The same process can be described by means of the Feynman diagrams in Fig. 2.2 (b).

2.2 Confinement of excitons

2.2.1 What is an exciton?

In the optical excitation described so far, the Coulomb interaction between the negative charged electron and the positive charged hole have been neglected (single-particle approach). However, since they have opposite charge, a hole and an electron attract each other via the Coulomb interaction. The bound state of an electron and a hole corresponds to another quasiparticle, with neutral charge, known as *exciton*.

The concepts of excitons was first introduced by Frenkel in 1931, as "excitation waves" when light is absorbed by a crystal [4, 80]. A Frenkel exciton is a tightly bound electron-hole pair compared in size to a single lattice site. This exciton is not bound to any particular ion composing the lattice and is capable of passing from one ion to the next through all the crystal, constituting what Frenkel called excitation waves [4]. Frenkel exciton is present mainly in organic molecular crystals and will not be discussed further in this thesis where only inorganic semiconductor samples have been studied.

On the other hand, in inorganic semiconductor such as Germanium, Silicon and GaAs, a different type of exciton, known as Wannier-Mott exciton, exists [81, 82]. These excitons appear to be larger than Frenkel excitons and usually extends to several lattices sites [83].

An exciton corresponds to the solid-state analogue of the hydrogen atom. In fact, by means of the effective mass approximation, Wannier-Mott excitons can be described by an hydrogen-like Hamiltonian with a Coulomb potential term due to the Coulomb

interaction between electron and hole [3]:

$$H = -\frac{\hbar^2}{2m_e^*}\nabla_e^2 - \frac{\hbar^2}{2m_h^*}\nabla_h^2 - \frac{e^2}{\epsilon\,|\mathbf{r}_e - \mathbf{r}_h|} \tag{2.4}$$

which is the same as the Hamiltonian of the hydrogen atom with the effective electron m_e^* and hole m_h^* masses instead of the electron and proton masses and with the dielectric constant of the crystal $\epsilon \neq 1$.

Similarly to the hydrogen atom, exciton is characterized by the *exciton Borh radius* [3]:

$$a_B = \frac{\epsilon\hbar^2}{\mu e^2} = \epsilon\frac{m_0}{\mu} \times 0.53\text{Å} \tag{2.5}$$

where m_0 is the electron mass in the hydrogen atom and μ is the electron-hole reduced mass:

$$\mu^{-1} = m_e^{*-1} + m_h^{*-1} \tag{2.6}$$

and by the *exciton Rydeberg energy* [3]:

$$R_y^* = \frac{e^2}{2\epsilon a_B} = \frac{\mu e^4}{2\epsilon^2\hbar^2} = \frac{\mu}{m_0}\frac{1}{\epsilon^2} \times 13.6eV. \tag{2.7}$$

Here R_y^* , is the analogue of the Rydberg constant in atomic physics and corresponds to the electron-hole binding energy or, alternatively, to the energy required to ionize an exciton from its lowest energy state ($n = 1$) [4]. Since the effective mass of the carriers inside a solid and consequently the electron-hole reduced mass μ are smaller than the free electron mass in vacuum m_0 (i.e., in GaAs the electron effective mass $m_e^* = 0.067\ m_0$ and the heavy hole $m_{hh} = 0.45m_0$) and the dielectric constant ϵ is bigger than that of the vacuum (i.e., for a typical inorganic semiconductor $\epsilon \approx 10$, while in the vacuum $\epsilon = 1$), Wannier-Mott excitons are characterized by a larger Bohr radius (see equation 2.5) and a smaller Rydberg energy (see equation 2.7) than hydrogen atoms. For the most common inorganic semiconductors, $a_B \approx 10 - 100$Å and $R_y^* \approx 1 - 100meV$ [3].

Within the effective mass approximation, the dispersion relation of the exciton can be calculated by considering the center of mass motion of a single uncharged particle (i.e., the exciton) with the total mass $M = m_e^* + m_h^*$:

$$E_n(\mathbf{K}) = E_g - \frac{R_y^*}{n^2} + \frac{\hbar^2\mathbf{K}^2}{2M} \tag{2.8}$$

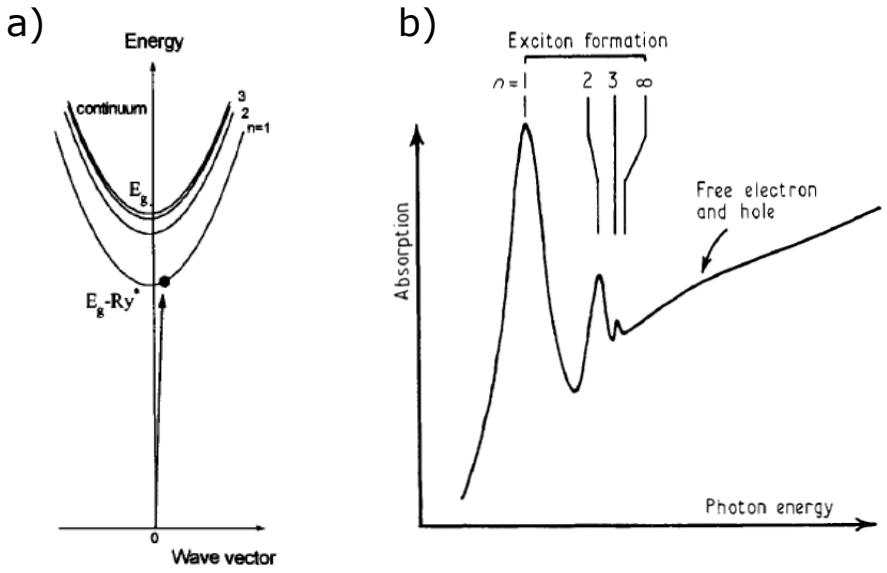

FIGURE 2.3: a) Dispersion curves of an exciton corresponding to the hydrogen-like set of energies $E_n = E_g - R_y^*/n^2$ at $K = 0$ and the optical transition corresponding to a photon absorption and exciton creation. For $E > E_g$ the exciton spectrum overlaps with the continuum of unbound electron-hole states [3]. b) Typical absorption spectrum of a semiconductor at low temperature, showing strong absorption peaks due to the Wannier-Mott exciton series ($n = 1, 2 \ldots \infty$) and the continuum absorption due to free electrons and holes at higher energies [4].

Equation 2.8 represents the hydrogen-like set of energy levels with $n = 1, 2, 3 \ldots \infty$ the principal quantum number, E_g the band gap energy and R_y^* the exciton binding energy defined by equation 2.7. The last term in the right side of the equation corresponds to the kinetic energy of the translational motion with $K = k_e + k_h$ the wave vector of the exciton.

Like in the case of an hydrogen atom, there are n quantized bound states, corresponding to the series of subbands shown in Fig. 2.3 that converge to a continuum of states (i.e. the series limit). The energy corresponding to the series limit is that required to produce a free e-h pair in the solid. The total momentum $\mathbf{K}$ of an optically generated exciton should be equal to the momentum of the absorbed photon which is very small compared to the carriers momentum. Therefore, the optical properties of excitons can be described by considering only the case of $\mathbf{K} = 0$ [84] and equation 2.8 can be simplified in:

$$E_n = E_g - \frac{R_y^*}{n^2} \tag{2.9}$$

Equation 2.9 identified the peaks observed below the energy band gap in a typical absorption spectrum of a semiconductor, as shown in Fig. 2.3 b). Each peak corresponds

to a different bound state, namely different transition energies E_n with $n = 1, 2$ etc. Recently the experimental observation of absorption peaks associated with excitons with principal quantum numbers as large as $n = 25$ has been reported for a high-quality natural crystal of copper oxide [85, 86].

2.2.2 Exciton in quantum well

Quantum Wells (QWs) are heterostructures composed by layers of different semiconductor materials, with the smaller band gap material, like for example GaAs, placed in between layers of material with larger band gap, like for example AlGaAs. In such heterostructures, both electrons and holes can be trapped inside the GaAs layer (forming the well) and experience confinement effects at the *mesoscopic regime*. In the case of QWs, this regime is realized when the thickness (d) of the well becomes comparable with the de Broglie wavelength (λ_{deB}) of the electrons (λ_e) and holes (λ_h) or the Bohr radius (a_B) of the exciton:

$$d \leq \lambda_e, \lambda_h, a_B, \tag{2.10}$$

with the de Broglie wavelength (λ_{deB}) for a generic particle of mass m at a temperature T is given by

$$\lambda_{deB} \sim \frac{h}{\sqrt{m k_B T}}. \tag{2.11}$$

For an electron in GaAs with an effective mass of 0.067 m_0, λ_{deB} is equal to 42 nm at $T = 300\ ^\circ K$. This implies that we need QWs of ~ 10 nm thickness in order to observe quantum-confinement effects at room temperature [5]. In Fig. 2.4 a schematic diagram of a GaAs/AlGaAs quantum well is shown. More details on the fabrication process and band gap engineering of a quantum well are reported in Appendix A.

When the condition 2.10 is satisfied, quasiparticles in QWs will experience quantum confinement resulting in the quantization of their motion along the confinement axis (i.e. the growth direction z) and free motion in the other two directions (i.e. the $x - y$ plane). Consequently, the energy states inside the QW will be quantized along the z direction, as indicated by the dashed lines in Fig. 2.4.

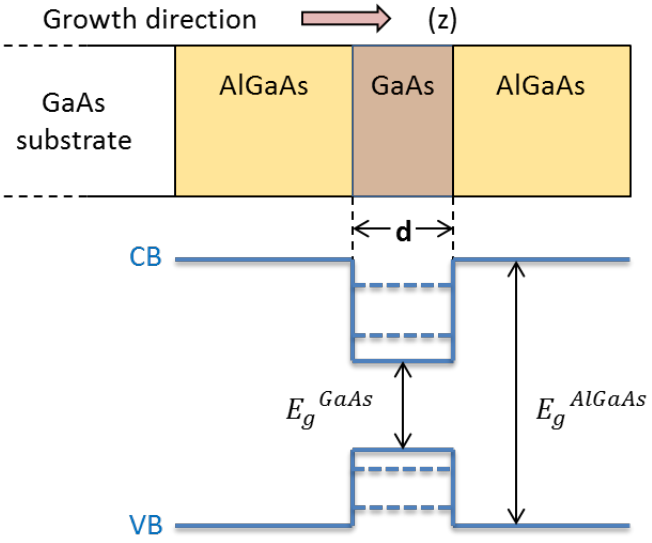

FIGURE 2.4: Sketch of a GaAs/AlGaAs quantum well of thickness d (top of the figure) together with the corresponding band diagram (bottom of the figure) along the growth direction (z). The dashed lines indicates the quantized levels. Note that in real structures a GaAs buffer layer is usually grown immediately above the GaAs substrate. Figure redrawn from Ref.[5].

The discrete energy levels can be calculated by solving the Schrödinger equation for the electrons and holes in a potential well. In the simplest approximation[1], this corresponds to calculate the Schrödinger equation for a particle in an infinite potential well of width d (i.e., particle in a box model). The eigen-energies are then given by:

$$E_n = \frac{\hbar^2 k_n^2}{2m_w^*} = \frac{\hbar^2}{2m_w^*}\left(\frac{n\pi}{d}\right)^2 \tag{2.12}$$

with $k_n = n\pi/d$ and m_w^* being respectively the wave vector and the effective mass of the particle inside the well. The quantum number n, is an integer (≥ 1) and indicates the energy levels inside the well.

A direct consequence of equation 2.12 is that, since E_n is inversely proportional to both the square of the well width (d) and the effective mass of the particle inside the QW (m_w^*), the confinement energies will be larger for narrow wells and small effective masses. This is at the origin of the splitting between light and heavy holes bands inside a QW. In

[1]In a more realistic model, the Schrödinger equation should be solved for the case of a particle confined in a finite potential well. The main difference between the two models is represented by the fact that, while in a infinite well the walls are "impenetrable" since the wavefunctions are zero at the wall position, in a finite well the wavefunctions decay exponentially in the barriers. As a consequence, the eigen-energies in the finite well are smaller than those of the infinite well [5]. However, even if the approximation gives an over-estimate of the values measured in a real QW, the consequences of the quantum confinement highlighted here apply to both models.

fact, for a QW of fixed d, light and heavy holes having different effective masses will also have different energies, in strong contrast to bulk semiconductors in which the two types of holes states are degenerate on top of the valence band [5], as discussed in section 2.1.1. A sketch of the band diagrams inside a QW is shown in Fig. 2.5 a), where $h1$ corresponds to the heavy hole valence band while $h2$ to the light hole valence band. The allowed transition between the electrons and valence subbands, corresponding to the absorption or emission of a QW, are also shown. Selection rules allow optical transitions between hole and electron states with the same quantum numbers, i.e. $\Delta n = 0$ transitions.

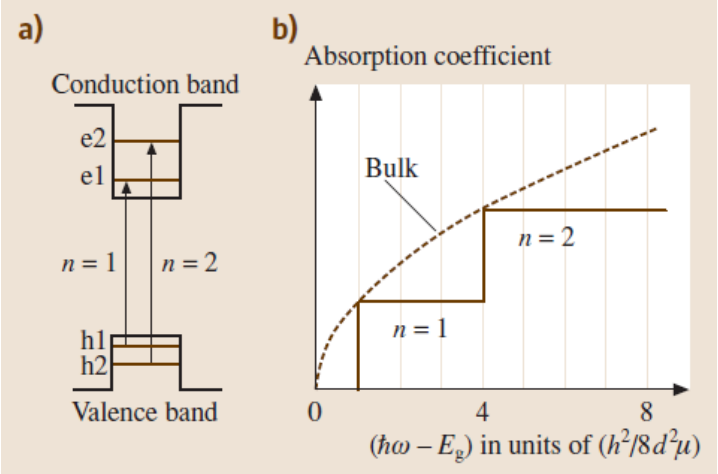

FIGURE 2.5: a) Band structures and interband optical transition inside a QW. As highlighted in the text, in a QW the confinement potential lifts this degeneracy, i.e. heavy hole (h1) and light hole (h2) have different energy, with the heavy hole energy level closer to the band edge than the light holes levels. The $\Delta n = 0$ optical allowed transition between the subbands are shown. b) Absorption spectrum for an infinite quantum well of thickness d with a reduced electronhole mass μ in the absence of excitonic effects. The absorption spectrum of the equivalent bulk semiconductor is shown by the dashed line for comparison. Figure taken from Ref. [5].

Together with the energy levels, also the density of states is profoundly modified by the quantum confinement effects. Therefore, if in a bulk semiconductor the electron density of states is proportional to $(\hbar\omega - E_g)^{1/2}$ with $\hbar\omega > E_g$ (where $\hbar\omega$ and E_g indicate respectively the energies of a photon and of the band gap) in a QW is characterized by a sequence of steps. In each of these steps, the density of states and consequently the absorption coefficient remains constant. This is shown in Fig. 2.5 b), where the absorption coefficient due to the interband optical transition of Fig. 2.5 a), is compared with the absorption curve in bulk GaAs.

Finally, also the properties of the exciton inside the QWs will be modified by the confinement. Although the exciton state inside a QWs can be still modeled as the 2D hydrogen

atom (like in the bulk exciton case, described in section 2.2.1), the dispersion relation 2.8 for the bulk exciton, has to be modified to take into account the free motion of the electron and hole in the $x-y$ plane and the confinement motion along the z direction. Consequently, the dispersion relation for the exciton in QW becomes [87]:

$$E_n^{2D} = E_g + E_{n,e} + E_{n,h} - \frac{R_y^*}{(n-1/2)^2} + \frac{\hbar^2(K_x^2 + K_y^2)}{2M} \tag{2.13}$$

here E_g is the band gap energy, $E_{n,e}$ and $E_{n,h}$ the confinement energies for electrons and holes, R_y^* the exciton Rydberg energy inside the QW and $K = k_e + k_h$ the wave vector of the exciton in the $x-y$ plane. The main consequences of the relation dispersions 2.13 are that, compared to the 3D case (i.e. bulk semiconductor),

- the band edges (E_g) in the QW are shifted to higher energy by a quantity equal to the sum of the electron and hole confinement energies, i.e. ($E_{n,e} + E_{n,h}$),
- the binding energy of the ground-state exciton inside the QW is four times larger,
- the exciton Bohr radius two times smaller.

Because of the quantum confinement, electron and holes are closer together inside the QWs than in bulk semiconductors. Consequently, excitonic effects are enhanced in QW and can be observed also at room temperature, whereas they are only usually observed at low temperatures in bulk semiconductors [5]. In Fig. 2.6, the band-edge absorption at room temperature between a bulk GaAs and a multiple quantum well sample is compared. Here, we notice that both the blue shift of the band edge absorption and the appearance of two peaks are clearly visible. In particular, these two peaks are due to light and heavy hole excitons and appear at energies given by the relation [5]:

$$\hbar\omega = E_g + E_{hn} + E_{en} - E^x \tag{2.14}$$

where $\hbar\omega$ is the energy of incident photon, E_g the optical band gap, E_{hn}, E_{nm} respectively the hole and electron nth energies level inside the QW and E^x the exciton binding energy. Above the excitons energies, on the other hand, the absorption is approximately constant. This is a consequence of the constant density of states in 2-D, which contrasts with the rising absorption of the bulk due to the parabolic 3-D density of states [5].

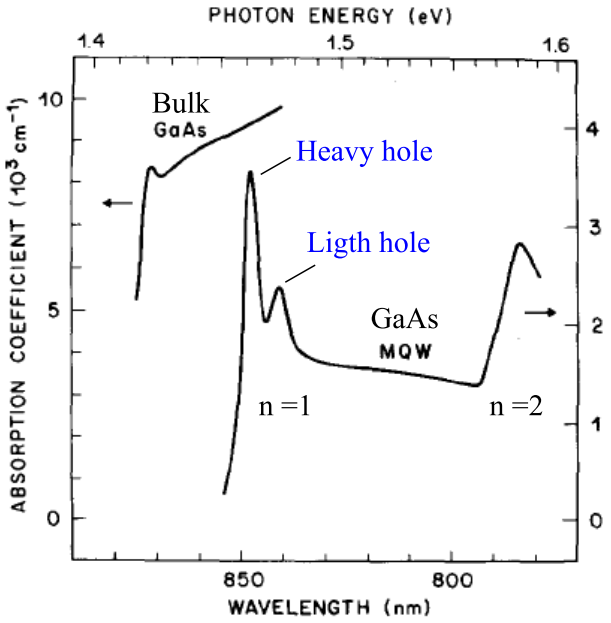

FIGURE 2.6: Absorption spectra at room temperature of a multiple quantum well (MQW) GaAs/AlGaAs structure and a bulk GaAs, as shown in Ref. [6]. In the case of QW separate transitions are observed for the heavy and light holes because of their different effective masses.

The sharp exciton lines are important for the observation of strong coupling effects in quantum well microcavities, as will be discussed in section 2.4.1.

2.3 Confinement of photons

2.3.1 What is a microcavity?

A microcavity is an optical resonator that confines light to small volumes (with sizes comparable to the wavelength of light) [88]. Over the years, microcavities with different shapes and materials have been realized for different applications [89]. In the simplest resonator, such as metal microcavities, the confinement of light is obtained by using two parallel high reflectivity mirrors (e.g. metallic mirrors) which repeatedly reflect light. In other microcavities, such as whispering gallery microcavities, light is confined thanks to total internal reflection within a high refractive index body of different geometries (e.g. spheres, disks or rings) [88, 89]. More complex microcavities can also be realized by using periodically patterned microstructures, like for example photonic crystals or planar multilayer Bragg reflectors. The latter are the microstructures that compose the microcavity samples studied in this thesis, as discuss below.

The microcavities studied in this thesis are planar Fabry-Perot resonators composed by two high reflectivity mirrors called distributed Bragg reflectors (DBRs) [88].

DBRs are periodic structures composed by an alternating sequence of layers of two different semiconductor materials. Each layer is characterized by different refractive indices n_a and n_b, with $n_a > n_b$ and with a thickness (d) satisfying the Bragg interference condition, i.e., $n_a d_a = n_b d_b = \tilde{\lambda}/4$ [77]. Here d_a and d_b are the thickness of two different layers and $\tilde{\lambda}$ is the wavelength for which the DBRs has been designed.

Inside the cavity, photons with wavelength $\tilde{\lambda}$ reflect back and forth between the two DBRs and interfere constructively giving rise to a broad band high reflectivity region, called *stop band* with oscillating side lobes on either side, as shown in Fig.2.7. The optical properties of a DBR have been calculated using the transfer matrix method described in details in Appendix B. In general, the reflectivity of the DBRs increases

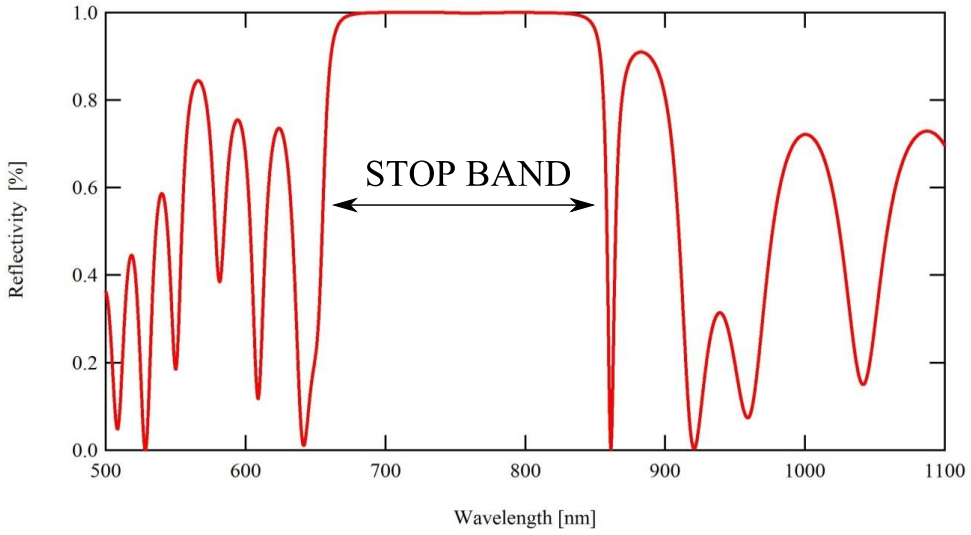

FIGURE 2.7: Reflectivity spectrum of a typical DBR composed by the alternation of 8 layers, i.e. $N_{SiO_2} = N_{Ta_2O_5} = 8$. The two layers used here are SiO_2 with $n = 1.458$ and thickness $\lambda/(4n_{SiO_2})$ and Ta_2O_5 with $n = 2.137$ and thickness $\lambda/(4n_{Ta_2O_5})$. This spectrum has been calculated with the the transfer matrix method reported in Appendix B.

with the number of periods and with the difference between the high and low refractive index layers, i.e. the refractive index contrast. The latter defines also the width of the stop band [77].

When a cavity layer with a thickness (L_c) equal to an integer number (N) of half-wavelength ($\lambda/2$), i.e. $L_c = N\lambda_C/2$ is placed between two of such DBRs, a optical microcavity is formed. Microcavities are structures very similar to Fabry-Perot cavities with planar mirrors [77]. They are characterized by the fact that at the frequencies

corresponding to the eigenmodes of the cavity, i.e. at the resonance frequencies ω_m, the transmission (T) sharply increases. Correspondingly, in the absence of absorption, the reflectivity (R) decreases at the resonance frequency (since $R = 1 - T$) as shown in Fig.2.8 where a minimum in the reflectivity spectrum is clearly visible at the resonance. As a consequence, photons incident on the microcavity are able to penetrate inside the cavity and be transmitted through it at these frequencies [77]. The resonant optical

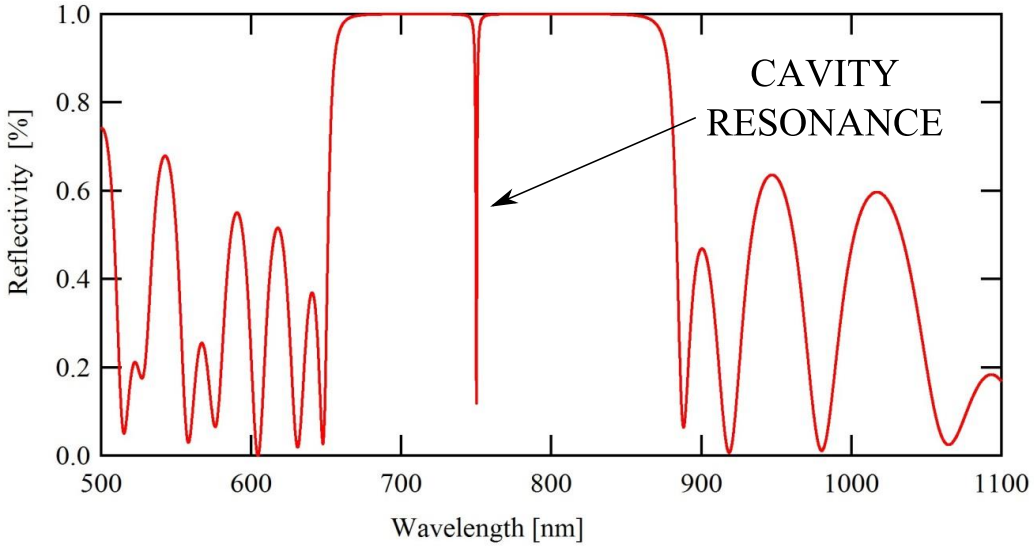

FIGURE 2.8: Reflectivity spectrum of a typical microcavities simulated by using two DBRs like the one reported in Fig.2.7 and a cavity AlAs layer of thickness $\lambda/2n_{AlAs}$. The dip in the reflectivity spectrum corresponds to the first eigenmode (N=1). This spectrum has been calculated with the the transfer matrix method reported in Appendix B.

modes ω_m of the microcavity are defined by

$$\omega_m = \frac{N\pi c}{L_{eff} n_c} \tag{2.15}$$

where N is an integer (N=1 is the first mode), c the speed of light, n_c and L_{eff} respectively the refractive index and the effective length of the cavity. The effective length L_{eff} of the cavity represents one of the main difference between semiconductor microcavities and metallic cavities. In particular, the penetration of the cavity field inside the DBRs is much larger for a semiconductor microcavity [30]. Consequently, the effective cavity length is extended and defined by [90]

$$L_{eff} = L_c + L_{DBR} \tag{2.16}$$

with L_c being the thickness of the cavity and L_{DBR} the mirror penetration depth defined as [90]:

$$L_{DBR} = \frac{\lambda_c}{2n_c}\frac{n_a n_b}{(n_b - n_a)} \quad (n_a < n_b), \tag{2.17}$$

where n_a and n_b are the the refractive indices of the DBR layers.

Real DBRs mirrors have a finite transmission probability [36] which corresponds to a finite probability for light to tunnel through the cavity even within the stop bands of the mirrors. Consequently the cavity mode is broadened and has a finite full width half maximum (FWHM) Δ_c, which for $R \to 1$ is given by [90]:

$$\hbar\Delta_c = \frac{\hbar c\ (1-R)}{n_c L_{eff}} \tag{2.18}$$

An important parameter for a microcavity is represented by the so called quality *Q-factor*, which is defined as the ratio between the resonant cavity frequency ω_c and the linewidth (FWHM) of the cavity mode $\delta\omega_c$ [77]:

$$Q = \frac{\omega_c}{\delta\omega_c} \tag{2.19}$$

The lifetime of the photons confined inside the cavity is directly connected with the quality Q-factor. The higher is the Q-factor (i.e. the smaller will be the FWHM of the cavity mode) the higher will be the lifetime of the photons confined into the cavity.

2.3.2 Photons in microcavity

Like in the case of an exciton confined in a QW (described in section 2.2.2), a photon confined in a high Q cavity will experience a quantization of its wave vector (k_z) in the direction of growth of the structure (z-direction) [36]:

$$k_z = \frac{2\pi}{L_c} \tag{2.20}$$

with L_c being length of the cavity. On the other hand, the wave vector ($k_{||}$) of the photon in the x-y plane will not be quantized. Therefore, just as for electronic state in

a QW the photon has an in-plane dispersion. From the total wave vector of the photons inside the cavity, i.e., $k_{tot}^2 = k_z^2 + k_{||}^2$, the energy dispersion (E_c) of the photons confined into the cavity can be calculated by Taylor expansion and corresponds approximately to [36]:

$$E_c \cong \frac{\hbar c}{n_c} k_{tot} = \frac{\hbar c}{n_c} \left[\left(\frac{2\pi}{L_c} \right)^2 + k_{||}^2 \right]^{1/2} \tag{2.21}$$

For small wave vector $k_{||}$, the energy dispersion corresponds to a parabola and, like

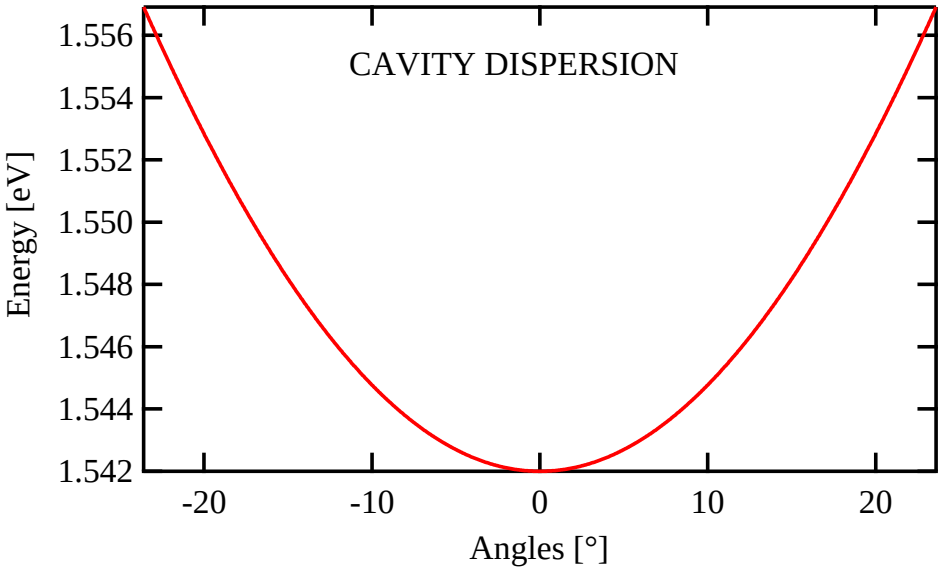

FIGURE 2.9: Typical parabolic dispersion of photons confined in a cavity.

an exciton confined in a QW, also the photon confined inside the cavity acquires an effective mass (m_{ph}^*), defined by [36]:

$$m_{ph}^* = \frac{h n_c}{c L_c} \tag{2.22}$$

which is typically of the order of $\sim 10^{-5} m_e$ with m_e being the free electron mass [91]. The photonic dispersion can be measured directly in angle turning experiments, because $k_{||}$ is directly proportional to the angle of incidence θ. In particular, the in-plane photonic mode dispersion is given by:

$$k_{||} = \frac{E_c(k)}{\hbar c} sin\theta \tag{2.23}$$

A typical example of parabolic photonic dispersion inside the cavity is shown in Fig.2.9. One of the main consequences of the equation 2.23 is that by changing the external angle of incidence, a particular $k||$ can be selected.

2.4 Microcavity polaritons: mixed exciton-photons states

2.4.1 What is a polariton?

When excitons confined into the QW (Section 2.2.1) strongly interact with photons confined into the cavity (Section 2.3.1), the eigenstates inside the microcavity are no longer the bare exciton and photon modes but a superposition of the two called exciton-polaritons or simply polaritons. Due to their mixed bosonic nature, i.e. half-light half-matter, polaritons inherit many of their properties from their components. In particular, from the photonic component they inherit a very light mass which is $10^{-4} - 10^{-5}$ times the mass of the free electron, while from the excitonic component the tendency to interact each other at high densities. Like in the case of confined excitons and photons, all the important properties of polaritons can be derived from its non-parabolic dispersion. Moreover, like all the other bosons, polaritons carry an integer spin which is also determined by the spin of the photons and excitons. The spin of polaritons will be discussed in details in section 2.7.

From the experimental point of view, one of the main advantage of polaritons is related to the fact that many of their properties can be directly accessed with well established optical techniques by measuring the light emitted from the cavity. This is due to the fact that the photons emitted from the cavity conserve the same energy, momentum ($k_{||}$) and spin of polaritons. Therefore, equation 2.23 which relates the in-plane wave vector to the angle of incidence of light, applies also in the case of polaritons. In the next section a more quantitative description of polaritons will be presented. In Table 2.1 some of the physical properties of polaritons are reported and compared with the atomic and excitonic case.

TABLE 2.1: Physical properties of polaritons compared with atomic gases and excitons as reported in Ref. [30]. Here m_e is the free electron mass.

Systems	Polaritons	Atomic gases	Excitons
Effective mass m^*/m_e	10^{-5}	10^{3}	10^{-1}
Bohr Radius a_B	10^{2} Å	10^{-1} Å	10^{2} Å
Lifetime τ	$(1-10)\ ps$	$1\ s$	$1\ ns$

2.4.2 Strong coupling

In order to maximize the interaction between the exciton and the photon, the QWs are placed at the antinodes of the resonant optical field inside the semiconductor microcavity [30] as shown schematically in Fig.2.10 a). In this way, if the the exciton energy is chosen to be at, or close to, resonance with the cavity mode [36], photons confined into the cavity strongly interact with the heavy hole excitons confined into the QWs. The physical origin of this interaction is to first order the coupling between the electric field ($\vec{E}$) and the dipole moment of the exciton ($\vec{\mu}$) which corresponds to a transfer of energy ($E = \vec{\mu} \circ \vec{E}$) between the exciton and photonic modes [92]. Depending on the rate ($g = E/\hbar$) at which excitons and photons exchange energy, different regimes can be individuated. In particular, when the rate of energy transfer (g) between the two modes is faster than the decays of photons (k) and excitons (γ), the so called *strong coupling regime* occurs ($g >> k, \gamma$) [92]. In this regime, the spontaneous-emission process of a photons becomes reversible, namely photons emitted by the excitons are absorbed and emitted multiple times before to leave the cavity, making the excitation energy of the system oscillate between the QW exciton and photon modes (Rabi oscillation). In the frequency domain, this corresponds to the appearance of two modes split around the QW exciton resonance which correspond to the two polariton eigenmodes of the microcavity. The distance between the two polariton modes corresponds to the so called Rabi splitting (see equation B.7 in Appendix B). This is shown in Fig. 2.10 b) and c), where the reflectivity spectrum of the bare cavity, previously shown in Fig. 2.7, exhibits two dips when the resonant condition is reached, namely when the frequency of the microcavity resonance (ω_{cav}) and the exciton resonance (ω_{ex}) are equal ($\omega_{cav} = \omega_{ex} = \omega_0$). The two dips appear at frequencies $\omega_{\pm} = \omega_0 \pm g$ and correspond to the solid-state analog of the vacuum Rabi splitting in the atom-cavity case [93].

The experimental observation of the Rabi splitting in the reflectivity spectrum of a microcavity with embedded QWs, was made for the first time by Weisbuch et al. [7]. In their work, the authors showed that the Rabi splitting corresponds to an *anticrossing* of the exciton-polariton modes, as shown in Fig. 2.11, when the energy of the cavity mode is scanned across the excitonic resonance (i.e. at different detunings). The observation of the anticrossing of the two polariton modes is still considered a clear signature of the strong coupling regime.

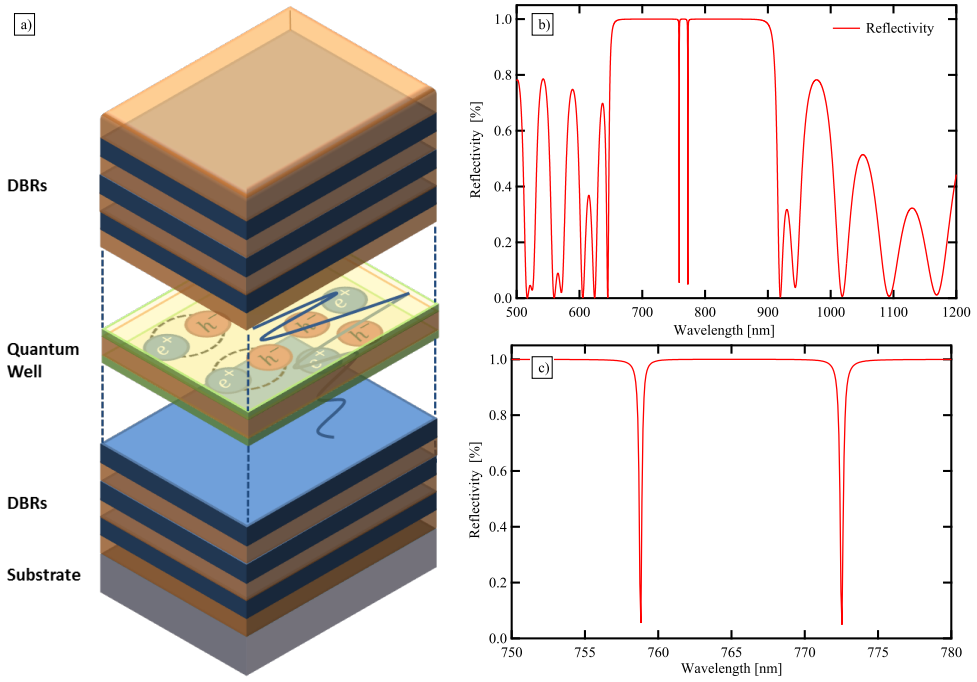

FIGURE 2.10: a) Schematic representation of a microcavity with an embedded quantum well placed at the antinode of the electric field (blue). The DBRs consist of alternating layers of different semiconductor materials, represented in blue and brown. b) Reflectivity spectrum of a typical microcavities simulated by using two DBRs like the one reported in Fig.2.7, with number of pairs of layers $N_{SiO_2} = N_{Ta_2O_5} = 8$, a cavity AlAs layer of thickness $\lambda/2n_{AlAs}$ (Fig.2.8) and one GaAs QW embedded at the center of the AlAs layer. c) Magnification of the spectrum b) on the two polariton resonance peaks. Both these spectra has been calculated with the the transfer matrix method reported in Appendix B.

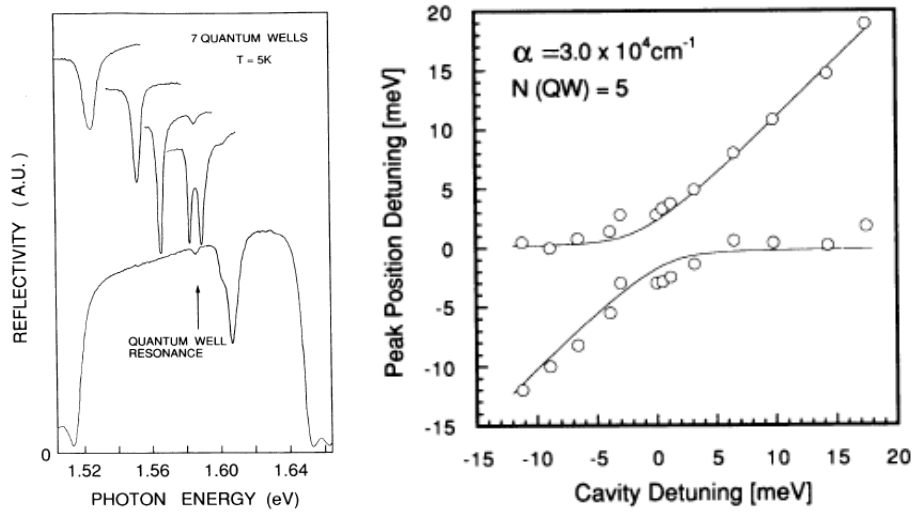

FIGURE 2.11: On the left, experimental reflectivity curves at different detunings showing the resonance mode splitting at the resonance energy (1.605 eV). On the right, reflectivity peak positions as a function of cavity detuning showing the anticrossing of the two polariton modes. Both figures were shown in the seminal work of Weisbuch et al.[7] which corresponds to the first observation of Rabi splitting in polariton microcavities.

2.4.3 Theoretical picture

From the theoretical point view, the strong coupling (i.e. strong interaction) between the cavity photon and the QWs exciton can be modeled as two dumped coupled harmonic oscillators. As discussed before, when the energy transfer between the two modes becomes larger than the decay rates, the two oscillators (i.e. the exciton and the photons), initially oscillating with different resonance frequencies, couple together by exchanging energy periodically (with period $2\pi/g$) for a certain number of periods, before the energy escapes the system [92]. As a consequence, the energy spectrum of the system is profoundly modified by the coupling and new modes, with frequencies different from those of the original oscillator modes, appear [94]. The new modes corresponds to the polariton modes, which are a mix of the original modes of the two oscillators.

Since the the theory of two harmonic oscillator can be treated by means of both a semiclassical and a quantum approach, both methods have been proposed to model the strong interaction between photons and excitons inside a microcavity [90, 95]. The two approaches are equivalent and produce the same results. General speaking, the semiclassical theory is more convenient for the computation of reflectivity, transmission and absorption spectra because it can be formulated with the Transfer Matrix method [90]. This method is the one used to calculate the spectra reported in Fig. 2.10 b) and Fig. 2.10 c) and is discussed in details in the Appendix B. In the following text the key points of the quantum theory are summarized.

The separation in energy between the two polariton modes is directly connected with the coupling energy between the photons confined into the cavity and the exciton confined into the QWs. The Hamiltonian of the coupled exciton photon system is [30]:

$$\widehat{H}_{pol} = \widehat{H}_{cav} + \widehat{H}_{exc} + \widehat{H}_I = \sum_{k_{||}} E_C(k_{||}) a^{\dagger}_{k||} a_{k||} + \sum_{k_{||}} E_X(k_{||}) b^{\dagger}_{k||} b_{k||} + \sum_{k_{||}} \hbar\Omega_R (a^{\dagger}_{k||} b_{k||} + b^{\dagger}_{k||} a_{k||}), \tag{2.24}$$

where $a^{\dagger}_{k||}, a_{k||}, b^{\dagger}_{k||}$ and $b_{k||}$ are respectively the creation and annihilation operators for photons and excitons with the corresponding in-plane wave vector $k_{||}$. The first two terms of the right hand side (RHS) of the equation 2.24 represent the term of the unperturbed system, with E_C and E_X being respectively the energy dispersion of the excitons and photons as discussed in sections 2.2.1 and section 2.3.1. The last term of the

RHS of equation 2.24, on the other hand, describes the interaction between exciton and photon modes, with $\hbar\Omega$ the interaction energy between the two modes. By diagonalizing the Hamiltonian 2.24, the eigenergies of the new eigenstates can be calculated. They corresponds to the eigenvalue of the matrix [96]:

$$M(k_{||}) = \begin{pmatrix} E_x(k_{||}) & \hbar\Omega \\ \hbar\Omega & E_c(k_{||}) \end{pmatrix} \tag{2.25}$$

which are given by [96]:

$$det(M - \lambda I) = 0 \Rightarrow (E_X - \lambda)(E_C - \lambda) - \hbar^2\Omega^2 = 0. \tag{2.26}$$

By solving the equation 2.26, two solutions can be found [96]:

$$\lambda_{1,2} = E_{UP,LP}(k_{||}) = \frac{E_C(k_{||}) + E_X(k_{||})}{2} \pm \frac{1}{2}\sqrt{(E_C(k_{||}) - E_X(k_{||}))^2 + 4\hbar^2\Omega^2} \tag{2.27}$$

which correspond to the so called *upper* (E_{UP}) and *lower* (E_{LP}) polariton energies. The energies dispersion of the upper (UP) and lower (LP) polariton modes are shown on the left column of Fig. 2.12. From equation 2.27 follows that at zero detuning, i.e. when $E_{exc} = E_{cav}$, the two polariton energies have the minimum separation, which corresponds to $E_{UP} = E_{LP} = 2\hbar\Omega$ and define the Rabi splitting in polariton microcavity, as shown in Fig. 2.12 c).

The new eigenstates of the systems are now a superposition of the photons and exciton modes. In particular, the exciton and photon fractions in each LP and UP is given by the amplitude squared of the Hopfield coefficients [97], which are [30]:

$$\left|X_{k_{||}}\right|^2 = \frac{1}{2}\left(1 + \frac{\Delta E(k_{||})}{\sqrt{\Delta E(k_{||})^2 + 4\hbar^2\Omega^2}}\right) \tag{2.28}$$

$$\left|C_{k_{||}}\right|^2 = \frac{1}{2}\left(1 - \frac{\Delta E(k_{||})}{\sqrt{\Delta E(k_{||})^2 + 4\hbar^2\Omega^2}}\right) \tag{2.29}$$

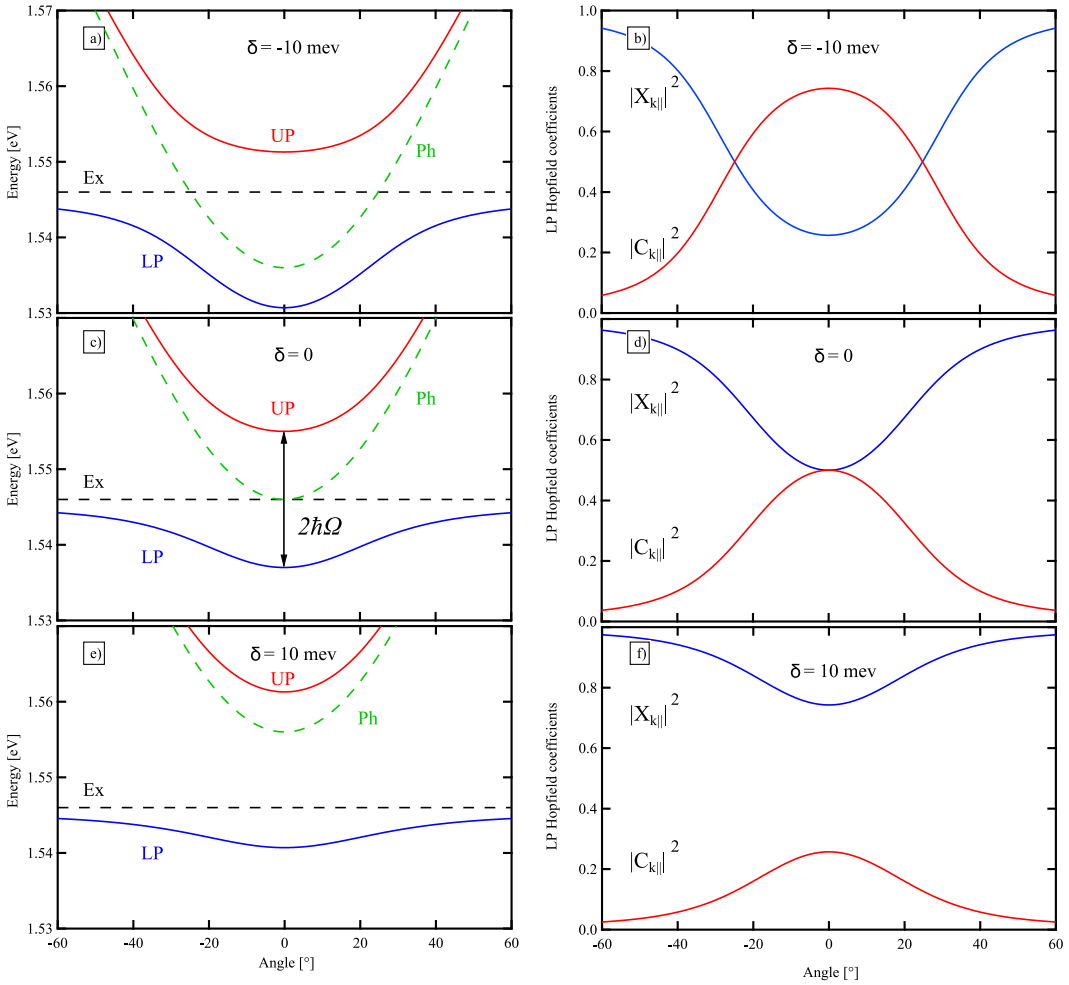

FIGURE 2.12: In the left column (a,c,e) the upper (red) and lower (blue) polariton dispersions together with the initial uncoupled exciton (dashed black line) and photon (green dashed line) dispersions are calculated respectively for a) negative , e) zero and f) positive detuning between the cavity and the exciton mode. In the right column (b,d,f) the corresponding Hopfield coefficients for the lower polariton dispersions are reported. The images reported here have been calculated with a program developed by Elena Kammann.

where $\Delta E(k_{||}) = E_X - E_C$ is the detuning between the exciton and the cavity modes. $\left|X_{k_{||}}\right|^2$ and $\left|C_{k_{||}}\right|^2$ quantify respectively the exciton and photon fraction of the polariton modes and are characterized by the normalization condition:

$$\left|X_{k_{||}}\right|^2 + \left|C_{k_{||}}\right|^2 = 1 \tag{2.30}$$

In Figure 2.12 the Hopfield coefficients for the lower polariton branch (LP) in the case of negative ($\delta < 0$), zero ($\delta = 0$) and positive ($\delta > 0$) detunings are shown. In the case of zero detuning, shown in Figs. 2.12 c) and d), the LP polariton dispersion is half photonic, half excitonic. On the other hand, at negative [Figs. 2.12 a),b)] and positive

[Figs. 2.12 e), f)] detunings, the LP polariton dispersion becomes respectively more photon- or exciton-like.

2.4.4 Weak coupling

On the basis of the discussion reported in section 2.4.2, when the rate of energy transfer (g) between the exciton and photon modes becomes smaller than the decays of photons (k) and excitons (γ), i.e. $g << k, \gamma$ the system is said to be in the *weak coupling regime* [92]. In this regime photons and excitons do not interact strongly with each other and the spontaneous emission of photons becomes irreversible and dissipative. In the case of weak coupling regime, which is typical of vertical-cavity surface emitting laser (VCSELs) there is no splitting between polariton eigenmodes at the crossing point [98]. In this regime, however, the exciton fraction in the polariton mode is not zero.

2.5 Excitation and relaxation mechanism

Polaritons in microcavity can be generated by means of three mainly excitation schemes: resonantly, non-resonantly and by parametric excitation. All the experiments reported in this thesis have been realized under non resonant excitation. As a consequence, the following discussion will focus mainly on this excitation scheme.

2.5.1 Non-resonant excitation

The non-resonant excitation is realized by tuning the pumping laser to the first reflectivity minimum above the high-reflectivity mirror stopband, as shown in Fig. 2.13 a). This corresponds to the creation of an electron-hole plasma at energy higher than the polariton dispersion which then relax in energy to populate the polariton dispersion.

In the case of non-resonant excitation, the relaxation process can be summarized as follow:

1. The excitation laser, at energy higher than the LP dispersion (generally $\sim 100\, meV$ above the LP), creates electron-hole pairs in the cavity and in the QWs above the semiconductor band gap.

2. The excess of energy of the free electron and holes is transferred to the lattice through the emission of longitudinal-optical (LO) phonons [99, 100] ($< 1\,ps$) followed by slower ($\sim 1\,ns$) acoustic phonon relaxation toward the high k exciton states on the exciton dispersion [8].

3. Here, due to the Coulomb interaction, electrons and holes bind together in pairs to form excitons. As excitons are formed, they accumulate at higher energy and wave vector compared to the polariton dispersion and form the so called *exciton reservoir*. These excitons do not couple to light because they have a wave vector larger than the light wave vector in the medium.

4. The exciton then relax in energy, from the reservoir to the region at high k of the polariton dispersion, as schematically shown in Fig. 2.13 b). The additional dissipation of energy, needed by the excitons to relax down toward the LP branch, is obtained through the emission of acoustic phonons.

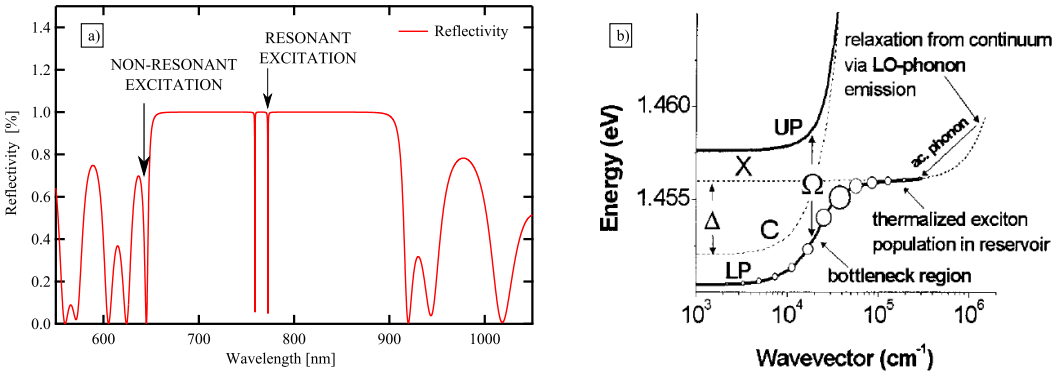

FIGURE 2.13: a) Resonant and non-resonant optical excitation scheme indicated on a typical reflectivity spectrum of microcavity sample. b) Relaxation mechanism in non-resonant excitation scheme as reported in Ref. [8]. Here UP and LP indicate respectively the upper and lower polariton branch (thick lines), X the uncoupled exciton dispersion and C the uncoupled cavity mode dispersion. The polariton population is represented schematically by the open symbols, with the maximum occurring at the edge of the polariton trap. Image taken form Ref. [8].

At this stage polaritons are formed but they do not strongly populate the bottom of the LP dispersion, i.e. the $k \sim 0$ region. Instead, they are more likely to accumulate in the region of the dispersion with higher wave vector ($k > 0$). This effect, known as "bottleneck effect" [101], occurs because the relaxation mechanism involving the emission of acoustic phonons is very inefficient due to the very steep energy dispersion of polariton states [102]. In this region the effective polariton mass is reduced from nearly the exciton mass to twice the photon mass, leading to a decrease of the density of states of the LPs

by four order of magnitude [10]. Moreover, the lifetime of the LP decreases from nearly the exciton lifetime ($\sim 500\,ps$) to photon lifetime ($\sim 10\,ps$) [10]. The process assisted by the acoustic phonons, on the other hand, needs about 50 ps, longer than the polariton lifetime in this region of the dispersion [77]. As a consequence, polaritons are more likely to populate the higher energy states of the dispersion from where the light is mainly emitted [103], i.e. polaritons escape from the cavity before to reach the states at $k = 0$. Thus, in angle and energy resolved experiments, the bottleneck effect results in the observation of a two-lobe emission patterns at $|k| > 0$ from the LP dispersion. However, by increasing the intensity of excitation, the excitons density increases and the bottleneck effect can be overcome thanks to the exciton-exciton scatterings [104] and LP-LP scattering [10] similar to the OPO scheme described in the next section 2.5.2. Thus, at higher density, when the polariton relaxation rate prevails on the radiative losses, a high occupation of polaritons in the bottom part of the dispersion (at $k = 0$) and a consecutive superlinear increase of the emission, can be observed [8, 10]. The relaxation mechanism just described lies at the basis of the polariton laser (section 2.6) and condensation (section 3.2.1) described in the next chapter.

It is worth noting that a very important role is played by the exciton reservoir in the condensation process. Polaritons, in fact, have a finite lifetime and leak out of the cavity through the DBR mirrors within $\sim$ 10 ps. Thus, the condensate is continuously replenished by the pump laser that creates a reservoir of hot excitons, which then relax in energy on the lower polariton dispersion and form polaritons. The exciton lifetime in the reservoir is usually much larger ($\sim$0.5 - 1 ns) than polariton lifetime.

2.5.2 Resonant and parametric excitation

As mentioned before, polaritons can also be excited resonantly. In the resonant excitation, the laser is tuned to the energy corresponding to the LP branch at a fixed wave vector (Fig. 2.13). The main difference with the non-resonant excitation are two:

1. In the case of resonant excitation, polaritons are generated directly on the polariton dispersion and the process is not mediated by the population of an exciton reservoir.

2. In resonant excitation, the phase of the polariton field and consequently its spatial and temporal coherence, are mainly determined by the excitation laser.

Finally, the parametric excitation scheme represents an intermediate case between the resonant and non-resonant case. In this scheme, polaritons are injected resonantly, at an energy above the ground state, by exciting the LP dispersion at a fixed angle (the so called magic angle) close to the inflexion point of the LP. Due to the conservation of energy and wave vector, two polaritons both with momentum k_p can elastically scatter in two different states on the LP dispersion, one at the ground state ($k_{signal} = 0$), called signal state, and the other at an excited state ($k_{idler} = 2k_p$), called idler. In this case the system is said to be in the optical parametric oscillator (OPO) regime [41], since a laser photon is converted into two polaritons.

As for the case of resonant pump, also in parametric excitation scheme polaritons are directly injected in the system and the exciton reservoir does not play a relevant role (point 1 above). On the other hand, differently from the resonant case (point 2 above), here only the sum of the idler and the signal is fixed by the pump laser while the single phase of the signal and the idler are chosen spontaneously due to the scatter [72].

2.6 Polariton laser

The possibility of realizing a polariton laser was first proposed by Imamoglu et al. [37] followed by the experimental observation in microcavity sample at both helium [10] and room temperature [42] under optical pumping. Recently, the implementation of electrically injected polariton laser has also been reported in GaAs [52] and in GaN at room temperature [53].

To demonstrate polariton lasing, the use of a non resonant excitation scheme (section 2.5.1), is preferred since it ensures that the original coherence of the laser is lost in the relaxation process. As discussed in section 2.5.1 and schematically represented in Fig. 2.14 a), the non resonant excitation produce a hot cloud of electrons and holes that relax down in energy toward the LP dispersion, dissipating their energy by phonon emission (i.e., scattering with the lattice). Due to the bottleneck effect, polaritons are more likely to populate the higher energy states of the dispersion from where the light is mainly

emitted [103]. However, by increasing the excitation power density, the excitons density also increases and the bottleneck effect can be overcome thanks to the elastic scattering of two polaritons into one near $k = 0$ and another one at higher energy [10]. This process is similar to the OPO described in section 2.5.2. The higher energy polariton can then relax again via phonon emission [9].

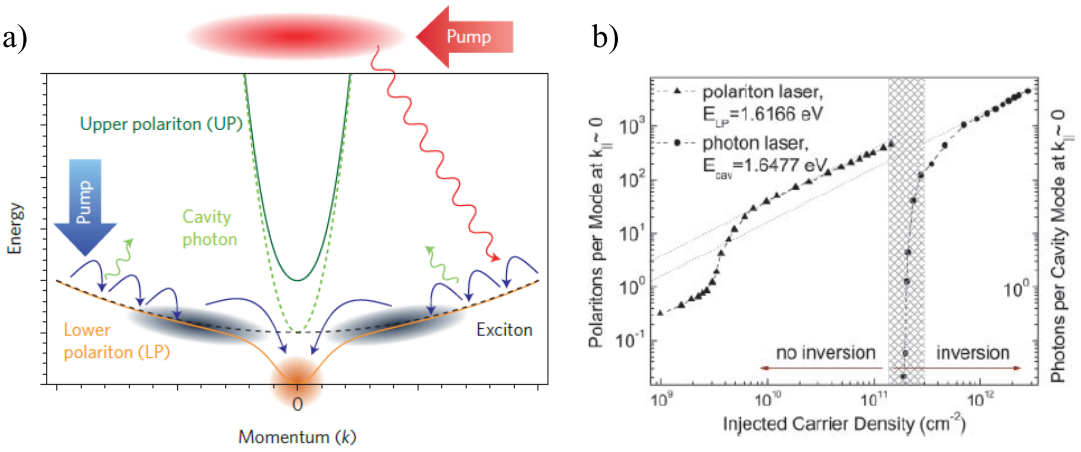

FIGURE 2.14: a) Schematically representation of the relaxation process under resonant (big blue arrow) and non-resonant (big red arrows) pumping scheme. High-energy excitons, generated by the pump laser, cool down via phonon emission (small blue arrows) towards the LP dispersion and accumulate in the bottleneck region (black clouds). At sufficient high density exciton-polaritons scatter into the condensate (orange cloud) via stimulated cooling. The image has been taken from Ref.[9]. b) Polariton population at bottom of the LP dispersion, i.e., at $k = 0$, for a polariton laser as a function of the pump power as reported in Ref. [10]. In the region labeled with "inversion", the threshold for photon laser measured on the same sample is reported for comparison.

When the LP population in the $k = 0$ states exceeds unity, the cooling of polariton toward $k = 0$ is enhanced by the bosonic final state stimulation [10, 103]. Due to the bosonic nature of polaritons, the probability (P) of non condensed polaritons scattering into the condensate at $k = 0$ is proportional to the number of condensed polariton already presents N_{final}, i.e., $P \propto (1 + N_{final})$, where 1 describes spontaneous processes [105, 106]. Thus, at higher density, when the polariton relaxation rate prevails on the radiative losses, a high occupation of polaritons in the bottom part of the dispersion ($k = 0$) and a consecutive superlinear increase of the emission, can be observed [8, 10]. This effect, known as Bose stimulation, is the at the basis of the formation of the Bose-Einstein condensate [106] (described in detail in the next chapter) and represents the gain mechanism in an optical laser where the presence of photons in the lasing mode stimulates the emission of more photons into it [105, 106]. The light emitted form the

condensate at $k = 0$ pass thorough the DBRs and presents all the main properties of a conventional laser light, i.e. it is monochromatic, unidirectional and coherent [98]. However, unlike conventional lasers, the polariton laser present many differences. In particular:

- in a conventional laser the stimulated emission takes place only if an inversion of population is realized, namely when the population of the excited state is greater than the population of the ground state. In the case of polaritons, on the other hand, no inversion of population is required and the underlying mechanism for the emission of a coherent light is due to the *stimulated scatter* of polaritons toward the condensate (i.e. bosonic final state stimulation) and not to the *stimulated emission* as in the convention laser.

- A polariton laser has no threshold linked to the population inversion and amplification of light in polariton lasers is governed by the ratio between the lifetime of exciton polariton and their relaxation time towards the condensate [98].

- Although both the laser and the polariton condensate emit coherent light, in the first case the particles that become coherent are photons while in the second are polaritons [9]. The superlinear emission, in fact is observed at the bottom ($k = 0$) of the LP dispersion [8, 10].

- In a polariton laser the system is in the strong coupling regime (section 2.4.3), while a conventional VCSEL laser emits in the weak coupling regime (section 2.4.4) [9].

- Polariton laser emits at threshold carrier density which is two orders of magnitude lower than carriers needed for a normal photon laser in the same structure [10], as shown in Fig.2.14 b).

Although the above mentioned properties draw a clear line between VCSEL and polariton laser, the very short life time of polariton ($\sim 10\,ps$) compared to the thermalization time, makes this distinction less defined. The macroscopic occupation of the lowest state, underling the polariton laser, would suggest the formation of a Bose-Einstein condensate (see section 3.1). Whether if this condensate is formed in a polariton microcavity is still matter of discussion, as discussed in section 3.2.2.

2.7 Spin of polaritons

Polaritons are bosons and as such have an integer spin. As many other properties, also the spin of polaritons is determined by its constituents, the excitons confined into the QW and the photons confined into the cavity. In the same way, the spin of an exciton is determined by the spin of the electron in the conduction band and the hole in valence band. Thus, the spin of polaritons is ultimately related with the band structure of the GaAs QWs. As discussed in section 2.2.2, in a QW the confinement effect lifts the

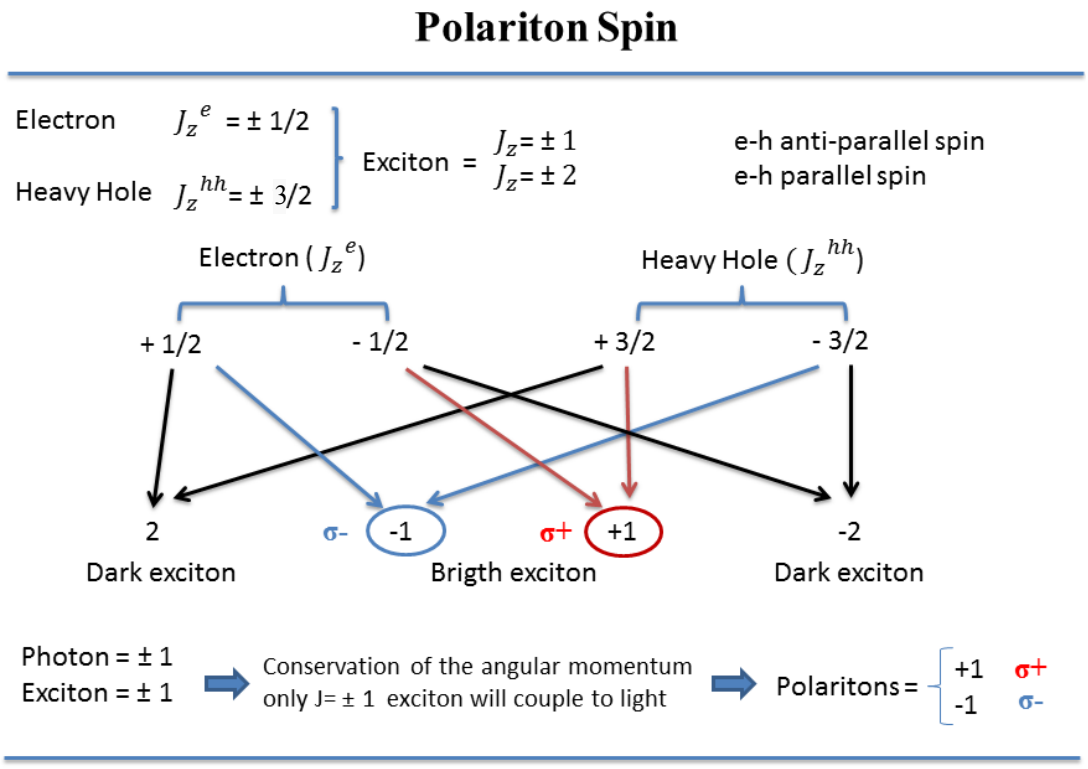

FIGURE 2.15: Schematic diagram summarizing the origin of the polariton spin. The arrows of the same color indicate the electron (J_z^e) and heavy hole (J_z^{hh}) values of the angular momentum that are added together to obtain the total angular momentum of the ground state exciton J_z inside the quantum well.

degeneracy of the hole state, so that the light-hole and heavy hole have different energy, with the heavy hole energy level closer to the conduction band than the light hole levels (Fig. 2.5). Therefore, inside the QWs, the projection of the total angular momentum (J_z) along the structure-growth axis (z), that is $J_z = l + s$, with l being the orbital angular momentum and s the spin, will be [107]:

- $J_z^e = \pm 1/2$ for electrons in the conduction band;

- $J_z^{lh} = \pm 1/2$ for light holes. In particular, they form when the spin projection of the hole s is anti-parallel to its orbital angular momentum l;
- $J_z^{hh} = \pm 3/2$ for heavy hole. In this case the projection of the spin s and its orbital angular momentum l are parallel.

Since the heavy hole states are at higher energies than the light holes, inside the QWs the exciton ground state is composed by an electron-heavy hole pair. Therefore, the total angular momentum of the exciton inside the QWs can have projections $J_z = \pm 1$ and $J_z = \pm 2$ on the structure-growth axis (z). This can be directly demonstrated by considering all the possible combinations in summing up the J_z^e of an electron and the J_z^{hh} of an heavy hole, as schematically shown in Fig. 2.15. The exciton states with $J_z = \pm 1$ and $J_z = \pm 2$ are split in energy due to the electronhole exchange interaction [107]. It is common, for convenience, to refer to the total angular momentum of the exciton as the exciton spin [77]. In the following, this denomination will be used.

Like electrons and holes, also photons have a spin angular momentum. In particular, photons of left (σ_+) or right (σ_-) polarized light have a projection of the angular momentum on the direction of their propagation (i.e. the helicity) equal respectively to $+1$ or -1 (in units of $\hbar$) [108]. A superposition of these two states, on the other hand, corresponds to linearly polarized photons.

Consequently, since in the photoabsorption process the spin of the photon is conserved, when a circularly polarized photon is absorbed only excitons with spin projections ± 1 can be optically excited and will couple to light, giving rise to polaritons with spin $S_z = \pm 1$. Thus, polaritons possess a spin with two possible projections of the angular momentum ($S_z = \pm 1$) on the structural growth axis (z) of the microcavity, which correspond to the left (σ_+) and right (σ_-) circular polarization of the photon and to the same spin component of the exciton. Superpositions of ($S_z = \pm 1$) states give rise to the linear or elliptical polarization of exciton polaritons [109]. It is common to refer to the exciton states with spin projections ± 1 as *bright states*. On the other hand, the exciton with spin projection ± 2 will not couple to light, i.e. cannot be optically excited and are usually called *dark states* [77].

2.7.1 Poincarré sphere

As discussed in the previous section, polaritons possess a spin with two possible projections of the angular momentum (± 1) on the structural growth axis (z) of the microcavity.

From the theoretical point of view, it is convenient to describe the spin dynamics of exciton-polaritons in terms of the pseudospin formalism [110], in which the polarization of the light emitted from the cavity is characterized by the four-component Stokes vector $\vec{s} = (s_0, s_x, s_y, s_z)$, where:

$$S_0 = \sqrt{S_x^2 + S_y^2 + S_z^2}, \tag{2.31}$$

is the total degree of polarization, while:

$$S_x = \frac{I_H - I_V}{I_H + I_V}, \qquad S_y = \frac{I_D - I_{AD}}{I_D + I_{AD}}, \qquad S_z = \frac{I_{\sigma_+} - I_{\sigma_-}}{I_{\sigma_+} + I_{\sigma_-}}. \tag{2.32}$$

are respectively the linear (S_x), diagonal (S_y) and circular (S_z) polarizations. Here I_{H,D,σ_+} and I_{V,AD,σ_-} are the intensities of the different polarization components, i.e. Horizontal (H), Vertical (V), Diagonal (D), Anti-diagonal (AD), Left-Circular (σ_+) and Right-Circular (σ_-). The intensity reported in 2.32 can be measured by using a polarimeter described in section 4.2.3. The formula 2.31 represents the equation of a

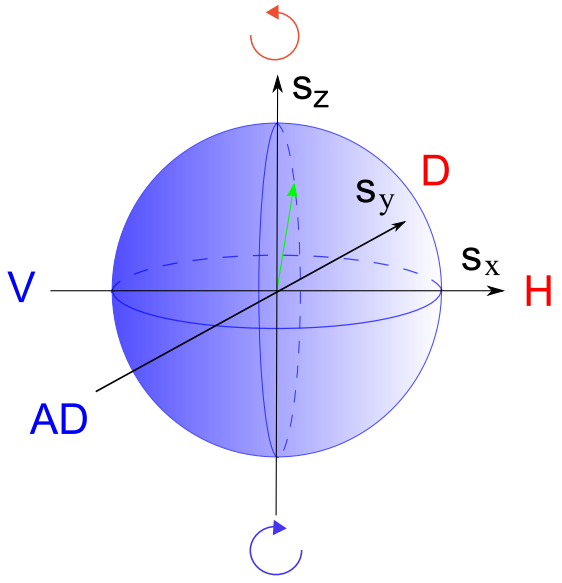

FIGURE 2.16: Poincarré sphere with the green arrow representing the pseudospin vector. The equators of the sphere correspond to different linear polarizations, while the poles correspond to two circular polarizations.

sphere in the (S_x, S_y, S_z) set of coordinates. It is common to refer to this sphere as

Poincarré sphere. The Stokes parameters constitute the cartesian coordinates of the polarization state, which is represented by a point on the surface of the sphere. The radius of the Poincarré sphere, instead, corresponds to the total intensity of the polarized part of the signal [110]. The components of Stokes vector have a direct analogy with the components of the quantum-mechanical pseudospin. For the latter, in fact, it is possible to use the Poincarré representation as well, in order to defines the different degree of polarization. As it is shown in figure 2.16, the equators of the sphere correspond to different linear polarizations, while the poles of the sphere correspond to two circular polarizations. Therefore the different degrees of polarization are tightly related to the different positions of the pseudospin vector in the sphere. In particular:

- the pseudospin vector orientated along the x-axis corresponds to horizontal (H) or vertical (V) polarized light (where H or V depends on the orientation of the pseudospin vector, respectively parallel or antiparallel to the x-axis);
- the pseudospin vector orientated along the y-axis corresponds to diagonal (D) or antidiagonal (AD) polarized light (with D parallel and AD antiparallel to the x-axis)
- the pseudospin vector orientated parallel to the z-axis corresponds to left-circular (σ_+), antiparallel to the right-circular (σ_-) polarized light.

Chapter 3

Polariton condensate and oblique dark solitons

Since its first theoretical prediction by the works of Bose [111] and Einstein [112] in 1924, Bose-Einstein condensate (BEC) has been extensively studied over the course of the last century and still today represents one of the most fascinating phenomena which continues to attract research interest. After its first experimental observation in 1995 with a vapor of rubidium-87 atoms at a temperature of 170 nK [113], BEC was studied in many other systems. In this regard, solid-state systems occupy a privileged position since quasiparticles (Section 2.1.2), such as excitons (Section 2.2.1) in semiconductor and polaritons (Section 2.4.1) in microcavity, are characterized by a smaller mass compared to the atomic case. As a consequence, they can undergo BEC at temperatures of $\sim (10 - 300)K$, several orders of magnitude higher than the atomic case. The possibility of observing BEC at temperatures accessible with standard cryogenic techniques is at the basis of the intense research which has characterized the polariton field during the last decades.

In the following chapters, after a brief introduction of the BEC theoretical formalism (Section 3.1.1), the main experimental evidence of polariton BEC is presented (Section 3.2.1). The second part of this chapter, is devoted to nonlinear effects in BEC, with particular emphasis on oblique dark solitons (Section 3.4). The chapter terminates with a brief section dedicated to polariton bright solitons (3.5).

3.1 Bose Einstein condensation

3.1.1 Ideal gas of bosons

As anticipated in the introduction, Bose and Einstein were the first to predict that a gas of non-interacting bosons can macroscopically occupy the ground-state, i.e. '*condense*' in the same quantum state, when the temperature is brought below a critical value. In first place, this is possible because *bosons* do not follow the Pauli exclusion principle which, instead, forbids fermions to share the same quantum state. This properties lie at the basis of Bose-Einstein condensation.

Bosons are particles with integer spin described by a symmetric wavefunction, which follows the Bose-Einstein statistics (from which they inherit their name). In a gas of non-interacting bosons, the number of particles n_{BE} in the quantum state with energy E at temperature T is given by the Bose-Einstein distribution function:

$$n_{BE}(E,T) = \frac{1}{e^{(E-\mu)/k_bT} - 1}, \tag{3.1}$$

where μ is the chemical potential [1] which is determined by requiring that the combined occupancy of all the levels must be equal to the total number of particles [115]. In the limit of high temperature, equation 3.1 reduces to the Maxwell-Boltzmann distribution:

$$n_{MB}(E,T) = e^{-(E-\mu)/k_bT}. \tag{3.2}$$

On the other hand, when T tends to zero, in order to keep the distribution function 3.1 positive and thus have a physical meaning for all values of $E \geq 0$, the chemical potential has to be negative $\mu < 0$. As T decreases, μ increases and approaches zero. If now we consider the particles present in in all the possible states i, we have that the total number of particles N is given by

$$N = \sum_i n_i = n_0 + \sum_{i \neq 0} n_i \tag{3.3}$$

[1] The chemical potential μ can be calculated from the Helmholtz free energy Φ as $\mu = \left(\frac{\partial \Phi}{\partial N}\right)_{T,V}$ and represents the energy that I need to add/subtract to a system to reduce/increase the number of particles N at constant T and V [114].

where n_i and n_0, defined by equation 3.1, represent respectively the number of particles in the state i of energy E_i and in the lowest energy state $i = 0$ of energy E_0. The reason why the state n_0 is separated from the others is due to the fact that when $\mu \to 0$ and $E = 0$, equation 3.1 diverges. Thus, by studying the limit $\mu \to E_0$, it is possible to demonstrate [116, 117] that the number of bosons n_0 in the lowest energy state E_0 becomes increasingly large, while in the states at $E > 0$ remains finite and reaches a maximum value N_{cr}, when $\mu = E_0$. Consequently, if the number of particle N is larger then the critical density N_{cr} then the remaining particle must occupy the lowest energy state E_0 according to equation 3.3. Thus, the states at $E > 0$ 'saturate' and any other particle introduced in the system will occupy the ground state E_0. In the thermodynamic limit, i.e., $N, V \to \infty$ with $N, V = constant$, n_0 diverges in a such a way that the condensate fraction n_0/N approaches a finite value. This macroscopic occupation n_0 of the lowest energy level is at the basis of BEC [117].

For an ideal (i.e., non interacting) gas of Bosons, the critical particle density is

$$n_{cr}(T_{cr}) = \frac{N_{E>0}}{V} = \frac{2.612}{\lambda_{dB}^3} \tag{3.4}$$

with $N_{E>0}$ being the number of particle at $E > 0$, V the volume and λ_{dB} the de Broglie wavelength

$$\lambda_{DB} = \sqrt{\frac{2\pi\hbar^2}{mk_BT}}. \tag{3.5}$$

Here m is the mass of the particles composing the condensate, k_B the Boltzmann constant and T the temperature. From equations 3.4 and 3.5, it follows that the critical temperature (T_c) for the occurrence of BEC for a 3-dimensional gas of non interacting bosons is

$$T_c = \frac{2\pi\hbar^2}{k_Bm}\left(\frac{n}{2.612}\right)^{2/3} \tag{3.6}$$

When $T \leq T_{cr}$, the condensate fraction $n_0/N = 1 - (T/T_c)^{3/2}$.

A more intuitively condition for the occurrence of the BEC can be drawn by means of the thermal de Broglie wavelength λ_{DB}. Atoms in a gas may be regarded as quantum-mechanical wave packets which have an extent on the order of a thermal de Broglie wavelength [118]. As T decreases, λ_{DB} increases (see equation 3.5). When λ_{DB} becomes

comparable to the interatomic separation $d(n)$,

$$d(n) \sim \lambda_{DB} \tag{3.7}$$

the wavefunctions of neighboring atoms overlap. Thus, at this temperature, the atoms form an extended state with a common wavefunction, i.e. the Bose-Einstein condensate. For an ideal, i.e. non-interacting bosonic gas in three dimensions at thermal equilibrium, the critical temperature for BEC occurs when $n\lambda_{dB}^3 = 2.62$ [118].

Finally, we note that since λ_{DB} scales with the inverse of the square root of T and m, for a fixed number of bosons (i.e. at fixed density n), the BEC condition 3.7 can be fulfilled at higher temperature in the case of bosons with lighter mass. This is the case of polaritons discussed in the next section.

3.2 Polariton BEC

3.2.1 Experimental evidence

Polaritons possess an effective mass which is 10^9 times lighter than rubidium atoms. Consequently, they can theoretically undergo BEC at standard cryogenic temperature [11], i.e., at T which are several orders of magnitude higher than the atomic case. Moreover, from the experimental point of view, polaritons possess the advantage that all their main properties, such as coherence, polarization and population distribution, can be investigate by directly analyzing the light emitted from the cavity. This is due to the fact that the photons emitted from the cavity conserve the same energy, momentum and spin of polaritons, as discussed in Section 2.4.1.

From equations 3.4 and 3.6, it follows that BEC can be obtained by lowering the temperature below the critical value (T_c) for a fixed number of bosons or by increasing the density of particles at fixed T. In the case of atomic BEC the first technique has been used, while in the case of polariton BEC the second. The density of polaritons can in fact be easily increased by increasing the excitation density. In Fig.3.1 the first experimental demonstration of polariton BEC, due to Kasprzak et al. [11], is reported. In this experiment a cadmium telluride (CdTe) microcavity was excited non-resonantly with

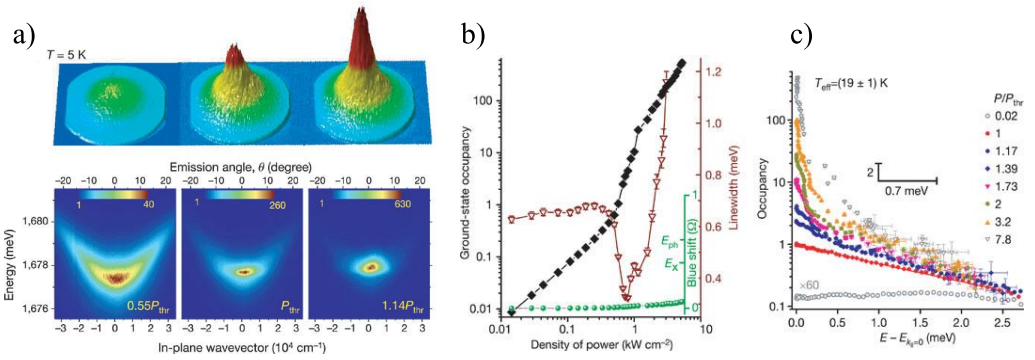

FIGURE 3.1: a) First experimental observation of a polariton condensate in momentum space. Polaritons initially broadly distributed in momentum and energy, eventually condense at $k = 0$ when the excitation power is increased above a threshold value (P_{thr}). In b) the solid black diamonds corresponds to the occupancy of polaritons at $k_{||} = 0$, the solid green circles to the energy blue shift of the condensate and the open red triangles to the linewidth of the polariton emission. All these quantities are plotted versus the excitation power. c) Polariton occupancy in ground- and excited-state levels plotted in a semi-logarithmic scale for various excitation powers. The threshold is represented by the red circles. Above threshold, the occupation of the lowest energy state increases and the ground state becomes massively occupied. Images form Ref. [11].

an excitation spot of about 35 μm. By performing power dependence measurements in momentum and real space, it was shown that:

- below condensation, polaritons are broadly distributed in both energy and momentum on the LP dispersion (left snapshot in Fig.3.1 a). As the excitation power is increased, the emission from $k_{||} = 0$ becomes predominant at the threshold power (center in Fig.3.1 a) and a sharp peak forms above threshold (right in Fig.3.1 a) [11].

- By increasing the excitation density, the polaritons population increases linearly with the pump power below threshold and nonlinearly when the threshold is reached (black line in Fig. 3.1 b). At the same time, the linewidth of the emitted polaritons shrink significantly at the nonlinear threshold (red line in Fig. 3.1 b).

- At the excitation threshold polaritons at $k_{||} = 0$ follows a Max-Boltzmann distribution (red line in Fig. 3.1 c). Above threshold, the ground state becomes macroscopically occupied and the population of polaritons at energy states higher than the ground state follows a Bose distribution. However, the low-energy part of the polariton occupancy cannot be fitted with a Bose distribution due to inter particle interactions that, in a non-ideal Bose system, are responsible for changes

in the density of states and depletion of the condensate in favor of excited states [11].

The macroscopic occupation of the ground state $k_{||} = 0$, the nonlinear threshold behavior and the narrowing of the linewidth represents the main properties of BEC. However, in the case of polaritons, these observations are not conclusive and they are, in general, not sufficient to conclude that BEC has occurred [9], as discussed in the next section.

3.2.2 An unusual condensate

One of the main limitations for the observation of a conventional BEC of polaritons is represented by the finite polariton lifetime ($\tau \sim 10\,ps$). A conventional BEC, as the one described in section 3.1.1, exists in a thermal equilibrium system, where the particles lifetime is much longer than the relaxation time [10]. In the case of polariton condensates, on the other hand, due to the leakage of the photonic components from the cavity, the lifetime of polariton is shorter than or comparable to the energy relaxation time [10], i.e. photons escape from the cavity before or at the same time that polaritons reach the thermal equilibrium with its host lattice. As a consequence, polariton condensates are in thermal equilibrium only under certain experimental conditions [119], namely at positive detuning when the exciton fraction in the polariton is larger than 0.5, which provides a higher polariton collision rate and therefore faster thermalization [48]. However, in the first observation of polariton BEC [11], the low energy part of the occupancy [Fig. 3.1(c)] could not be fitted with a Bose distribution and, consequently, the thermal equilibrium could not be inferred, making the temperature and the chemical potential of the polariton condensate undefined [120]. Moreover, a polariton condensate is, by definition, a *nonequilibrium* condensate since it results from the dynamic balance between the injection of polaritons and the leak of photons from the cavity. Due to the losses, the number of polaritons forming the condensate is not conserved. Thus, a stable population (i.e. the steady state) into the condensate is reached only when the external pumping counter balance the polariton loss. On the basis of this major difference with the conventional BEC, it has been pointed out that, although polariton condensates exhibit properties similar to atomic condensates (see section 3.2.1), describe polaritons in term of BEC may not be appropriate [47] and that the coherent polariton emission

observed experimentally [11] resembles more a laser, for which thermal equilibrium is not required.

However, a major difference exists also between the polariton emission mechanism and the conventional laser mechanism. As discussed in section 2.6, in a polariton laser no inversion of population is required and the underlying mechanism for the emission of a coherent light is due to the stimulated scatter of polaritons toward the condensate (and not to the stimulated emission as in the convention laser). Due to the stimulated relaxation mechanism, polaritons accumulate at $k = 0$ of the LP dispersion, forming a condensate that emits coherent light via leakage of their photonic components through the microcavity mirrors [9]. Although both the laser and the polariton condensate emit coherent light, in the first case the particles that becomes coherent are photons while in the second polaritons [9].

These arguments make polariton condensate a unique case of condensate which differs from the conventional BEC, due to its non equilibrium nature, but differ also from a standard photon laser because it does not require the electronic population to be inverted. Whether, would be more appropriate to refer to polariton condensate as BEC or a polariton laser it is still matter of debate in the community [46–48]. The fabrication of samples with higher Q-factor and consequently higher polariton lifetime could in principle resolve this controversy, allowing the observation of polariton condensate at thermal equilibrium.

3.2.3 The Gross-Pitaevskii equation

In BECs, the particles undergo a phase transition during which the ground state of the system becomes macroscopically occupied. Thus, all the particles forming the condensate can be described by a single wavefunction. Due to their finite lifetime, polaritons form nonequilibrium condensates. The condensate population reaches the steady state as the results of a dynamical balance of pumping and losses [49]. The collective wavefunction $\psi(\mathbf{r})$ of the condensate is described by a Gross-Pitaevskii equation (GPE), which is similar to the time-dependent Schrödinger equation apart from the nonlinear term $\hbar g\,|\psi(\mathbf{r})|^2$, which is due to the interactions within the condensate. In the case of nonequilibrium polariton condensates, the GPE include also loss and amplification

terms [121]:

$$i\hbar\frac{\partial\psi(\mathbf{r})}{\partial t} = \left\{E_0 - \frac{\hbar^2}{2m}\nabla^2_{\mathbf{r}} + \frac{i\hbar}{2}\left[R\left[n_R(\mathbf{r})\right] - \gamma_c\right] + V_{ext}(\mathbf{r}) + g\left|\psi(\mathbf{r})\right|^2 + V_R(\mathbf{r})\right\}\psi(\mathbf{r}). \tag{3.8}$$

Since polaritons condense in the bottom of the lower polariton dispersion, usually the dispersion is approximated by a parabolic one with $E_0 = \hbar\omega_0$ and m being, respectively, the minimum and the effective mass of the lower polariton dispersion. $n_R(\mathbf{r})$ is the local density of polaritons and $g > 0$ a constant that quantifies the strength of the repulsive polariton-polariton interactions. Condensate polariton have a linear loss rate γ_c and are continuously replenished by stimulated scattering of polaritons from the reservoir at a rate $\mathrm{R}(n_R)$. Thus, $\mathrm{R}(n_R)$ represents the amplification rate term and is a monotonically growing function of $n_R(\mathbf{r})$ [49, 121]. The interaction between the condensate polaritons and the exciton reservoir produces a repulsive potential $V_R(\mathbf{r})$ that can be approximated as $V_R(\mathbf{r}) \cong \hbar g_R n_R(\mathbf{r}) + \hbar G P(\mathbf{r})$, where $P(\mathbf{r})$ is the pumping rate and g_R, $G > 0$ are phenomenological coefficients to be extracted from the experiment. $V_{ext}(\mathbf{r})$ represents an external potential term that takes into account exciton and cavity disorder. The GPE equation 3.8 for the condensate is then coupled with a rate equation for n_R [121]:

$$\frac{\partial n_R}{\partial t} = P(\mathbf{r}) - \gamma_R n_R(\mathbf{r}) - R\left[n_R(\mathbf{r})\right]\left|\psi(\mathbf{r})\right|^2. \tag{3.9}$$

Polaritons are injected into the reservoir at a rate $\mathrm{P}(\mathbf{r})$ and relax at an effective rate $\gamma_R >> \gamma_c$ [121]. The term $R\left[n_R(\mathbf{r})\right]\left|\psi(\mathbf{r})\right|^2$ takes into account the scattering of reservoir polariton into the condensate [49, 121].

In the equation 3.8, the term $g\left|\psi(\mathbf{r})\right|^2$, which includes polariton-polariton interactions, is responsible for many non linear effects, such as superfluidity, quantized vortices and solitons, theoretically predicted in polariton condensates [122]. In section 3.3, a more detailed discussion of these effects will be presented.

3.2.4 Healing length

In the case of BECs, an important quantity is represented by the *healing length* ξ of the condensate, which represents the length-scale of the system. The healing length ξ, in fact, is defined as the distance where the kinetic energy balances the interaction energy

[123]. Thus, if the BEC density grows from 0 to n within a distance ξ, the two terms in the equation 3.8 that correspond to the kinetic energy and the interaction energy are respectively $\sim \frac{\hbar^2}{2m\xi^2}$ and $\sim g\,|\psi(\mathbf{r})|^2$. By equating them, one obtains the healing length [123]:

$$\xi = \frac{\hbar}{\sqrt{2mgn}} \tag{3.10}$$

with $n = |\psi(\mathbf{r})|^2$ being the density of the polariton condensate. The name healing length comes from the fact that ξ represents the distance over which the BEC wavefunction $\psi(\mathbf{r})$ "heals" over defects [124] or, similarly, the distance over which $\psi(\mathbf{r})$ tends to its bulk value.

The healing length is of particular importance for the observation of nonlinear excitations in BECs since it defines the typical size of the core of quantized vortices in superfluid [123] or the spatial width of dark solitons in BECs [16].

3.3 Quantum fluids

3.3.1 Superfluidity in 2D

Liquid helium (^{4}He) can flow without friction below 2.17 K (at atmospheric pressure). In other words, at low temperature liquid helium becomes *superfluid* with properties completely different than normal fluids. A superfluid, in fact, has zero viscosity and an infinite thermal conductivity. As a consequence, it is able to flow without dissipation. Moreover, in a superfluid, quantized currents persist indefinitely and temperature fluctuations propagate like waves [125]. Such properties, cannot be described with classical mechanics, but requires a quantum approach. For this reason it is common to refer to the superfluid helium as a *quantum fluid*.

The first observation of superfluidity date back to 1938 and was realized independently by Kapitza [126], in Moscow and Allen and Misener in Cambridge [127]. In the same year, London [128] suggested that superfluidity of the liquid helium was a direct consequences of BEC [129]. However, the connection between superfluidity (flow without friction) and BEC (macroscopic occupation of a single state) remained speculative for many years and has been the subject of long-standing controversy started already few years after

London's proposal. In 1941, in fact, Lev Landau published an alternative interpretation [130] based on a two-fluid model. In this work, the fluid was described as composed by a 'normal' component that has a viscous flow and a 'superfluid' component that has flows without friction [54] but no reference to the BEC was present. Only after the experimental measurement of the momentum distribution by means of neutron scattering experiments [131] the relation between superfluidity and BEC was confirmed. However, fundamental questions remain for example on the number of atoms occupying the lowest energy state. At the lowest temperature, although the liquid helium is a superfluid, the strong interactions between the helium atoms limit the condensate fraction to only 10% [54].

In the case of ultracold atomic gases, the situation is different. Unlike liquid helium, atomic gases are weakly interacting and, as consequence, more suitable to be studied with the theory of the ideal (i.e. non interacting) BEC (see section 3.1). Thus, soon after the experimental observation of BEC for a gas of rubidium-87 atoms in 1995 [113], it was shown that atomic BECs are also superfluids [132, 133], since they satisfy the so-called Landau criterion [130]. According to this criterion, an object (i.e., a focused laser spot [132] or a defect [133]) will propagate through a superfluid without dissipation when its velocity is lower than a critical velocity v_c. In the case of BEC, this critical velocity is represented by the speed of sound in the condensate [133]:

$$v_c = c \equiv \sqrt{\frac{\mu}{m}} \tag{3.11}$$

with μ being the chemical potential and m the mass of the condensate. In the case of 3D atomic gas, differently from the liquid helium, the condensate fraction and superfluid fraction are essentially equals, so that clearly the condensate is also a superfluid [54].

Instead, in the case of 2D ultra-cold gas, the relation between BEC and superfluidity becomes more complicated. In one- and two-dimensional systems, in fact, BEC can occurs only for sufficiently confining potentials [134]. However, the long range order, typical of a BEC, cannot occur in 2D. According to the Mermin-Wagner theorem [135], in a 2D system of bosons, a BEC can be realized only at $T = 0$ since, at finite temperatures, the long-wavelength fluctuations destroy the long-range order [30]. However, this is not the case for superfluidity. A transition, known as the Berezinskii-Kosterliz-Thouless (BKT) transition allow superfluidity at finite temperature ($T > 0$) but without the long

range order that is typical of a BEC [54]. For example, in the case of 2D liquid helium film (adsorbed on an oscillating substrate), it has been demonstrated that liquid helium cannot condense at temperature $T \neq 0$ but it becomes superfluid above a critical density [136]. The critical temperature of the BKT transition is [30]:

$$k_B T_{BKT} = n_s \frac{\pi \hbar^2}{2m^2} \tag{3.12}$$

where n_s is the superfluid density. In terms of the de Broglie wavelength (λ_{DB}), equation 3.12 is [30]:

$$\lambda_{DB}(T) = \sqrt{\frac{2\pi\hbar^2}{m k_B T}} \tag{3.13}$$

From equation 3.12 and equation 3.13, the condition for BKT reads [30]:

$$n_s \lambda_{DB}(T_c)^2 = 4 \tag{3.14}$$

Recently, the observation of superfluidity in 2D atomic gases [137] and in polariton microcavity [57] was also demonstrated.

Microcavity polaritons, as 2D system, can undergo a BKT transition [138]. However, the system size is small enough such that a finite-size BEC phase transition is expected before a BKT transition [30]. In principle, BEC in microcavity can be reached when a sufficient small confining potential is present. The first observation of polariton BEC, described in section 3.2.1, was in fact followed by the observation of BEC in confined potential created by mechanically induced stress traps [139] or in micropillars [140]. However, the non conventional nature of the polariton BEC, discussed in sec. 3.2.2, remains.

We conclude this paragraph by highlighting that the connection between BEC and superfluidity are still not completely clear even thought it is accepted that the two phenomena are related. However, while superfluidity requires interactions between the atoms, Bose-Einstein condensation does not [54]. Thus, a gas of interacting bosons undergo BEC and it is also superfluid, while an ideal Bose gas (i.e. without interactions) undergo BEC but it is not a superfluid.

3.3.2 Hydrodynamic regimes in quantum fluids

Superfluidity in atomic BEC can be demonstrated by considering the motion of an impurity (i.e., a focused laser spot [132] or a defect [133]) in the condensate and verify that the Landau criterion is satisfied. The Landau criterion, as mentioned in the previous chapter, determines the maximum speed at which an impurity can travel across a fluid without experiencing any friction force [122]. Thus, in the fluid reference frame,

- if the velocity v of the impurity is smaller than the critical velocity v_c (see equation 3.11), the impurity should propagate through the condensate without dissipation. In this case the condensate is a superfluid.
- Instead, if $v > v_c$, the condensate is not a superfluid and effective friction forces are present. As a consequence, a large number of excitations, such as quantized vortices appear in the fluid [122]. This is shown in Figs. 3.2 a) for the case of a repulsive Gaussian obstacle [12].

Since in atomic condensates, the critical velocity v_c coincides with the speed of sound in the condensate, it is common to refer to the above regimes as subsonic ($v < v_c$) and supersonic ($v > v_c$) regime. Thus, the appearance of quantized vortices in a condensate marks the breakdown of superfluidity. Quantized vortices, by definition, are characterized by a topological charge of $n\,2\pi$ (with n an integer number), which corresponds to the rotation of the phase around the vortex and a vanishing condensate population at their core [59]. In atomic gases and liquid helium, they can be thought as the quantum counterparts of the turbulence in classical fluids [141]. Owing to the strong relation with superfluidity, quantized vortices have been extensively studied both theoretically and experimentally in atomic gases BEC [56, 142], liquid helium [143] and polariton microcavity [59, 141]. However, in many experiments involving the motion of a macroscopic object across liquid helium, e.g., (^3He-B) [144] or atomic gases [132, 133], the critical velocity for the onset of dissipation has been found to be lower than the prediction of the Landau criterion. Only when microscopic particles, such as negative ions [145], were dragged through liquid ^{4}He, the Landau criterion was satisfied.

The experimental results discussed above show a strong dependence of the critical velocity from the shape and the dimension of the objects used to test the Landau criterion.

These dependence is confirmed also theoretically. For example, it has been calculated that the critical velocity is larger for an impenetrable square barrier, and lower for a penetrable Gaussian object [146]. Moreover, when a macroscopic object is used, quantized vortices can appear also in the subsonic regime, due to the strong modification of the velocity pattern around the defect [122]. As explained by Frish et al. [147] , due to a spatial suppression of the stream lines against the defect, the local velocity on the surface of the defect can exceed the critical velocity [122, 147]. Thus, at the surface of the object, the flow velocity can exceed the critical velocity and quantized vortices start to being nucleate and give rise to a drag force.

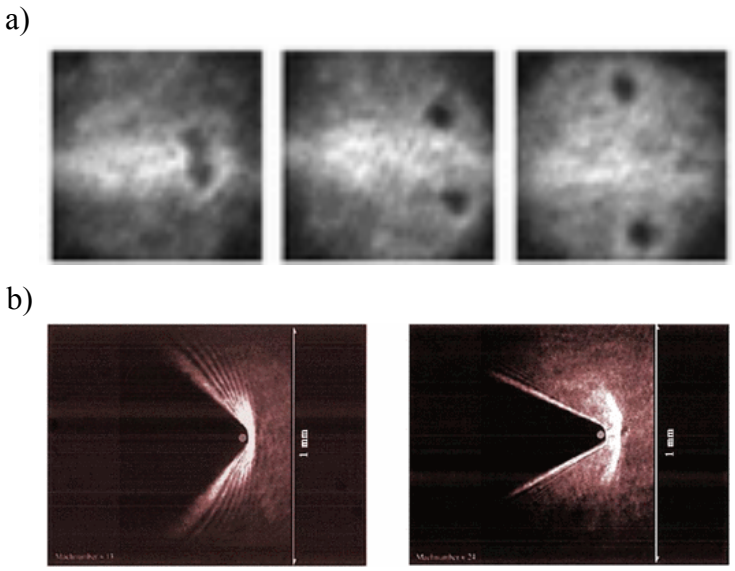

FIGURE 3.2: a) Sequences of images showing the dynamics of vortices nucleated by the repulsive Gaussian obstacle (i.e. a blue detuned laser) within the BEC. The laser is scanned across the condensate from left to right. Images from [12]. b) Experimental density images of a BEC hitting an obstacle (from right to left) at supersonic velocities $M = 13$ (left) and $M = 24$. The angles of the conical wave fronts are $sin(\theta) = 0.73$ and $sin(\theta) = 0.43$, respectively. Images from [13].

By studying the dynamics in the laboratory reference frame, i.e., with the defect at rest and the condensate moving toward the defect, and considering the velocity of the condensate v_0 respect to the speed of sound c_s, i.e. the *Mach number* M defined as:

$$M = \frac{v_0}{c_s}, \tag{3.15}$$

four different regimes of the condensate flow past an obstacle can be theoretically explored. In particular, for the case of an impenetrable object, when [148]:

1. $0 < M < 0.43$, the flow is in the superfluid regime and no perturbations will be observed [146, 147].

2. $0.43 < M < 1$, superfluidity is lost and quantized vortices appear in the condensate [148].

3. $1 < M < 1.44$, a *Mach cone* located downstream of the defect appears with an aperture angle θ defined as $\theta = sin^{-1}c_s/v_0$ [122] (Figs. 3.2 b). This emission is analogous to the Cherenkov radiation, emitted by charged particles when traveling through a dielectric medium at a speed larger than the mediums phase velocity [13]. Instead, upstream and laterally to the defect, curved wave patterns appear, resulting from the interference of the incident plane wave and the spherical scattered wave [122, 148]. It has been shown that these waves are generated outside the Mach cone [149].

4. $M > 1.44$, vortex nucleation is replaced by the appearance of oblique dark solitons which are expected to form inside the Mach cone [65].

By summarizing, when the condensate flows at subsonic speed ($v < c_s$), superfluidity and vortex formation are predicted (point 1 and 2), while at supersonic speed ($v > c_s$), Cherenkov radiation and oblique dark solitons appear (point 3 and 4). The latter will be treated in more detail in the next section.

3.4 Dark solitons

3.4.1 What is a soliton?

Solitons are solitary waves that preserve their shape while propagating through a dispersive medium [15, 150] due to the compensation of the dispersion-induced broadening by the nonlinearity of the medium [151]. Thus, an optical soliton is the result of the balance between diffraction and nonlinearity.

Over the years, spatial solitons have been observed by employing a variety of nonlinearities ranging from Kerr nonlinear media [152] to photorefractive [153] and quadratic [154] materials. Solitons are classified in *bright* and *dark*. A bright soliton is a peak in the amplitude while a dark soliton feature a density node accompanied by a π phase jump.

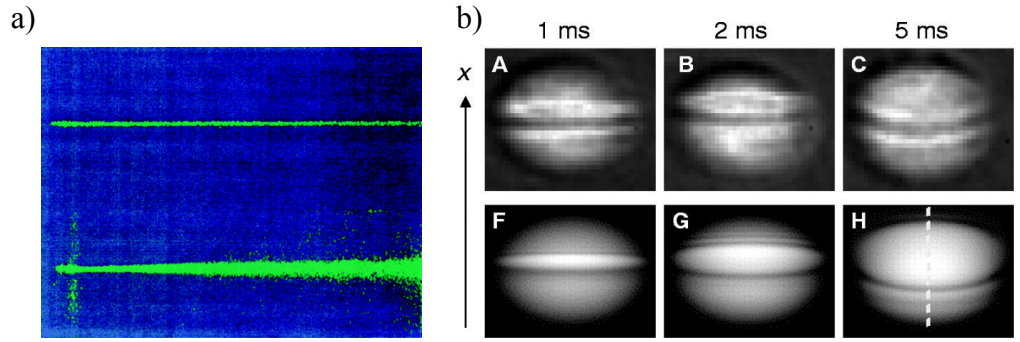

FIGURE 3.3: a) In the upper part of the figure it is shown a $10\mu m$ wide spatial soliton propagating in strontium barium niobate photorefractive crystal while in the bottom part, for comparison, the same beam diffracting naturally when the nonlinearity is "turned off". Image originally from [14], taken from [15]. b) Experimental (top row) and theoretical (bottom row) images of the integrated BEC density for various times after a phase step of $\sim 1.5\pi$ was imprinted on the top half of the condensate. The dark solitons is moving toward the bottom of the figures (i.e., in the $x < 0$ direction) and is formed due to the repulsive interactions in the sodium condensate. The simulations are performed with the Gross-Pitaevskii equation. Images from [16].

An example of bright solitons is reported in Fig. 3.3 a) for the case of photorefractive material where the self-focusing effect is due to an increase of the refractive index of the medium with an applied electric field. Similarly, in Kerr nonlinear materials, the self-focusing effect is due to an increases of the refractive index of the medium with the intensity of the incident beam.

Apart from their potential application in optical communications [155, 156], solitons are important features of interacting Bose-Einstein condensates (BECs) and superfluids. The nonlinear properties of BEC, in fact, can give rise to the formation of quantized interacting vortices and solitons, the latter resulting from the cancellation of the dispersion by interactions, for example in atomic condensates. If the interactions are attractive, bright solitons are created while for repulsive interactions, like for example in the sodium atomic condensate shown in Fig. 3.3 b), dark solitons are formed. Since the first theoretical prediction in the context of Bose-Einstein condensates (BECs) [157], dark solitons were studied and observed first in the field of nonlinear optics [158] and then in cold-atom BECs [16]. This thesis focuses mainly on the dark solitons. However, a brief description of bright soliton in polariton microcavity will be also given in section 3.5.

3.4.2 Theory of dark and oblique dark solitons in atomic BEC

The dynamics of a weakly interacting BEC can be described by the GrossPitaevskii equation (GPE), discussed in Section 3.2.3, which admits soliton solution [16, 65, 159]. The GPE in the case of trapped atomic condensates reads [16]:

$$i\hbar\frac{\partial\psi}{\partial t} = \frac{-\hbar^2}{2m}\nabla^2\psi + V\psi + g\left|\psi\right|^2\psi \tag{3.16}$$

where $\psi(\mathbf{r})$ is the condensate wave function normalized to the number of atoms, m is the atomic mass forming the condensate, V is the trapping potential and $g = 4\pi\hbar^2 a/m$ describes the strength of the atom-atom interaction, with a being the scattering length (e.g., in the case of sodium condensate reported in Fig.3.3b), a = 2.75 nm [16]). In equation 3.16 the non spreading nature of the soliton is due to the two terms $g\left|\psi\right|^2$ and $\frac{-\hbar^2}{2M}\nabla^2$, describing respectively the nonlinear interactions within the condensate and the kinetic energy. The balance of the dispersion due to the nonlinearity, in fact, allow dark soliton to propagate without diffract. The sign of g, on the other hand, determine whether a bright or a dark soliton solution is allowed. Attractive interactions, $g < 0$, support the formation of bright solitons while for repulsive interaction, $g > 0$, dark solitons.

As anticipated in section 3.3.2, solitons are predicted to appear only in the supersonic regime, i.e. when the speed of the condensate is greater than the speed of sound. The local speed of sound $c_s(r)$ is given by an equation first derived by Bogoliubov [16, 160, 161]:

$$c_s(r) = \sqrt{\frac{gn}{m}} \tag{3.17}$$

with $n = \left|\psi\right|^2$ being the unperturbed condensate density. The solitons speed v_s, on the other hand, is related either at the phase jump δ, or the solitons "depth" n_d, which is the difference between n and the density at the bottom of the notch [16]:

$$\frac{v_s}{c_s} = cos\left(\frac{\delta}{2}\right) = \left(1 - \frac{n_d}{n}\right)^{1/2} \tag{3.18}$$

Therefore, for $\delta = \pi$, the soliton has zero velocity, zero density at its center and a discontinuous phase step [16]. Moreover, the width of the soliton is comparable to the

healing length of the condensate [16, 159]:

$$\xi = \left(\frac{2nmg}{\hbar^2}\right)^{-1/2} \tag{3.19}$$

When an impenetrable defect is introduced into the condensate, oblique dark solitons have been predicted to appear [65]. In particular, the formation of oblique dark solitons has been studied in the case of a condensate flowing toward an impenetrable defect. In equation 3.16, if one consider as V the potential arising from the presence of an impenetrable obstacle inside the BEC and assume that far enough from the obstacle, this potential can be neglected, i.e. $V(r) = 0$ when $r \to \infty$, *oblique dark soliton* solutions can be obtained for the density n when a supersonic flow (i.e., $M > 1$) is created [65]:

$$n(\theta) = 1 - \frac{1-p}{cosh^2\left[\sqrt{1-p}\theta/\sqrt{1+a^2}\right]} \tag{3.20}$$

with $p = M^2/(1+a^2)$. Here M is the Mach number (see equation 3.15) while a is the slope of the soliton center respect to the direction of the flow. The inverse half-width of the soliton is [65]:

$$k = 2\sqrt{\frac{1-p}{1+a}} \tag{3.21}$$

Equations 3.20 and 3.21, gives the exact dark spatial soliton solution of the GP equation [65]. The name *oblique dark solitons* (ODS) comes from the fact that they appear as notches in intensity (i.e., dark) and are always inclined (i.e., obliques) with respect to the direction of the supersonic flow [65], as for example shown in Fig. 3.4 (c) (the flow is parallel to vertical axis).

3.4.3 Theory of oblique dark solitons in polariton microcavity

Also in the case of polaritons, the formation of oblique dark solitons has been studied by considering a condensate flowing against an impenetrable defect. However, in the specific case of polaritons, the derivation of oblique dark solitons solutions cannot neglect the non equilibrium nature of polariton condensates. Consequently, the GPE equation 3.16 has to be modified to take into account the need of a continuous pumping to compensate

the polariton losses [17, 162]:

$$i\frac{d}{dt}\begin{pmatrix}\psi_C\\ \psi_X\end{pmatrix} = \begin{pmatrix}F_p(\mathbf{x})\\ 0\end{pmatrix} e^{i(\mathbf{k}_p)\mathbf{x}-\omega_p t)} + \left[\mathbf{h}^0 + \begin{pmatrix}V_C(\mathbf{x}) & 0\\ 0 & g\left|\psi_X\right|^2\end{pmatrix}\right]\begin{pmatrix}\psi_C\\ \psi_X\end{pmatrix}, \quad (3.22)$$

where ψ_C and ψ_X are respectively the cavity-photon and exciton wavefunction, $F_p(\mathbf{x})$ is the spatial envelope, $\hbar\mathbf{k}_p$ is the in-plane momentum, $\hbar\omega_p$ is the energy of the pump field and $V_C(\mathbf{x})$ is the photonic potential due to the defect in the sample. The exciton-exciton interactions are described by a nonlinear interaction term g, which represents a local repulsive interaction potential ($g > 0$). $\mathbf{h}^0$ is the matrix [17, 162]:

$$\mathbf{h}^0 = \begin{pmatrix}\omega_C(-i\nabla) - i\frac{\gamma_C}{2} & \Omega_R\\ \Omega_R & \omega_X(-i\nabla) - i\frac{\gamma_X}{2}\end{pmatrix} \quad (3.23)$$

with $\omega_{X(C)}(\mathbf{k})$ being the dispersion of the excitons (cavity photons) as a function of in-plane momentum $\mathbf{k}$, $\gamma_{X(C)}$ the decay rate of the excitons (cavity photons) and Ω_R is the vacuum Rabi frequency of the photon-exciton coupling.

In the case of polaritons, the flow velocity v_{flow} is [17, 18]:

$$v_{flow} = \frac{\hbar\mathbf{k}}{m_{LP}} \quad (3.24)$$

with m_{LP} being the effective mass and $\mathbf{k}$ the in-plane wave vector of polaritons. Thus, the flow velocity v_{flow} is controlled by $\mathbf{k}$, which in turn depends on the angle of incidence θ of the excitation beam with respect to the normal to the microcavity plane[2]. On the other hand, the speed of sound (c_s) in a polariton condensate [17, 18]

$$c_s = \sqrt{\frac{\hbar g\left|\psi\right|^2}{m_{LP}}} \quad (3.25)$$

is proportional to the polariton density $|\psi|^2$ and inverse proportional to the their mass (m_{LP}), as in the atomic case (see equation 3.17). Here, the constant g represents the polariton-polariton interaction constant [17, 18]. Thus, the speed of sound in polariton condensate can be controlled by varying the density of polaritons (i.e. by varying the excitation power) or by varying the pump detuning (i.e., the energy of the pump respect

[2] $\mathbf{k} = k_0 sin(\theta)$ with $k_0 = 2\pi/\lambda_0$ being the wave vector of the laser and λ_0 its wavelength.

to the lower polariton branch) [162]. Consequently, by fixing v_{flow} at constant value and varying c_s, it is possible to realize different hydrodynamic regimes. In Fig. 3.4 (a-e), the theoretical simulations, realized by solving the GPE equations 3.22 and 3.23, show a transition from subsonic ($v_{flow} < c_s$) to supersonic ($v_{flow} > c_s$) regime.

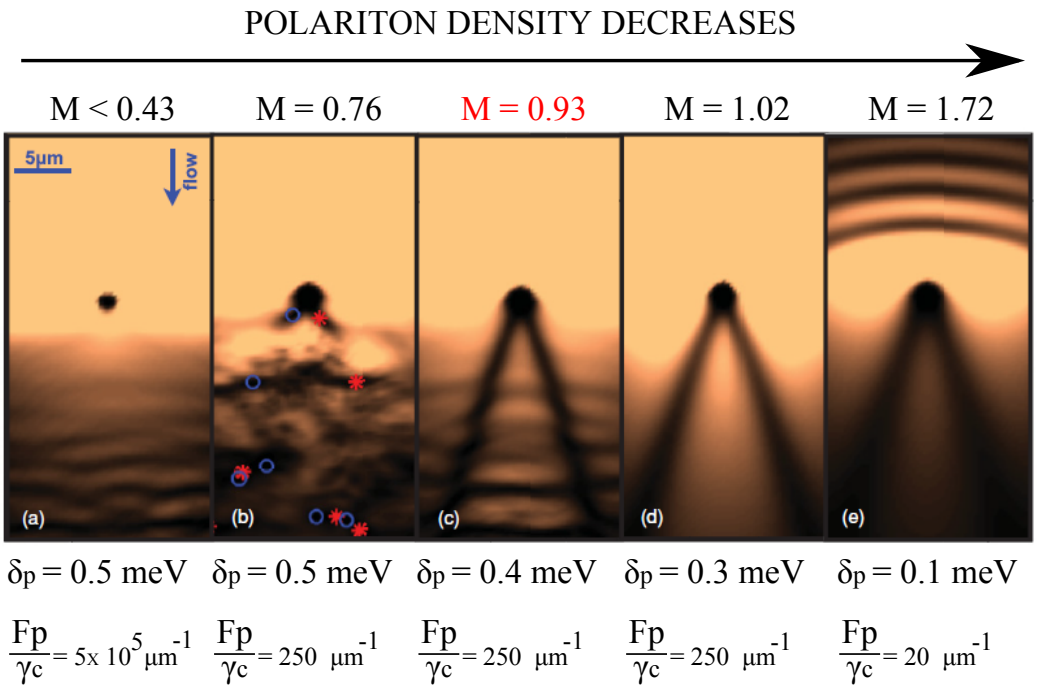

FIGURE 3.4: Normalized real-space photonic density for different value of pump detuning and power, which corresponds to a decrease of the polariton density from left (a) to right (e), as indicated by the top black arrow. Different regimes are reported: (a) superfluid regime, (b) vortex regime, (c) oblique dark soliton regime (inferior limit) (d) and (e) oblique dark soliton regime, with the appearance of parabolic precursors propagating upstream of the defect (e). The M, on top of the figures, represents the the Mach number, calculated as the ratio between the flow velocity v_{flow} and the value of the speed of sound at the defect position. The parameters reported below the figure are the pump energy detuning (δ_p) and the pump intensity (F_p/γ_c) normalized for the decay rate of the cavity photons (γ_c). The photonic defect has a depth of $V_c = 20\,meV$. Images from Ref. [17].

We notice that, differently from the atomic case discussed in sec. 3.4.2, here oblique dark solitons appear already in the subsonic regime (i.e. with $M < 1$). This is one of the main differences between dark soliton in polariton [17] and the atomic condensate [65]. On the other hand, in both polariton [17] and atomic [65] condensate, it has been predicted that by increasing the size of the defect also the number of oblique dark solitons increases and the formation of a high order oblique dark soliton is expected.

3.4.4 Oblique dark solitons in polariton microcavities

The experimental observation of BEC [11] and superfluidity [57, 58] of exciton-polaritons, has sparked interest in the quantum-hydrodynamic properties of polariton fluids. In particular, the nucleation of solitary waves in the wake of an obstacle (i.e. defect) has been claimed recently [18–22]. Here, the source of nonlinearity, essential for the formation of such a solitary wave, has been identified in the repulsive polariton-polariton interactions [18–22]. In all these works, the observation of dark notches in the intensity profiles together with a π shift in the phase have been used as sufficient signatures for dark and half-dark solitons in microcavities.

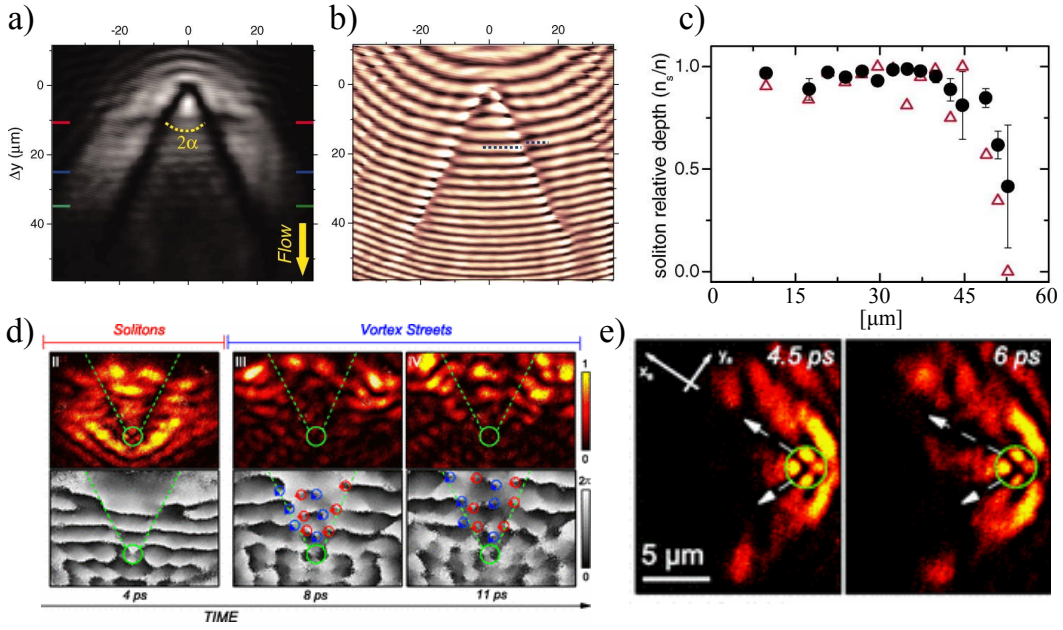

FIGURE 3.5: Experimental real space emission and interference patterns showing the soliton fingerprints as reported in the polariton microcavity literature [18–21]. Two dark notches in intensity (a), which correspond to phase dislocations in the interferogram (b), as shown in Ref.[18]. c) Soliton depth n_d obtained from the interferogram in b) (black circles) and from the measured phase jump and equation 3.18 (open triangles). Image from [18]. d) Time resolved measurements of the density (top row) and phase (bottom row) of polariton wave packet as reported in [19]. In the first column (II) the dark solitons are shown, while in (III) and (IV) solitons decay in vortex street (red and blue circles). e) Another example of time resolved dark solitons as reported in [20].

As discussed in section 3.4.3, a local defect induced into a polariton fluid gives rise to the formation of vortices and oblique dark solitons [17, 18]. Depending on the flow speed, polaritons can either flow almost unperturbed around the defect or experience the nucleation of vortices and/or oblique dark solitons at the position of the defect [17]. Due to the polariton-polariton interaction [18] solitons can propagates away from the

defect.

As mentioned before, the main fingerprints of such oblique dark solitons are two:

- two dark notches in the intensity profile
- π phase shift across its intensity minima.

Both these features are showed in Fig. 3.5 for a polariton fluid interacting with a spatially extended defect [18–21].

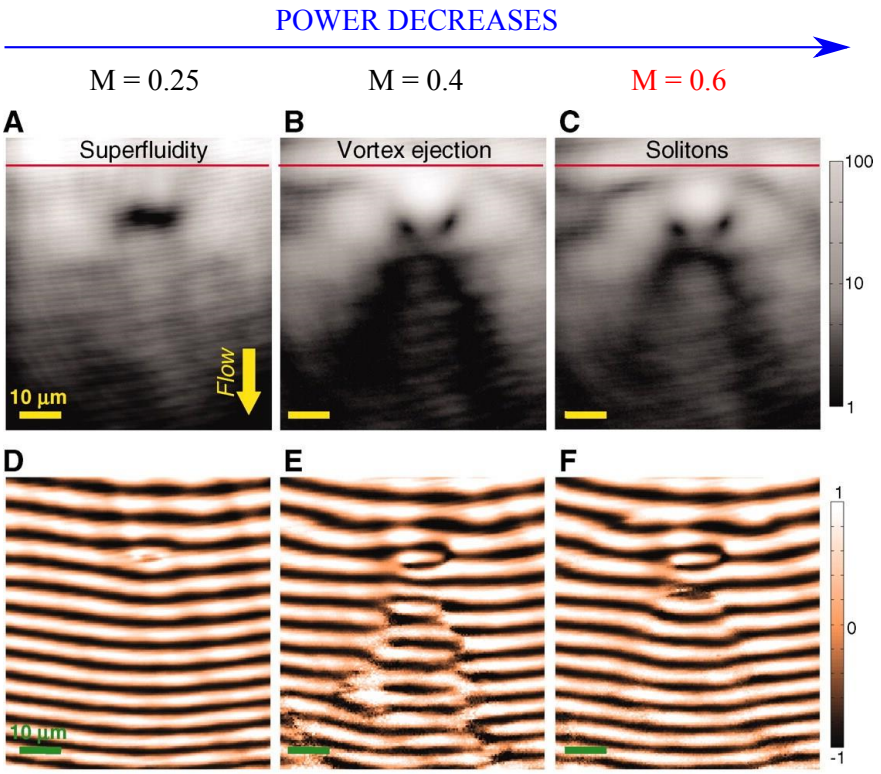

FIGURE 3.6: Experimental real space intensity (**A-C**) and interferograms (**D-F**) images showing a polariton condensate flowing downward toward a defect. By varying the excitation density, three different regimes are observed: A) and D) superfluid regime; B) and E) vortices regime; C) and F) dark soliton regime. Above the figures the Mach number (M) for each excitation density is reported. Image from [18].

For the specific case of the dark soliton reported in Fig. 3.5 a) and b), the characteristic equation 3.18 of dark solitons, has also been verified. From equation 3.18 follows that, as the depth of the solitons (n_d) increases, (i.e. n_d approaches n, see equation 3.18) the phase jump δ becomes equal to π. This is shown in Fig. 3.5 c), where the depth of the dark solitons remain stable up to the first 40 μm, corresponding to phase jump close to π in Fig.3.5 d). At longer distances, on the other hand, both the depth of the solitons and the phase jump decrease.

Solitons exist thanks to a nonlinearity presents in the system. In the case of polariton microcavities the source of nonlinearity is represented by the polariton-polariton interactions [17, 18] that, in turn, depend on the excitation density. Solitons are predicted to appear only at certain values of excitation density or, in other words, when the repulsive interparticle interactions is greater enough to stabilize the shape of the solitons as they propagate [18]. However, as discussed in section 3.4.3, when the excitation density is varied, other hydrodynamic regimes such as superfluidity and vortices regimes can be accessed. This is shown in Fig.2.2 for the case of a polariton condensate. At high excitation density, polaritons are reported to be in the superfluid regime [Fig.3.6A and Fig.3.6D]. This interpretation is justified by the fact that both the soliton fingerprints disappear. When the excitation density is decreased, polaritons enters respectively in a turbulent regime characterized by the appearance of vortices [Fig.3.6B and Fig.3.6E] and a soliton regime [Fig.3.6C and Fig.3.6F].

Finally, it has been predicted in both polariton [17] and atomic [65] condensates, that by increasing the size of the defect and the ratio v_{flow}/c_s, the appearance of a high order dark soliton (i.e. a "soliton quadruplet") could also be observed. The quadruplet dark soliton reported in the case of a polariton condensate is shown in Fig.3.7b).

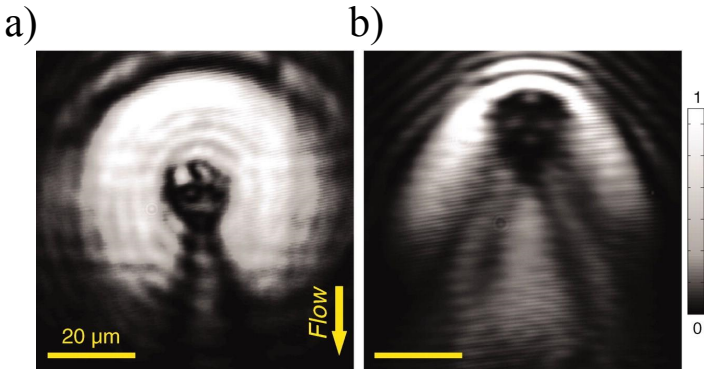

FIGURE 3.7: Real space image of a polariton condensate hitting a large defect ($17\mu m$ in diameter) at low a) $k = 0.2\,\mu m^{-1}$ and high b) $k = 1.1\,\mu m^{-1}$ injected wave vectors. In b) the formation of a high order soliton is claimed. Images from Ref.[18].

3.4.5 Oblique half-dark solitons in polariton microcavities

As in the case of dark solitons, half-solitons can also be generated by a polariton condensate hitting an extended defect [163]. The main features of an oblique half-solitons are the same of a dark solitons (i.e. a dark notch in the polariton density together

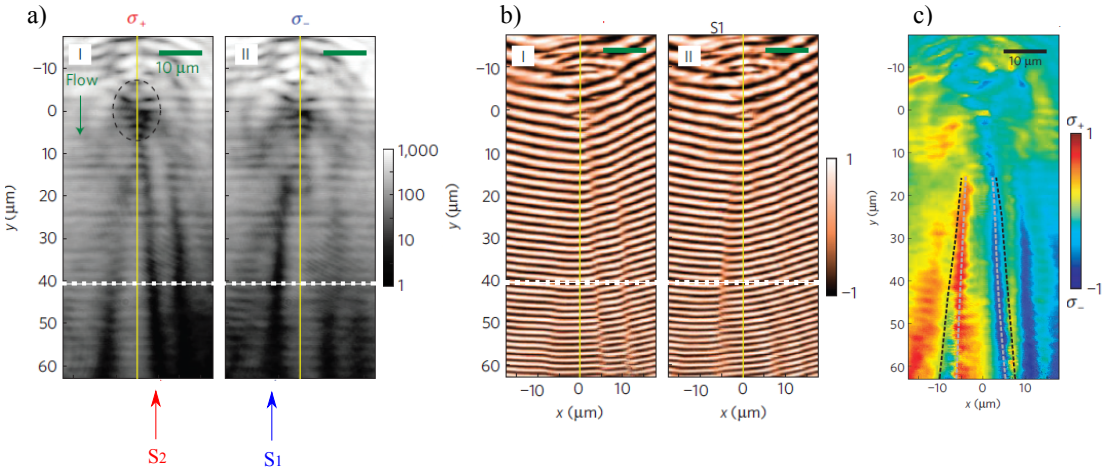

FIGURE 3.8: Emitted polariton intensity a) and their respective interferograms b) of the σ_+ (I) and σ_- (II) circularly polarized components. S_1 and S_2 indicate respectively the σ_- and σ_+ half dark solitons. c) Measured degree of circular polarization. The dashed lines correspond to the position of the dark notches S_1, S_2 observed in Figs. a). Images from [22].

with a π phase shift in the interferograms) but present in only one circular polarization component. In polarization-resolved images, this corresponds to the appearance of two traces of opposite circular polarization [22, 163], as shown in Fig. 3.8.

3.5 Bright polariton solitons

Bright solitons appear as peak in intensity preserving their shape as they propagate through the condensate. In the case of polariton condensates, it has been predicted that the repulsive interactions within the condensate can sustain the formation of a bright solitons when polariton are injected with negative mass [23]. This corresponds to in-plane momentum k $> k_d$, where k_d is the wave vector at the inflection point of the LP dispersion, as indicated in Fig.3.9(a). The evolution of the amplitude (A) of the polariton wave packet is described by [23]

$$i\partial_t A + iD_1\partial_x A + D_2\partial_x^2 A - iD_3\partial_x^3 A - D_4\partial_x^4 A - \delta A - \alpha\left|A\right|^2 A = i\eta E_0, \tag{3.26}$$

where $\delta = \Omega_-(k_0) - \omega/\Omega_R$, with Ω_- being the eigenfrequency of the lower polariton branch, Ω_R the Rabi frequency. Reδ is the polariton detuning from the pump frequency and Imδ is the loss. $D_1 = \partial_k\Omega_-|_{k_0}$ is the transverse group velocity and $D_2 = \frac{1}{2}\partial_k^2\Omega_-|_{k_0}$, $D_3 = \frac{1}{6}\partial_k^3\Omega_-|_{k_0}$, $D_4 = \frac{1}{24}\partial_k^4\Omega_-|_{k_0}$ are the dispersion coefficients shown in Fig.3.9(b), α

is the effective nonlinearity and ηE_0 is the normalized amplitude of the external pump (with $|E_0|^2 \propto I_{inc}$, and I_{inc} being the incident intensity).

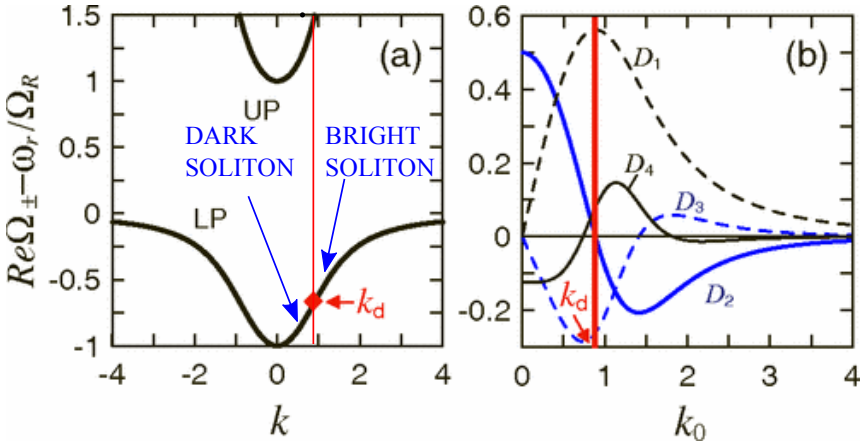

FIGURE 3.9: (a) Energy-momentum diagram showing the low (LP) and upper (UP) polariton branches. k_d indicates the inflection point, where the polariton mass experience a transition from positive (at $k < k_d$) to negative (at $k < k_d$). (b) Dispersion coefficients vs wave vector of the the polariton wave packet. At the inflection point k_d the second order dispersion disappear and bright soliton solution are allowed. Image from Ref.[23].

Depending on which region of the LP dispersion polaritons are created, different dispersion coefficients dominate in equation 3.26 and, consequently, different solutions can be found. In particular, when [23]:

- $k < k_d$, $D_2 > 0$ dominates over $D_m > 2$. Since the nonlinearity is repulsive, the only stable solution is the dark soliton. Bright soliton exist, but are unstable [23].
- $k > k_d$, the polariton dispersion is determined by the competing $D_2 < 0$ and $D_4 > 0$ terms, which both support the existence of bright solitons in the case of repulsive nonlinearity [23]. Moreover, since at $k > k_d$, the group velocity is non zero (i.e., $D_1 \neq 0$) the bright solitons are expected to propagate.

By injecting polaritons with momenta above the point of inflection [Fig.3.10(a)], where polaritons have negative effective mass, the experimental observation of bright solitons was reported in a GaAs semiconductor microcavity [24]. In the experiments, bright solitons were generated by using two beams: a CW *pump* beam focused to a large spot (with FWHM of $70\,\mu m$) and a *"writing"* pulsed beam of smaller dimension (with pulse duration of 5 ps and FWHM of $7-15\,\mu m$) [Fig.3.10(b)]. The main purpose of the pump beam is to sustain the formation of the bright soliton which is instead generated by the

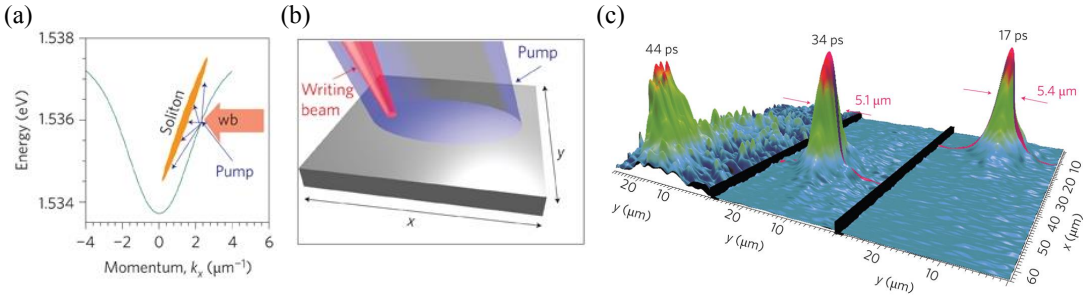

FIGURE 3.10: (a) Energy-momentum dispersion of the lower polariton branch and schematic representation of the excitation scheme used in the experiments to excite polaritons with a negative effective mass. (b) Sketch of the excitation scheme used to generate bright solitons in polariton microcavity. The pump beam is focused to a larger spot than the writing beam (see text for details). (c) Time resolved measurements showing the bright solitons propagating in the microcavity plane. Images from Ref.[24].

writing beam. The strongly variation of the polariton density across the bright soliton profile can, in fact, be balanced by the pump beam, which tends to hold the density of the bright soliton at a quasi-constant level across the much larger pump spot [24]. Time resolved measurements showing the propagation of bright solitons are reported in Fig.3.10(c). The bright soliton wave packet propagates in the plane of the microcavity with a transverse dimension of about $5\,\mu m$ for 17 ps before to decay at 44 ps.

Chapter 4

Experimental method & samples

4.1 Real & k-space imaging

It is common practice in the field of polariton microcavities to build up experimental setups that allow to measure, at the same time, the near- and far-field emission of the sample. The near-field corresponds to the real space image of the sample surface, while the far-field corresponds to the angular distribution (k-space or momentum distribution) of the photon emitted by the sample. An example of both real and momentum space basic setups are shown in Fig. 4.1.

In real space imaging, the light emitted by the microcavity is collected using a microscope objective (L_1) and focused on a charge-coupled device (CCD) camera by a convex lens (L_2) to produce an image in real space (Fig. 4.1 a). To perform k-space imaging an extra lens (L_k) is added to the real-space setup in Fig. 4.1 a), to project the image of the Fourier plane onto either the entrance slit of a spectrometer or a CCD camera (Fig. 4.1 b). As mentioned before, the image of the Fourier plane corresponds to the angular distribution of the light collected by the objective. Each point of the Fourier plane is given by the superposition of photons emitted by the source along a given direction (θ, ϕ), where θ is the emission angle with respect to the normal to the microcavity plane and ϕ is the azimuth angle [164]. Since photons emitted from the microcavity at an angle θ correspond to polaritons with in-plane wave vector $k_{||} = k_0 \sin(\theta)$, with $k_0 = 2\pi/\lambda_0$ and λ_0 being the emission wavelength, the image of the Fourier plane corresponds to a map of the polariton momentum. The angles θ and consequently the wave vectors k

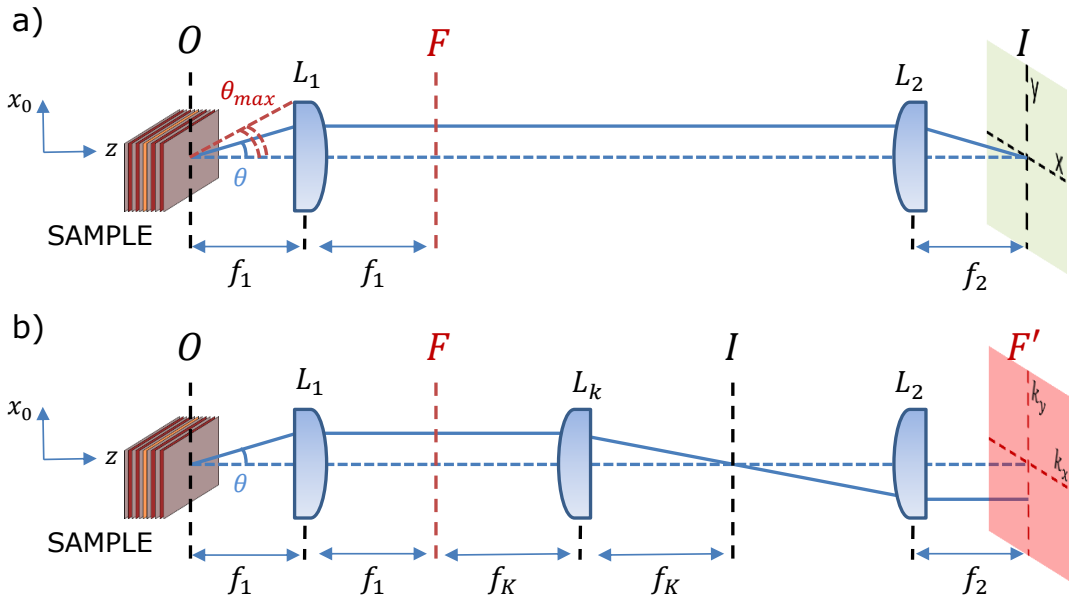

FIGURE 4.1: Sketch of a) real and b) momentum space setups. The light emitted from the sample propagates into a variety of directions, one of which is shown (solid blue line). Only light propagating at $|\theta| \leq \theta_{max}$ can pass through the lens. $\mathbf{L}_1$ is the microscope objective (with focus f_1), $\mathbf{L}_2$ is the convex lens (with focus f_2) to focus the light into the CCD and $\mathbf{L}_k$ is an extra lens (with focus f_k), mounted on a kinematic mount, to measure the far-field emission of the sample (k-space). O and I represent respectively the objective plane (i.e. the surface of the sample) and the image plane in real space (green plane), while F and F' represent respectively the Fourier plane in its original position and its projection into the entrance slit of a spectrometer or into the CCD (red plane).

that is possible to resolve, depend on the numerical aperture (NA) of the objective used for collection, with $\theta_{max} = sin^{-1}(\frac{NA}{n})$ (where n is the refractive index of the medium).

When a microscope objective is used for collecting the light emitted by the sample, the Fourier optical plane (F) lies at rear aperture of the objective and by means of L_k and L_2 can be projected on the entrance slit of the spectrometer (Fig.4.1 b). The latter, is equipped with both CCD and a streak camera with $2\,ps$ temporal resolution. The grating of the spectrometer can be interchanged with a mirror allowing direct imaging of real or momentum space without energy resolution. Thus, if the spectrometer is used, energy resolved measurements of the k-space allow the measurements of the energy (E) versus the momentum (k) of polaritons, namely the polariton dispersion (E,k). An example of polariton dispersion is shown in Fig.8.1(a) and Fig.8.2(a-c). On the other hand, if the CCD camera is used (without energy resolution) the polariton emission in k-space (k_x, k_y) can be measured [see inset in Fig.6.3(b)]. By using the streak camera, a time resolved measurements of the k-space can be performed (see Fig.7.9).

In the next section, the spatially filtered k-space technique will be discussed. The details of all the experimental setups used in the different experiments will be given in section 4.2.

4.1.1 Spatially filtered k-space

The basic setup to produce spatially filtered image in real space is shown in Fig.4.2 a). Here, an aspheric lens (L_1) focuses the Gaussian beam to the aperture (A) of the pinhole and another lens (L_2) collimates the beam, whose size depends on the focus (f_2). By placing this system into the setup in Fig. 4.1 a) (between the F plane and L_2), the spatial filtered emission of the sample can be obtained since the pinhole, mounted on a x-y translator, allow to select a specific region in real space.

When the pinhole, is introduced at the position of the image plane (I) in Fig. 4.1 b), the momentum space of a selected region in real space can be separately imaged. This corresponds to spatially filter the momentum space and image only a specific region of interest (Fig. 4.2 b). In this way, the momentum of polariton can be measured in a specific region away from the position where polariton are generated, i.e. away from the excitation spot. Thus, the propagation of polaritons in the microcavity plane can be verified. In Fig.6.1(c), for example, the propagation of polaritons is confirmed by the fact that 90 μm away from the excitation spot, polaritons have nonzero momentum.

4.2 Experimental techniques

4.2.1 Mach-Zehnder interferometer

The study of the soliton-like features reported in Chapter 5, requires phase measurements. To this purpose, a Mach-Zehnder interferometer has been built up, as shown in Fig. 4.3. Here, the optical elements enclosed in the dashed box ($\lambda/4$ and LP_2) are introduced in the setup only in the case of polarization measurements (i.e., half soliton like features) corresponding to data reported in section 5.10.

The intensity measurements have been performed in transmission configuration, by blocking Arm 2 of the interferometer. The phase, on the other hand, is acquired using

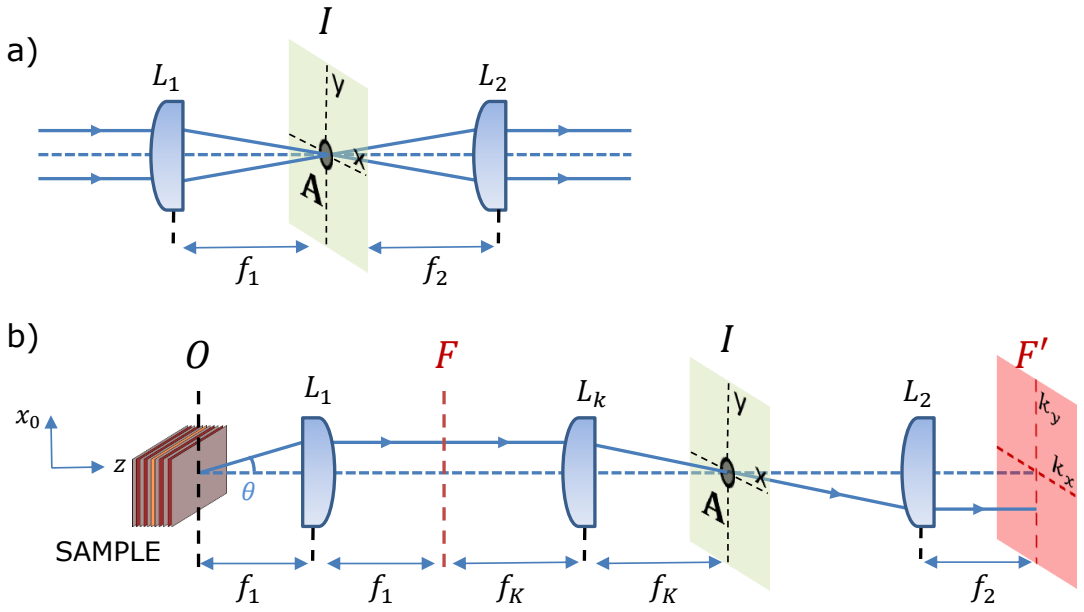

FIGURE 4.2: Sketch of the spatial filtering setup in a) real and b) momentum space. a) $\mathbf{L}_1$ and $\mathbf{L}_2$ are two aspheric lenses with focus f_1 and f_2 respectively. **A** is the pinhole aperture while the green plane **I** is the real space plane (x,y). b) Respect to the k-space setup in Fig. 4.1 b), here a pinhole (**A**) is introduced at the position of the image plane (I). By moving the pinhole along x and y directions, a specific region of the k-space can be imaged. The optical components are the same as in Fig. 4.1 b).

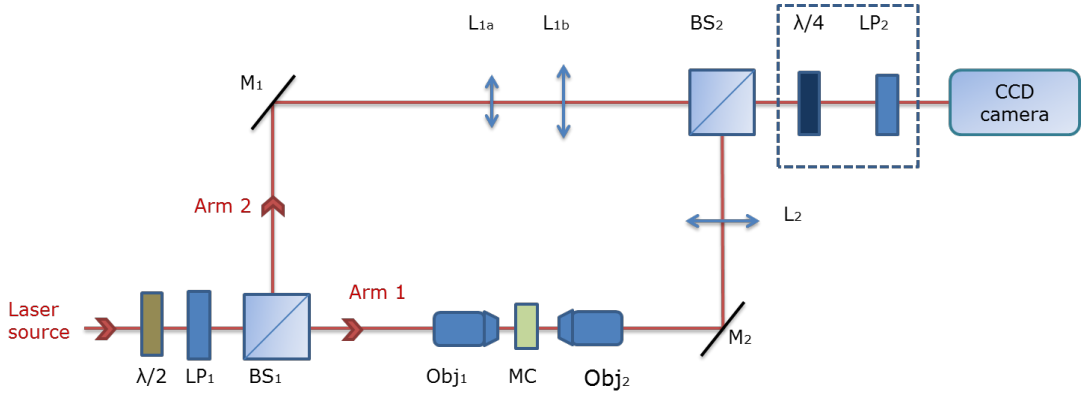

FIGURE 4.3: Sketch of the Mach-Zehnder interferometer used in the experiments discussed in in Chapter 5. List of the optical components: BS_1 and BS_2 are non-polarizing beam splitters; M_1 and M_2 are mirrors; Obj_1 is the excitation objective with a 20x magnification and 0.4 numerical aperture; Obj_2 is the objective used for collection of the transmitted beam, with 10x magnification and 0.25 numerical aperture; L_{1a}, L_{1b} and L_2 are convex lenses; $\lambda/4$ and LP_2 are respectively the quarter-wave plate and the linear polarizer used to measure the circular Stokes parameters while $\lambda/2$ and LP_1 are respectively a half-wave plate and a linear polarizer used to control the excitation power. The optical elements enclosed in dashed box ($\lambda/4$ and LP_2) are introduced in the setup only in the case of polarization measurements (i.e. half-soliton like features) corresponding to Fig.5.12 and Fig.5.14(a).

both Arm 1 and Arm 2. In this arrangement the setup correspond to a Mach-Zehnder interferometer, in which a laser is split into two arms: one is used to excite the sample (Arm 1), while the other with a flat phase is used as the reference (Arm 2). The excitation beam (Arm 1) is focused by a 0.4 NA microscope objective to a spot on the sample with a full width at half maximum (FWHM) $2\sqrt{ln\ 2}\sigma$ of $3\,\mu m$ (with σ being the standard deviation of the 1D Gaussian curve used to fit the spot intensity profile), resulting in a circular distribution in momentum space (i.e. k-space) with a diameter of $3\,\mu m^{-1}$. The light transmitted through the sample is then collected using a 0.25 NA microscope objective and focused on a charge-coupled device (CCD) camera by a convex lens (L_2). In this way, the transmitted beam is imaged in real space. The reference beam (Arm 2) is expanded by a telescope (formed by L_{1a} and L_{1b} in Fig. 4.3) so that a bigger area of the sample could be investigated and then interfered with the transmitted beam on the CCD camera. The incidence angle of the reference beam was adjusted in order to obtain interference fringes along y. The power of the excitation beam is adjusted by means of a half-wave plate ($\lambda/2$) and a linear polarizer (LP_1).

Polarization measurements. The investigation of half-soliton features (section 5.10), requires a polarization-resolved measurement. To this end we use a linear polarizer (LP_1) to prepare the excitation beam in the linearly polarized basis (parallel to the y-axis in Figs.5.12) and we introduce in the setup a polarimeter composed by a quarter-wave plate ($\lambda/4$) and a linear-polarizer (LP_2), oriented at 45° with respect to one another, to measure the circular Stokes parameter of the transmitted signal. In this way, by rotating the wave-plate it is possible to measure the two circularly polarized intensities I_{σ_+} and I_{σ_-} and then use equation 2.32 to calculate the circular component (S_z) of the Stokes vector shown in Fig.5.14(a).

4.2.2 Half-Gaussian excitation scheme

The half-Gaussian beam was created by a confocal excitation scheme as described in the supplementary information of Ref. [18]. In this scheme, a razor blade is placed between two lenses (at a distance equal to the focal lengths of the lenses) before the excitation objective (Obj_1 in Fig.4.3). The first lens focuses the laser on a razor blade while the second collimates the image of the razor blade on the sample. In this way, by adjusting the position of the razor blade it is possible to shape the excitation beam with

a half-Gaussian profile, as shown in Fig.5.3(e). The experimental data acquired with this excitation scheme are shown in Fig.5.3.

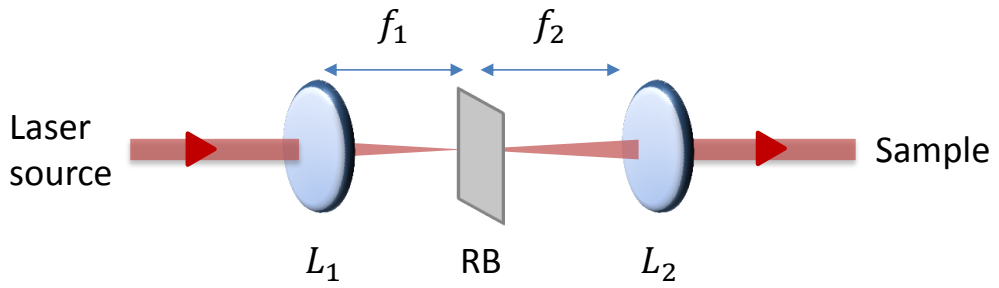

FIGURE 4.4: Sketch of the optical components used to produce the half-Gaussian excitation beam. L_1 and L_2 are two aspherical lenses with focal length f_1 and f_2 respectively. RB indicates the razor blade. These components have been introduced in the setup shown in Fig.4.3, between the first beam splitter (BS_1) and the excitation objective (Obj_1).

4.2.3 Reflection-like geometry

In reflection-like geometry, the same objective is used for excitation and collection, as shown in Fig.4.5. This setup geometry has been used to study the spin textures reported in Chapter 6 and Chapter 7. In all the experiments, the sample is held in a helium cryostat at temperature $T = (6 - 7)$ K and all the experiments are performed under non-resonant excitation. The polarized emission is collected by the same objective, sent through a long pass filter (to filter out the excitation laser reflections) and then projected with an achromatic lens L_1 on the entrance slit of a spectrometer. The latter is equipped with both a charge coupled device (CCD) and a streak camera with $2\,ps$ temporal resolution. The grating of the spectrometer can be interchanged with a mirror allowing direct imaging of real or momentum (k) space without energy resolution. To measure the far field emission of the microcavity, i.e., the k-space, an extra lens L_k is introduced into the setup to form the image of the Fourier plane onto the entrance slit of the spectrometer (i.e. only for k-space measurements).

The polarization of the emitted light is analyzed by a polarimeter composed of a quarter wave plate ($\lambda/4$) or half wave plate ($\lambda/2$) and a linear polarizer (LP_2). The circular Stokes component (S_z) are measured by means of the $\lambda/4$ wave plate and the linear polarizer (LP_2), while the linear Stoke components (S_x, S_y) by the $\lambda/2$ wave plate and the linear polarizer (LP_2). In this way, by rotating the wave-plates it is possible to

select the component of the Stokes parameter of which one wants to measure the relative intensity (see section 2.7.1). Then, by using equations 2.32, the different components of the Stokes vector can be calculate.

Both time integrated and time (or energy) resolved measurements have been performed by using the setup shown in Fig.4.5. However, depending on the type of measurements, different optics and components have been used, as summarized below.

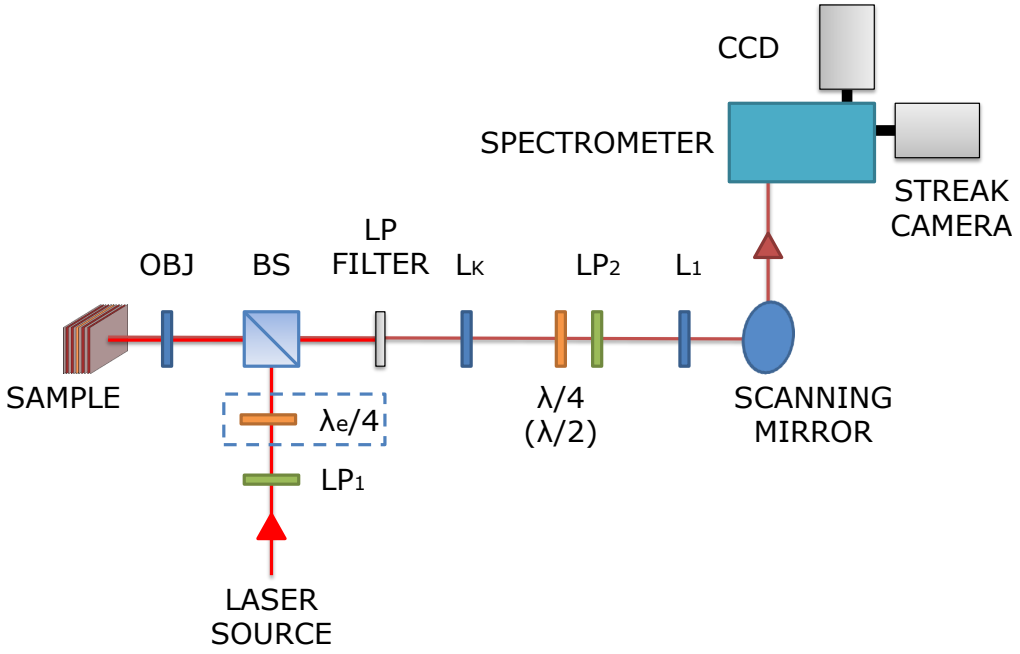

FIGURE 4.5: Sketch of the experimental setup used to acquire the data reported in Chapter 6, Chapter 7. Lists of the optical components: $\mathbf{LP}_1$ is the linear polarizer with extinction ratio higher than 1000:1; $\lambda_e/4$ is the quarter-wave plate to create a circularly polarized excitation beam. This has been used only for the data presented in Chapter 6; **BS** is the non-polarizing beam splitter; **OBJ** is the 20x, 0.4 NA objective; **LP Filter** is the long pass filter; $\mathbf{L}_k$ is the lens used to imagine the k-space; $\lambda/4$ ($\lambda/2$) is the quarter-wave plate (half-wave plate); $\mathbf{LP}_2$ is a linear polarizer and **L1** is the 10 cm focal length lens. The motorized scanning mirror and the spectrometer, equipped with both a charge coupled device (CCD) and a streak camera, are also shown.

Time integrated measurements. The data reported in Fig.6.3 and Fig.6.5 (Chapter 6), have been acquired by using a single-mode continuous-wave Ti:Sapphire ($Ti:Al_2O_3$) laser, with a beam focused to a $\sim 5\,\mu m$ size spot through a 10x, 0.25 NA objective (Obj). The excitation laser is intensity modulated using an acusto-optic modulator (AOM) at 10 KHz with a 5 % duty cycle. The AOM, apart from reducing the sample heating, it makes also possible to perform power dependence measurements in an automated way. The excitation laser is passed through a linear polarizer (LP_1), with polarization extinction ratio higher than 1000:1, and a quarter wave plate ($\lambda_e/4$) oriented at 45°

with respect to LP_1. In this way, the sample is excited with a circularly polarized beam σ_+. The light emitted by the sample is filtered with a 780 Long Pass Filter (LP filter) and focused onto a water-cooled CCD camera by an achromatic lens L_1. Thus, the real space emission of the sample is studied.

Real time measurements of the Stokes vector. The data reported in Fig.6.10 have been acquired with the same setup described above (in "Time integrated measurements") but using a linearly polarized beam, obtained by removing the quarter wave plate $\lambda_e/4$ (see Fig.4.5), a 20x, 0.4 numerical aperture objective (obj) and a Wollaston prism. The latter has been placed instead of the linear polarizer LP_2 shown in Fig.4.5. Thus, the polarized emission, collected by the same objective, is analyzed by a polarimeter that now is composed of a $\lambda/2$ or $\lambda/4$ plates and a Wollaston prism, with $\sim 20°$ polarization splitting angle. The emission is then imaged in real space by a 10 cm focus lens (L_1) directly on a CCD camera (time integrated measurements). In this way, both the polarizations components are imaged simultaneously and the Stokes parameters calculated in real time by an appropriate software. This software was realized by me in LabVIEW.

Time and Energy resolved measurements. The dynamic of the spin textures (Fig.6.7 in section 6.5.2 and all the data presented in Chapter 7), is studied by using the same experimental setup described above (Fig. 4.5) but employing a pulsed laser, with pulse width of 250 fs and a pulse frequency of 80 MHz. The excitation laser, is focused to a spot of $\sim 2\,\mu m$ FWHM ($2\sqrt{\ln(2)}\sigma$) (with σ being the standard deviation of the 1D Gaussian curve used to fit the spot intensity profile), by means of a 20x, 0.4 numerical aperture objective (obj). In the case of the spin whirls (Chapter 7) the excitation beam is linearly polarized with polarization extinction ratio higher than 1000:1 (LP_1) (i.e., in this experiment the quarter wave plate $\lambda_e/4$ is not present in the setup shown in Fig. 4.5). The polarized emission is collected by the same objective, sent through a long pass filter (LP filter), analyzed by a polarimeter composed of a $\lambda/2$ or $\lambda/4$ plate and a linear polarizer (LP_2) and then projected with an achromatic lens L_1 (f = 10 cm) on the entrance slit of a spectrometer. For time resolved measurements, the grating is interchanged with a mirror and the emission is projected onto a streak camera. On the other hand, for energy resolved measurements the emission is focused into the entrance slit of a spectrometer with a 1200 groove/mm grating.

4.2.4 Michelson interferometer

BEC is characterized by a buildup of long range coherence. One way to measure the degree of coherence of the condensate is by performing interferometer measurements and measuring the fringe visibility V [165]:

$$V \equiv \frac{I_{max} - I_{min}}{I_{max} + I_{min}} \tag{4.1}$$

with I_{max} and I_{min} being respectively the intensities corresponding to the maximum and adjacent minimum in the fringe system.

To show the coherence build up above threshold of a polariton condensate (Chapter 8), we measure the fringe visibility by means of an actively stabilized Michelson interferometer in a mirror-retroreflector configuration [11]. The use of a stabilized Michelson interferometer is preferred respect to the Mach-Zehnder interferometer because, by limiting the effects of vibrations of the setup, it guarantees a greater accuracy in fringe visibility measurements.

4.3 Methods

4.3.1 Real space calibration

In order to calibrate the real-space setup, a target with known dimensions is used and placed at the position of the sample in Fig. 4.1 a). The target is a Thorlab positive *1951 USAF* test target ∅1"(Mod. R1DS1P), which consists of groups of horizontal and vertical lines. Each group is composed by three lines and the spacing between the lines is equal to the thickness of the line itself. By using a white light source it is possible to image the target (Fig. 4.6 a) and calibrate the image system by extracting the length in pixels of 1 line pair. This is shown in Fig. 4.6 b), where Δx corresponds to the 1 line pair, i.e. 1 black and 1 orange line in Fig.4.6a). Since the length of 1 line pair, for each specific group of lines, is known in line/mm (see USAF resolution test chart), it is possible to work out the value of 1 pixel for the system of lenses used in the setup.

The same method can be used, to characterize the size of the laser spot in real space. By illuminating the target with both a white light and a laser source, the target and

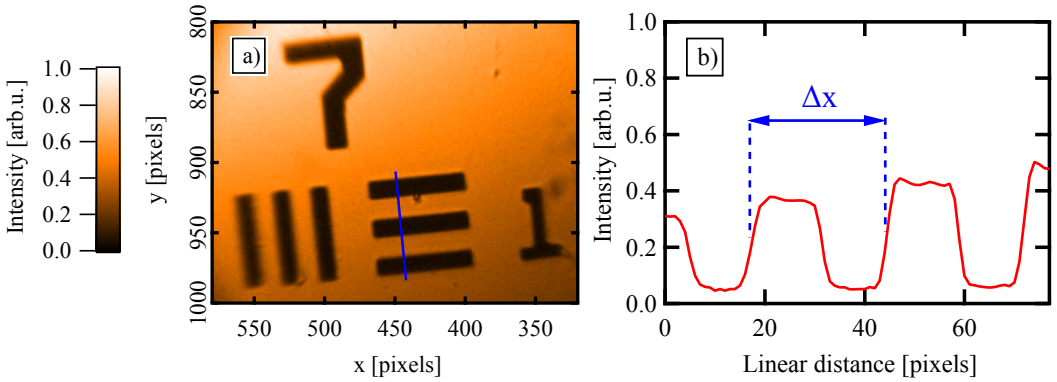

FIGURE 4.6: a) Real space image of the USAF target obtained by illuminating the sample with light in transmission geometry. b) Intensity profile extracted along the blue line in a). Δx corresponds to 1 line pair, whose length is known in line/mm (see USAF resolution test chart).

the laser spot can be imaged simultaneously in real space, as shown in Fig. 4.7. If one compares the FWHM of the laser spot, calculated from the fitting of the beam with a Gaussian function of width σ, i.e. FWHM $= (2\sqrt{\ln(2)}\sigma)$, and the line pair distance (line/mm) of a specific group of lines (e.g. group number 6 in Fig.4.7), the FWHM of the beam spot can be calculate in μm.

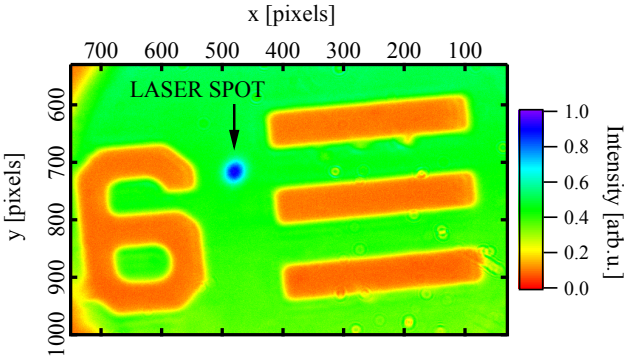

FIGURE 4.7: Real space image of the USAF target and laser beam that allow the calculation of the FWHM of the laser spot.

Finally, the USAF target allows also to test the maximum resolution of the image system. The largest set of horizontal and vertical lines which cannot be resolved, corresponds to the resolving power of the imaging system.

4.3.2 Tomography techniques

When time or energy resolved measurements are performed, the emission from the sample is projected onto the entrance slit of a streak camera or a spectrometer. In both

cases, the 2D data acquired have only one spatial component (x) while the other is the time (t) or the wavelength (λ) respectively for time- and energy-resolved measurements. However, by means of a motorized scanning mirror (Fig. 4.5), 2D real space images (x,y) as function of time (or energy) can be reconstructed. All the data presented in Chapter 7 have been acquired with this technique.

To study the polarization dynamics in both real and k-space, without energy resolution, the intensity emitted by the microcavity is time-resolved. By using the tomography scanning technique, the near field intensity I(t,x,y) [far field I(t,k_x,k_y)] emitted by the microcavity is imaged on the entrance slit of the streak camera for a fixed y [k_y]. By using a motorized mirror, it is possible to scan the y [k_y] dimension and acquire I(t,x) [I(t,k_x)] at different y [k_y]. In this way, a 2D real space image I(x,y) [2D k-space image I(k_x,k_y)] at different times can be reconstructed. In the case of k-space this is possible since photons, emitted from the microcavity at an angle θ (where θ is the emission angle with respect to the normal of the microcavity plane), correspond to polaritons with in-plane wave vector $k_{||} = k_0 \sin(\theta)$ (with $k_0 = 2\pi/\lambda_0$ and λ_0 being the emission wavelength). The data reconstruct with this technique are Figs.6.7(a-c), Figs.7.1(a-c),Fig.7.2(b) and Figs.7.8(a-b) for the 2D real space and Figs.7.9(a-b) for the k-space. The same technique can also be applied for energy resolved measurements. In this case, the motorized mirrors scan the x [k_x] dimension and acquire I(λ,x) [I(λ,k_y)] at different x [k_x].

4.3.3 Correction for time delay

In time resolved polarization measurements (Chapter 7), to take into account the different delays introduced by the waveplates when the different polarization components are measured, the experimental data have been rescaled to have a common zero (Fig. 4.8). The zero time is defined at the photoluminescence onset, as shown in Fig. 4.8(a) and (b). This correction has been applied to both the Stokes images and the intensity profiles which have been time resolved (Fig.6.7 and all the data reported in Chapter 7).

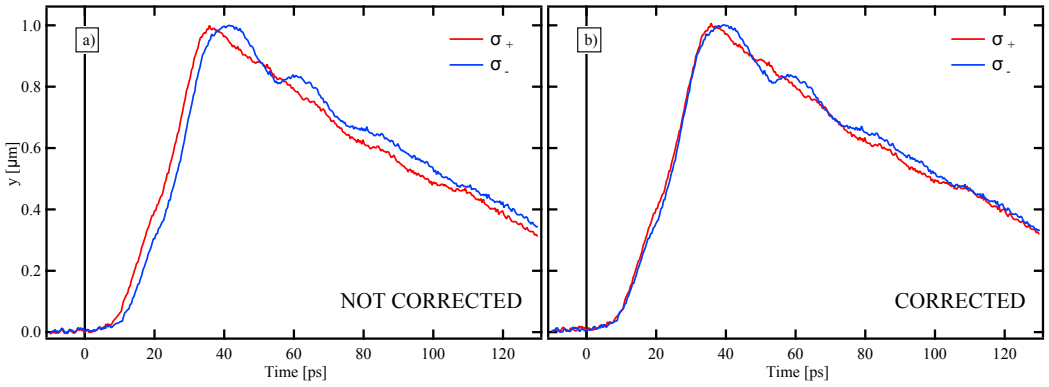

FIGURE 4.8: Time-resolved, spatially integrated measurements linearly polarized excitation and circular detection. In a) no corrections on the intensity profile has been applied, while in b) the experimental data have been rescaled to have a common zero, where the zero time is arbitrarily defined at the photoluminescence onset (vertical black line). In both cases the intensity profiles versus time have been integrated over an area $460\,\mathrm{x}\,340\mu m^2$ corresponding to the one imaged in Figs.7.1(a-c).

4.4 Samples

4.4.1 Bare photonic cavity

The sample used to study the formation of dark solitons presented in Chapter 5, was provided by Prof. Wolfgang Langbein (Cardiff University). This sample was grown by molecular beam epitaxy. It consists of a λ bulk GaAs microcavity surrounded by 27 (top) and 24 (bottom) distributed GaAs/AlAs Bragg reflector pairs (DBRs) and does not contain quantum wells. No strong coupling phenomena have been observed on this sample. The resonant mode of the cavity is centered around $1.46\,eV$ at normal incidence.

4.4.2 AlGaAs/AlAs microcavities

The works concerning the spin of polaritons and the formation of spin textures has been carried out on two AlGaAs/AlAs microcavity samples. In particular, the formation of the spin textures under circularly polarized excitation (section 6.5) and the spin whirls experiments (Chapter 7), were carried out on the sample grown at the FORTH institute in Crete by the group of Prof. Pavlos Savvidis. In the following, this sample will be refereed as sample A.

Sample A, is a $5\lambda/2$ AlGaAs/GaAs microcavity, composed by 32 (35) top (bottom) distributed Bragg reflectors (DBRs) and 4 triplets of $10\,nm$ thick GaAs quantum wells (QWs) placed at the antinodes of the cavity electric field. The cavity quality factor

is measured to exceed Q$\gtrsim$ 8000, with transfer matrix simulations giving Q= 20000, corresponding to a cavity photon lifetime $\sim 9\,ps$. The Rabi splitting is $9\,meV$. On the same sample, other authors have reported lasing under continuous wave (CW) excitation [166].

The work concerning the formation of spin textures under linearly polarized excitation (i.e. the skyrmion-like patterns), presented in section 6.6, has been carried out on another microcavity sample (sample B), which was provided by Prof. Sven Höfling from the University of St. Andrews (UK).
Sample B is composed by 23 (27) pairs of AlGaAs/AlAs layers, forming the top (bottom) Distributed Bragg Reflectors (DBRs) and 4 triplets of $7\,nm$ thick GaAs quantum wells. The quality factor is experimentally determined to exceed 9000 corresponding to a cavity photon lifetime of $\sim 3.8\,ps$. Strong coupling is obtained with a characteristic Rabi splitting between upper and lower polariton energies of $14.5\,meV$. On this structure, a superlinear increase of the emission together with a drop of the linewidth and a buildup of coherence was reported under non-resonant CW excitation [167]. These features are characteristic for lasing and condensation.

In both samples, the microcavity wedge allows to choose the detuning between the cavity and photonic modes. This is a really important features of the microcavity samples because, due to the wedge-shaped cavity, the cavity mode shifts across the sample as the length of the cavity changes. Thus, by simply moving the excitation spot across the sample, different detunings (Δ) between the cavity (E_{cav}) and exciton (E_{exc}) mode, i.e., ($\Delta = E_{cav}$ - E_{exc}), can be obtained.

4.4.3 InGaAs strain-compensated microcavity

The work reported in Chapter 8, has been carried out on a strain-compensated planar microcavity with InGaAs quantum wells. This sample was provided by Professor Wolfgang Langbein (Cardiff University).

Generally, AlAs/GaAs MCs described in section 4.4.2, are currently the preferred system for the study of polariton fluidics due to low photonic and QW disorder combined with a moderate exciton binding energy (~ 10 meV). Nevertheless, the presence of cross-hatched dislocations (see section 4.5) affects the dynamics of polaritons giving rise to

localization [25] and scattering [168–171] phenomena that limit the propagation of polaritons within the cavity plane. In a previous work [172] it was shown that one can reduce the cross-hatched dislocation density by introducing strain-compensating AlP layers into the centre of the AlAs layer of the distributed Bragg reflectors (DBRs). On

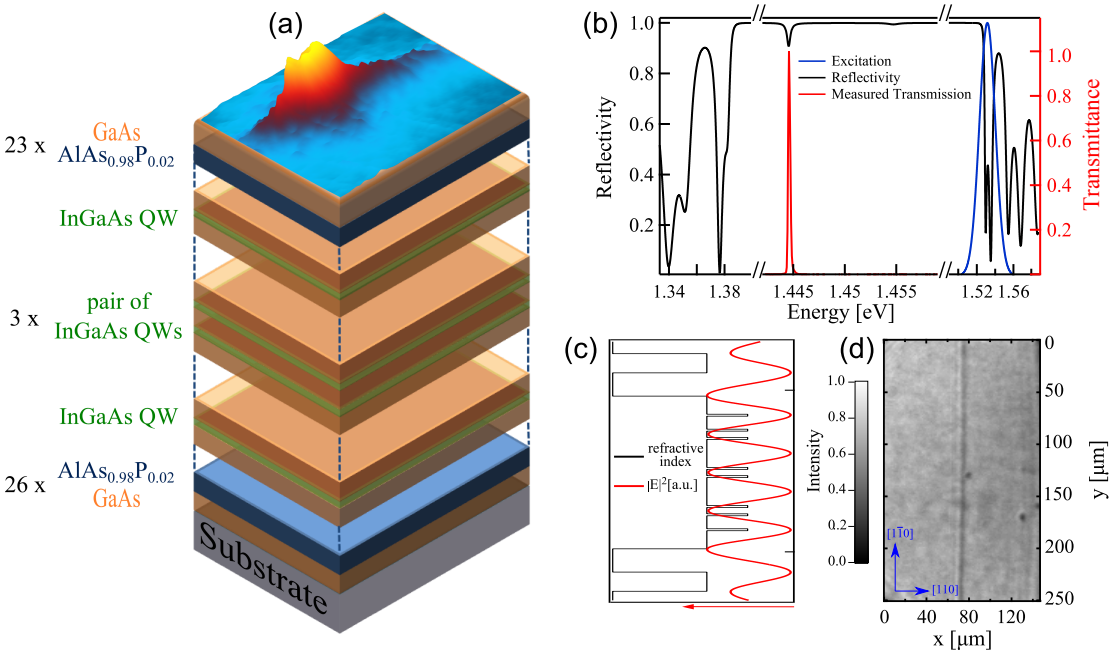

FIGURE 4.9: **(a)** Sketch of the microcavity structure and condensate emission. (b) Calculated reflectivity of the cavity stop band with the transfer matrix method (black line), spectra of pulsed excitation (blue) and experimental transmittance spectrum (red) for detuning $\Delta = -5.8$ meV. (c) Sketch of the refractive index (black line) along the growth direction and the corresponding square of the electric field of the cavity mode (red line). (d) Real space transmission intensity image of the sample surface under white light illumination on a linear gray scale, as indicated.

the basis of this work, another strain-compensated microcavity sample was realized at University of Sheffieled. This sample, provided by Professor Wolfgang Langbein (Cardiff University) has been used for the work reported in the Chapter 9 of this thesis. It is composed by a strain compensated 2λ GaAs microcavity with embedded InGaAs QWs. Strain compensation was achieved by $AlAs_{0.98}P_{0.02}$/GaAs DBR layers instead of the thin AlP inserts in the AlAs layers used in Ref. [172] as their effective composition could be better controlled. The bottom DBR consists of 26 pairs of GaAs and $AlAs_{0.98}P_{0.02}$ while the top has 23 of these pairs as shown in Fig.4.9(a), resulting in very high reflectance (>99.9%) in the stop-band region of the spectrum as shown in Fig.4.9(b). Three pairs of 6 nm $In_{0.08}Ga_{0.92}As$ QWs are embedded in the GaAs cavity at the anti-nodes of the field as well as two additional QWs at the first and last node to serve as carrier collection wells, as shown in Fig.4.9(c). The large number of QWs was chosen to increase the Rabi

splitting and keep the exciton density per QW below the Mott density [173] also for sufficiently high polariton densities to achieve polariton condensation. A wedge in the cavity thickness allows access to a wide range of exciton-cavity detuning. The average density of hatches along the [110] direction was estimated from transmission imaging to be about 6/mm, while no hatches along the $[1\bar{1}0]$ direction were observed, as exemplified in Fig.4.9(d).

From the transmitted spectra at $\Delta = -5.8\,\text{meV}$ shown in Fig.4.9(b), at which the LP has a linewidth of 120 ± 50 μeV and an exciton fraction of 20.5%, we obtain a LP Q-factor of ~ 12000 while the calculated bare cavity Q-factor, neglecting in-plane disorder and residual absorption, is ~ 25000. [1]

4.5 Structural defects in microcavity

Microcavities are characterized by the presence of structural defects. The most common types of defects in planar GaAs based samples, grown by molecular beam epitaxy (see Appendix A), are the *cross-hatch misfit* dislocations (MD) and *point-like* defects (PD) [25, 26] (see Fig. 4.10 a).

The first type of dislocations are due essentially to lattice mismatch of the GaAs/AlAs Bragg mirrors [25]. The point-like defects, on the other hand, are due to Gallium droplets emitted occasionally during the growth [174, 175]. In a recent study [25] of the structural and optical properties of GaAs/AlAs microcavities grown by molecular beam epitaxy it was shown that the most common point-like defects (PD), with a surface density of about $10^4/cm^2$, were characterized by a circular or elliptical shape [26], as shown in Fig. 4.10 b) and c). These defects give rise to a dome-like modulation of surface, which is translated into the cavity structure and leads to a lateral modulation of the cavity polariton energy [25]. Thus, the presence of the defect has the effect of modifying the effective thickness of the cavity layer, as shown in Fig. 4.10 d), which typically results in an attractive potential for the cavity mode inside the defect [26]. Consequently a series of bound states can form inside the defect, as shown for example in Ref. [25, 26].

[1] The transfer matrix simulations were performed using the low temperature ($\sim$ 6K) refractive indices of 3.556 and 3.015 for the GaAs and $AlAs_{0.98}P_{0.02}$ layers, respectively, at the cavity resonance.

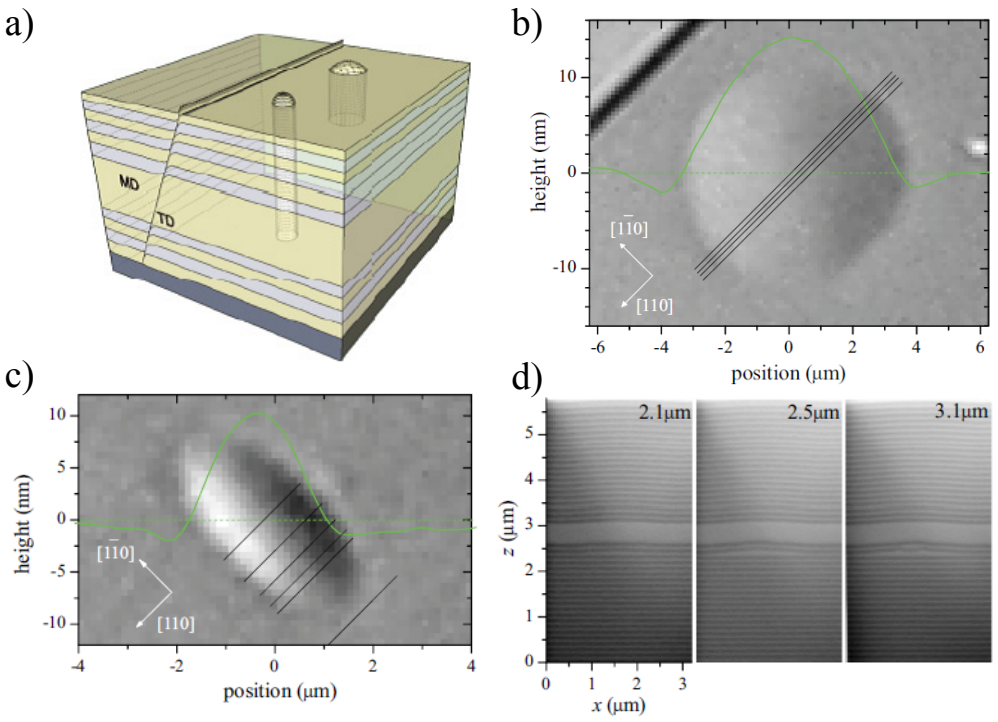

FIGURE 4.10: a) Sketch of a microcavity sample structure characterized by the presence of point-like defects (PD), cross-hatch misfit (MD) and threading (TD) dislocations. Image from Ref.[25]. b) Differential interference contrast microscopy (DIC) image showing a circular defect, with a diameter of 6 μm, on the surface of the sample (linear gray scale). The green profile corresponds to the height (h) profile of the defect center, corresponding to a h = 15 nm. Image from Ref. [26]. c) Same DIC image of the sample surface as in b) but for an elliptical defect, with major and minor axes of 1.2 μm and 0.6 μm respectively and height of 100 nm. Image from Ref. [26]. d) Scanning electron microscope (SEM) images of cross sections of the microcavity structure, taken along the black lines in c) at different distances from the edge of the defect. The distances are indicated in the right top corner of the images. Image from Ref. [26].

Structural defects in polariton microcavities played a key role in the study of superfluidity and dark solitons. The formation of dark soliton has, in fact, been claimed by interacting a polariton fluid with a spatially extended defect (see section 3.4.4). However, the experimental evidences reported in literature to claim the formation of dark solitons in polariton microcavities are not conclusive, as discussed in the next chapter.

Chapter 5

Study of the formation of dark and half-dark solitons in semiconductor microcavities

5.1 Introduction

The experimental observation of BEC [11] and superfluidity [57, 58] of exciton-polaritons, has sparked interest in the quantum-hydrodynamic properties of polariton fluids. In particular, the nucleation of solitary waves in the wake of an obstacle (i.e. defect) has been claimed recently [18–22] (see section 3.4.4 and section 3.4.5). Here, the source of nonlinearity, essential for the formation of such a solitary wave, has been identified in the repulsive polariton-polariton interactions [18–22]. In these previous works, the observation of dark notches in the intensity profiles together with a π shift in the phase have been used as sufficient signatures for dark solitons in microcavities. In addition, half-dark solitons have been found to carry a non-zero degree of circular polarization in presence of the TE–TM splitting of the cavity mode [22].

In this chapter we demonstrate that these features previously used as dark soliton fingerprints [18–22] can also be observed without the presence of nonlinearity (section 5.3), which is the fundamental ingredient differentiating solitons from linear wave propagation. Specifically we investigate the propagation of polaritons with a small exciton

fraction and at low polariton densities, excluding a relevant influence of nonlinearities (section 5.4). We show that polariton propagation in this linear regime across an extended defect can create deep notches in the intensity profile accompanied by a π phase shift. We model the observation using linear wave propagation (section 5.5), clarifying that these features are not indicative for a nonlinear interaction between polaritons, but are interference patterns created by scattering from the defect. Different features can appear in dependence on the scattering geometry, i.e. the direction of propagation of polaritons and the size of the defect (section 5.6). Moreover, we show that the appearance/disappearance of these features for different in-plane kinetic energies is reproduced in the linear regime and thus does not provide evidence of an interacting quantum fluid (section 5.7). Additionally, we show that the analogy between linear and nonlinear waves goes beyond the mere observation of the same features and is effectively more profound. Indeed, as shown in section 5.8, the intensity, the phase jumps as well as the relative depth of the dark-notches in the linear regime satisfy the same mathematical expression (equation 3.18) as in the quantum fluid case [18–21]. In particular, also in our linear system the relative depth of the dark-notches remains constant up to 42 μm. Finally, we study the half-dark soliton features (section 5.10) and show that they can also be observed in the linear regime, without the presence of nonlinearity.

Before describing the experimental work and the results obtained, a brief review of the unconventional properties of dark solitons in polariton condensates respect with atomic condensates, is presented in the next section.

5.1.1 Unconventional dark solitons

Many differences exist between the dark solitons observed in atomic condensate and the oblique dark solitons reported in polariton microcavities. Oblique dark solitons in polariton microcavity represent an unicum in the typology of dark solitons. At present, "oblique" dark solitons, although predicted for both atomic [65] and polariton condensates [17], has been experimentally reported only for polariton condensates [18–21]. On the other hand, in atomic BECs, only single "straight" dark solitons have been experimentally observed [16] (see Fig. 3.3 b).

More importantly, in polariton microcavity, oblique dark solitons are claimed at subsonic velocity, i.e. for a Mach number $M < 1$. However, in atomic condensates, the formation

of stable dark solitons has been theoretically predict only at supersonic velocities ($M > 1$) [65, 176]. The oblique dark solitons in Fig.3.5 (a,b) have a Mach number of 0.49 (already at $14\,\mu m$ from the defect)[1]. Similarly, the dark solitons in Fig.3.6 (c,f) have a Mach number of 0.6, where oblique dark solitons are *"absolutely unstable"* [176] and vortex nucleation is predicted in both atomic [176] and polariton [17] condensates. In Table 5.1, a comparison between the main theoretical and experimental results reported in literature is reported.

TABLE 5.1: Comparison between the theoretical and experimental Mach number reported in quantum fluids literature. Here **Exp.** = experimental work; **Th.** = theoretical work; **N.R.** = Not Reported.

Paper	Vortex Regime	Soliton Regime	Notes
Th. - Ref. [17]	$M > 0.43$	$M = 0.93$	Limit inferior of stable solution
Th. - Ref. [176]	$M > 0.45$	$M > 1$	Stable solutions [a]
Exp. - Ref. [18]	$M = 0.4$	$M = 0.6$	Reported (capture Fig.3 [18])[b]
Exp. - Ref. [19]	$M = 0.5$	$M = 0.6$	Calculated from equation 5.11 [c]
Exp. - Ref. [22]	N.R.	N.R.	

[a] In Ref. [176], oblique dark solitons are defined *"absolutely unstable"* when $M < 1$. The theoretical model is also based on the GPE equation.

[b] In Ref.[18], the Mach number can be directly extracted from the value they report in the capture of Fig.3.

[c] In the case of Ref.[19], the authors write: "The Mach number is estimated from the values of n_s/n_0 to be larger than 2, which confirms that our experiments are placed in the supersonic regime". However, by using: the angle $\alpha = 30°$ reported in Ref. [19], the value of $n_s/n_0 = 0.92$ extracted from the profile 5 mW (red curve) in Fig.3b [19] at 4 ps (note that 4 ps corresponds to the time where dark solitons are claimed in Fig.1 of the same work [19]) and equation 5.11, the value of the Mach number is M=0.6.

5.1.2 Other considerations

In Ref.[18], the excitation detunings are undefined, even though it has been shown theoretically that they control the injected polariton density and the fluid regime [see Fig.3.4]. Additionally, in this work [18], the claims of dark solitons have been done using different defects as obstacles, so that a dependence of the features observed from the defect it is not excluded.

[1] This value of the Mach number has been calculated from the data reported in Ref.[18]: flow velocity $v_{flow} = 1.7\,\mu m/ps$, speed of sound $c_s = 3.5 \pm 1\,\mu m/ps$ at $14\,\mu m$. The ratio of these two quantities corresponds to Mach number reported in the text.

Moreover, the excitation power dependence shown in Fig.3A-C in Ref.[18] (Fig.3.6 in this thesis) taken on a different defect than previous observations, is then claimed to display a transition from a subsonic regime to dark solitons. However:

- the turbulent regime claimed in Fig.3.6B is at a smaller power than Fig.3.5(a),
- the dark soliton candidate in Fig.3.6B does not presents the "dark solitons fingerprints", in particular the *phase jump* are absent already at $\sim 15\,\mu$m from the defect, as seen in Fig.3.6F.

In Ref. [22] half-solitons are claimed, but no excitation power dependence is provided, neither a measurement of the excitation power nor of the fluid density. Consequently, since the formation of dark solitons is predicted to depend on the density of polariton within the condensate (section 3.4), linear effects are not excluded, as it will be demonstrated in the next sections.

5.2 Experimental method

The investigated sample is a bulk λ GaAs microcavity described in section 4.4.1. The sample is held in a cold-finger cryostat at a temperature of 15 K and is illuminated by a narrow linewidth ($\approx$ 30 kHz) single-mode continuous wave Ti:Sapphire laser, tuned to cavity resonance at 1.485 eV (see section 4.2.1 for information on the sample). The

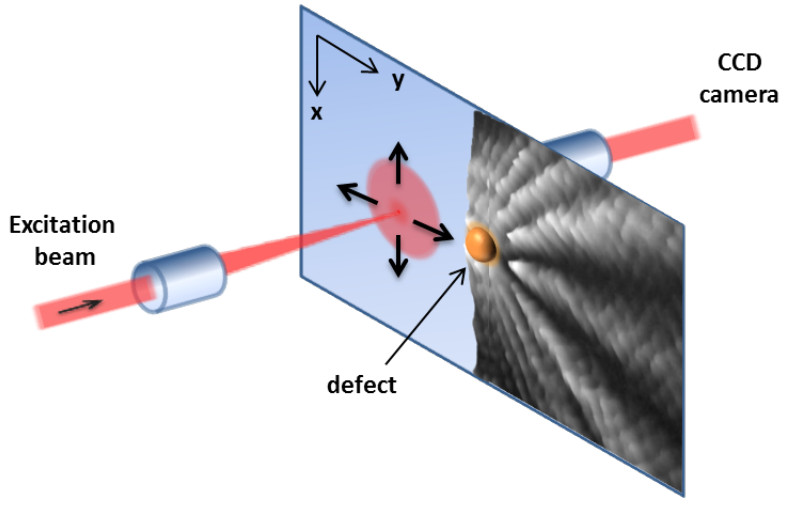

FIGURE 5.1: Sketch of both the excitation method used in the experiments and the linear wave dynamics in the x-y-plane of the microcavity.

measurements were performed in transmission configuration. The phase was measured using the shearing Mach-Zehnder interferometer described in section 4.2.1. Our experiments were performed in the linear regime, facilitated by the large negative detuning of -29 meV of the cavity photon mode from the exciton resonance at 1.514 eV, resulting in a small exciton fraction of the polariton of about 1%. Fig.5.1 shows a sketch of both the excitation method and the linear wave dynamics in the x-y-plane of the microcavity. Polaritons propagate along the positive direction of the y-axis and are scattered by a circular defect giving rise to phase singularities at points where the amplitude vanishes, i.e. at the dark notches of the intensity profile. The total detected polariton field is given by the interference of the incoming wave and the scattered wave.

5.3 Observations of dark soliton-like features

The real space intensity and interference of a polariton wave propagating across a defect are shown in Fig. 5.2. The experimental results show the presence of two dark notches

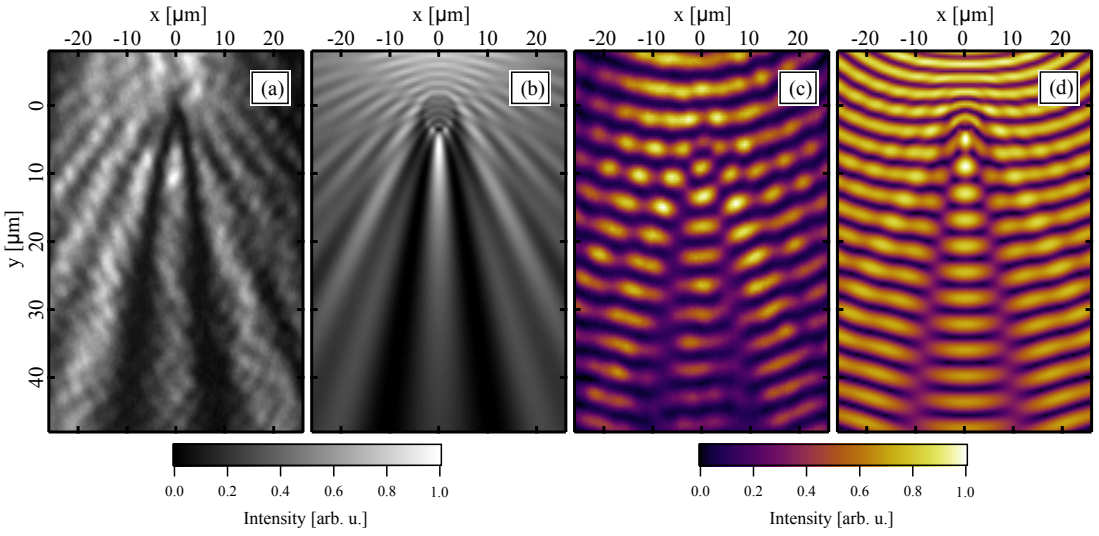

FIGURE 5.2: Experimental (a) and simulated (b) real space intensity and experimental (c) and simulated (d) interference patterns showing the two "soliton fingerprints" generated by the scattering of a beam with a point-like defect: a dark notch in the intensity pattern together with π phase dislocations. In the images the polaritons propagating downwards, along the y-axis, are injected with a wave vector of 1.5 μm^{-1} and are scattered by a defect positioned 25 μm away from the excitation spots.

in the intensity pattern [Fig. 5.2(a)] along with a π phase shift visible in Fig. 5.2(c) as paths of vortices merging in succession with alternating topological charge ± 1. Simulations of the measurements using the realistic experimental parameters are shown in

Fig. 5.2(b) and Fig. 5.2(d). The details of the theoretical model, based on the Maxwell equations, will be discussed in section 5.5. The model, together with the simulation images reported in this chapter, has been developed by Tomas Ostatnicky.

Thus, the propagation of the coherent polariton wave across an extended defect creates phase and intensity patterns with identical qualitative features previously attributed to dark and half-dark solitons of polaritons (see section 3.4.4). However, in the case of Fig. 5.2, these features occur in the linear regime, as demonstrated in the next section.

5.4 Excitation density & linear regime

In this section we demonstrate that the two "dark soliton fingerprints", i.e. dark notches in intensity and phase jumps in interferograms, do not depend qualitatively on the excitation power or on the shape of the excitation beam.

5.4.1 Power dependence with half-Gaussian excitation beam

To verify the linear regime, we studied the excitation density dependence of our results by performing power dependent measurements with both Gaussian and half-Gaussian excitation beams (see section 4.2.2 for information on the experimental setup).

In Fig. 5.3 we show the data acquired with a half-Gaussian excitation beam, focused to a spot with FWHM of 3.5 μm (see Fig. 5.3 e), 90 μm away from the defect. Here we vary the excitation power by 5 orders of magnitude, from 20 mW (Fig. 5.3 a,b) to 400 nW (Fig. 5.3 c,d) and do not observe significant changes in the spatial structure. Two notches in intensity together with phase vortex lines in the interferograms appear in the linear regime as the result of the scattering and interference. This is confirmed by the intensity profile and by the FWHM calculated for the left dark-notches in Fig. 5.3 a) and Fig. 5.3 c), which is respectively 4.2 $\pm$ 0.5 at 20 mW and 3.7 $\pm$ 1 at 400 nW (see Fig. 5.3 f). Thus, also in this case, as in the case of a Gaussian excitation beam [Fig. 5.2 (a) and (c)] we observe the formation of the two "dark soliton fingerprints".

In the microcavity polariton literature, the observation of dark solitons has been claimed using both a Gaussian excitation beam [18, 177] and half-Gaussian excitation beam [18,

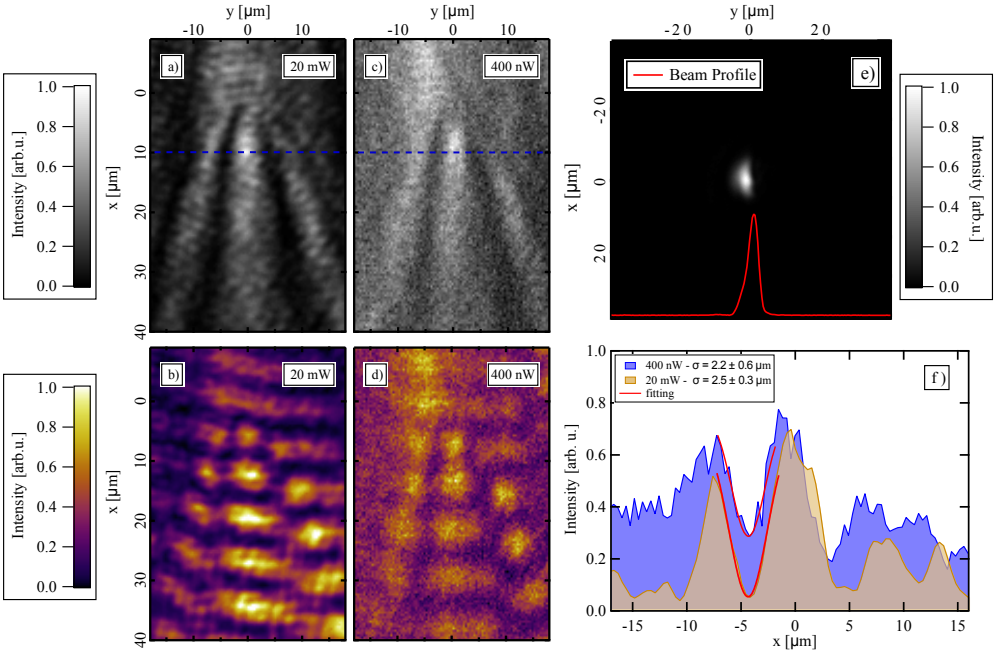

FIGURE 5.3: Measured real space intensity (a), (c) and interference patterns (b), (d) acquired at 20 mW and 400 nW excitation power. (e) Half-Gaussian excitation spot. (f) Intensity profiles calculated along the dashed blue lines in a) and c), 10 μm away from the defect. The red line represents the inverse Gaussian fitting used to calculate the FWHM of the left dark notches in Figs. (a) and (c). The σ of the two fits used for the calculation of the FWHM $2\sqrt{\ln 2}\sigma$ are also reported in the legend. The 400 nW profile (blue) reported in Fig. (e) has been shifted to the left by about 1 μm for clarity.

22]. We have used both excitation shapes and find that they do not affect the observed structure significantly.

5.4.2 Polariton density in the linear regime

The polariton density inside the cavity has been estimated from the number of photons transmitted through the sample and detected on the CCD camera. For a microcavity, in fact, the polariton population is proportional to the detected intensity. At the lowest excitation density of 3.8 W/cm^2, the polariton density inside the microcavity is estimated to be $D_{pol} = 2.3 \times 10^2 cm^{-2}$, seven orders of magnitude lower than the lasing threshold observed in standard microcavities [10]. The density of polaritons have been estimated by using the following formula:

$$D_{pol} = \Phi_{hv} \times \tau, \tag{5.1}$$

where $\Phi_{hv} = 2.3 \times 10^{13}\, cm^{-2}\ s^{-1}$ is the flux of photons transmitted through the sample and $\tau = 10\ ps$ is the polariton lifetime. The flux of photons Φ_{hv} has been calculated as:

$$\Phi_{hv} = \frac{C_{px} \times \alpha_{phe}}{t \times Q \times\ A_{px} \times \eta_{obj} \times \eta_{lens}}, \tag{5.2}$$

where $C_{px} = 7186$ is the maximum pixel counts corrected for the background, $\alpha_{phe} = 7.3$ is the number of photoelectrons per count (determined from the shot-noise), $t = 10\,\mathrm{s}$ is the integration time, $Q = 0.3$ is the quantum efficiency of the CCD camera at the wavelength used in the experiment and $A_{px} = 0.1225\,\mu m^2$ is the real-space area of a single CCD pixel on the sample, $\eta_{obj} = 0.7$ and $\eta_{lens} = 0.9$ are the assumed intensity transmission factors due respectively to the objective (Obj_2) and the lens (L_2) used in the experiment (see the experimental setup in Fig. 4.2.1).

The investigated sample has a large negative detuning of -29 meV of the cavity photon mode from the exciton resonance (1.514 eV), resulting in an exciton fraction of the polariton mode of less than 1%. The interaction energy scales with the excitonic content, and can be estimated using Eq. (9) in [178]. For the highest density used ($1.1\times10^{8}\,\mathrm{cm}^{-2}$), we find a renormalization energy of 33 neV, using the bulk exciton binding energy of 4.2 meV, a Rabi splitting of 5 meV, the bulk GaAs exciton Bohr radius of 14 nm, and an excitonic fraction of 1%. The parameters used here are approximate values, and the resulting renormalization is an order of magnitude estimate. However, since it is three orders of magnitude lower than the polariton linewidth, it is sufficiently accurate to predict that it has a negligible effect on the polariton dynamics, consistent with the experimental observation.

5.5 Theory of the cavity mode scattering by a point defect

As shown in section 5.4, our experimental observations are independent of excitation density over a range of 4 orders of magnitude. This shows that our experiments are in the linear regime. Consequently, we choose to model our result by using a theory based on the classical theory of electromagnetism using a linear material susceptibility, as discussed in details in the next sections.

5.5.1 Dislocation lines in interference patterns

As has been shown by Berry *et al.* [179, 180], wave fronts resulting from interference can contain dislocation lines [Fig. 5.4]. In the case of a scattered beam, dislocations are composed of phase shifts at positions where the amplitude of the electromagnetic wave and, thus, the intensity vanishes, representing nodes of the wave. It is worth mentioning that nonlinearities are negligible close to nodes also in the nonlinear regime, and phase dislocations at zero intensity (i.e., at the dark notches) are features of both linear [63, 64] and nonlinear waves.

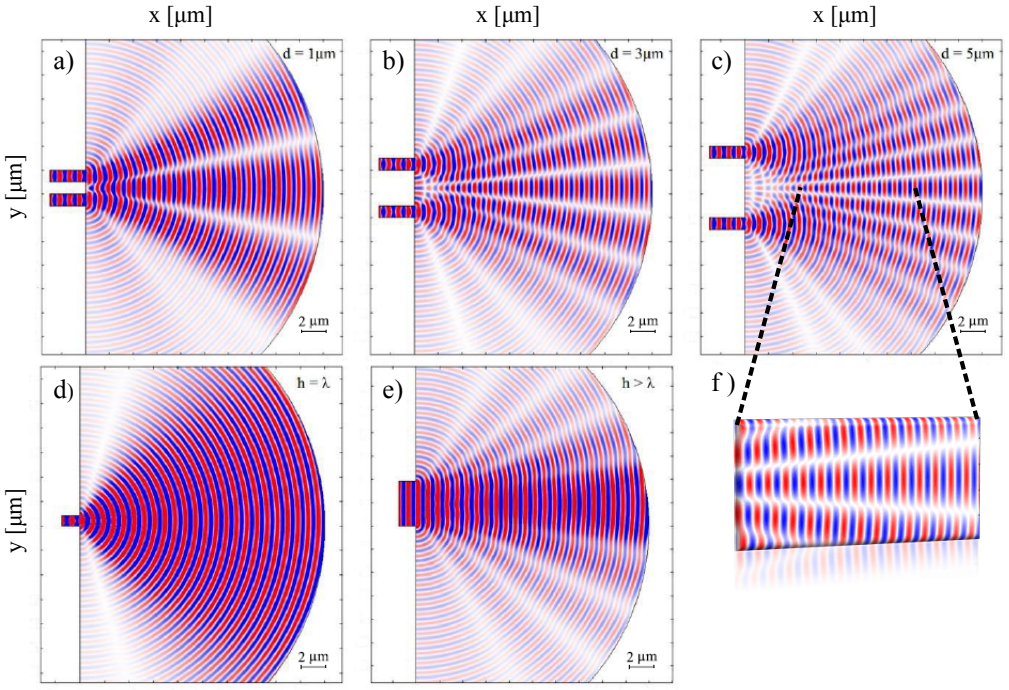

FIGURE 5.4: (a-c) Double slit and (d,e) single slit experiment simulation in GaAs cavity, performed by varying respectively the distance (d) between the two slits and the height (h) of the slit . f) Magnification of the interference area indicated by the dotted lines in c). The simulations clearly show the presence of wavefront dislocations, composed by phase shifts at the point where the amplitude of the electromagnetic wave vanish.

This is displayed in Fig. 5.4, for the case of an electromagnetic wave with a wavelength of 835 nm, like in the experiment, propagating along the positive x-direction and impinging on a double [Fig. 5.4 (a-c)] and single slit [Fig. 5.4 (d,e)] in a GaAs cavity. The images show that, by increasing the distance (d) between the two slits, an increase of the number of phase dislocations is observed. On the other hand, in the case of a single slit experiment, the phase dislocations appear when the height (h) of the slit is bigger than the the wavelength (λ) of the incoming wave.

5.5.2 Phenomenology of wave scattering from a defect

As discussed in section 4.5, the most common point-like defects (PD) present in GaAs/AlAs microcavities grown by molecular beam epitaxy, is characterized by a circular or elliptical shape [181]. The presence of the defect has the effect of modifying the effective thickness of the cavity layer, which typically results in an attractive potential for the cavity mode inside the defect [181]. Consequently, the wave vector of the photonic mode in the region of the defect is higher than in the rest of the cavity.

The polariton scattering by the defect depends on the wave vector mismatch between the polaritons outside and inside the defect at the energy of excitation. When the energy shift of the defect photon mode with respect to the unperturbed cavity mode is large enough to make the coupling between them inefficient, the defect behaves like a hard scatterer and the spatial intensity distribution is similar to the complementary case of a single-slit diffraction [182]. In our case, however, there is a finite transmission through the defect, producing dark and bright traces with a more complicated phase pattern.

Beyond the qualitative discussion above, we performed simulations of the experiments, based on a numerical solution of the linear scattering problem using the classical theory of electromagnetism. The choice of such a model is justified by the fact that we operate in the linear regime and with a small exciton fraction of about 1%, such that the polariton dispersion is dominated by the cavity mode. In the model, we consider the propagation of quasi-two-dimensional photons with a parabolic dispersion in a cavity with a fixed width. The incident wave has been treated as coming from a linearly polarized point-like source with polarization in the plane of the cavity. Defects have been modeled as disk-shaped perturbations of the cavity thickness resulting in an energy shift of the photon dispersion (see Fig. 5.5). To model the defect parameters, which are not experimentally known, we use a disk shape with a radius of $3\mu m$ and a polariton potential of -2.3 meV (consistent with Ref. [181]). Maxwell's equations are then solved using an expansion of the fields into the planar cavity eigenmodes in cylindrical coordinates fulfilling the boundary conditions for tangent components of electric and magnetic fields on the interface between the cavity and the defect. This linear wave dynamics model reproduces the intensity notch and the phase dislocation previously used as dark soliton fingerprints, as shown in Fig. 5.2 (b) and (d). The details of the theoretical models are discussed in the next section.

5.5.3 Theoretical model

The classical theory of electromagnetism is used in order to calculate the distribution of electric and magnetic fields inside the cavity in the presence of a disk-shaped defect and illumination of the cavity by a monochromatic laser beam. As already mentioned in the manuscript, the choice of such a model is justified by the fact that we operate in the linear regime with a polariton dispersion dominated by the cavity mode. In the model, we consider the propagation of two-dimensional photons with a quadratic dispersion in the microcavity plane, as shown in Fig. 5.5. A quadratic dispersion is found for all planar microcavity polaritons for small in-plane momenta plane. In our case, the large negative detuning provides a large range over which the dispersion is to a good approximation quadratic, covering all the relevant excitation wave vectors used.

The field distribution in a bare cavity obeys Maxwell's equations for the electric field $\boldsymbol{E}(x, y, z, t)$ and magnetic field $\boldsymbol{H}(x, y, z, t)$. Symmetry of the planar cavity allows one to separate the solutions as follows:

$$\begin{aligned} \boldsymbol{E}(x, y, z, t) &= \boldsymbol{E}_\omega(x, y)\chi(z)\exp[-i\omega t] \\ \boldsymbol{H}(x, y, z, t) &= \boldsymbol{H}_\omega(x, y)\xi(z)\exp[-i\omega t] \end{aligned}$$

The subscript ω denotes that the in-plane components of the fields depend on the energy of radiation while the normal components $\chi(z)$ and $\xi(z)$ are independent of energy under consideration of small in-plane wave vector $k_\parallel$:

$$k_\parallel \ll \frac{n_{\text{cav}}\omega}{c}$$

where n_{cav} is the refractive index of material of the cavity and c is the vacuum speed of light. The normal components $\chi(z)$ and $\xi(z)$ of the fields can be estimated inside the cavity where the most of light energy is concentrated: $\chi(z) \propto \xi(z) \propto \cos(n_{\text{cav}}\omega_0 z/c)$ where ω_0 is the cavity resonance frequency at normal incidence. The in-plane wave vector then can be deduced as

$$k_\parallel(\omega) = \frac{n_{\text{cav}}}{c}\sqrt{\omega^2 - \omega_0^2}.$$

The cavity defect is given by a change of the Bragg mirror composition by the presence

of additional GaAs due to the Ga droplet formation during the growth process [174, 175]. The presence of the defect has the effect to modify the effective thickness of the cavity layer, resulting in a red-shift of the photonic dispersion inside the defect [181]. As a

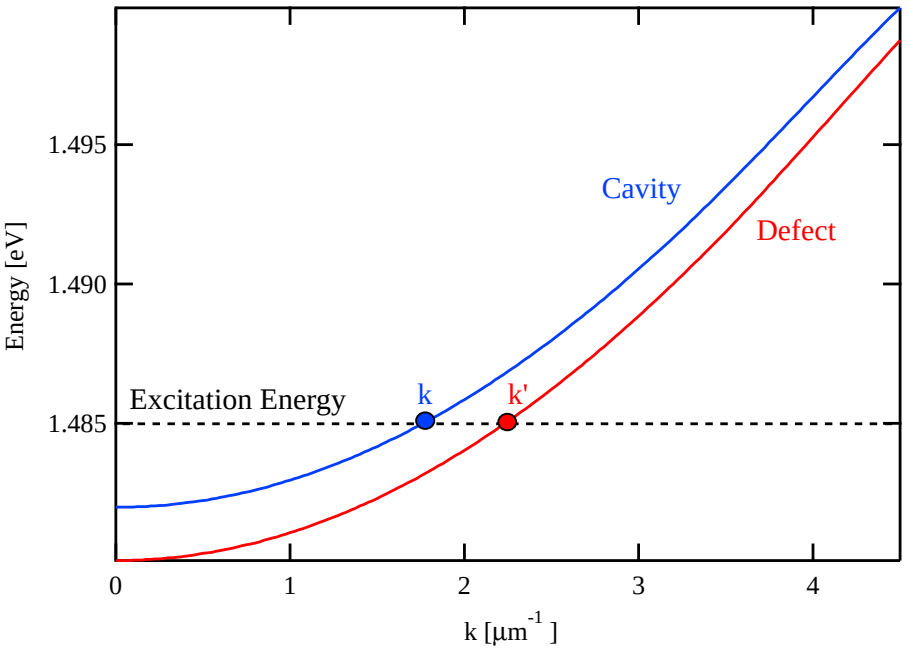

FIGURE 5.5: Theoretical dispersion inside (red) and outside (blue) the defect. The presence of the defect has the effect to modify the effective thickness of the cavity layer, resulting in a red-shift of the photonic dispersion inside the defect. Consequently, for a fixed energy, the wave vector of the photonic mode in the region of the defect is higher than in the rest of the cavity ($k' > k$). The black dashed line indicate the excitation energy used in the experiment.

result, the resonance frequency inside the defect shifts from ω_0 to ω_0' with respect to the bare cavity and accordingly the in-plane wave vector $k_{\|}$ to $k_{\|}'$, with $k_{\|}' > k_{\|}$ (Fig. 2.4). The energy shift of the cavity mode represents an attractive potential in the two-dimensional polariton propagation.

Besides the change of the resonance condition, also the normal components of the fields vary the spatial distribution and become $\chi(z) \to \chi'(z)$ and $\xi(z) \to \xi'(z)$. In our model, however, we assume that these changes are small (the relative change of the cavity energy considered in our case is only about 0.1%) and therefore we neglect them. Within this approximation, the solution of the problem of light propagation through a cavity with arbitrarily shaped defect is reduced to the solution solely in the xy plane because boundary conditions are independent of the position on the axis z. First we find two basis sets of solutions of Maxwell's equations for the bare cavity and the perturbed

cavity. We denote these sets as $\boldsymbol{E}^{\mathrm{cav}}_{\omega,j,m}$, $\boldsymbol{H}^{\mathrm{cav}}_{\omega,j,m}$ and $\boldsymbol{E}^{\mathrm{def}}_{\omega,j,m}$, $\boldsymbol{H}^{\mathrm{def}}_{\omega,j,m}$ respectively. Here the index j stands for polarization (TE or TM) and m is the discrete index of the mode in the expansion.

The two respective sets of fields defined above are local solutions of Maxwell's equations outside and inside the defect area. In order to solve the whole problem of scattering, we have to find a solution on the boundary between the bare cavity and the defect where the in-plane wave vector is not continuous. Here we assume that the boundary behaves like an ordinary boundary between two dielectrics, i.e. we require continuous tangent components of all fields. Let us write the fields in the bare cavity and in the defect area in the following form:

$$\boldsymbol{E}^{\mathrm{cav}}_{\omega} = \boldsymbol{E}_{\mathrm{incident}} + \sum_{j,m} c^{\mathrm{cav}}_{j,m} \boldsymbol{E}^{\mathrm{cav}}_{\omega,j,m} \tag{5.3}$$

$$\boldsymbol{H}^{\mathrm{cav}}_{\omega} = \boldsymbol{H}_{\mathrm{incident}} + \sum_{j,m} c^{\mathrm{cav}}_{j,m} \boldsymbol{H}^{\mathrm{cav}}_{\omega,j,m} \tag{5.4}$$

$$\boldsymbol{E}^{\mathrm{def}}_{\omega} = \sum_{j,m} c^{\mathrm{def}}_{j,m} \boldsymbol{E}^{\mathrm{def}}_{\omega,j,m} \tag{5.5}$$

$$\boldsymbol{H}^{\mathrm{def}}_{\omega} = \sum_{j,m} c^{\mathrm{def}}_{j,m} \boldsymbol{H}^{\mathrm{def}}_{\omega,j,m} \tag{5.6}$$

The coefficients c^{cav} and c^{def} are finally set so that the boundary conditions are fulfilled. If the basis sets are chosen properly, the solution is unambiguous. For the case of a circular defect, it is convenient to use the basis of fields in cylindrical coordinates [183] whose boundary conditions reduce to simple algebraic equations for the unknown coefficients. Once the coefficients are known, the spatial field distribution is evaluated using the definitions above, performing the summation on right hand side. To include the TE–TM splitting in cylindrical coordinates, it suffices to discriminate between the in-plane wave vectors $k_{\parallel,\mathrm{TE}}$ and $k_{\parallel,\mathrm{TM}}$ and the same inside the defect.

5.6 Dependence of the soliton-like features on the scattering geometry

In this section we study the dependence of the soliton-like features on the scattering geometry. The observed features depend on the shape and size of the defect and the direction and polarization of the incoming polariton wave relative to the defect. For an

elliptical defect, the phase and amplitude of the scattering depend on the direction of the incoming wave. Also the polarization contributes to the anisotropy of the effect because for a given absolute polarization direction a different angle of incidence corresponds to a different polarization relative to the defect.

Fig. 5.6 shows an example of the beam incident on the defect at an angle in the experiment. We use the same parameters of Fig. 5.2 (b) and Fig. 5.2 (d) of the manuscript to perform the simulations, but we change the direction of the incoming beam. In the previous case (Fig. 5.2), the excitation beam is polarized orthogonal to the incidence direction, while in Fig. 5.6 the beam direction has a 28 degree angle to its polarization (y), and generates a phase dislocation only in the upper dark line but not in the lower one, as indicated by the arrow in Fig. 5.6(c).

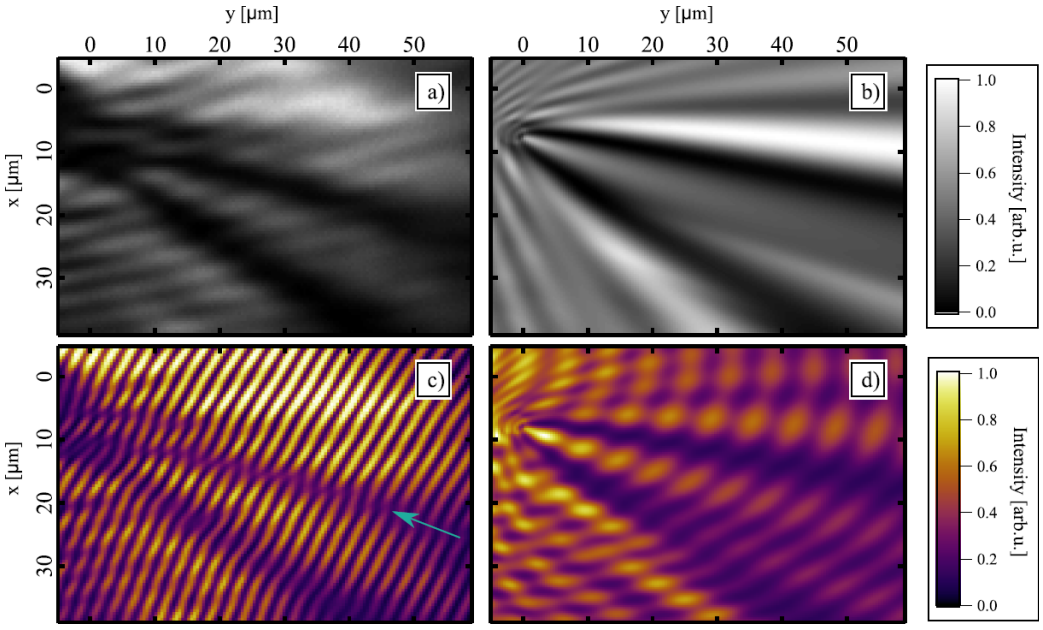

FIGURE 5.6: Experimental (a),(c) and simulated (b),(d) real-space intensity and interference pattern showing soliton-like fingerprints generated by the interaction of the beam with a defect. Unlike Fig. 5.2, the phase shift is only present in correspondence of the upper soliton-like feature as indicated by the light blue arrow in (c).

Moreover, we have investigated the case of a larger defect. The number of dark lines increases with increasing defect size, allowing the formation of quadruplet solitons-like features. This is confirmed by the simulations shown in Fig. 5.7(b) and Fig. 5.7(d). Once again we refer to the simulations shown in Fig. 5.2 (b) and (d) to simulate high-order dislocations. In particular, Fig. 5.7(b) and Fig. 5.7(d) have been calculated by using the same parameters as Fig. 5.2 (b) and Fig. 5.2 (d) of the manuscript except for

increasing the radius of the defect from 3 μm to 5 μm.

In Fig. 5.7(a) and Fig. 5.7(c) the experimental observation of a high order soliton-like features is shown in both intensity and phase. In the case of a bigger defect, it is possible to note how the wave appears to bend around the edges of the defect.

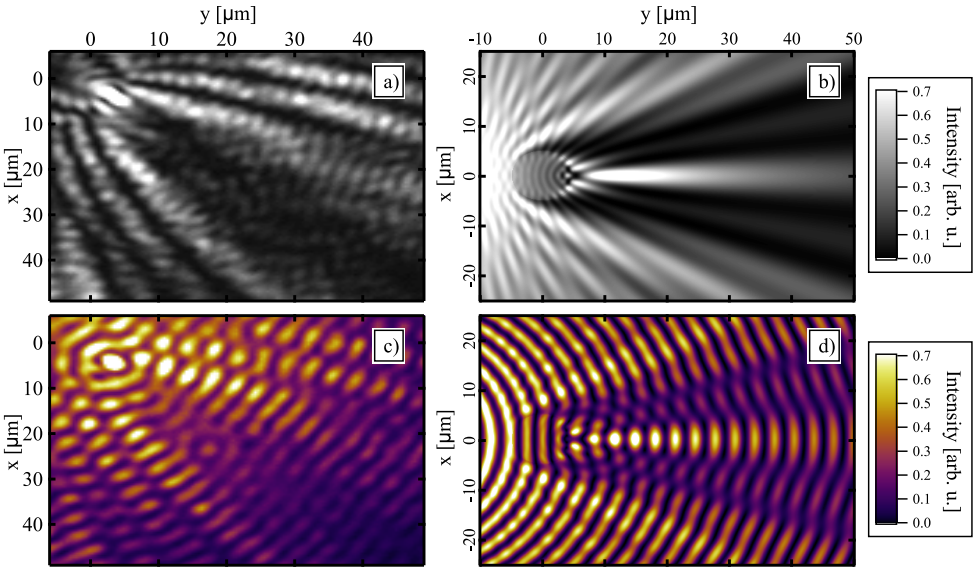

FIGURE 5.7: Experimental (a),(c) and simulated (b),(d) real-space intensity and interference pattern showing higher-order soliton features generated by the interaction of the beam with a defect bigger than the one present in Fig. 5.2.

5.7 Energy dependent measurements

In a nonlinear cavity-polariton system, a polariton fluid has been predicted to flow almost unperturbed around the defect (i.e., disappearance of the features) or experience the nucleation of vortices and/or solitons at the position of the defect (i.e. appearance of the features), depending on the excitation density or on the energy of the pump [17] (see section 3.4.3 and Fig. 3.4). We evaluated the possibility of observing these features, ascribed in the literature to dark solitons resulting from the interaction within the polariton fluid, in the absence of nonlinearities. Fig. 5.8 (a) and (b) show the phase and the intensity of soliton-like fingerprints in real space. Instead of increasing the excitation power, which has no effect in the linear regime, we tune the energy of the excitation beam, and observe the appearance and disappearance of soliton-like features. As discussed above, the appearance of the intensity minima and phase dislocations is a

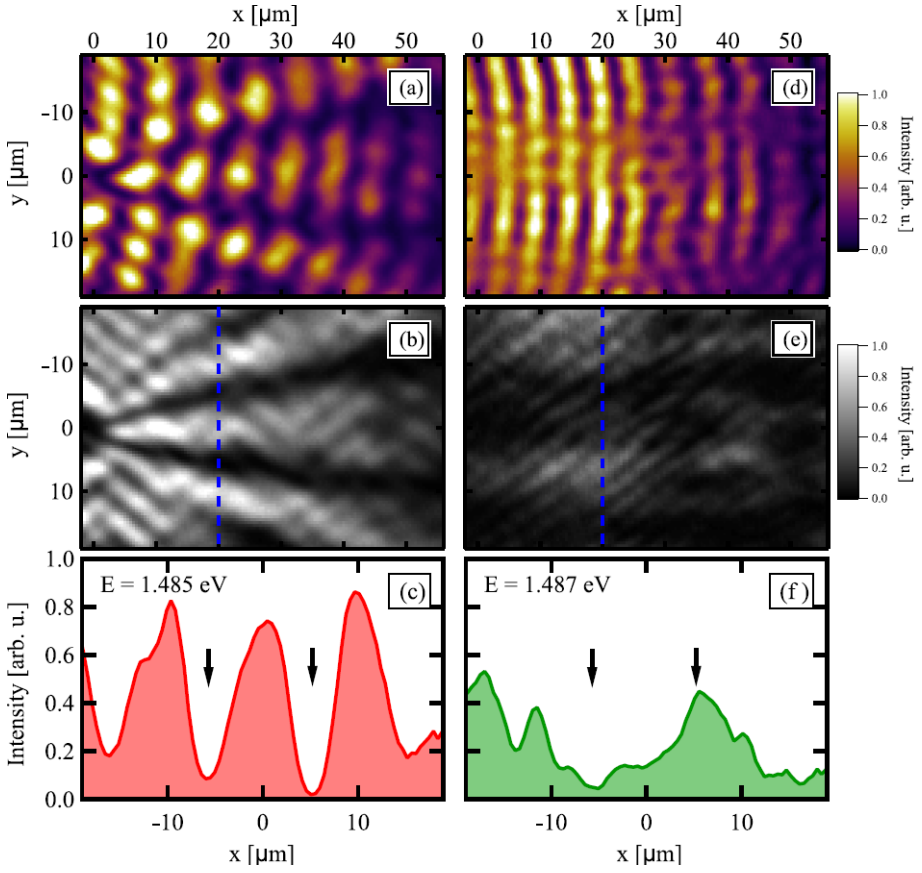

FIGURE 5.8: Experimental interference (a),(c) and intensity (b),(d) showing the transition between the regime where the soliton features are well defined 1.485 eV to a regime where they vanish 1.487 eV. The intensity profiles (e),(f) calculated along the blue dashed line, 20 μm away from the defect, confirm that the dark notches disappear when the energy of the excitation beam is increased. The two arrows indicate the positions of soliton-like fingerprints.

result of interference which is sensitive to the intensity and relative phase of contributing waves. The increase of the energy of the excitation beam by 2 meV causes an increase of the in-plane wave vector of the propagating polariton mode that, in turn, changes the interference condition so that the straight dark notches [Fig. 5.8 (c)] and the phase dislocations [Fig. 5.8 (d)] disappear. The wave vector dependence of such transitions will depend on the defect structure and the related bound polariton states [181], so that they could be observed also with decreasing wave vector for other defects. Intensity profiles measured at a fixed distance from the defect [Fig. 5.8 (e) and (f)] confirm the observed transition. Thus it becomes apparent that the appearance/disappearance of soliton-like features, although independent of the excitation density, strongly depends on the wave vector of the propagating mode. It is worth noting that an increase of the polariton density corresponds to an energy blueshift of the polariton dispersion. For

polaritons excited resonantly with a given energy, this results in an increase of the polariton wave vector with decreasing density along the polariton propagation. Specifically in non-resonantly excited experiments [184], this blueshift is dominated by the exciton density in the reservoir at high wave vectors. The interaction with the exciton reservoir is not a polariton-polariton interaction within the condensate which could provide the non-linearity needed for the formation of solitons, but instead represents an external potential sculpting the polariton energy and gain landscape.

5.7.1 Energy dependent measurements for a different defect

In this section we demonstrate that the disappearance of the two "dark soliton fingerprints" with detuning can be observed for different defects and can be considered a typical behavior. By using the same experimental setup described in section 4.2.1, we

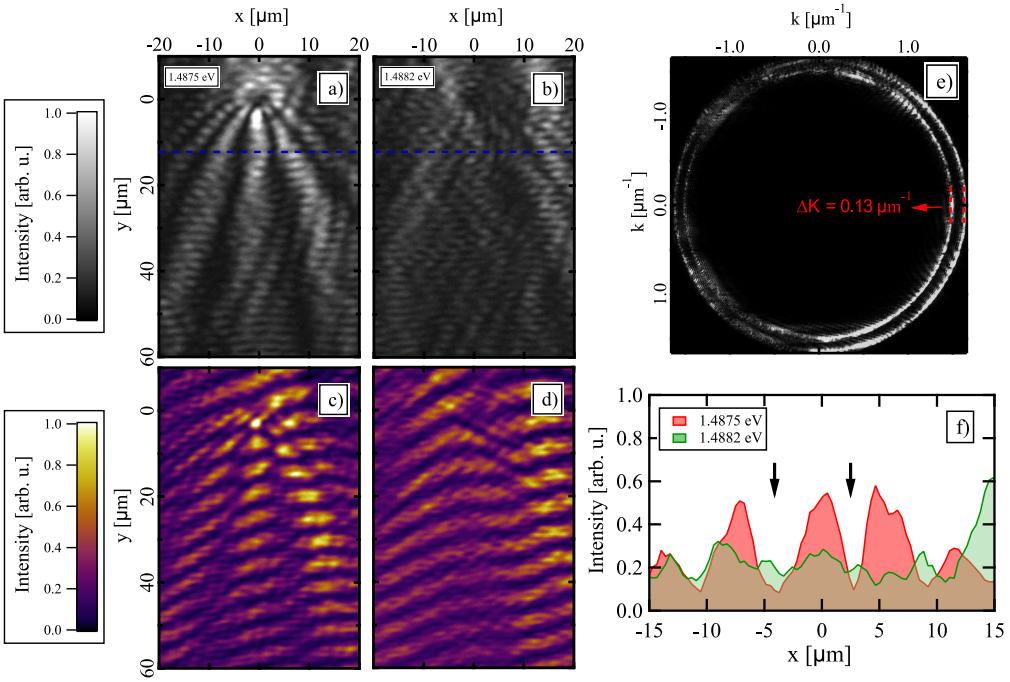

FIGURE 5.9: Experimental real space intensity (a), (b) and interference patterns (c), (d) showing the appearance (at 1.4875 eV) and disappearance (at 1.4882 eV) of both dark notches and phase shifts when the energy of the excitation beam is increased. In this case the excitation spot is focused 50 μm away from the defect. (e) Experimental K-space images showing the increase of polariton wave vector with the increase of the energy. The ΔK measured is 0.13 μm^{-1}. (f) Intensity profiles calculated along the blue dashed line, 12 μm away from the defect confirm the disappearance of the features (green profile). The two arrows indicate the positions of the soliton-like features.

study the scattering of polaritons from various defects and observe the appearance and disappearance of the soliton-like features when the energy of the excitation beam and

consequently the wave vector of polaritons is varied. Depending on the defect, different variation of the polariton wave vector is needed in order to observe the transition. The increase/decrease of the polariton wave vector changes the interference condition of the polaritons scattered by the defect so that both the dark notches and the phase dislocations disappear. In the case of Fig. 5.9, the dark soliton-like features disappear when the energy of the the excitation beam is increased by 0.7 meV, which corresponds to an increase of the wave vector of 0.13 μm^{-1}, as shown in Fig. 5.9 (e). The disappearance of the dark notches is confirmed by the intensity profiles extracted 12 μm away from the defect (Fig. 5.9 f). We have investigated several defects and found that a similar transition could be observed by decreasing the wave vector of the propagating polariton mode since also in this case the interference condition changes.

5.8 Evaluation of the dark soliton conditions for measurements in the linear regime

Since the first observation of dark solitons in atomic Bose-Einstein condensates (BECs) [16], the soliton speed (v_s) has been expressed in terms of either the phase shift ($0 < \delta < \pi$) or the soliton depth (n_s), the latter being the difference between the density of the condensate (n) and the density at the bottom of the notches (n_d):

$$\frac{v_s}{c_s} = \cos\ \frac{\delta}{2} = \sqrt{1-\frac{n_s}{n}} \tag{5.7}$$

In the above formula, already discussed in section 3.4.2 (equation 3.18) but rewritten here for convenience, c_s represents the speed of sound in the BEC, which is directly proportional to the square root of the density of the condensate [16] (see also equation 3.17). Equation 5.7 dictates the conditions that have to be satisfied in order to identify dark solitons in BECs. In particular, when δ tends to π:

1. $\frac{n_s}{n} \rightarrow 1$, i.e. the dark soliton becomes deeper ($n_s = n_d$)
2. $\frac{v_s}{c_s} \rightarrow 0$, i.e. the velocity of the dark solitons tends to zero.

Furthermore, due to the repulsive interactions within the BEC, the width of the dark soliton tends to the healing length ξ of the condensate [16, 159]:

$$\xi \rightarrow \left(\frac{2nMg}{\hbar^2}\right)^{-1/2}.$$

Here M is the atomic mass, g is the atom-atom interaction and $\hbar$ is the Planck constant divided by 2π.

As in the atomic BECs, also in the case of polariton condensates equation 5.7 has been used to identify dark solitons [18–21]. However, in all the previous works the healing length condition which is related to the width of the soliton has been neglected. This aspect will be discussed in the last part of this section.

First we evaluate the conditions 1 and 2 in the linear regime.

5.8.1 Depth and velocity of the dark-notch

In our case, as for the polariton quantum fluid, dark notches are characterized by a minimum of the intensity (n_d) at their center compared to the surrounding polaritons (n). Consequently, we can evaluate the depth (n_s) of a dark notch in the same way as in the quantum fluid case:

$$n_s = n - n_d \tag{5.8}$$

and calculate the relative depth of the dark notch ($\frac{n_s}{n}$) at different distances from the defect, where the phase shift δ is close to π.

Fig. 5.10 (c) shows the relative depth ($\frac{n_s}{n}$) of the dark notch for the left notch of Fig. 5.10 (a). The depth of the dark notch has been determined by fitting the line profile of the notch with an inverse Gaussian distribution at different distances from the defect. The intensity of the surrounding polaritons (n) has been estimated from the maximum intensity along the red dotted line in Fig.5.10 (a). The fitting (red line) and the quantities n, n_s and n_d are shown in Fig. 5.10 (c).

Similar to the case of a quantum fluid, in our linear system the relative depth of the dark notch remains approximately constant up to 42 μm as shown in Fig. 5.10 (d), which corresponds to a close to π phase shift in the interferogram [Fig. 5.10 (b)]. It is worth noticing that the ratio n_s/n oscillates around the mean value of 0.87 and it reaches the max value of 0.91 at 24 μm away from the defect, similar to the critical value of 0.9 reported in the literature [19, 21] for the formation of "vortex streets".

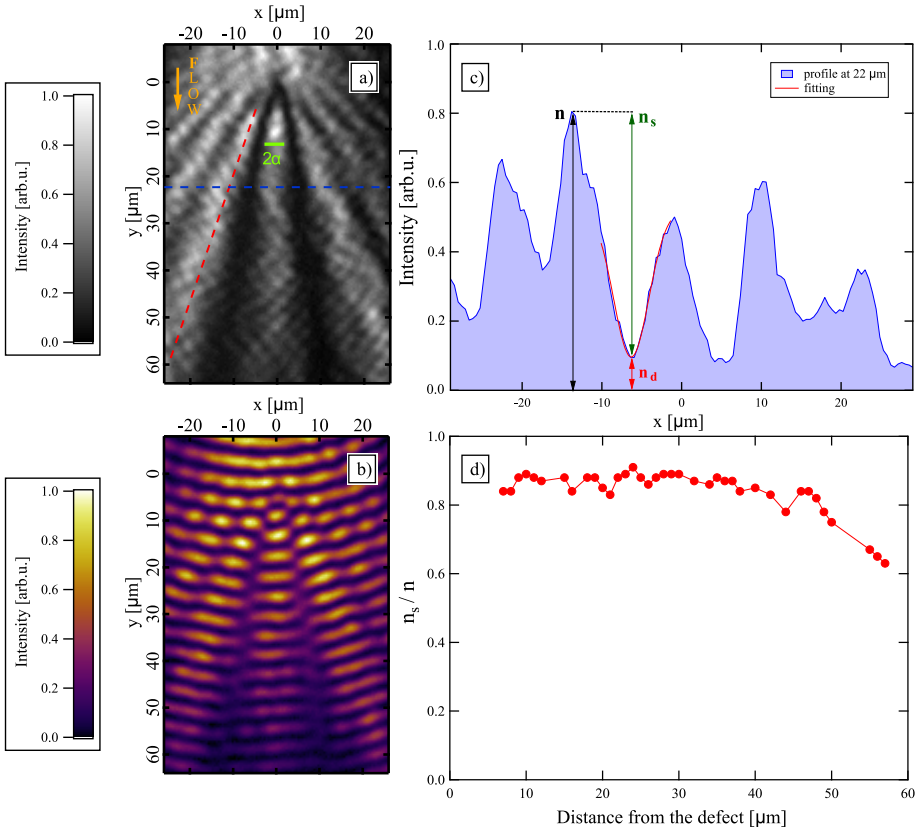

FIGURE 5.10: Experimental real space intensity (a) and interference (b) patterns showing the two "dark soliton fingerprints". These images are the same as Fig. 5.2 (a) and (c) of the main manuscript but plotted over a larger y axis range. (c) Horizontal intensity profile calculated along the blue dashed line in (a), 22 μm away from the defect. The inverse Gaussian fit is also shown (red line) together with the quantities n (black arrow), n_s (green arrow) and n_d (red arrow). (d) Dark-notch depth ($\frac{n_s}{n}$) calculated from (a) at different distances from the defect. As in the polariton quantum fluid case, the depth of the dark notch is stable up to 42 μm.

Moreover, at longer distances, at about 50 μm away from the defect we observe a decrease of the relative depth of the dark notch together with a decrease of the phase shift. In agreement with equation 5.7, when the dark notch is deeper (n_s/n tends to one in the equation 5.7) the ratio v_s/c_s decreases.

These observations show that a similar trend as in the polariton quantum fluid can be observed also in the linear regime.

5.8.2 Equivalent of the Mach number

In the case of a polariton quantum fluid it has been shown that different hydrodynamic regimes are connected to the Mach number (M), which is the ratio between the local

flow velocity v_{flow} and the local speed of sound c_s [18–21].:

$$M = \frac{v_{flow}}{c_s}. \tag{5.9}$$

Dark solitons in polariton microcavities have been claimed to appear for $M > 1$, with values depending on the nature of the obstacle [18–21]. In our linear system there is no sound, i.e. no linear dispersion range. However, we can evaluate the equivalent of the Mach number in our system, namely taking $(\frac{v_{flow}}{c_s})$ from the measured values of n_s/n (Fig. 5.10 d) and using the geometrical relation [18–21]:

$$v_s = v_{flow}\ \sin(\alpha) \tag{5.10}$$

where v_{flow} is the velocity of the polariton flow along the y-direction and α is the aperture angle of the oblique-dark notch with respect to the flow direction. In our case α is measured to be 16.3°.

By combining equations 5.7, 5.9 and 5.10 we can estimate the equivalent M of the quantum fluid case:

$$M = \sqrt{1 - \frac{n_s}{n}}\ \frac{1}{sin(\alpha)} \tag{5.11}$$

In our case the ratio $\frac{n_s}{n}$ varies between 0.91 and 0.63 (measured respectively at 24 μm and 57 μm from the defect [see Fig. 5.10(d)], which corresponds to a variation of M from a minimum value of 1.07 to a maximum value of 2.17. Dark solitons have been predicted to appear in polariton microcavities when $M \geq 1.02$ [17]. This analysis shows that the condition on the Mach number to observe dark solitons can be satisfied along the whole path of the dark notch in the linear regime.

Therefore, $M > 1$ together with the constant relative depth of the dark notch $(\frac{n_s}{n})$ and related phase shifts in the interferograms are conditions necessary but not sufficient to identify dark solitons, since these conditions can be observed also in the linear regime.

5.9 Healing length condition

By comparing our results [Fig. 5.2(a)] with the first experimental observation of dark soliton in polariton microcavity [18] [reported in Fig.3.5(a)] it is possible to observe similar spreading of the dark notches over the same distance ($\sim 40\,\mu$m). In other relevant works [19, 20] the claimed "solitons" [see Fig.3.5(d) and Fig.3.5(e)] travel for a quarter of the distance ($\sim 10\,\mu$m) compared to our case, showing a pronounced spreading that is contradictory with the definition of a non-spreading wave. We believe that a more reliable feature to identify dark solitons is to consider the non-spreading of the wave while it propagates, as it should be by definition (section 3.4).

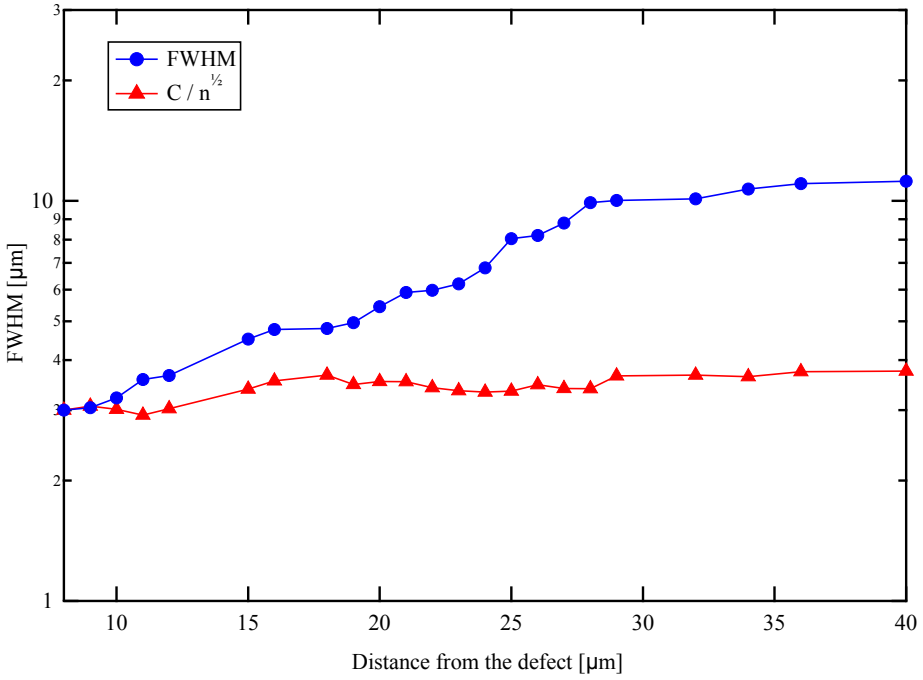

FIGURE 5.11: The blue circles show the measured FWHM of the left notch in Fig. 5.10 a) at different distances from the defect. The red triangles show $C/n^{1/2}$ proportional to the healing length using a suitable chosen constant C. The density n has been calculated by averaging the intensity of the left and right sides of the left dark-notch in Fig. 5.10 a).

Equation 5.7, initially proposed for atomic BECs [16], has been used also in polariton microcavities to identify dark solitons [18–21]. However, in all the previous works, the healing length condition which is related to the width of the soliton has been neglected even though it represents a direct application of the definition of a soliton.

A soliton, in fact, is a solitary wave that preserves its shape while propagating through a dispersive medium [15, 150]. This feature can be considered as universal fingerprints

since has been observed in all the physical systems where solitons have been studied [185]. As discussed in section 5.1.1, the formation of "oblique" dark solitons, although predicted for both the atomic [65] and polariton condensates [17], has been experimentally reported only for polariton condensates [18–21]. On the other hand, in atomic BECs, only single "straight" dark solitons have been experimentally observed [16].

The above healing length condition specifies that solitons propagating in a condensate of homogeneous density are characterized by a constant width (i.e. nonspreading wave) which is given by the healing length ξ of the condensate [16]. When the excitation density is increased, the FWHM of the dark notch should scale as $n^{-1/2}$, proportional to the healing length of the condensate.

We compare in Fig. 5.11 the measured width of the dark notch in our linear system with the expected scaling $C/n^{1/2}$ using the measured intensity as function of distance. We find that the healing length condition is not respected by this data in the linear regime, indicating that it is suited to discriminate dark solitons from linear propagation. We therefore propose to use the healing length condition to verify dark soliton formation, which should be fulfilled over a range of polariton excitation densities to exclude coincidental matches with specific scattering patterns in linear propagation.

5.10 Half-soliton-like features

In a different experiment, we address the observation of half-soliton fingerprints, which requires polarization-resolved measurements. The intensity images [Fig. 5.12(a) and (b)] are measured using an excitation linearly polarized parallel to the y-direction.

The interferograms [Fig. 5.12(c) and (d)], are obtained by selecting the same polarization for the excitation and reference beam (see section 4.2.1 for information on the experimental setup). The signature of an oblique dark half-soliton (ODHS) is a notch in only one circular polarization component [22, 163] (section 3.4.5). We excite the sample with a linearly polarized beam and detect the two circular polarization components (σ_-, σ_+) separately. The measurements are performed with the same excitation energy (1.485 eV) and negative detuning (-29 meV) as in the case of dark soliton-like features (section 5.3). The measured intensity and the interferogram for the σ_+ component are given in Fig. 5.12(a) and Fig. 5.12(c) respectively. The images show the presence of a

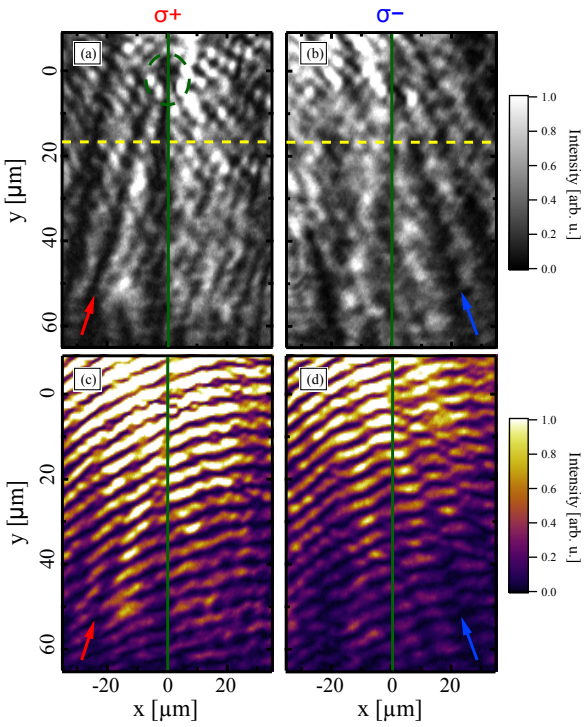

FIGURE 5.12: Experimental intensity pattern (a-b) and real space interference (c-d) showing two half-soliton features as indicated by the arrows. The red and blue arrows indicate respectively the position of the σ_+ and σ_- soliton-features: a dark-notch with an associated phase jump present in only one circular component. The green vertical line is a guide for eyes to distinguish the two different regions while the dashed circle in (a) indicates the defect.

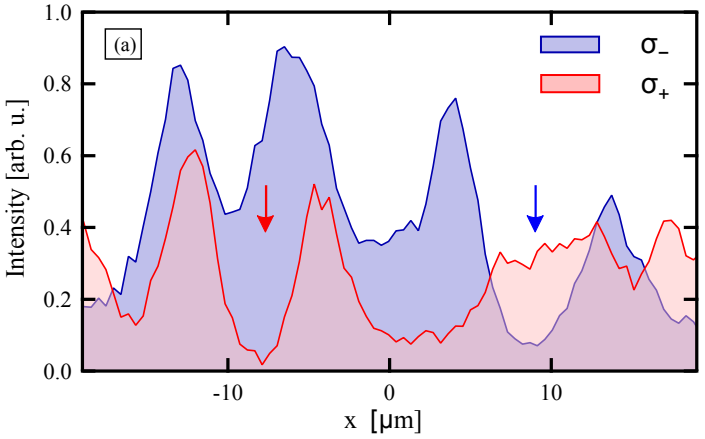

FIGURE 5.13: (a) Intensity profile extracts from the yellow dotted line in Fig. 5.12 (a) and (b), displaying the two dark notches present respectively in only one of the opposite polarization basis, as indicated by the arrows.

σ_+ soliton fingerprint, indicated by the red arrows, that is absent in the σ_- component [Fig. 5.12 (b), (d)]. The same applies to the σ_- counterpart, where a half-soliton fingerprint is observed only on the right side of the image as confirmed by the intensity profiles in Fig.5.13 (a), extracted along the yellow dashed line in Figs. 5.12 (b) and (d).

By calculating the degree of circular polarization, given by S_z in equation 2.32, we measure the pseudospin state inside the cavity [Fig. 5.14]. Here, if we look at the same position where the soliton features have been observed [Fig. 5.12], indicated by the black dotted lines in Fig. 5.14 (a), we note the presence of a pair of oblique traces with opposite circular polarization, resembling the predictions and observations attributed to a polariton superfluid [22, 163] (section 3.4.5). The high degree of circular polarization that we observe is due to the polarization splitting of transverse electric and transverse magnetic optical modes (TE-TM splitting) [186] (see section 5.10.1). The latter gives rise to the optical spin Hall effect [27] that has been observed in both polariton [187] and purely photonic microcavities [188]. In our simulations [Fig. 5.14 (b)] a linearly

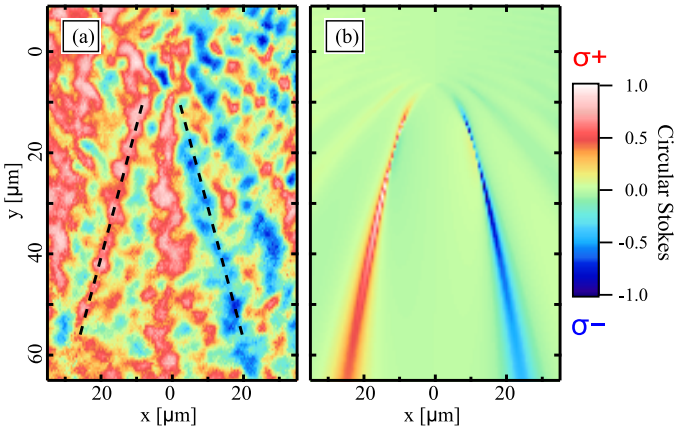

FIGURE 5.14: Experimental (a) and simulated (b) circular Stokes parameter showing half-soliton features. The two black dotted lines correspond to the position of the dark notches present in Fig. 5.12(a) and (b).

polarized incoming beam propagates along the y-direction and is scattered by a defect positioned at $25\,\mu m$ away from the excitation spot, inducing the formation of two traces propagating in oblique directions. The detected field is a superposition of the incoming linearly polarized wave and the scattered wave. The TE-TM splitting of the optical mode in a photonic cavity is responsible for an anisotropy in the polarization flux, as previously shown on the same sample in Ref. [188]. Here the same values of the TE-TM splitting have been used to perform the simulations. The polaritons scatter from the defect with wave vectors of equal modulus but in different directions both in

the real and momentum space. Because of the birefringence induced by the TE-TM splitting, polaritons propagating in different directions experience different polarization rotation and shift. Polaritons traveling to the right gain a σ_+ component while polaritons traveling to the left gain a σ_- component. The anisotropy of the effect manifests itself in the intensity pattern, where it is possible to observe the features of an oblique soliton in one circular component and not in the other.

5.10.1 Half-soliton-like features caused by TE-TM splitting

In our simulations a linear y-polarized incoming beam, propagates along the y direction and is scattered by a defect positioned at 25 μm away from the excitation spot, inducing the formation of two traces propagating in oblique directions. In the case of half-soliton

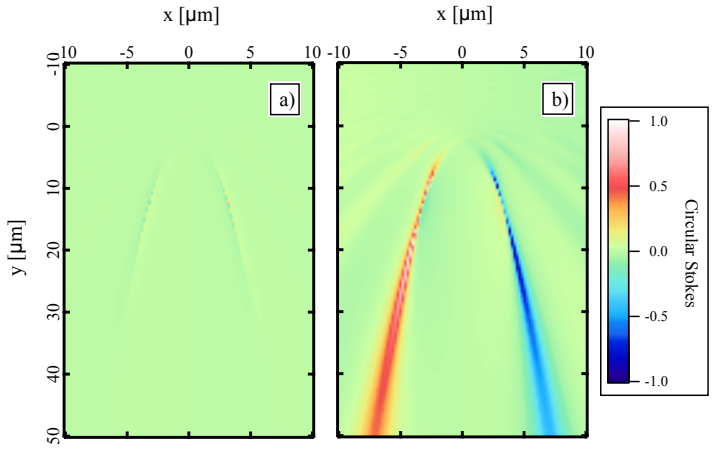

FIGURE 5.15: Simulated circular Stokes parameters showing half-soliton features. The images have been calculated by considering a beam hitting a circular defect in absence (a) and in presence (b) of the TE-TM splitting.

features in the circular polarization basis, we found that the birefringence in the scattering by the defect can be explained by the intrinsic TE-TM splitting of the polariton dispersion. This is confirmed by the simulations shown in Fig. 5.15 where the scattered field, produced by the wave hitting the defect, is calculated in absence, Fig. 5.15(a), or in presence, Fig. 5.15(b) of the TE-TM splitting. In the latter case we use $\vec{k}_{\parallel L}/\vec{k}_{\parallel T} = 1.004$ which is the same value that has been used in reference [188] for the same sample. In order to simplify the theoretical discussion, we consider the TE-TM splitting constant across the whole cavity including the defect and no additional splitting in the defect is considered.

5.11 Conclusions

In conclusion, we have shown that the previously reported experimental signatures of oblique dark solitons and half-solitons in polariton condensates can be observed in the case of polaritons propagating in the linear regime. In our experiments these features are the result of the interference of the incoming wave with the waves scattered by the defect. Their phase jumps and the relative depth of the dark notches satisfy the same analytical expression as in the polariton quantum fluid. In the case of the polarized counterpart (i.e., half-soliton-like features) the intrinsic TE-TM splitting of the cavity dispersion gives rise to oblique straight traces with opposite polarization.

Our results clarify that phase vortex lines in polariton propagation together with dark notches of constant relative depth in the intensity patterns, used as fingerprints of oblique-dark solitons and half-solitons in the literature, are present in the linear propagation regime. Consequently, these features are necessary, but not sufficient, evidence to identify solitons. We believe a more reliable criterion for identifying dark solitons, based on the definition of solitons (i.e., solitary nonspreading wave), would be the size of the observed features which should be determined by the healing length of the condensate, as proposed in section 5.9.

5.12 Contributions & Publications

The experiments reported in this chapter have been carried out mainly by the author, with the supervision of Hamid Ohadi and Alexis Askitopoulos. The theoretical model has been developed by Tomas Ostatnicky from the Faculty of Mathematics and Physics at Charles University in Prague. All the data presented in this chapter have been published previously in Ref.[31]. Parts of the text have been quoted verbatim from this work [31].

Chapter 6

Spin textures in polariton microcavities

6.1 Introduction

The formation of geometrically regular patterns represents one of the most attractive topic in science. Patterns formation phenomena, in fact, can be found everywhere in nature, from the animal coat patterns such as zebra stripes to the more complex fractal structure of a snowflake. In the case of atomic and polaritonic systems, the formation of these patterns corresponds essentially with the formation of spin [189] and polarization textures [32, 190, 191] within the condensate.

Since the very beginning, semiconductor microcavities have represented a model system for a wide range of fundamental [66] and applied studies [68] focused on the spin properties of exciton-polaritons. Polaritons in strongly coupled semiconductor microcavities, in fact, possess highly interesting spin dynamics. The spin of a polariton is directly connected with the polarization of the light absorbed or emitted by the microcavity (see section 2.7) enabling the use of polaritons in polarization sensitive devices [71, 192]. In particular, due to their long range coherence [73] and fast spin dynamics, polaritons have been proposed as a potential candidate for the realization of a new generation of optoelectronic devices [69, 70]. The manipulation and control of polariton propagation and their polarization is therefore a fundamental step toward the realization of such optical spin devices.

In this chapter we study the pseudospin dynamic of a propagating polariton condensate within the plane of the microcavity. We use non resonant linearly and circularly polarized optical excitation, to create a polarized condensate and observe ballistic propagation radially out of the excitation spot [73, 193] (section 6.3). Polaritons propagate over macroscopic distances, while their spin collectively precess within the plane of the microcavity due to the optical spin Hall effect [27] (section 6.4.1). As a consequence, the linear, diagonal and circular components of the Stokes vector reveal a 2D textures expanding over a distance of hundreds of microns. By using polarization- and time-resolved emission spectroscopy, we analyze the spatial and temporal behavior of these spin textures. We observe different spin textures depending on the polarization of the excitation pump. The spin textures observed in the case of circularly and linearly polarized excitation beam are shown respectively in section 6.5 and section 6.6.

6.2 Experimental method

The experiments reported in this chapter have been carried out on two AlGaAs/AlAs microcavity samples, i.e., sample A and sample B, both described in section 4.4.2. On sample A, the spin texture are studied under circularly polarized excitation (section 6.5), while on sample B under linearly polarized excitation (section 6.6). The use of two different samples was due to causes related with the overlap of different experiments in the group. The two sample give equivalent results and the spin textures observed on Sample A, under circularly polarized excitation, have been reproduced also on sample B. However, due to the similarity of these results with the one presented in section section 6.5, they have not been included in this thesis.

All the data presented are recorded at negative detuning and under non-resonant excitation. The excitation laser is tuned to the first spectral dip above the high-reflectivity mirror stopband at 1.653 eV for sample A and 1.687 eV for sample B. We perform both CW and pulsed experiments in reflection geometry, by using the experimental setup described in section 4.2.3. By using a CW laser and a CCD camera, time integrated images are obtained (see "Time integrated measurements" in section 4.2.3), while by means of a pulsed laser and a streak camera the dynamics of the polariton is studied (see "Time and Energy resolved measurements" in section 4.2.3). The polarized emission, analyzed by a polarimeter ($\lambda/2$ or $\lambda/4$ and a linear polarizer (LP) in Fig. 4.5) is studied in both

real- and k-space. By using a Wollaston prism instead of the linear polarizer and an appropriate software the spin textures can be visualized and measured in real time (see "Real time measurements of the Stokes vector" in section 4.2.3). To study the polarization dynamics, the intensity emitted by the microcavity is time-resolved by using the tomography scanning technique described in section 4.3.2.

6.3 Ballistic propagation of polaritons

6.3.1 Polaritons propagation in k-space

By using the filtered k-space setup described in section 4.1.1, the propagation of polaritons can be demonstrated in both momentum and real space. We use a $\sim 5\,\mu m$ excitation spot to generate a ballistic propagating polariton condensate [121, 194]. At

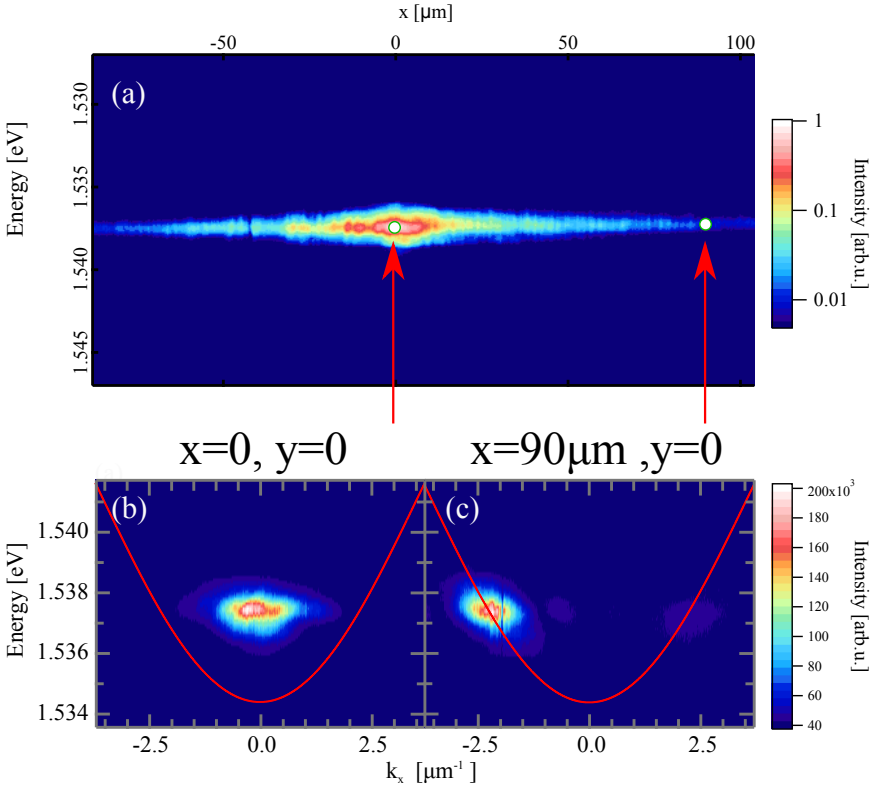

FIGURE 6.1: (a) Energy resolved intensity in real space, showing polariton emission above threshold (2 x P_{thr}). Spatially filtered energy dispersion calculate at (b) the excitation spot position and (c) $90\mu m$ away from the excitation spot, as indicated by the red arrows and the white circle. The red lines in (b) and (c) represents the lower polariton branches at low power.

the pump spot position, due to the repulsive interactions between polaritons and the

exciton reservoir, polaritons condense at blue-shifted energy compared with the lower polariton brunch, as indicate by the k-space filtered image calculated at the position of the excitation spot [Fig.6.1 (b)]. While excitons experience just a limited diffusion,

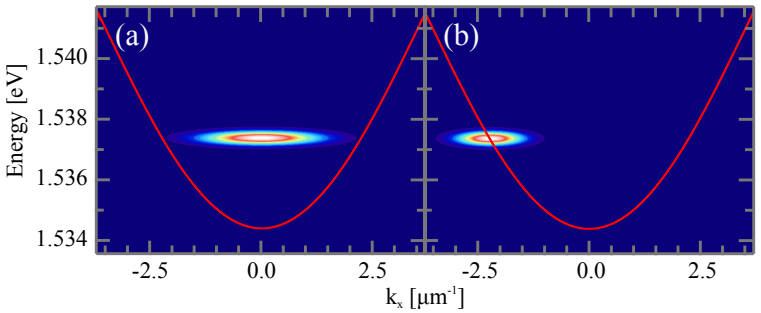

FIGURE 6.2: Theoretical simulation obtained from Fourier transforms in the time and space domain. The red lines indicate the low polariton dispersion at low excitation power. Calculated by Tim Liew.

polaritons propagate away from the excitation spot, in both directions, converting their potential energy into kinetic energy, characterized by a non-zero value of the polariton wave vector. This is confirmed by the k-space filtered image measured 90 μm away from the excitation spot [Fig.6.1 (c)] where it is shown that polaritons have a non-zero momentum and, consequently, the polariton emission originates from the high k-vector values of the lower polariton branch. Theoretical simulations of a radially expanding polariton condensate in k-space, calculated from the Fourier transform of the spectral distribution in real space, are shown in Fig. 6.2.

6.3.2 Polaritons propagation in real-space

We also study the polaritons propagation in real space by performing a series of power dependence measurements [Figs.6.3(a) and (b)] and extracting the intensity profile [Fig.6.3(c)] and the linewidth [Fig.6.3(d)] at different distances from the excitation spot. When the excitation intensity is increased above the threshold value ($\sim 25\, mW$), it is possible to observe a non-linear increase of the emission intensity, as far as 300 μm away from the excitation spot, due to polaritons propagating away from the excitation spot [Fig.6.3 (c)], which corresponds to a rapid reduction of the linewidth [Fig.6.3 (d)]. Both these features represent some of the main indications of lasing and condensation. Moreover, polaritons form a ring in k-space confirming that, in the non-linear regime, they have well defined k-vector values [inset in Fig.6.3(b)].

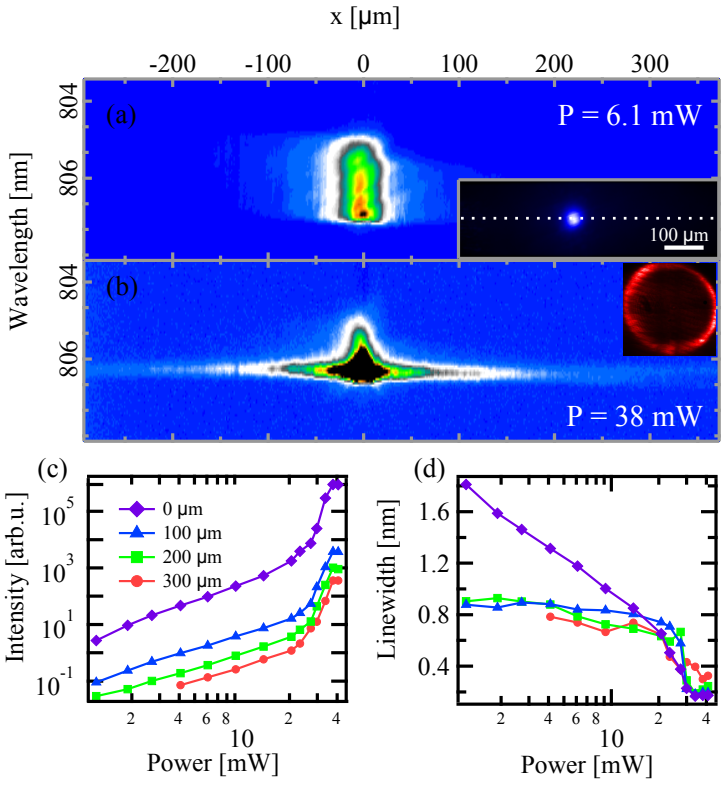

FIGURE 6.3: Energy resolved emission images measured below (a) and above (P= 1.5 P_{thr}) (b) threshold. The two insets in (a) and (b) show the intensity of the emission respectively in real and k space above threshold. The white dashed line indicates the position where the profiles were extracted. Emission intensity profile (c) and linewidth (d) as function of power, extracted at different distances from the excitation spot (see legend reported in c). At the threshold value ($\sim 25\,mW$), the intensity emission increases non-linearly while the linewidth rapidly decreases.

6.4 Theoretical picture

6.4.1 Optical spin Hall effect

One of the main mechanism affecting the spin dynamics of polaritons is the so called *optical spin Hall effect* (OSHE). The OSHE, predicted by Kavokin and co-workers in 2005 [27] and experimentally observed in both polaritonic [187] and photonic [188] microcavities, consists in the precession of the polariton pseudospin in the plane of the microcavity. The effect is enabled by the energy splitting between transverse-electric (TE) and transverse-magnetic (TM) polarized modes [186] and the longitudinal-transverse (LT) splitting of the exciton states inside the microcavity [195]. The TE-TM splitting arises from the fact that different polarized optical modes will have different phase and penetrations into the Bragg mirrors. The LT splitting of the excitonic states, on the other

hand, is mainly due to the long-range exciton exchange interaction and arises from the different alignment of the dipole moments (i.e., exciton states having dipole moments in different directions will have different energies [110]).
In the case of polariton microcavities, this splitting (Δ_{LT}) acts as a wave vector dependent effective magnetic field ($\mathbf{H_{eff}}$), making the pseudospin of polaritons precess if the latter is not parallel to it [27].

To take into account the precession of the pseudospin induced by the OSHE, polaritons propagation in microcavities is described by the following effective Hamiltonian [27]:

$$\widehat{H} = \frac{\hbar^2 k^2}{2m^*} + \mu_B\, g(\boldsymbol{\sigma} \cdot \mathbf{H_{eff}}), \tag{6.1}$$

where m^* is the polariton effective mass, μ_B the Bohr magneton, g the effective exciton Zeeman factor, $\boldsymbol{\sigma}$ the Pauli matrix vector and $\mathbf{H_{eff}}$ the effective magnetic field [27]:

$$\mathbf{H_{eff}} = \frac{\hbar}{\mu_B\, g}\mathbf{\Omega_k} \tag{6.2}$$

and $\mathbf{\Omega_k}$, which lies in the plane of the microcavity and has the following components [27]:

$$\Omega_x = \frac{\Delta_{LT}}{\hbar k^2}(k_x^2 - k_y^2), \qquad \Omega_y = \frac{\Delta_{LT}}{\hbar k^2}\, 2k_x k_y, \qquad \Omega_z = 0. \tag{6.3}$$

Here, $\vec{k} = (k_x, k_y)$ is the in-plane polariton wave vector. As indicated by equation 6.3, the orientation of the effective magnetic field in the plane of the microcavity, depends on the direction of the polariton wave vector, whose components are:

$$k_x = k\, cos\theta, \qquad k_y = k\, sin\theta \tag{6.4}$$

with θ being the angle between the direction of propagation and the x-axis [see Figs.6.4]. Thus, by combining equations 6.3 and equations 6.4, the components of the effective magnetic field ($\mathbf{\Omega_k}$) can be determined[1]:

$$\Omega_x = \frac{\Delta_{LT}}{\hbar}\, cos(2\theta), \qquad \Omega_y = \frac{\Delta_{LT}}{\hbar} sin(2\theta), \qquad \Omega_z = 0 \tag{6.5}$$

Equations 6.5 determines the orientation of the effective magnetic field in the plane of

[1] In the calculations the following trigonometric relations have been used: $cos^2(\theta) - sin^2(\theta) = cos(2\theta)$ and $2\, cos(\theta)\, sin(\theta) = sin(2\theta)$.

the microcavity, which depends on the direction of the polariton wave vector. The values of the effective magnetic field, calculated for different angles of propagation of polaritons, are reported in the table 6.1 (for the first and second quarter) and schematically represented in Fig. 6.4(a).

The L-T splitting of the polariton dispersion is zero at $\vec{k} = 0$ and increases as a function of k, following a square root law at large k [110]. Since the magnitude of the effective magnetic field ($\mathbf{\Omega_k}$) is proportional to the L-T splitting ($\frac{\Delta_{LT}}{\hbar}$), also $\mathbf{\Omega_k}$ is zero at $k = 0$.

TABLE 6.1: Distribution of the effective magnetic field in the k_x-k_y plane as function of the angle θ, which defines the direction of propagation of polaritons [see Fig. 6.4(a)].

Angle	Ω_x	Ω_y
$\theta = 0$	$\frac{\Delta_{LT}}{\hbar}$	0
$\theta = \frac{\pi}{4}$	0	$\frac{\Delta_{LT}}{\hbar}$
$\theta = \frac{\pi}{2}$	$-\frac{\Delta_{LT}}{\hbar}$	0
$\theta = \frac{3\pi}{4}$	0	$-\frac{\Delta_{LT}}{\hbar}$
$\theta = \pi$	$\frac{\Delta_{LT}}{\hbar}$	0

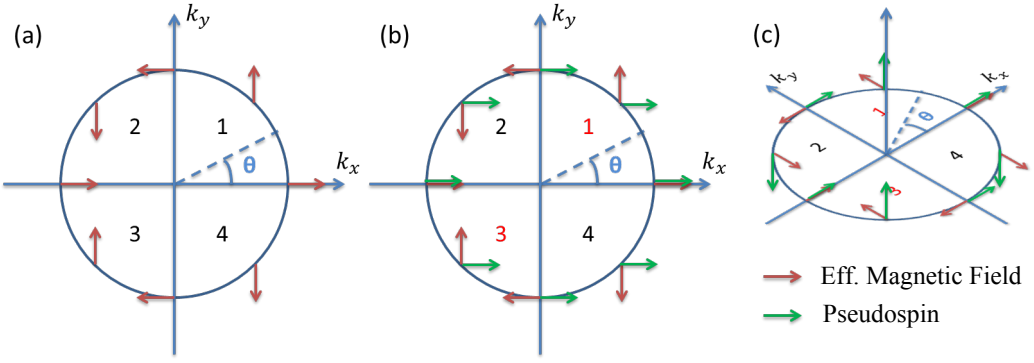

FIGURE 6.4: (a) The red arrows show the distribution of the effective magnetic field in k-space induced by the TE-TM splitting (see equations 6.5). (b) The green arrows indicate the linearly polarized pseudospin (i.e., the pseudospin is parallel to the x-axis) while the red arrow correspond to the effective magnetic field. Note that at at $\theta = \pi/4, 3\pi/4, 5\pi/4, 7\pi/4$ (i.e., along the diagonal directions with respect to the coordinates axes) the pseudospin is perpendicular to the effective magnetic field. (c) The initially linearly polarized pseudospin precess and, due to the orientation of the effective magnetic field, it becomes parallel to the z direction in the quarters 1 and 3 and antiparallel to the z axis in the quarters 2 and 4. Thus, the first quarters (1,3) correspond to σ_+ while the other quarters (2,4) to σ_- circularly polarized emission. Images adapted and redrawn from Ref.[27].

As shown in section 6.3, by means of a tightly focused excitation spot, a radially expanding polariton condensate can be generated with a well defined wave vector [see Fig.

6.1 and insets in Fig. 6.3 (b)]. Since the orientation of the effective magnetic field depends on the polariton wave vectors (equation 6.3), polaritons propagating in different directions experience different effective magnetic fields, which corresponds to rotation of the pseudospin in different direction. In particular, polaritons propagating in opposite directions (i.e. at opposite angles θ) experience precession in opposite directions [first and second quarter in Fig.6.4(b)]. This results to an angular dependent polarized emission of the polaritons and, consequently, to the appearance of alternating circularly or linearly polarized domains in the plane of the microcavity. Thus, different polarized spin domains develop in different quadrants of the x-y plane [Fig.6.4(c)].

6.4.2 Pseudospin precession

As discussed in section 2.7, polaritons possess a spin with two possible projections of the angular momentum (± 1) on the structural growth axis (z) of the microcavity. From the theoretical point of view, it is convenient to describe the spin dynamics of exciton-polaritons in terms of the pseudospin formalism, in which the polarization of the light emitted from the cavity is characterized by the four-component Stokes vector $\vec{s} = (s_0, s_x, s_y, s_z)$ [66], with $s_{0,x,y,z}$ being the total (s_0), linear (s_x), diagonal (s_y) and circular (s_z) degree of polarization (see section 2.7 for details and equations). The pseudospin components correspond directly to the Stokes parameters of light emitted from the microcavity [107]. Thus, by measuring the polarization of the emitted light (equations 2.32) we can measure the pseudospin state of the polaritons propagating in the plane of the microcavity.

The components of the pseudospin $S = (s_x, s_y, s_z)^T$ in the 3D Poincarré sphere (see Fig.2.16) are defined by [28]:

$$S = \begin{pmatrix} s_x \\ s_y \\ s_z \end{pmatrix} = \frac{1}{2} \begin{pmatrix} \psi_+ \psi_-^* + \psi_+^* \psi_- \\ i\psi_+ \psi_-^* - i\psi_+^* \psi_- \\ |\psi_+|^2 - |\psi_-|^2 \end{pmatrix} \tag{6.6}$$

where ψ_-, ψ_+ are the polariton wavefunction in the two spin components. If equation 6.6 is normalized to the total density, i.e. $n_{tot} = |\psi_+|^2 + |\psi_-|^2$, s_x, s_y and s_z corresponds to the degrees of linear, diagonal and circular polarization of the polariton emission [28]. The dynamics of the polariton pseudospin $\boldsymbol{S_k}$ in presence of the effective magnetic field

$\mathbf{\Omega_k}$ (see equation 6.3) can be described by the equation [107]:

$$\frac{d\boldsymbol{S_k}}{dt} = [\boldsymbol{S_k} \times \mathbf{\Omega_k}] \tag{6.7}$$

Equation 6.7 describe the precession of the polariton pseudospin around an effective magnetic field, typical of the optical spin Hall effect (see section 6.4.1). Experimentally, dynamical effects are observed under pulsed excitation. When polaritons are generated under CW excitation, on the other hand, the steady state is observed (section 6.5.1 and section 6.6). Thus, in CW experiments, the spin textures observed for a radially expanding condensate are described by the spatial equivalent derivative of equation 6.7, that is:

$$v_r \frac{d\boldsymbol{S_r}}{dr} = \boldsymbol{S_r} \times \mathbf{\Omega_k} \tag{6.8}$$

whit v_r being the radial velocity. The solution for the three spin components are [196]:

$$\begin{aligned} S_x &= Asin\left(\frac{\Delta_{LT} m_p}{\hbar k^2} r + \phi\right) sin(2\theta), \\ S_y &= Asin\left(\frac{\Delta_{LT} m_p}{\hbar k^2} r + \phi\right) cos(2\theta), \\ S_z &= Acos\left(\frac{\Delta_{LT} m_p}{\hbar k^2} r + \phi\right), \end{aligned} \tag{6.9}$$

with $A = 1$ being the amplitude in spin space (in the pseudo spin space this corresponds to $A = 1/2$) and ϕ a phase factor. In the case of circularly polarized excitation, the boundary condition $S_z(r = 0) = 1$, leading to $\phi = 0$ [196].

The pseudospin representation is useful to track the polarization of polaritons under the effect of the TE-TM splitting in microcavities, because it allows to directly represents the variation of polarization in the Poincarré sphere [see for example Figs.6.8(e-g)]. A more formal approach to describe the dynamics of polariton condensates with internal spin, the so-called *spinor condensates*, consists in solving the Gross-Pitaevskii equation (see section 3.2.3, eq. 3.8) for the polariton spinor wave functions (ψ_-, ψ_+), coupled with an exciton reservoir (see equation 3.9). The GPE takes into accounts the nonequilibrium nature of the polariton condensate due to polariton finite lifetime, while the exciton reservoir equation describes the formation of a hot exciton reservoir typical of the non-resonant excitation experiments described in this thesis. Both these equations, will be described in details in the next section.

6.4.3 Gross-Pitaevskii equation for a spinor polariton condensate

To take into account the spin of the polariton condensate, the mean field polariton wavefunction has to be expressed in the circular polarization basis ($\sigma = \pm$):

$$\Psi_\sigma(x, y, t) = \begin{pmatrix} \Psi_+ \\ \Psi_- \end{pmatrix} \tag{6.10}$$

To accurately model the spin dynamics in the exciton-polariton system, an open-dissipative Gross-Pitaevskii equation describes the polariton spinor order parameter ($\Psi_\pm$), which is then coupled with the exciton reservoir density ($\mathcal{N}_\pm$) [49]:

$$i\hbar\frac{d\Psi_\pm}{dt} = \left[\hat{E} - \frac{i\hbar}{2\tau_p} + \alpha|\Psi_\pm|^2 + G\sigma_\pm P(\mathbf{r}, t) + \left(g_R + \frac{i\hbar r_c}{2}\right)\mathcal{N}_\pm\right]\Psi_\pm + \hat{H}_{\mathrm{LT}}\Psi_\mp, \tag{6.11}$$

$$\frac{d\mathcal{N}_\pm}{dt} = -\left(\frac{1}{\tau_x} + r_c|\Psi_\pm|^2\right)\mathcal{N}_\pm + \sigma_\pm P(\mathbf{r}, t). \tag{6.12}$$

These equations model the process of polaritons being generated from a hot exciton reservoir and then scattered into the ground state of the condensate. The coupled equations take into account the energy blueshift of the condensate due to interactions with excitons (with interaction strength g_R). $\hat{E}$ is the condensate kinetic energy, τ_p and τ_x are the polariton and exciton lifetimes respectively. The same-spin polariton interaction strength is characterized by the parameter α. We neglect interactions between polaritons with opposite spins, which are typically small in magnitude [197] at energies far from the biexciton resonance [198]. The exciton reservoir is driven by a Gaussian pump, $P(\mathbf{r}, t)$, as in the experiment, and feeds the polariton condensate with a condensation rate (r_c). An additional pump-induced shift is described by the interaction constant G to take into account other excitonic contribution to the blueshift [49]. The polarization of the pump is controlled by the parameters σ_+ and σ_- so that:

- a horizontally (vertically) polarized pump corresponds to $\sigma_+ = \sigma_- = 1$ ($\sigma_+ = \sigma_- = -1$),
- a σ_+ (σ_-) circularly polarized pump corresponds to $\sigma_+ = 1, \sigma_- = 0$ ($\sigma_+ = 0, \sigma_- = 1$)
- an elliptically polarized pump corresponds to any linear combination of σ_+ and σ_- with $\sigma_+ \neq \sigma_- \neq \pm 1$.

$\hat{H}_{\mathrm{LT}}$ is the TE-TM splitting which mixes the spins of the polaritons (equation 6.3), written in the operator basis:

$$\hat{H}_{\mathrm{LT}} = \frac{\Delta_{LT}}{k_{LT}^2}\left(i\frac{\partial}{\partial x} \pm \frac{\partial}{\partial y}\right)^2, \tag{6.13}$$

with Δ_{LT} being the TE-TM splitting at wave vector k_{LT}. The TE-TM splitting is defined by the ratio Δ_{LT}/k_{LT}^2, while the in-plane wave vector of polaritons is given by the operator in the round brackets. Here the polariton dispersion is approximated as parabolic, with effective mass m, which is valid since the observed energies and in-plane wave vectors in the experiment lie in the parabolic part of the dispersion.

In equation 6.11, a potential term V(x,y) can be added in order to take into accounts the disorders typical of semiconductor microcavities (see section 4.5). In the case of the simulations reported in Fig.6.5 (e-g), V(x,y) is chosen as random Gaussian correlated potential [187]. However, the formation of the spin textures does not depend on the presence of the this term. Consequently, the scattering from a defect is not necessary to observe the formations of the polariton spin patterns. This is in contrast with the original demonstration of the optical spin Hall effect [27, 187, 188], where Rayleigh scattering was utilized to populate a ring in reciprocal space. In our case polaritons condense at the laser spot position with a blue-shifted energy due to their interactions with uncondensed hot excitons [32]. While these hot excitons experience a limited diffusion, polaritons ballistically fly away from the laser spot, converting this interaction energy into kinetic energy (see section 6.3 for details). The kinetic energy is characterized by the non-zero wave vector of polaritons, which due to the circular symmetry of the excitation corresponds to a ring in reciprocal space [32] [inset in Fig. 6.3(b)]. The results of the simulations, performed by Tim Liew, are reported in Figs. 6.5(e-g).

6.5 Circularly polarized excitation

6.5.1 Steady state

By using the experimental setup described section 4.2.3, we excite sample A (section 4.4.2) non-resonantly with a σ_+ circularly polarized beam at $2 \times \mathrm{P}_{Thr}$ power and measure the linear (S_x), diagonal (S_y) and circular (S_z) Stokes components of the intensity

emitted by the microcavity. The values of the three Stokes components (see section 2.7.1) measured in real space, are shown in Fig. 6.5(a-c).

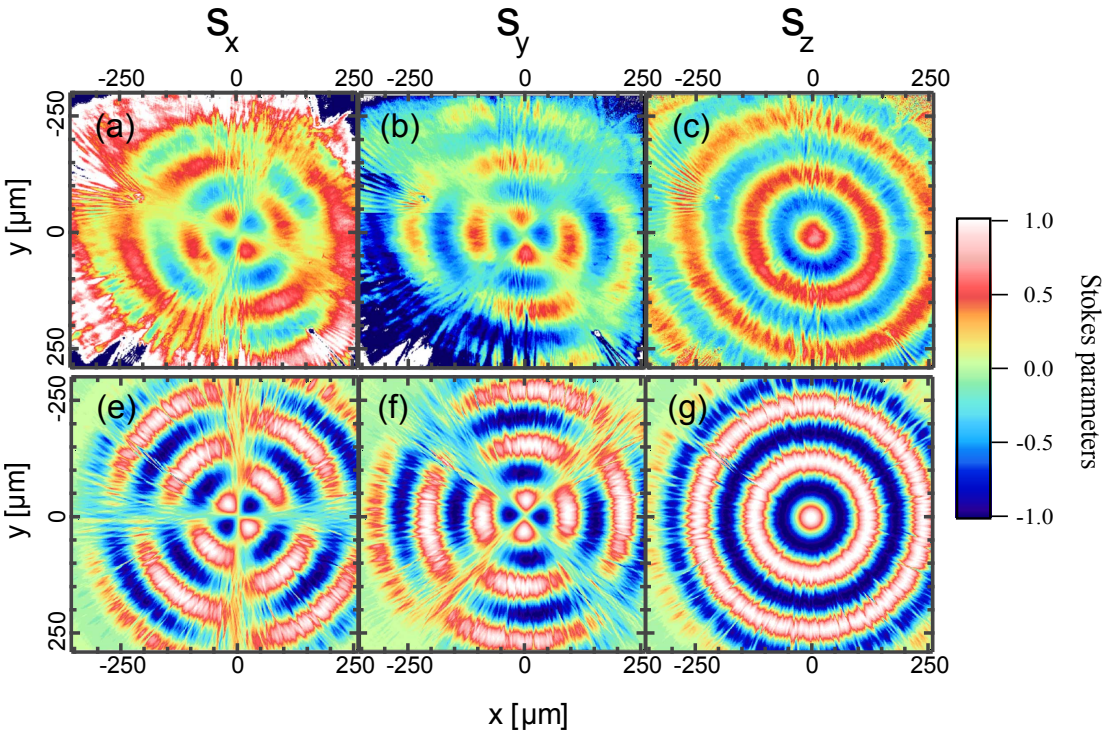

FIGURE 6.5: Experimental (a) linear (S_x), (b) diagonal (S_y) and (c) circular (S_z) Stokes components of the intensity emitted by the microcavity in real space and respective simulations (d-f). The sample was excite non resonantly, with a circular polarized beam and with an excitation power of 2 x P_{Thr} value. The simulations have been done by Tim Liew, by using the following parameters: $m = 7x10^{-5}$ of the free electron mass, $\Delta_{LT} = 0.05meV$, $k_{LT} = 2.05\mu^{-1}$, $\alpha = 2.4\mu eV\,\mu m^2$, $\gamma = 0.2ps{-}1$, $\Gamma = 10\gamma$, $\hbar r = 0.1meV\mu^{-2}$, $G = 0.03\mu m^2$. The disorder potential was generated with 0.05 meV root mean squared amplitude and 1:5 μm correlation length. The pump intensity was chosen to match the experimentally measured blueshift of the polariton condensate.

As polaritons propagate through the sample, the pseudospin precess around an effective magnetic field, due to the optical spin Hall effect (section 6.4.1). This is shown in Figs. 6.5 (a-c), by the three components of the Stokes vector, performing 3 complete revolutions over 250 microns distance. Figs. 6.5 (d-f), show the numerical simulations performed by solving the Gross-Pitaevskii equation for the polariton field (equation 6.11), coupled to a hot excitons reservoir generated by the non-resonant pump (equation 6.12). The spacing of two successive rings of the same circular polarization ($\Delta r_{\sigma_+,\sigma_-}$) is determined by the solution of equation 6.8 and, therefore, depends on the radial velocity of the polaritons and the TE-TM splitting that corresponds to the in-plane k-vector ($\Delta r_{\sigma_+,\sigma_-} = \frac{\pi\hbar^2}{m}\frac{k}{\Delta_{LT}}$) [32]. The non perfect circular shape of the textures, is determined by a slightly different value of the wave vectors in different radial directions.

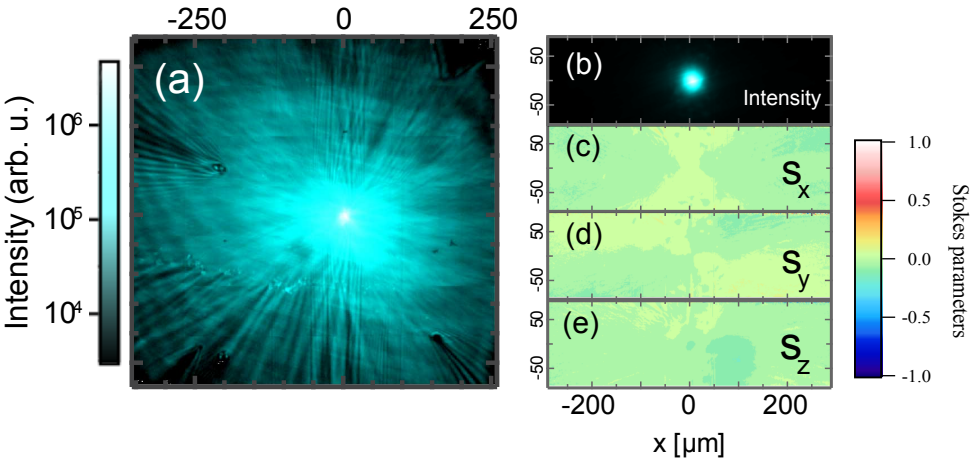

FIGURE 6.6: (a) Real space intensity emission plotted in log scale, at the excitation power of 2 x P_{Thr} value (i.e. above threshold). (b) Real space intensity emission below threshold. Experimental (c) linear (S_x), (d) diagonal (S_y) and (e) circular (S_z) Stokes components below the condensation threshold. The spin textures observed in Figs. 6.5 are not observed the lasing threshold.

To demonstrate that it was possible to observe the effect only in the non-linear regime, we performed the same measurements at low excitation power, i.e., at $P < P_{Thr}$. Below threshold, polaritons are uniformly distributed in k-space and, therefore, experience different effective magnetic fields [32]. Consequently, the formation of the spin textures observed in Fig.6.5 does not occur, as shown in Fig.6.6 (c-e).

6.5.2 Time resolved measurements

In order to have a deeper insight in the formation process of the spin textures, we have repeated the same experiment as in section section 6.5, but now using a pulsed excitation. As in the steady state case (section 6.5) we excite our sample non resonantly (at 1.653 eV), with a circularly polarized beam (σ_+). The use of a streak camera (section 4.2.3) and the tomography technique described in section 4.3.2, allow us to study the dynamics of the formation of the spin textures on a picoseconds scale. The time resolved measurements of the linear and circular Stokes parameters are reported respectively in Figs.6.7 (a-b) and Figs.6.7 (e-g), which show the formation and evolution of the polariton spin textures at 10 ps, 20 ps and 40 ps.

Polaritons propagate over macroscopic distances, while their spin collectively precess within the plane of the microcavity due to the optical spin Hall effect (section 6.4.1). Since the pseudospin corresponds to the Stokes vector (see section 2.7), it is particularly

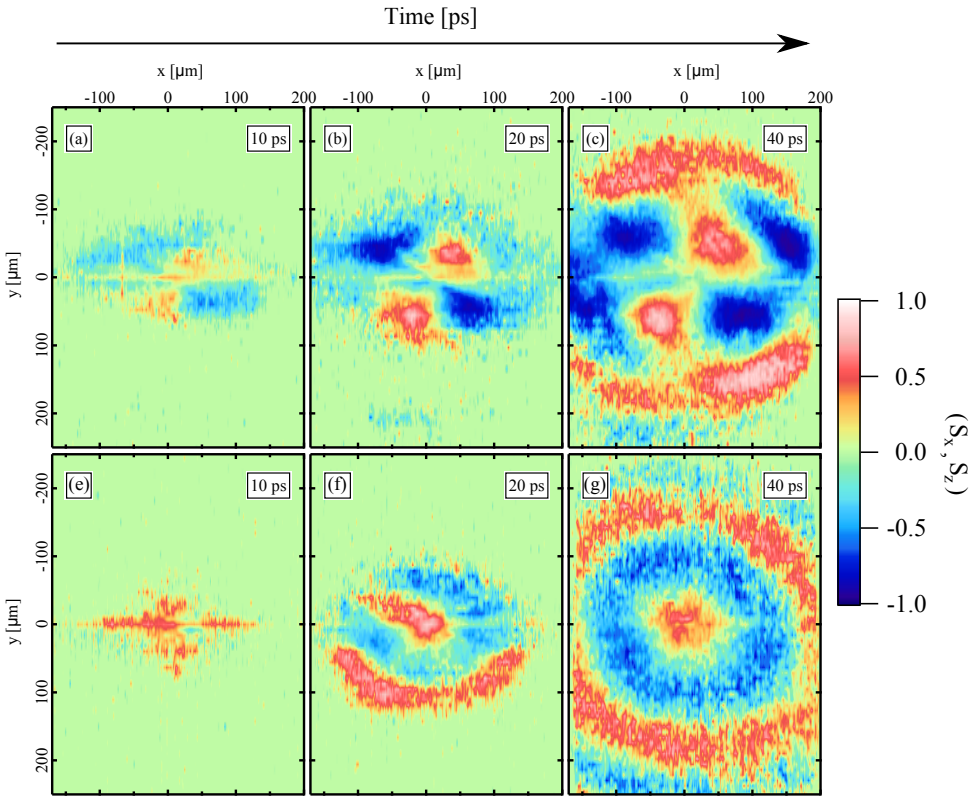

FIGURE 6.7: Real space experimental linear (a-c) and circular (d-f) Stokes parameters showing the formation dynamics of spin textures after pulsed optical excitation at 1.653 eV (sample A, section 4.4.2). The excitation beam is circularly polarized (σ_+).

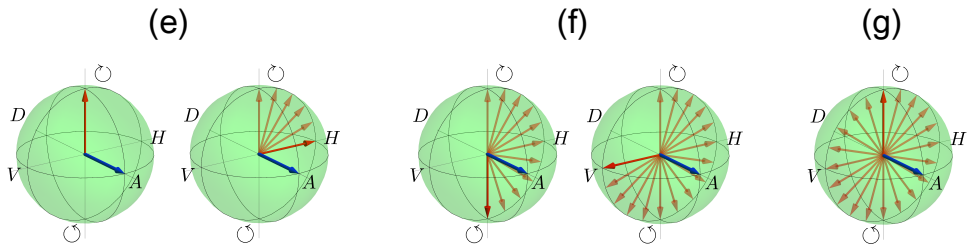

FIGURE 6.8: The precession of the pseudospin vector in the Poincaré sphere at points where $\frac{\Delta_{LTm}}{\hbar^2 k}|\vec{r}| = 0, \pi/2, \pi, 3\pi/2, 2\pi$ is shown, with m being the effective polariton mass. The letter (e), (f) and (g) indicate the relative position of the pseudospin respect with the effective magnetic field to generate the alternate polarized spin rings observed in Figs.6.7 (e-g).

useful to describe the precession of the pseudospin in the the Poincarré sphere. For example, in Fig.6.8 the evolution of the pseudospin vector in the Poincarré sphere for the case of the circular Stokes component S_z [Figs.6.7 (e-g)] is schematically represented. Let us compare Fig.6.8 with the spin rings textures shown in Figs.6.7 (e-g). A picture of the formation of the spin texture can be drawn. In particular, by exciting with a σ_+ excitation beam, we notice that:

1. initially the pseudospin is parallel to the z-axis [Fig.6.8 (e)], representing the σ_+

polarization in the Poincarré sphere. This state corresponds to Fig.6.7 (e), where only a σ_+ emission (red) is visible. Thus, the initial polariton state inherits the polarization from the excitation laser.

2. As polaritons propagate out of the excitation spot, the pseudospin starts to rotate around the effective magnetic field, until it becomes anti-parallel to the z-axis (Fig.6.8f). In the Poincarré sphere, this position of the pseudospin corresponds to a σ_- circular polarization. Thus, the initial polarization is reversed and the formation of the opposite circularly polarized ring (σ_-) can be observed. This stage, corresponds to Fig.6.7 (f) where a blue ring, surrounding the inner spot, is clearly visible.

3. When the pseudospin have performed a complete revolution in the Poincarré sphere (i.e., it come back to the initial position, parallel to the z-axis in Fig.6.8) another σ_+ spin ring is generated [Fig.6.7 (g)].

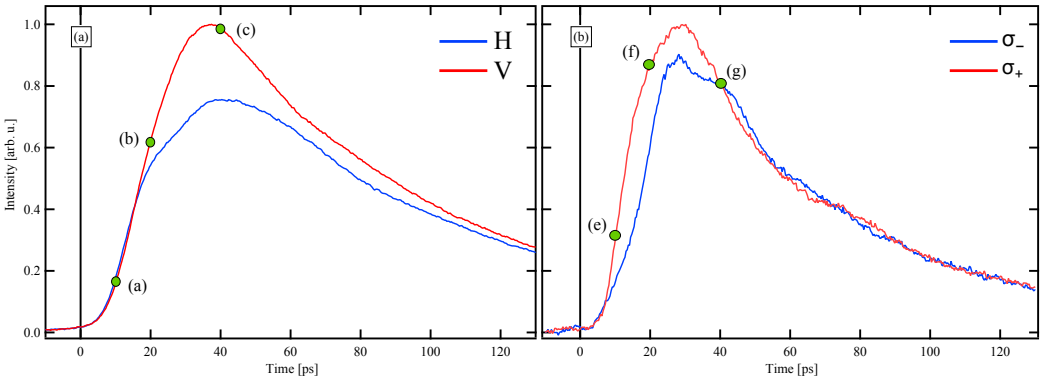

FIGURE 6.9: Time-resolved, spatially integrated measurements of the two (a) linear (H,V) and (b) circular (σ_+, σ_-) polarization components PL intensity, normalized and integrated over the area imaged in Figs. 6.7(a-f), i.e., (460 x 340) μm^2. The green solid circles annotated with (a-c) and (d-f) refer respectively to the three snapshots of Figs. 6.7(a-c) and Figs. 6.7(d-f). The black vertical lines define zero time at the PL onset (see section 4.3.3 for details).

The circularly polarized pump results in a condensate with unbalanced spin population [199]. This is shown in Figs.6.9(a-b) where the time-resolved, spatially integrated intensity profile of the polariton emission are reported for the linear and circular Stokes components. In the case of the circular Stokes components, the dominant population is the one with polarization parallel to the pump, confirming the unbalanced nature of the polariton condensate.

6.6 Linearly polarized excitation

By using the experimental setup described in section 4.2.3 ("Real time measurements of the Stokes vector"), we excite sample B (section 4.4.2) non-resonantly with a linearly polarized beam at $5 \times P_{Thr}$ (with $P_{Thr} \cong 15$ mW) power and measure the linear (S_x) and circular (S_z) Stokes components of the intensity emitted by the microcavity. The details on the excitation setup have been discussed in section 6.2. The values of the Stokes components (see section 2.7.1) measured in real space, are shown in Fig.6.10(a-b), while in Fig.6.10(c) the total circular intensity, i.e. the sum of the two circular polarization intensities (I_{σ_+} and I_{σ_-}), is reported.

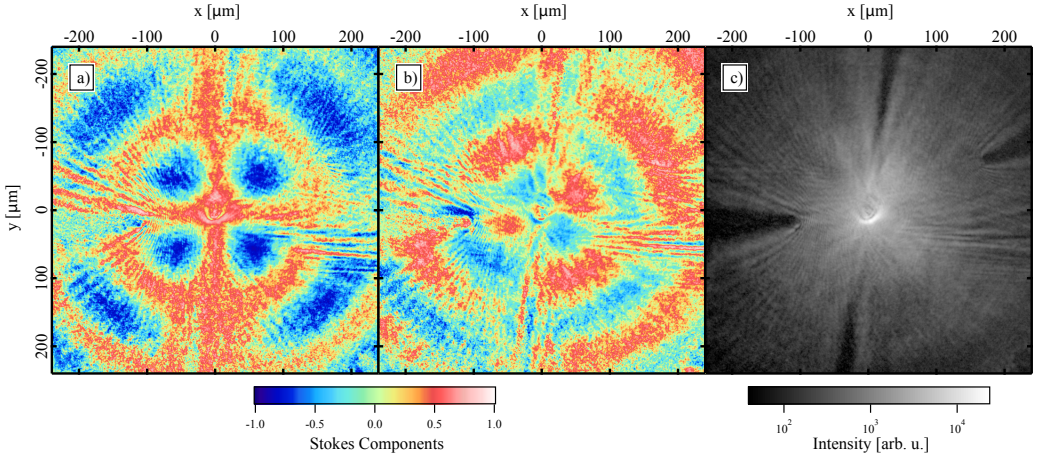

FIGURE 6.10: Experimental linear (a) and circular (b) Stokes parameters showing the formation of 2D pseudospin textures in real space. (c) Total circular intensity $I_{tot} = I_{\sigma_+} + I_{\sigma_-}$ corresponding to the sum of the two circular polarization components. The excitation beam is linearly polarized and at 1.687 eV (sample B, section 4.4.2). The spin textures observed here resemble the one theoretically predicted in Ref.[28] [Fig.2(a-b)].

In CW experiments, polaritons decayed or emitted from the cavity are continuously replenished by the CW excitation so that, once a macroscopic ground state population is reached (i.e. the relaxation rate of polaritons into the ground state becomes greater than its radiative decay rate), a steady state polariton condensate is formed.

Here, differently from the previous study (section 6.5), we investigated the formation mechanism of the spin textures under linearly polarized CW excitation and observe pseudospin textures resembling the Skyrmion patterns theoretically predicted for both atomic [189] and polariton condensate [28] and the polarization beats experimentally observed in microcavity for a pulsed excitation [200]. However, the typical fork-like

dislocations (i.e. vortex) present in one of the two circular polarization domains in the case of Skyrmions, is absent here. Consequently, Fig.6.10 do not represent a conclusive finding to claim the observation of Skyrmions, which would require the observation of fork like dislocations, present in only one polarization component domains, when the phase of the condensate is measured in interferometry measurement.

The Skyrmion-like pattern reported here, can be also explained in the framework of the optical spin Hall effect (OSHE) [28], previously described in section 6.4.
By means of a tight focused spot of about 5 μm FWHM, we generate a radially expanding polariton condensate with a well defined wave vector. Due to the interaction with the exciton reservoir, polaritons are radially expelled out of the excitation spot. As they propagate outside of the excitation spot, the potential energy is converted in kinetic energy, with wave vector determined by the blueshift of the condensate. The TE-TM splitting acts as a wave vector dependents effective magnetic field ($\vec{H}_{\text{eff}}$) in the plane of the microcavity and induces the pseudospin of the polaritons to precess, similarly to the Dresselhaus and Rashba field in the case of electron spin in doped quantum well [201]. In the case of GaAs microcavities this phenomenon is known as Optical Spin Hall Effect (OSHE) [27]. Essentially, the OSHE consists in the angular polarized emission of the polaritons resulting in the appearance of alternating circularly or linearly polarized domains in the plane of the microcavity (Fig.6.4).

Depending on the wave vector, polaritons propagating in different directions experience different polarization rotation due to k-dependent precession of the polariton pseudospin around the effective magnetic field ($\vec{H}_{\text{eff}}$). For both linear [Fig.6.10(a)] and circular [Fig.6.10(b)] Stokes components, the formation of the spin texture is angle dependent. The polarization emission, in fact, shows maxima in the diagonal direction while it is almost suppressed in the vertical and horizontal direction, reproducing the polarization quadrature of the OSHE [27]. Specifically, as shown in Fig. 6.4(b), the horizontal and vertical directions correspond to the position where the effective magnetic field is parallel or antiparallel to the pseudospin, thus no precession occurs. On the other hand, the diagonal directions (i.e., within the quarters of the x-y axis) correspond to the positions where the pseudospin precess around a perpendicular oriented effective magnetic field, giving rise to spin texture that appear as domains of opposite polarization. In the specific case of Figs.6.10(a) and (b), the presence of defects modulate the spatial emission and

additional features, due to the scattering of polaritons with structural defects, appear along the horizontal/vertical axis [Fig.6.10(c)].

At excitation power P = 9.2 mW, i.e. lower than the condensation threshold ($P < P_{thr}$), the spin textures are not observed confirming, as in the case of circularly polarized excitation, that they appear only in the non linear emission regime.

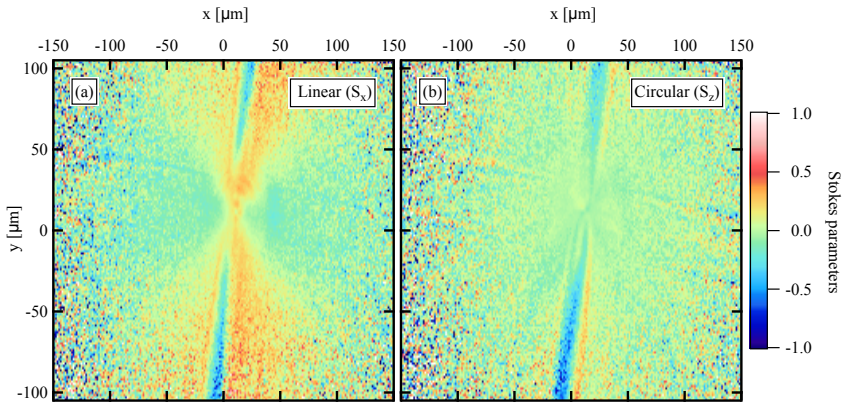

FIGURE 6.11: Experimental linear (a) and circular (b) Stokes parameters in real space at excitation power of 9.2 mW, i.e. below condensation threshold. The excitation beam is linearly polarized and at 1.687 eV (sample B, section 4.4.2).

6.7 Conclusions

In this chapter, the formation of spin textures in the non linear emission regime of a polariton microcavity has been reported. Depending on the polarization of the excitation, different spin textures can be generated. Polaritons ballistically propagate radially out of the excitation spot over hundreds of microns distance, while their spin coherently precess due to the optical spin Hall effect. The effective magnetic field, due to the TE-TM splitting naturally presents into the cavity, induces a precession of the polariton pseudospin analogous to the precession generated by a real magnetic field on the spin of an electron. However, if the initial demonstration of the optical spin Hall effect [187] relied on resonant Rayleigh scattering with disorder [202], in our case, the spin currents have been generated using a tightly focused laser spot. This allows the generation of polaritons with a non zero wave vector which populates a ring in k-space, also in absence of Rayleigh scattering from a defect. Moreover, differently from the first observation of

the optical spin Hall effect [187], we use a non-resonant excitation scheme. The non-resonant excitation is indispensable to ensure that the effect observed is not due to the excitation laser, since the original coherence of the laser is lost in the relaxation process.

6.8 Contributions & Publications

The experiment with the circularly polarized excitation (section 6.3 and section 6.5) was mainly conducted by Elena Kammann. All the data presented section 6.3 and section 6.5.1 have been published previously in Ref.[32]. My contribution to this work (which compose the first part of this chapter) was related to the analysis of the data and the execution of detuning and power dependent measurements, shown in Figs.6.3(c-d). On the other hand, the second part of the chapter, specifically the time resolved measurements (section 6.5.2) and the experiments with the linearly polarized excitation (section 6.6), is mainly the result of my work, with the supervision of Hamid Ohadi. The theoretical simulations were performed by Tim Liew from the School of Physics and Mathematical Science at Nanyang Technological University in Singapore.

Chapter 7

Rotating spin textures: polariton spin whirls

7.1 Introduction

In the previous chapter, the formation of spin textures were investigated under circularly and linearly polarized pump. However, in the case of linearly polarized excitation only time integrated measurements, obtained under CW pump, were shown. By conducting the same experiments described in the previous chapter, but now exciting with a linearly polarized pulsed excitation, the rotation of the whole spin texture in the plane of the microcavity is observed. These rotating spin textures represent the *polariton spin whirls* described in this chapter.

With polariton spin whirl we identify a spin texture that rotates in the microcavity plane due to the interplay between the TE-TM splitting and the interaction with an exciton reservoir. The TE-TM splitting alone is responsible for the formation of 2D spin textures, which is intrinsically a linear effect [200]. As a consequence, the orientation of the spin current in the microcavity plane remains fixed in time. However, in the case of a radially expanding condensate, nonlinear interactions with the exciton reservoir at the spatial center of the condensate produce a spiralling effect, which culminates in a coherent rotation of the whole spin texture.

We excite our sample with a linearly polarized beam (section 7.2) and surprisingly observe symmetry breaking which culminates in a coherent rotation of the whole spin

texture in the plane of the microcavity (section 7.3). The rotation is traced in the highly focused optical excitation which introduces an ellipticity at the pump spot (section 7.4) responsible for the creation of a spin imbalanced exciton reservoir. The imbalance in the exciton reservoir acts as an effective magnetic field due to the anisotropic exciton-polariton interactions (section 7.5). The rotation of the spin textures is observed also in energy resolved measurements (section 7.7). Simulations based on the Gross-Pitaevskii equation coupled with the exciton reservoir unveil the crucial role of spin imbalanced exciton reservoir in reproducing the experimental observations.

In the following we will refer to the two circularly polarization of the polariton emission with the symbol Ψ_+ and Ψ_-. On the other hand, the circularly polarization components of the excitation pump and the exciton reservoir will be indicated respectively with σ_+, σ_- and N_+, N_-.

7.2 Experimental method

This experiment has been carried out on sample A (see section 4.4.2 for details) characterized by a cavity photon lifetime of $\sim$ 9 ps and a Rabi splitting of 9 meV. All the data presented here are recorded at negative exciton-photon detuning Δ = -4 meV and under non-resonant excitation (1.653 eV). The dynamics of polaritons is studied by using a pulsed laser, with a pulse width of 250 fs and a pulse frequency of 80 MHz, focused to a $\sim 2\mu m$ FWHM spot by a 0.4 numerical aperture objective. The polarized emission is collected by the same objective, analyzed by a polarimeter composed of a $\lambda/2$ or $\lambda/4$ plate and a linear polarizer and then projected on the entrance slit of a streak camera, with 2 ps temporal resolution. To take into account the different delays introduced by the waveplates, the intensity profiles have been scaled in order to have a common zero (see section 4.3.3), where zero has been set at the onset of the photoluminescence emission (see intensity profiles in Figs.7.7). More details about the experimental setup and the tomography scanning technique used to acquire the data are reported respectively in section 4.2.3 and section 4.3.2.

7.3 Polariton spin whirls

As anticipated in the previous section, we excite our samples non resonantly with a linearly polarized beam. Time resolved polarization measurements reveal a clockwise rotation of the entire spin texture in the plane of the microcavity at an angular velocity of about 0.11 rad/ps. This is shown in Figs.7.1(a-c) for the z-component of the Stokes vector (S_z), corresponding to the circular polarization degree (see equation 2.32, S_z).

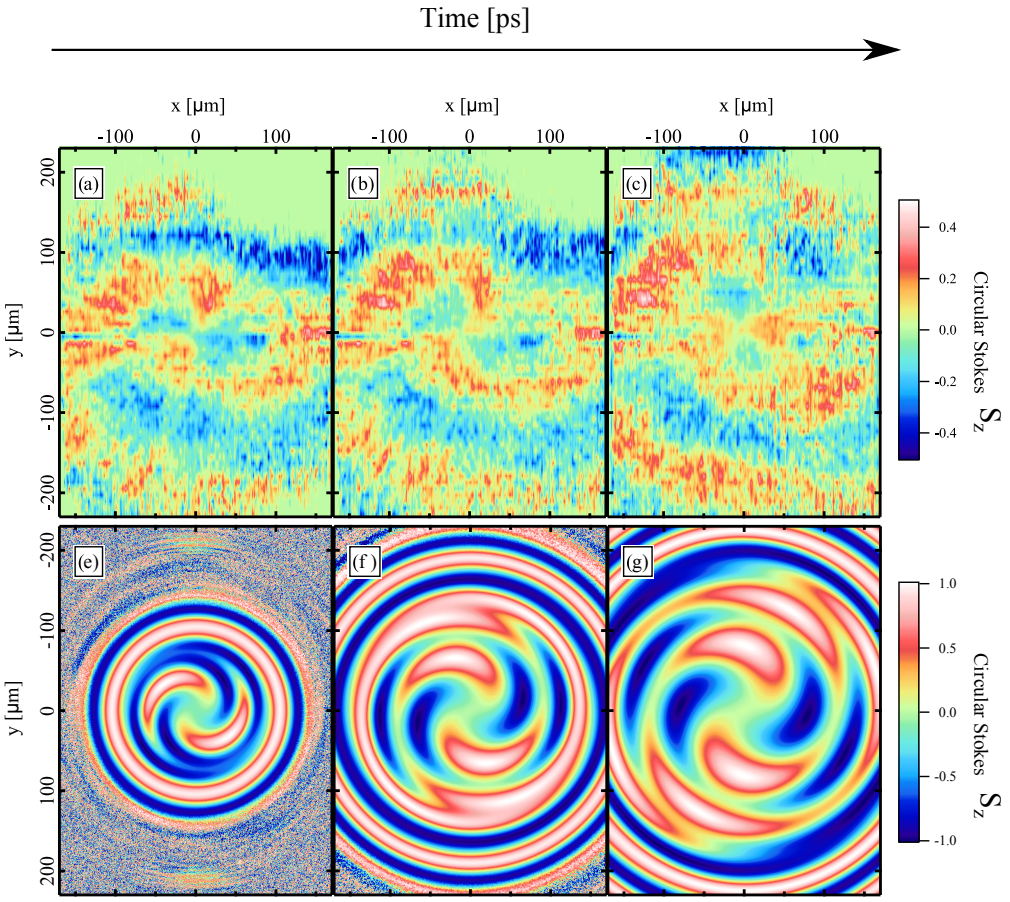

FIGURE 7.1: (a-c) Real space experimental circular components of the Stokes vector (S_z) at a) 38 ps, b) 41 ps and c) 46 ps showing the clockwise turn of the circular component within the microcavity plane. The excitation beam is linearly polarized and at 1.653 eV energy, exciting polaritons with $|k| \leq 2.8\mu m^{-1}$ at negative detuning $\Delta = -4meV$. (e-g) Theoretical simulations performed with the GP equation, showing the evolution of the spin texture S_z at: (d) 30 ps, (e) 45 ps and (f) 60 ps.

The nonresonant excitation creates electron-hole pairs in the cavity and in the QWs, which rapidly relax to populate the lower polariton dispersion and form a polariton condensate [11, 119]. The tight focused pump spot ($\sim 2\mu m$ FWHM) generates polaritons that propagate radially out of the excitation spot, as previously described in section 6.3. At the pump spot position, due to the repulsive interactions between polaritons and

the exciton reservoir, the condensate is blueshifted in energy compared to the lower polariton branch. Outside the pump spot, this potential energy is converted to kinetic energy with an in-plane wave vector determined by the cavity lifetime and the gradient of the potential. Thus, the tightly focused Gaussian excitation ($\sim 2\,\mu m$ FWHM), produces a cylindrically symmetric potential (V) that leads to the radial expansion of polaritons in the plane of the microcavity [Figs. 7.2 (a,b)]. Polaritons rolls down the potential and acquire an in-plane momentum $p = \hbar k = \sqrt{2mV}$ (where m is the polariton effective mass). In this case the wave vector measured by imaging the polariton dispersion is $|k| \leq 2.8\mu m^{-1}$. As polaritons propagate away from the excitation spot, their spin coherently precess due to an effective magnetic field oriented in the plane of the cavity (equation 6.3), giving rise to the formation of spin textures. This process, known as optical spin Hall effect, has already been described in section 6.4.1 of the previous chapter. However, the rotation of the spin texture, i.e. the spin whirls, are instead due to the contribution of another effective magnetic field oriented perpendicularly to the microcavity plane (i.e., along the z-direction), as described in section 7.5.2. The appearance of this field is due to an imbalance between the two spin populations (Ψ_+, Ψ_-), which in turn is induced by a small ellipticity introduced by the tightly focused excitation beam, as discussed in the next section.

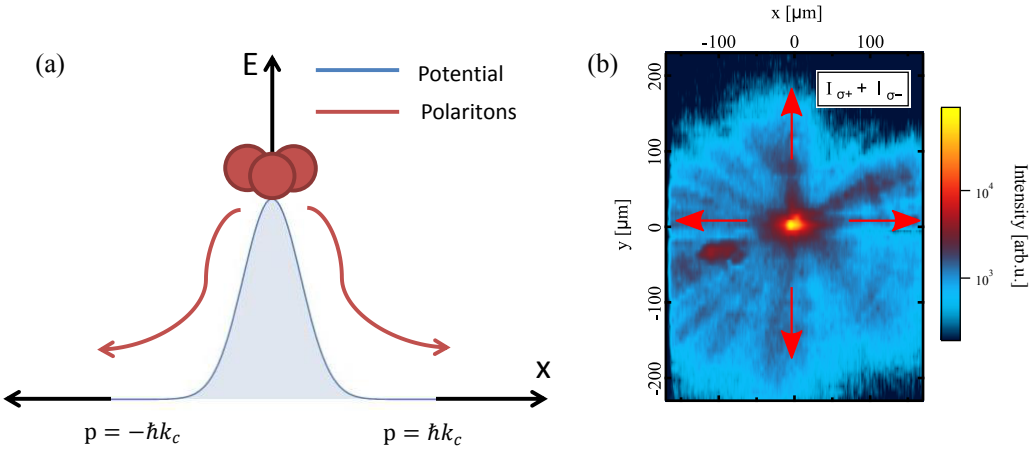

FIGURE 7.2: (a) Sketch of the potential created by a Gaussian excitation spot. Due to the repulsive interaction of the excitons at excitation spot, polaritons are blue shifted in energy, i.e. they lay on top of a potential (V). Polaritons roll down the potential acquiring in plane momentum. This corresponds to a radially expansion of the condensate. (b) Experimental total intensity equals to the sum of the two emission components Ψ_+ and Ψ_- at 41 ps plotted in log scale.

7.4 Ellipticity of the excitation spot

As has been shown by Richards and Wolf [203], the tight focusing of a polarized Gaussian beam through a high numerical aperture (NA) lens, results in the modification of the polarization at focal plane. In particular, the electric field of a linearly polarized beam, when focused by a high NA objective, acquires non-zero components in the two directions perpendicular to the polarization of the incident field (i.e., at the focus plane the electric field vector sweeps an ellipse) [203–206]. Thus, the tight focus of a linearly polarized excitation beam, breaks the rotational symmetry of the σ_+ and σ_- polarizations and introduces an ellipticity in the pump spot. We have measured an ellipticity of 10% for the excitation conditions used in the experiment, as shown in Fig.7.3.

The polarization at the pump spot has been measured by focusing a linearly polarized beam with a 0.4 NA objective (the same used in the experiment) on a glass. The transmitted intensity has been collected with a 100x, 0.7 NA objective. In order to measure the polarization of the beam, we used a polarimeter composed of a $\lambda/2$ or $\lambda/4$ plate and a linear polarizer. The emission is then imaged in real space by a 20 cm focus lens directly on a CCD camera. The linear (S_x), diagonal (S_y) and circular (S_z) Stokes parameters measured are reported respectively in Figs. 7.3 (a-c). The Stokes parameters have been calculated by using equations 2.32. We estimate the circular value of ellipticity by averaging the circular Stokes parameters over an area of $1.78 \times 1.78\,\mu m^2$ comparable with the area of the 2 μm FWHM excitation spot used in the experiment, as shown in Fig.7.3(d). The average value of the circular stokes parameters is -0.14 justifying the 10% ellipticity used in the theoretical simulations discussed in the next section. In Fig.7.3(e) and Fig.7.3(f) the intensity of the beam in real space for the circular component (σ_-) and the total degree of polarization calculated as $S_{tot} = \sqrt{S_x^2 + S_y^2 + S_z^2}$ are also reported for the sake of completeness.

7.5 Theoretical picture

The theoretical model used to describe the dynamics of a spinor condensate has been already described in section 6.4 of the previous chapter. The spinor Gross-Pitaevskii equation 6.11 coupled with the exciton reservoir density (eq. 6.12) is used also in the case of the spin whirls.

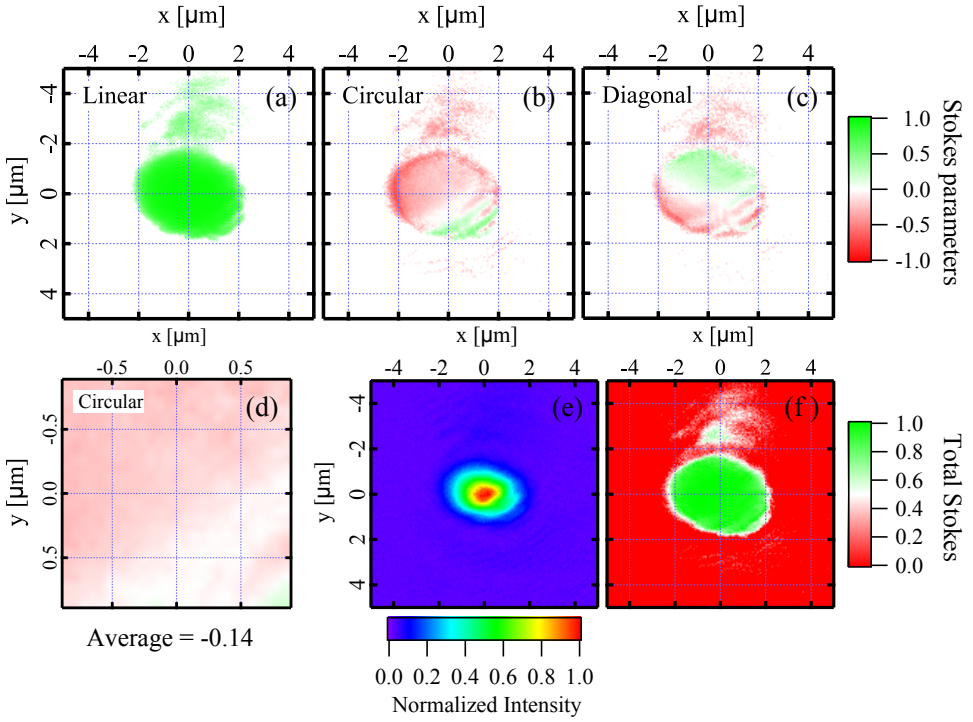

FIGURE 7.3: (a) Linear, (b) circular and (c) diagonal Stokes parameters of the beam spot focused by a 0.4 numerical aperture objective. (d) Zoom of the circular component reported in (b) on an area of $1.78 \times 1.78\,\mu m^2$ comparable with the area of the 2 μm FWHM excitation spot used in the experiment. The average of the circular Stoke components is -0.14. (e) Real space intensity of the circularly polarized pump spot (σ_-). (f) Total degree of polarization S_{tot} calculated from (a), (b) and (c).

The theoretical model has been developed by Helgi Sigurdsson, Tim Liew and Ivan Shelykh. All the simulations presented in this chapter have been performed by Helgi Sigurdsson. In the simulations, as for example Fig. 7.1(e-g), the spin whirls appear at different time. The differences in the time dynamics observed in experiment and theory are due to differences in the reservoir dynamics occurring at the pump spot position. Typically polariton condensation is described with the use of a single reservoir model [193]. While modeling using multiple reservoir levels may offer a closer fit to the dynamics [207], we do not expect significant changes in the spatial patterns, which are the main focus of this work.

In all the theoretical calculations the following parameters were set to: $\alpha = 2.4$ μeV μm^2, $g_R = 1.5\alpha$, $G = 4\alpha$, $r_c = 0.01$ μm^2 ps^{-1}, $\Delta_{LT}/k_{LT}^2 = 11.9$ μeV μm^2, $\tau_p = 9$ ps, $\tau_x = 10$ ps.

7.5.1 Polarization of the excitation

In Fig.7.4, the theoretical circular Stokes (S_z) polarization patterns obtained with nearly circularly [Fig.7.4 (a)], linearly [Fig.7.4 (b)] and elliptically [Fig.7.4 (c)] polarized pump are shown.

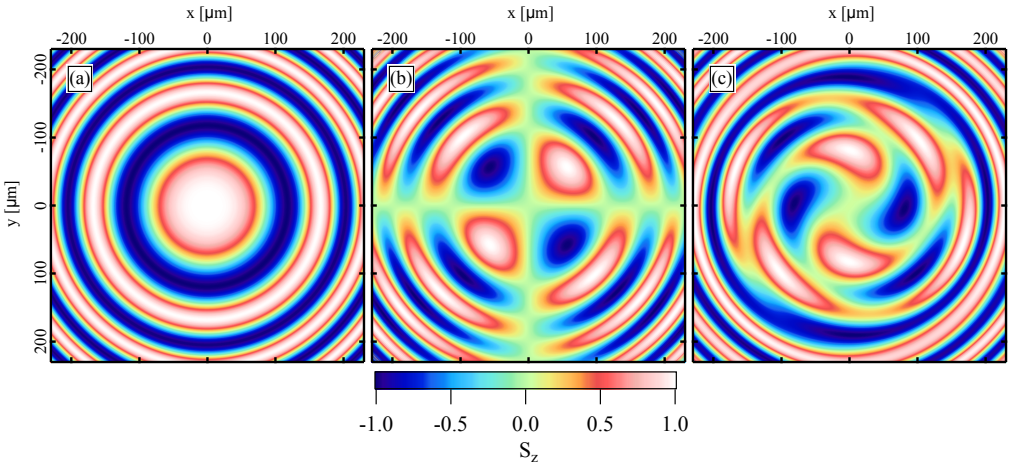

FIGURE 7.4: Spin textures showing the evolution of the degree of circular polarization S_z after 50 ps in a system excited with (a) nearly circular ($\sigma_+ = 1; \sigma_- = 0.1$), (b) linear ($\sigma_+ = \sigma_- = 1$) and (c) elliptical ($\sigma_+ = 1; \sigma_- = 0.9$) pump polarization.

As previously discussed in section 6.5, the circularly polarized pump results in the formation of a spin unbalanced condensate, with the dominant population being the one with spin parallel to the pump. In the regime of nonlinear emission, this spinor condensate evolves to concentric rings of alternating spin due to the optical spin Hall effect, as shown in Fig.7.4(a). The cylindrically symmetric patterns observed here are due to the fact that the polariton pseudospin, directed along the z-axis in the Poincarré sphere, is always perpendicular to the effective magnetic field, lying on the x-y plane (see Fig.6.8). On the other hand, the linearly polarized pump, being a linear combination of the two circular polarization components, results in a condensate with equally populations of spin-up ($S_z = +1$) and spin-down ($S_z = -1$). In this case, the typical OSHE pattern is retrieved due to the Stokes vector precessing at 45° to the x,y axis, as shown in Fig. 7.4 (b), which corresponds to the experimental patterns reported in Fig.6.10(b), section 6.6. When a 10% ellipticity is introduced in the linearly polarized pump, i.e., elliptical pulse with $(\sigma_+, \sigma_-) = (1, 0.9)$, the circular polarization pattern shows rotational behavior, as shown in Fig.7.4(c). The 10% ellipticity used in the simulations coincides with the value experimentally measured for the excitation conditions used in the experiment (see section 7.4).

7.5.2 Spin whirls formation

To understand the rotational behavior, we must first appreciate that polaritons can only be generated in the vicinity of the localized pump spot, which serves as the source for the entire spatial spin pattern. The time-dependent spatial rotation observed in our configuration is, in fact, a manifestation of varying polarization at the pump spot location. The varying polarization at the pump spot is generated by the ellipticity of the Gaussian pump, which populates one circular component of the reservoir faster than the other. This leads to a splitting $g_R(\mathcal{N}_+ - \mathcal{N}_-)$ of polaritons, which can be thought of as an effective Zeeman splitting at the pump spot. Here, the imbalance between the two populations induces an effective magnetic field along the z-direction (Ω_z) [208], which causes the precession of the Stokes vector in the Poincaré sphere, as shown schematically in Fig.7.5(a).

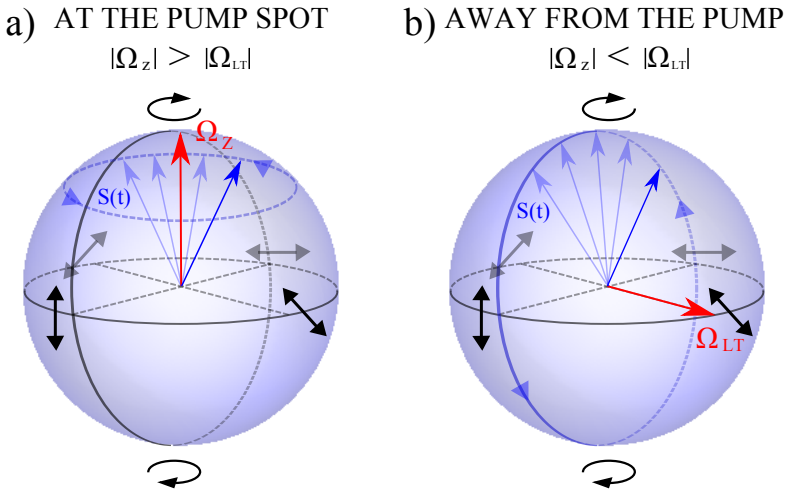

FIGURE 7.5: The pseudospin vector S(t) (blue arrows) in the Poincaré sphere at: (a) the pump spot and (b) outside the pump. At the pump spot position, (a), S(t) precesses around the z-direction since $|\Omega_z| > |\Omega_{LT}|$. Outside the pump spot, (b), S(t) precess around Ω_{LT} since $|\Omega_{LT}| > |\Omega_z|$.

Due to its excitonic nature, Ω_z exists only at the pump spot position where the exciton reservoir is localized. Away from the excitation spot, the polariton pseudospin dynamics is essentially driven by the TE-TM splitting of the polariton mode (see equations 6.5), represented by an in-plane effective magnetic field, Ω_{LT} [27] [Fig.7.5(b)]. The combination of these two rotations is at the origin of the polariton spin whirls. The rotating polarization at the source results in the appearance of rotating spiral arms in the spatial

distribution of the circular polarization degree (S_z), in analogy to the water jets created by a rotating sprinkler head [Figs.7.1(d-f)]. The energy splitting between Ψ_+ and Ψ_- states at the pump spot can also be generated by interactions between polaritons, $\alpha(|\Psi_+|^2 - |\Psi_-|^2)$, where the corresponding precession in linear polarization was previously described [67], however, we find that the dominant contribution to the splitting is caused by the exciton reservoir splitting, $g_R(\mathcal{N}_+ - \mathcal{N}_-)$.

7.5.3 Polariton and exciton reservoir dynamics

In Fig.7.6 the dynamics of the polariton condensate and exciton reservoir [Fig.7.6 (a)], under elliptically polarized pump, is studied and compared with the energy splitting [Fig.7.6 (b)] and the polarization at the pump spot position [Fig.7.6 (c)]. Starting from a linearly polarized condensate shown in Fig.7.6 (a), the evolution of the polarization follows hand in hand with the splitting [Fig.7.6 (b)]. Specifically, one should note the sudden change in the polarization behavior as the splitting reverses (grey dashed line), corresponding to the Stokes vector reversing its precession in Fig.7.6 (c). The rotational direction is controlled by the sign of the splitting. Positive splitting induces anti-clockwise rotation while negative splitting a clockwise one. When Ψ_+ polaritons are generated faster they deplete the $\mathcal{N}_+$ excitons, causing the density to suddenly drop faster than $\mathcal{N}_-$ and thus changing the sign of the splitting. Numerically, the spin +1 polaritons condense first since they are being pumped at a higher rate due to the ellipticity of the pump. This is displayed as a concentric polarization ring which expands outward. Then, as $S_z = -1$ polaritons condense and the reservoir densities deplete (i.e. the splitting switches from weak positive to strong negative) the spin whirl appears.

A notable difference exists between the experiment and the simulation. Experimentally, as noted earlier, there is an equal and steady formation of the spin components (under elliptical pumping) which at their maximum intensity suddenly rotate [Fig. 2.4 (a)]. From the GPE model [Eqs. (1) and (2), main manuscript] the imbalance set by the pump immediately causes an imbalance in the exciton reservoir components, $\mathcal{N}_\pm$. When the polaritons condense, the $\Psi_\pm$ populations grow at different rates [blue and red line in Fig.7.6(a) unlike the steady growth seen in Fig.7.7(a)] leading up to the whirl. This causes an immediate appearance of the spin whirl in the simulations from the moment of condensation and splitting reversal (Fig.7.6, gray dashed line). Qualitatively the

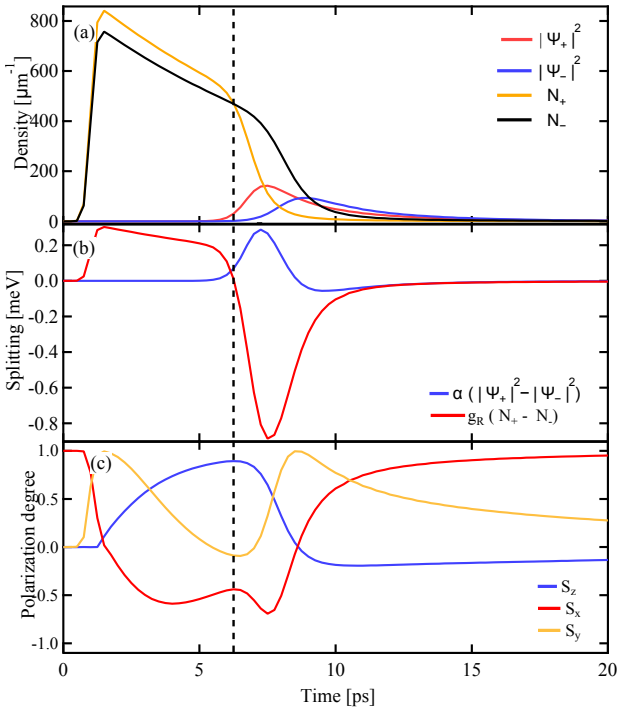

FIGURE 7.6: Dynamics of the condensate and reservoir at the pump position under elliptical pumping extracted from the simulation in Fig.7.4(c). (a) Density versus time of the $\Psi_{\pm}$ polariton condensate and $\mathcal{N}_{\pm}$ exciton reservoir. (b) Energy splitting versus time of the polariton condensate (blue line) and exciton reservoir (orange line). (c) Linear (S_x), diagonal (S_y) and circular (S_z) Stokes components versus time, extracted at the pump spot position. The dashed grey line indicates the position where the energy splitting in (b) and the Stoke vector in (c) reverse.

rotation observed in experiment is the same as depicted by the GPE model. To achieve more accurate dynamics, a multiple-reservoir model would be more suitable.

7.6 Variation of the pump spot polarization and picosecond oscillations

In Fig.7.7(a), the intensity of the polarization components integrated over space is plotted versus time in the case of linearly polarized excitation and circular Stokes (S_z) detection. In Fig.7.7 (b), the case of circularly polarized excitation and linear Stokes (S_x) detection is also reported for comparison. Both these measurements, have been realized at the same condition of detuning, power and excitation spot (see section 7.2). Fig.7.7 (a) and Fig.7.7 (b) correspond respectively to the intensity profiles of Figs.7.1(a-c) and Figs.6.7 (a-c). In both cases the area of integration is $460 \times 340 \mu m^2$.

The small imbalance between Ψ_+ and Ψ_-, induced by the ellipticity of the pump polarization, results in picosecond scale oscillation in the circular emission [red and blue profile in Fig.7.7(a)] indicated in the literature as features of bosonic stimulation [68, 209]. Experimentally, the rotation of the polarization at the pump spot is confirmed by the average of the degree of circular polarization calculated at the pump spot position, which oscillates between ± 0.1, as shown in Fig.7.7 (a) (green profile) and coincides with the rotation of the spin textures [Figs.7.1(a-c)].

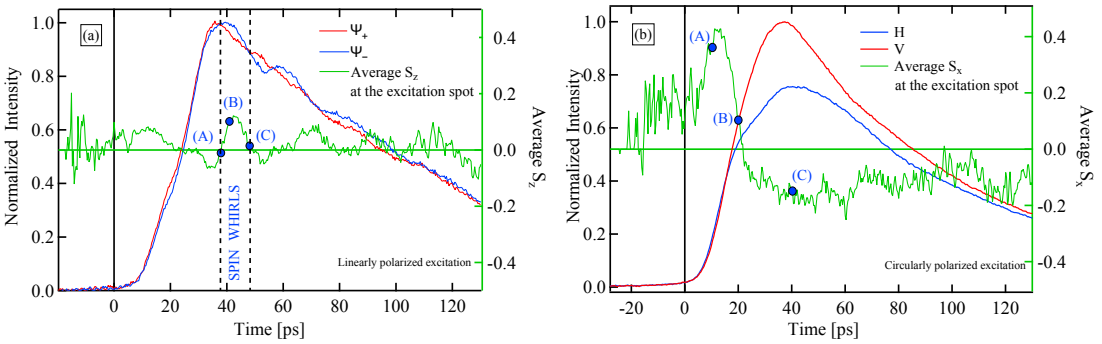

FIGURE 7.7: (a) Time-resolved, spatially integrated measurements of the two circular polarization components (Ψ_+, Ψ_-) PL intensity under linearly polarized excitation. (b) The same as in (a) but for the two linear polarization components (H,V) under circularly polarized excitation. Both profiles have been normalized and integrated over the area imaged in Figs.7.1 (a-c) and Figs.6.7 (a-c), i.e., $460 \times 340\,\mu m^2$. In green we show the time resolved degree of circular polarization S_z in (a) and the linear polarization S_x in (b) averaged over an area $1.78 \times 1.78 \mu m^2$, centered at $(0,0)\mu m$ in Figs.7.1 (a-c) and Figs.6.7 (a-c), comparable with the 2 μm FWHM excitation spot. The blue solid circles in (a) and (b), annotated with (A), (B), (C), refer to the three snapshots of Figs.7.1 (a-c) and Figs.6.7 (a-c) respectively.

In Fig.7.7(a) the green profile corresponds to the average of the circular Stokes parameter S_z while in Fig.7.7(b) to the average of the linear Stokes parameter S_x. In both cases, the average is calculated at the excitation spot position, over an area $1.78 \times 1.78\,\mu m^2$ comparable with the $2\,\mu m$ FWHM excitation spot area. The oscillation that we observe in Fig.7.7(a) is a consequence of the rotation of the spin textures: as the spin texture rotates in the excitation spot area, the polarization oscillates between Ψ_+ and Ψ_- (i.e. between the two circular polarization components), which corresponds on average to oscillation between +0.1 and -0.1. The presence of this oscillation confirms the rotation of the polarization at the source, which is due to the effective magnetic field Ω_z , present only at the pump spot position where the exciton reservoir is localized. Under circularly polarized excitation [Fig.7.7(b)],the same calculation at the spot area do not show these oscillations, in line with the fact that the patterns shown in Figs.6.7 (a-c) do not rotate. In the case of circularly polarized excitation, polariton condensate results in

an imbalanced population [red profile in Fig.7.7(b)] and the small ellipticity induced by the tightly focused spot will not play a relevant role as in the case of linearly polarized pump. As a consequence, the imbalance between the two polariton populations is set by the pump and preserved throughout the entire process so that no oscillation in the density and in the polarization at the pump spot appear [green profile in Fig.7.7(b)] and the spin texture does not rotate.

By referring to Fig. 7.7 (a), we can identify three different regimes in the formation dynamics of the spin whirl:

1. Up to 38 ps, the dynamics of the polariton is mainly characterized by the propagation of polaritons radially out of the excitation spot, which corresponds to the formation of a 2D spin texture in the plane of the microcavity.

2. Once the 2D spin texture is formed, corresponding to the point of maximum intensity of Ψ_+ and Ψ_- polaritons [Fig.7.7(a)], it starts to rotate. This regime, indicated in Fig. 7.7 (a) as "spin whirls" regime, corresponds to the swirling of the spin texture [Figs.7.1 (a-c)] and the inversion of the polarization at the pump spot position [green profiles in Fig.7.7(a)].

3. Eventually at about $\sim$ 120 ps, the emission from the cavity decay and the spin textures disappear.

7.7 Spectral and time resolved measurements in real and k-space

The rotation of the spin textures has been studied also by performing energy resolved measurements, under the same excitation conditions as in Figs.7.1(a-c). This is shown in Figs.7.8(a-b).

In non resonant experiments, the pseudospin dynamics of polaritons is strongly connected with the energy relaxation of the exciton reservoir immediately after the arrival of the excitation pulse. The decay of the exciton reservoir in time results to a gradual decreasing potential energy that polaritons experience at the pump spot. Consequently, polaritons are generated with a decreasing energy at the excitation position. The interplay between the polariton spin and the energy relaxation of the exciton reservoir give

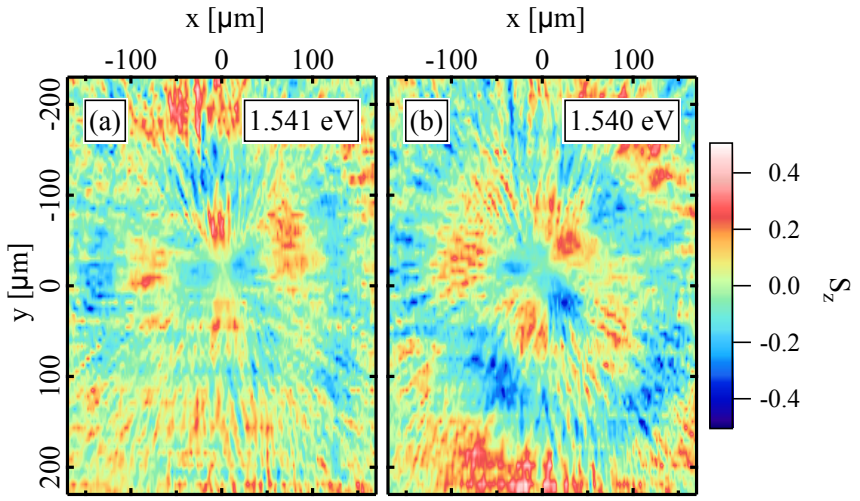

FIGURE 7.8: Experimental real space spectral tomography of the degree of circular polarization S_z at: (a) 1.541 eV and (b) 1.540 eV showing the clockwise rotation of the spin whirls within the microcavity plane under nonresonant linearly polarized excitation.

rise to spin textures with different chirality (i.e., their image does not coincide with their respective mirror image) at different energies, similarly to the spin vortices at different energy observed in atomic condensate with ferromagnetic interactions [210]. The typical quadrature of the OSHE rotates by $\sim 45°$ in the plane of the microcavity due to the rotation of the linear polarization axis by $\sim 90°$ in the Poincaré sphere. This is also confirmed in k-space, where the variation of the linear polarization at the source results in the appearance of rings of opposite circular polarization [211]. Thus, due to the varying polarization at the pump spot and the decrease of the blue shift with time, polaritons with spin up/down (Ψ_+/Ψ_-) populate concentric rings in k-space [see Figs.7.9(a-b)].

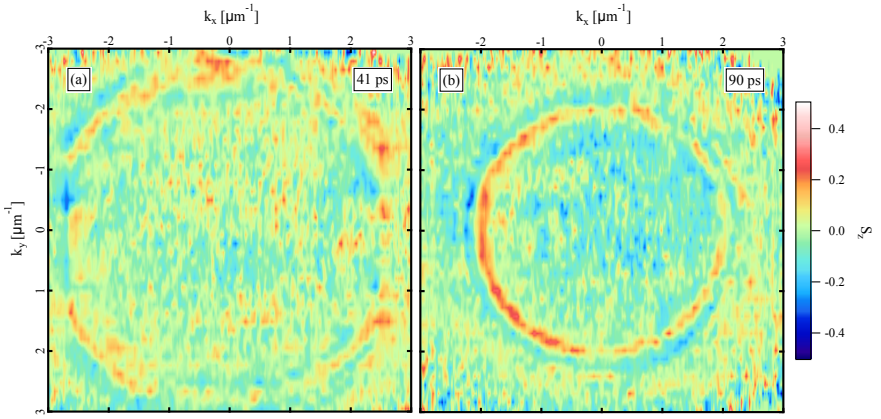

FIGURE 7.9: Experimental time resolved polariton emission in k-space, after (a) 41 ps and (b) 90 ps the onset of the PL emission (see method in section 4.3.3).The microcavity is excited with a linearly polarized pulse and the circular degree of polarization (S_z) is measured.

7.8 Conclusions

In conclusion, we have observed and studied the dynamics of spin textures in polariton microcavities. We demonstrated theoretically and experimentally that the appearance of spin whirl in polariton microcavity is due to a dynamical optical spin Hall effect, which originates from the TE-TM splitting of propagating modes and a self-induced Zeeman splitting at the pump spot. The strong nonlinear interactions between polaritons and the exciton reservoir induce a collective rotation of the 2D textures in the plane of the microcavity.

An analogous but static rotation of indirect exciton spin currents was observed under continuous wave excitation and real magnetic field in coupled quantum wells [212]. Here, we emphasize the dynamical induction of an effective magnetic field on the picosecond scale and the resulting dynamical control of spin currents, which is an additional step toward applications of the optical spin Hall effect in polariton spintronics.

7.9 Contributions & Publications

The experiments reported in this chapter have been carried out mainly by the author, with the supervision of Hamid Ohadi. The theoretical model was realized by Tim Liew and Helgi Sigurdsson (section 7.5). The simulations reported in Figs.7.1 were realized by Helgi Sigurdsson. The data presented in this chapter are part of a work, called "polariton spin whirls", submitted for publication and currently under review.

Chapter 8

Polariton condensation in a strain-compensated microcavity

8.1 Introduction

Polariton condensates represent a unique case of condensate which differs from the conventional BEC, due to its non equilibrium nature (i.e., photons leak out of the cavity before polaritons reach the thermal equilibrium), but differ also from a standard photon laser because it does not require the electronic population to be inverted (section 3.2.2). Whether, would be more appropriate to refer to polariton condensate as BEC or a polariton laser it is still matter of debate in the community [46–48]. This controversy could be, in principle, be resolved with the fabrication of samples with higher Q-factor and, consequently, higher polariton lifetime.
Beyond the controversy on the correct terminology to use, the spontaneous formation of a coherent ensemble of exciton-polariton at temperatures higher than the atomic case, still remain a fundamental aspect, which has been experimentally reported in different samples [77]. However, under non-resonant optical excitation, condensation in InGaAs quantum well based microcavities has not previously been achieved.

To demonstrate the formation of a polariton condensate, it is important to show that:

1. the polariton emission above threshold displays intensity nonlinearities, linewidth narrowing, continuous blueshift of the energy mode,

2. the system is in the strong coupling regime,

3. the lasing occurs at the polariton mode,

4. a second threshold occurs when the power of the excitation is increased.

The last three points trace a clear distinction between polariton lasing and the photon lasing observed in the conventional VCSEL. In particular, the observation of the second threshold, proposed by Bajoni et al. [74] as additional criterion to distinguish between polariton and photon lasing, marks the transition to the photon lasing regime and, consequently, prove that the first threshold is associated with polaritons.

In the last chapter of this thesis, we demonstrate the formation of a polariton condensate in a strain-compensated planar microcavity with InGaAs quantum wells. This new sample, provided by Professor Wolfgang Langbein (Cardiff University), is characterized by a limited number of cross-hatch dislocations [see Fig.4.9(d)] thanks to 2% of phosphorous (P) introduced in the AlAs DBR layer (i.e. $AlAs_{0.98}P_{0.02}$/GaAs DBRs), as previously discussed in section 4.4.3. Using real and reciprocal space spectroscopic imaging, under non-resonant optical excitation (section 8.2), we observe the anticrossing of the polariton branches (section 8.3), proving the strong coupling regime, the formation of a polariton condensate (section 8.4) and a second threshold (section 8.5) marking the onset of photon lasing, (i.e., the transition from the strong to the weak-coupling regime).

8.2 Experimental method

The sample is described in details in section 4.4.3. In the experiments the sample was held in a cold finger cryostat at a temperature of $T = 6\,\mathrm{K}$. The optical excitation, for all the measurements reported in this work, was at the first reflectivity minimum above the cavity stop band (i.e. non resonant excitation), as shown in Fig.4.9(b) (section 4.4.3). To observe the formation of a polariton condensate at $k = 0$ (see Fig.8.2), we use a puled laser. The optical excitation pulses of 180 fs duration and 80 MHz repetition rate are provided by a Ti:Sapphire laser.

The photoluminescence from the lower polariton (LP) was acquired with $\pm 40°$ collection angle, by a 0.65 NA microscope objective and was spectrally resolved using a 1200 grooves/mm grating in a 300 mm spectrometer coupled to a cooled charge coupled device.

As the emission energy of the InGaAs QWs is lower than the absorption of the GaAs substrate we can study the photoluminescence of the sample both in reflection and transmission geometry. The transmission geometry, which is not available for GaAs QWs, allows to filter the surface reflection of the excitation, and has been widely utilized to probe the features of polariton fluids [141, 213] under resonant excitation of the polaritons. We use non-resonant excitation from the epi side, and detect the emission from the substrate side, so that the excitation is filtered by the absorption of the GaAs substrate.

8.3 Strong coupling regime

The spectrally and in-plane wave vector (k) resolved emission intensity at low excitation fluence and at a detuning of $\Delta = -5\,\text{meV}$ is shown in Fig.8.1(a). The measured lower polariton dispersion has a clear non parabolic shape, contrarily to the parabolic dispersion typical of the photonic (C) mode [white dashed lines in Fig.8.1(a)].

As discussed in section 2.4.2, the first demonstration of strong coupling in polariton microcavity, made for the first time by Weisbuch et al.[7] relied on the observation of the *anticrossing* of the two polariton modes (see Fig.2.11), which represents the main signature of the strong coupling regime. We observe the anticrossing of the lower (LP) and upper (UP) polariton branches, when the energy of the cavity mode is scanned across the excitonic resonance (i.e. at different detunings). Thus, extracting the upper polariton (UP) and LP energy at $k \sim 0$ across the thickness gradient of our sample, we find the detuning dependence shown in Fig.8.1(b). To fit the experimental data we use two coupled harmonic oscillators model [90]. The strong coupling between the exciton resonance and the cavity mode is observed with a vacuum Rabi-splitting of $2\hbar\Omega \sim 8\,\text{meV}$.

8.4 Formation of a polariton condensate

In order to achieve condensation into the LP ground state at $k \sim 0$ we excite with a spot of $35\,\mu\text{m}$ full width half maximum (FWHM). The non-resonant excitation create electron-hole pairs in the InGaAs QWs and GaAs cavity which rapidly relax to populate

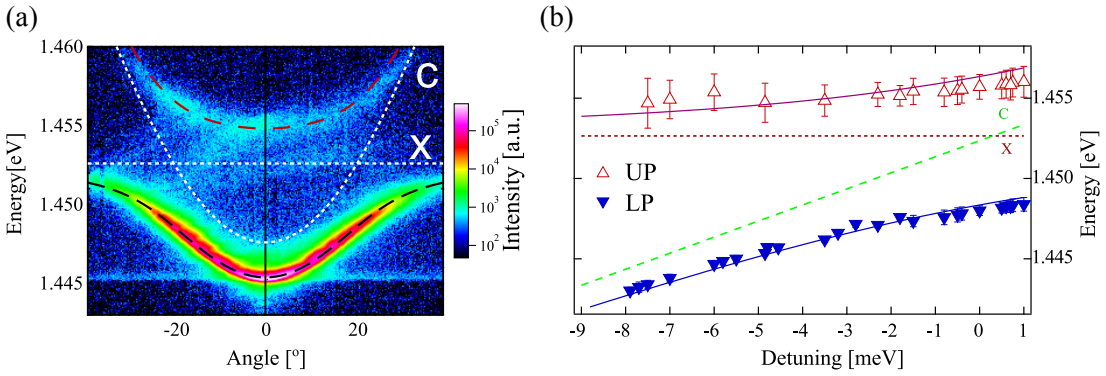

FIGURE 8.1: (a) Lower and upper polariton branches at low excitation fluence on a logarithmic color scale. The white dashed lines indicate the bare exciton (X) and cavity (C) modes while the blue and red solid lines the calculated UP and LP dispersions. (b) UP and LP energy at normal incidence for different detuning conditions. The error bars correspond to the FWHM of a Gaussian fit to the spectra, the blue (purple) line show the calculated LP (UP), and the dashed green (red) line shows the bare cavity (exciton) mode.

the LP dispersion and the weakly coupled QW exciton reservoir. With increasing exciton and polariton density the polariton relaxation rate increases, eventually overcoming the threshold for condensation when the relaxation into the ground state of the LP supersedes its radiative decay, resulting in a macroscopic ground state population [11]. Fig.8.2(a) shows the energy and wave-vector resolved emission intensity in the low fluence regime, where renormalization is insignificant. Both the upper and lower polariton branches are visible.

With increasing excitation fluence P we observe a threshold at $P_{\mathrm{thr}} = 26\,\mu\mathrm{J/cm}^2$ at which the emission shrinks in momentum space as shown by the intensity profiles in Fig.8.2(a-c) extracted at peak energy of the k=0 emission. Also above threshold the emission at high k is following the expected LP dispersion, confirming the strong coupling regime. The LP spectrum at $k \sim 0$ also displays the expected features for polariton condensation, namely, a linewidth narrowing in Fig.8.2(d), a blueshift of the polariton mode in Fig.8.2(e), and a nonlinear increase in intensity in Fig.8.2(f). Increasing the fluence above threshold, interactions between the polariton condensate and the exciton reservoir increase, resulting in a broadening and blueshift of the condensate emission [214].

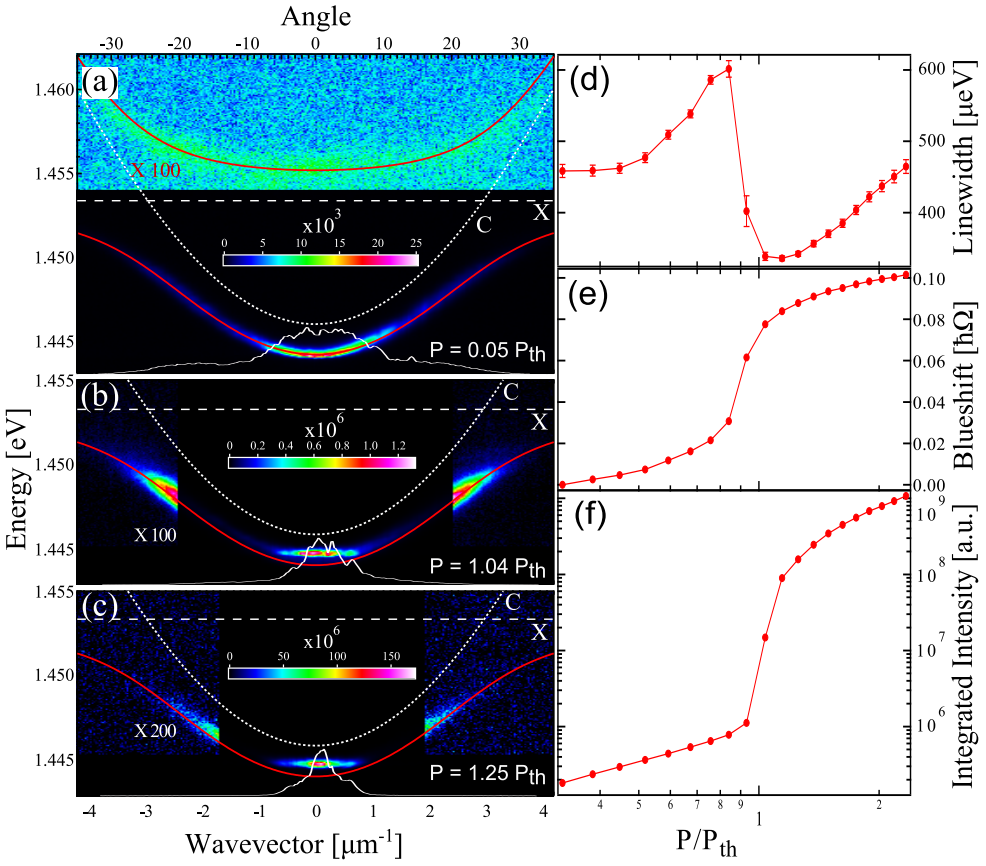

FIGURE 8.2: Energy and wave vector resolved emission intensity on a linear color scale as indicated, (a) below, (b) at, and (c) above threshold. The red lines show the calculated LP and UP dispersions, and the dotted and dashed white lines show the uncoupled low-density cavity (C) and exciton (X) dispersion, respectively. In (a) the UP energy range is also shown, scaled as indicated. The data has been scaled in (b) for $|k| > 2.5\,\mu\text{m}^{-1}$ and in (c) for $|k| > 1.8\,\mu\text{m}^{-1}$ as indicated. Profiles of the LP emission along k are also shown as white lines. (d) LP linewidth, (e) energy shift in units of the Rabi Splitting $2\hbar\Omega$ and (f) intensity, at $k \sim 0$ versus excitation fluence.

8.5 Two-threshold behavior: from polariton lasing to photons lasing

To observe the transition from polariton condensation to photon lasing in the weak coupling regime, we need a significantly higher excitation fluence, for which we reduce the excitation size to $9.2\,\mu m$ FWHM.

The smaller excitation spot leads to polariton condensation at $|k| > 0$ due to a steeper potential profile induced by the repulsive exciton-exciton interactions in the reservoir. To record the evolution of the emission intensity with increasing excitation fluence between the two regimes, we integrate the emission over the entire LP, from 1.441 eV to 1.458 eV and $|k| < 3.4\,\mu m^{-1}$. As shown in Fig.8.3(a), we now find two thresholds, with

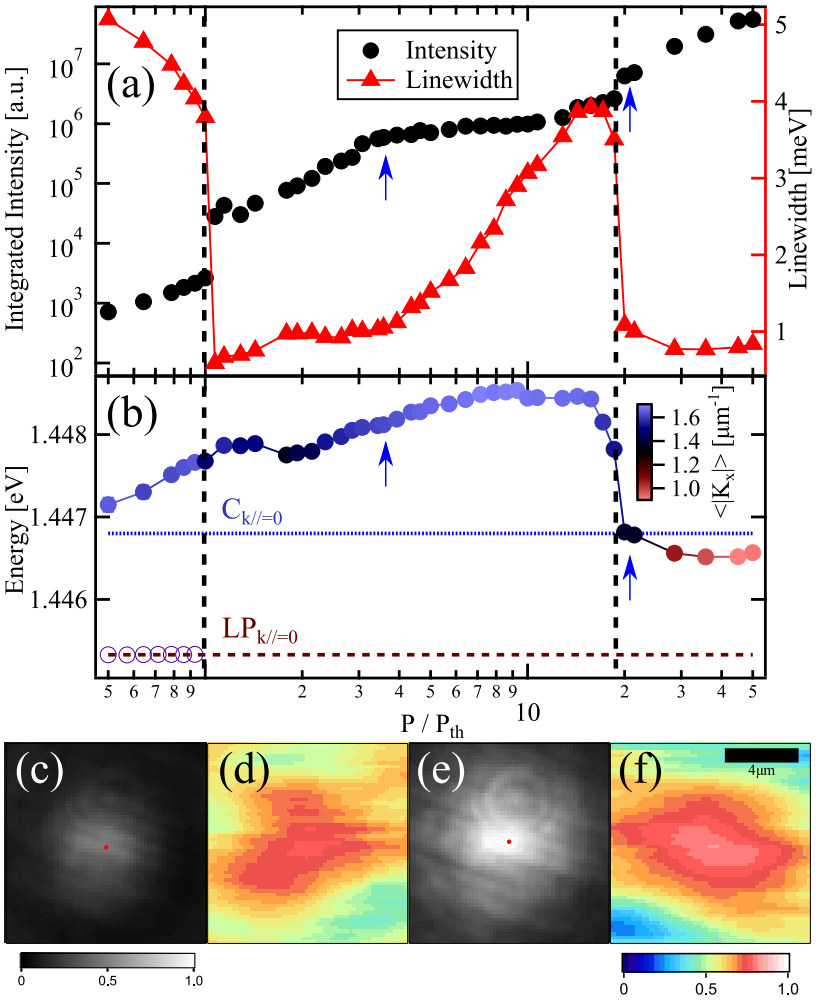

FIGURE 8.3: LP emission using an excitation size of 9.2 μm FWHM, as function of the excitation fluence P relative to the polariton condensation threshold $P_{\mathrm{th}} = 28\,\mu\mathrm{J/cm^2}$. (a) linewidth, and spectrally integrated intensity, collected over $|k| < 3.4\ \mu\mathrm{m}^{-1}$. (b) Average energy, color coded with the average wave vector $\langle|\mathrm{k}|\rangle$. The empty circles show the emission from the LP branch at $k = 0$ below threshold. The dotted lines indicate the energy of the cavity (blue) and the LP (brown) at $k = 0$. (c),(e) Spatially resolved emission intensity and (d),(f) fringe visibility in the regime of polariton condensation at $P = 3.8P_{\mathrm{th}}$ (c,d) and photon lasing at $P = 20P_{\mathrm{th}}$ (e,f), as indicated by the two blue arrows in (a,b). The visibility is averaged over 24 different phase shifts. The red spots in (c) and (e) indicate $\mathbf{r} = 0$ used in (d), (f).

the second one at about 20 times higher fluence than the first, showing an abrupt increase in intensity and decrease in linewidth. We note that directionally integrating the emission broadens the resulting linewidth compared to Fig.8.2 and reduces the intensity difference between the linear and nonlinear plateau. Fig.8.3(b), shown the energy shift of the emission color-coded with the average $\langle|k|\rangle$ of the emission over the intensity distribution along the measured direction. As expected for a small excitation spot, the LP population build up occurs at $|k| > 0$, increasing with the excitation fluence. However,

upon crossing the second threshold, the emission shifts towards the energy of the uncoupled cavity mode and k=0. This second threshold is thus attributed to the transition to photon lasing [215] which occurs in the weak coupling regime and is due to the dissociation of excitons into electron-hole pairs. This second threshold is defined by the so called Bernard-Douraffourg condition [216], which in turns is based on the Fermi-Dirac distribution of the electron hole plasma created by the high fluence excitation. If the condition is fulfilled the electron hole population is inverted and conventional lasing can be observed [215].

To show the coherence build up above threshold, we carried out interference measurements using an actively stabilized Michelson interferometer in a mirror-retroreflector configuration [11] (section 4.2.4) measuring the coherence of the emission at r relative to r, with r=0 set to the emission peak as indicated in Figs.8.3(c) and Figs.8.3(e). The extracted fringe visibility (equation 4.1) in the polariton condensate and photon lasing regime is shown in Figs.8.3(d) and Figs.8.3(f). The measured visibility V of both the photon lasing and polariton condensate regime is extended and reaches up to about 80%, consistent with the expected coherence of the emission.

8.6 Conclusions

In conclusion, we have presented experimental evidence of non-resonantly excited polariton condensation in a strain compensated GaAs-based cavity with InGaAs QWs. The observed nonlinear increase of intensity, along with a linewidth narrowing, and the observation of a second threshold to photon lasing represents, on the basis of the present knowledge, clear evidences of polariton condensation in the strong coupling regime.

The work reported in this chapter represents the first observation of polariton condensation in the family of III-V microcavities with QWs of this material. The strain compensation of the DBRs limits the optical disorder of the system and minimizes cavity defects, making this cavity a potential optimum candidate for the study of intrinsic interactions and fluidics phenomena in polariton condensates, which are currently limited by the photonic disorder of semiconductor microcavity structures.

8.7 Contributions & Publications

The experiments reported in this chapter have been carried out mainly by the author and Alexis Askitopoulos. All the data reported in this chapter have been published previously in Ref.[33]. Parts of the text have been quoted verbatim from this work [33].

Chapter 9

Conclusions and future perspectives

Exciton-polaritons are bosonic quasiparticles formed by the strong coupling between QW excitons and the photonic mode of a planar semiconductor microcavity. When the polariton population is increased above a threshold density, the stimulated scattering leads polaritons to macroscopically occupy the ground state of the dispersion and gives rise to an inversion-less amplification of the polariton emission (Chapter 2). The resulting macroscopic ground state population is a nonequilibrium BEC. Solid state polariton condensates have been used to explore fundamental concepts such as superfluidity and quantum turbulence phenomena (Chapter 3). In particular, the study of hydrodynamic processes such as the nucleation of vortices and dark soliton at the surface of defects naturally occurring in microcavities, has been a hot topic in the last four years [18–22, 122]. Here, the source of nonlinearity, essential for the formation of such a solitary wave, has been identified in the repulsive polariton-polariton interactions [18–22].

9.1 On the oblique dark solitons in polariton microcavities

In the first part of this thesis, the question whether the observations reported in polariton literature are sufficient to claim the formation of dark and half-dark solitons in polariton microcavity was investigated. First it should be emphasized that this work

does not question the theoretical framework of the Gross-Pitaevskii equation, which admits soliton solutions. However, it suggests that the experimental evidence provided in literature [18–22] is insufficient to claim the observation of dark and half-dark solitons in polariton microcavities, as summarized below.

9.1.1 Unconventional dark solitons: literature review

The unconventional properties of dark solitons observed in polariton microcavities were highlighted in section 5.1.1. In particular, we note that:

1. Dark solitons in polariton microcavities are claimed at subsonic velocity, i.e. for a Mach number $M < 1$ (see table 5.1 for details) where oblique dark solitons are *"absolutely unstable"* [176] and vortex nucleation is predicted in both atomic [176] and polariton [17] condensates. Thus, for $M < 1$ diffraction features are not excluded.

2. The transition from a superfluid to a dark solitons regime claimed in Fig.3A-C of Ref.[18] [Fig.3.6 in this thesis] takes place again in the subsonic regime. The turbulent regime claimed in Fig. 3.6B is at a smaller power than previous observations on the same work [Fig.3.5(a)]. The *phase jump* in the dark solitons candidate [Fig. 3.6F] is absent already at $\sim 15\,\mu$m from the defect, thus not showing one of the main "solitons fingerprints".

3. In Ref. [22] half-solitons are claimed, but no excitation power dependence is provided, neither a measurement of the excitation power nor of the fluid density. As a consequence, the presence of the same features in the linear regime is not excluded.

9.1.2 Experimental results

The study on the formation of dark solitons, presented in this thesis, demonstrated experimentally and theoretically that phase vortex lines in polariton propagation together with dark notches, previously used as fingerprints of oblique-dark solitons [18–21] in literature, are also present in the linear propagation regime, namely with no polariton-polariton interactions. To verify the linear regime, we studied the excitation density dependence of our results with both a Gaussian and half-Gaussian excitation beam (see

Fig.5.3) and we found that they were independent of both the shape of the beam and the excitation density over a range of four orders of magnitude and they persisted at polariton density which was seven orders of magnitude lower than the lasing threshold observed in standard microcavities [10]. This confirms that our observation were in the linear regime. A theoretical model, based on the the classical theory of electromagnetism (section 5.5), corroborate the key message of our work: the observations of the "dark soliton fingerprints" do not require nonlinearity, since the same features can be observed as the result of interference.

Moreover, by combining both experimental and theoretical analysis in this thesis it was demonstrated that the analogy between linear waves and quantum fluids observations [18, 22] goes beyond the mere observation of the same features and is effectively more profound. Specifically, it was shown that:

1. the observed features depend on the scattering geometry, i.e. the size of the defect and the direction of propagation of the polariton wave (section 5.6). In particular, a bigger defect can produce soliton quadruplet-like features, qualitatively identical to the one reported in the literature [18] (Fig.5.7).

2. Different density patterns can be observed as a function of the polariton wave vector in the linear regime (section 5.7). Thus, the appearance/disappearance of soliton-like features, independent of the excitation density does not provide evidence of an interacting quantum fluid. Moreover, the disappearance of the two "dark-soliton fingerprints" with detuning can be observed for different defects and can be considered a typical behavior (section 5.7.1).

3. The analytical expressions relating the phase jump, the width and depth of the soliton to the fluid velocity and density (equation 1 in Ref. [18], reported in this thesis as equation 3.18) can also be satisfied in the linear regime, as explicitly shown in section 5.8.

4. Half-dark soliton-like features are also observed in the linear regime due to the TE-TM splitting of the cavity mode (section 5.10).

9.1.3 A new criterion to identify polariton dark solitons and future work

In this thesis, a new criterion based on the healing length of the condensate has been proposed to distinguish between the linear and nonlinear regime (section 5.9). It should be emphasized that, differently from the linear regime, in the case of polariton quantum fluid, the healing length can be exactly calculated since it is defined by the same variables used to calculate the speed of sound, for example in Ref. [18] and, more importantly, the healing length conditions should be fulfilled over a range of polariton excitation densities to exclude coincidental matches with specific scattering patterns in the linear propagation regime. The latter, in particular, is a crucial point in the studying of nonlinear effects in polariton microcavities.
When demonstrating nonlinear behavior in a system, one first has to establish the linear behavior at low densities, and then show deviations from it at higher densities. Polariton dynamics depend strongly on the depth and the size of the scattering defects and the excitation conditions used. It is therefore crucial to perform a suited study for each investigated defect to provide necessary and sufficient evidence for dark soliton formation.

A way to generate both bright and dark solitons, not yet explored in polariton condensates, is to take advantage of the possibility to reverse the sign of the effective mass of polaritons, by pumping below and above the inflection point of the lower polariton dispersion [see Fig.3.9(a)], corresponding respectively to the injection of polaritons with positive and negative effective mass. As discussed in section 3.5, in the case of repulsive interactions within the condensate, the formation of bright soliton is theoretically admitted provided that polaritons are injected with negative mass [23]. Similarly, dark soliton solution exists in the case of polaritons with positive effective mass [23].
Following this consideration, it is in principle possible to envisage an experiment where the observation of dark and bright solitons can be tested on the same sample. By changing the angle of excitation, while keeping the energy constant, polaritons with positive and negative mass could be generated, thus setting the theoretical condition for the observation of both types of solitons under the same excitation parameters. However, in both cases, the healing length conditions should be satisfied over a range of polariton excitation densities so as to exclude similar observation in the linear regime.

9.2 On the polariton spin dynamics

In this thesis, the spin dynamics of polariton condensates was investigated. In a radially expanding condensate, polaritons with opposite spin arrange themselves in geometrically ordered spin textures, which propagate over hundreds of microns in the plane of the microcavity. Depending on the polarization of the excitation pump, different spin textures were observed (Chapter 6). Moreover, spin textures rotating in the plane of microcavities on a picosecond scale, i.e. the so called polariton spin whirls, were reported for the first time (Chapter 7).

Although the observed spin textures appear only in the non-linear regime, the mechanism underlying the formation of these patterns, namely the optical spin Hall effect, remains intrinsically a linear effect [188]. As for the case of the "dark solitons fingerprints" studied in this thesis, also the optical spin Hall effect has been already observed in the absence of nonlinearity (on the same sample) [188]. Both these observations highlight the photon-like behavior of polaritons. In the case of the spin whirls, namely the spin textures that rotate in the plane of the microcavity on a picosecond scale, simulations suggests that the rotation is mainly driven by exciton-exciton interaction at the position of the excitation spot. The interaction with the exciton reservoir is not a polariton-polariton interaction within the condensate. This is the case of nonresonantly excited experiments, where the blueshift of the condensate is dominated by the exciton density in the reservoir at high wave vectors.

However, it has to be underlined that the non-resonant excitation scheme used in these experiments allow to observe, above a certain threshold, the spontaneous build up of coherence, which represents a fundamental common point between polariton and atomic condensates. In this regards, since many other aspects underlying atomic BECs have been also observed in polariton microcavities, the nonequilibirum nature of polariton condensates could represent a resource which would allow a better understanding of the physics behind equilibrium atomic BECs.

9.2.1 On the spin-optronics

The works on the polariton spin dynamics studied in this thesis demonstrate that polaritons can carry information over hundreds of micron with minimal losses (Chapter

6) and allow the control of the spin on the picosecond scale (Chapter 7). Both these works confirm the potential of semiconductor microcavity for the realization of novel "spinoptonics" device.

In the last decades, many works have explored the possibilities for the realization of the basic building blocks of polariton based spin circuits. Polariton spin switches [71], AND and OR gates [217], spin memories [218] and spin transport in 1D channel [219] are only few examples of the results already achieved. However, although these works confirm the great properties of polaritons in the realization of new devices, allowing switching times [71] and transport of information [217] much faster than standard optoelectronics, the implementation of the first polariton spin device still remains a challenge. Due to the use of massive external polarization optics, for example, their integrability is still limited [71]. Apart from technological problems, the main obstacle in the implementation of new devices is represented by the well established expertise, infrastructure and processing technology of silicon based circuits. Started more than 60 years ago with the invention of the first silicon chips in the late 1950s, silicon industries limit the possibilities of new optical devices to compete with standard silicon chip. Thus, it is reasonable to think that at least in the near future, the only new device concepts to be implemented will be the one that can be integrated within conventional chip technology [220].

9.3 On the condensation in a strain-compensated microcavity & future work

In the last chapter of the thesis, the condensation of polaritons in a strain compensated microcavity was investigated. The features supporting polariton lasing and condensation, according to the current understanding of polariton condensates, are experimentally observed, including the observation of a second threshold which marks the transition from the strong to the weak-coupling regime. The latter was proposed as an additional criterion, to prove polariton condensation [74].

A major advancement in this work is represented by the material used in the growth of the microcavity. The incorporation of phosphorus in DBRs allows to reduce the density of the cross-hatch dislocations, while InGaAs QWs allow more versatility in planning the experiments. In particular, since the the emission energy of the InGaAs QWs is

lower than the absorption of the GaAs substrate, the photoluminescence of the sample can be studied, under non-resonant excitation, both in reflection and transmission geometry. The transmission geometry, which is not available for GaAs QWs, allows to filter the surface reflection of the excitation and has been widely utilized for the study of condensate fluidics phenomena, such as superfluidity [57, 58] and polariton spin devices [71, 217] under resonant excitation of polaritons. Thanks to the InGaAs QW, on the other hand, our sample can be excited non-resonantly from the epi side while the emission is detected from the substrate side, so that the excitation is filtered by the absorption of the GaAs substrate and no external filter is needed to cut out the excitation laser. This represents a first step toward the integrability of microcavity structures. At the same time, condensation in a structure with suppressed photonic disorder is particularly suitable for the study of polariton fluidics, involving long range propagation, and periodic lattices of interacting condensates [221].

9.4 Prospective & future work

The field of polariton microcavities presents several open questions that are still matter of debate in the community. Apart from the oblique dark solitons studied in this thesis, many other fundamental aspects of polariton condensates require further investigations.

The most fundamental question, whether the polariton condensate is a laser or BEC still remains unresolved. This aspect raises many questions, not only on the nature of polariton condensate itself but also on the physics of BEC. Many features of atomic BEC, such as the macroscopic occupancy of the ground state, the nonlinear threshold behavior, and the narrowing of the linewidth are all properties that nonequlibrium polariton condensates share with equilibrium atomic BECs [9]. So, *"what are the features that unequivocally identify BEC?"*. In this regards, the study of atomic BEC effects in nonequilibrium systems could give a possible answer. In the same way, the study of polariton effects in laser systems (e.g. VCSEL) will help to better identify the unique properties of polaritons.

At the present, polariton condensates can be seen as an intermediate case between atomic BEC and laser. All of them share the phenomenon of long range spatial coherence. The second threshold behavior observed also in this thesis (section 8.5) demonstrates that

it is possible on the same sample, at the same position, to go from polariton BEC to a standard laser, at a different density [222]. So, *"Is it possible to envisage to these effects as merely different regimes of the same phenomenon?"* [9]

With regards to applications, it is still not clear whether polaritons would ever give birth to new technological devices. However, their capacity to operate at room temperature [43–45] represents a great potential to be exploited in future applications. Moreover, the enormous advances in the growth and fabrication of the samples, allow to engineer different ad hoc microcavity configurations, which can be particularly convenient for applications in quantum simulations [9]. In this regards, condensation in a structure with suppressed photonic disorder, like the one investigated in this thesis (Chapter 8), can represent a further step towards the implementation of periodic lattices of interacting condensates, providing a potential platform for on chip quantum simulations [223]. Periodic polariton condensate lattices, in fact, can be imprinted on such a structure by means of a spatial light modulator (SLM), allowing the study of the coupling effects between single condensates in the lattice [221]. The use of the SLM, in principle, guarantees the flexibility to control each node of the lattice individually by adjusting the parameters of the excitation (such as the intensity or the distance between the lattice points). The use of a strain compensated microcavity, on the other hand, guarantees the limited influence of photonic disorder on transport and coupling effects between two neighbor condensates. The manipulation and control of the coupling (i.e. the interactions) between the condensates of a lattice represents the first step toward the realization of polariton quantum simulations.

Many research groups all over the world are dreaming for the realization of quantum computers that would allow, one day, to simulate difficult quantum many-body problems [223] and reach a deeper understanding of physical laws [224], with many implications in future technologies and our everyday life. New realms of physics, unknown today, will appear. The edge of human knowledge will be pushed further. Other goals will be set, other dreams will come true, again!

Appendix A

A small insight into the fabrication process

Quantum Wells (QWs) and Distributed Bragg Reflectors (DBRs), discussed respectively in section 2.2.2 and 2.3.1, are examples of heterostructures, namely structure composed by alternating layers of two different semiconductor materials.

The samples studied in this thesis have been fabricated by means of molecular beam epitaxy (MBE). In this technique, the samples are grown in ultra high vacuum conditions ($\leq 10^{-11}\ Torr$) to limit the concentration of residual gases, which could contaminate the sample [1]. The reactants, that eventually will form the layers of the heterostructure, are vaporized by heating a source material in a cell with a very small orifice. As the vapor escapes from the cell, its molecules (or atoms) form a collimated beam, called *molecular beam*, aiming to the sample and depositing the layer. Typically several molecular beams containing the necessary elements for forming the semiconductor and for doping the sample are aimed at the substrate [1].

A single QW, as mentioned in section 2.2.2, is a heterostructure where a thin layer of a semiconductor material with small band gap, like for example GaAs, is sandwiched between two thick layers of another semiconductor material with larger band gap, like for example AlGaAs. The choice of the semiconductor materials that will eventually form the QW, is determined mainly by two variables: the energy band gap of the two materials and their lattice constants. These parameters are in general different for different materials.

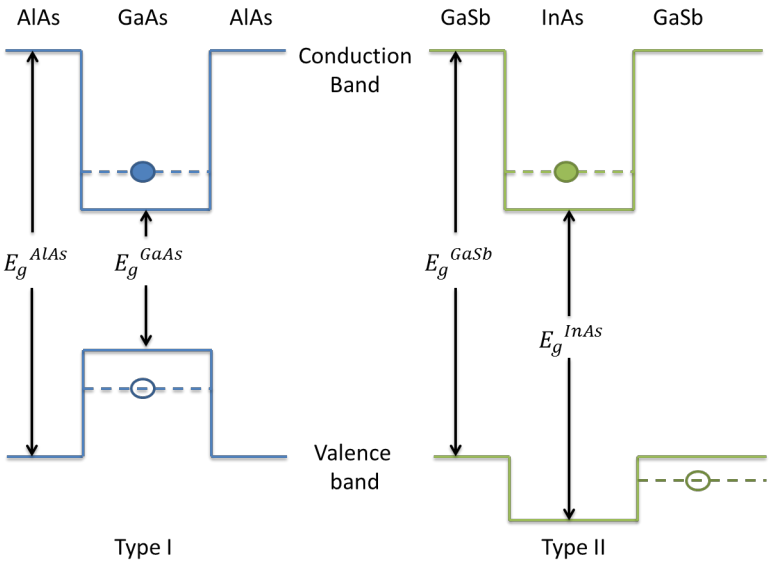

FIGURE A.1: Sketch of the band structure of two different quantum wells. On the left (blue profiles) a quantum well of type I, composed by AlGaAs/GaAs where the band edge discontinuities of the conduction and valence band have opposite signs. On the right (green profiles) a quantum well of type II, composed by GaSb/InAs where the band edge discontinuities have the same direction. The open and filled circle represents respectively the hole in the valence band and the electron in the conduction band. Figure redrawn from [29].

When two different semiconductor materials are joined together to form a QW, the conduction and valence band of these materials do not align with each other. The difference between their band edges, known as *band off-set*, will determine the size and profile of the confinement potential. Although there is no successful predictive theory, the band off-set can be estimate experimentally by means of the band off-set ratio, introduced for the first time by Dingle et al. [225], which corresponds to the ratio between the conduction band offset and the band gap difference of the two materials [1]. In the case of GaAs/AlGaAs heterostructures the band offset ratio is approximately 67 : 33, namely 67% of the difference in the band gap energies is in the conduction band offset while 33% is in the valence band offset [226]. Consequently, in GaAs/AlGaAs QWs, both electrons and holes see higher energies in the AlGaAs than in the GaAs, giving a so called "Type I" system. This type of QWs are the ones present in the sample studied in this thesis. On the other hand, heterostructures in which electrons and holes have their lowest energies in different materials are called "Type II" [226]. In Fig. A.1 both types of QWs are shown. The main differences between the two types of QWs lies in the fact that in type I QW electrons and holes are both confined within the same layer (forming the well) while in type II QWs electrons and holes are confined in

different layers and a more complex unit cell than just a single layer is needed for the confinement.

As mentioned before, apart from the energy band gap, another critical parameters for the correct design of QWs is represented by the lattice constant of the two materials. In particular, it is necessary that the lattice constants of the two materials match each other. Lattice-matching, in fact, reduces the number of dislocations in the epitaxial layer (i.e, the layer grown in the course of MBE deposition). However, it also imposes tight restrictions on the band gaps that can be engineered [5].

Thus, in order to obtain the desired band gap in a heterostructure with matched lattices, it is indispensable to choose the right material and composition for each layer. This goal can be reached by using for example ternary or quaternary alloy with different composition, such for example $Al_xGa_{1-x}As$ and adjust the percentage (x) of materials to obtain the desired lattice constant and band gap.

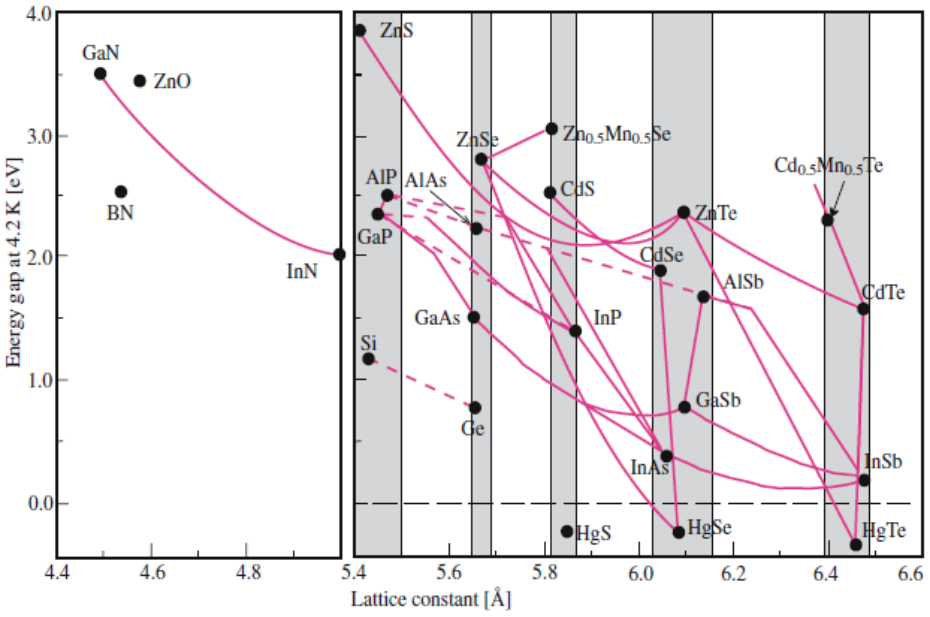

FIGURE A.2: A plot of the low temperature energy band gaps for several semiconductors with the diamond and zinc-blende structure versus their lattice constants. The shaded regions highlight several families of semiconductors with similar lattice constants. Solid lines are used to connect semiconductors that can form a stable alloys while dashed lines indicate semiconductors with indirect band gap. The negative gap in semiconductors usually indicate an inverted band structure. This image has been taken from Ref. [1].

In Fig. A.2, the band-gap energy E_g as a function of the lattice constant for several semiconductors with the diamond and zinc-blende structure is shown. We notice that

GaAs and AlAs have very similar lattice constants (they lie on the graph within the same shaded region), justifying the wide use of AlGaAs in the fabrication of multilayer heterostructures, such as QWs and DBRs composing the microcavity samples.

Appendix B

Transfer matrix formalism applied to a planar microcavity with quantum well

In the first months of my PhD, I worked on a program to simulate how the Rabi splitting changes in a microcavity, when the number of DBRs is changed. Caryl Richards had already written a program to calculate the Rabi splitting with the Transfer Matrix method. Her program was based on the "linear dispersion model" where each quantum well embedded in the microcavity is treated by a local Lorentz oscillator [77]. However, with this program, there was not relation between the Rabi splitting and the structural properties of the microcavity. Thus, for example, by changing the number of DBRs, the Rabi splitting calculated by the program was not changing at all.
By following the semiclassical model developed by Savona et al.[90], I have modified Caryl's program so that a correlation between the Rabi splitting and the cavity's properties (number of DBRs, Q factor, etc.) could be studied. The program has been used to calculate some of the reflectivity spectra shown in Chapter 2.

B.1 Theory

The transfer matrix (TM) formalism represents a really powerful method to simulate the reflectivity and transmission spectra of multilayer structures, such as distributed Bragg

reflectors (DBR), quantum well (QW) and microcavities (MCs) described in Chapter 2. Basically, the TM method allows to solve Maxwell equations in multilayer dielectric structures by imposing, as boundary conditions, that the electric field and its derivative are both continuous at the interface between two layers [77]. Each layer is represented by a matrix, so that by multiplying all the layers the amplitude of the electric field can be calculated across the whole multilayer structure. From the amplitude of the electric field the reflectivity and transmittance coefficient, i.e the ratio of reflected and transmitted incident energy flux, can be calculated. Here the main results will be summarized and only the matrices used in the program will be indicated. For a more accurate description refer to Refs. [77, 90].

Let us consider a symmetric multilayer structures, i.e. a microcavity, composed by two symmetric DBRs and one QW at the center of the cavity. The two DBRs are structures composed by the alternation of two layers with different refractive index (n_a and n_b). At normal incidence, the transfer matrices across the two layers n_a and n_b, with width a and b respectively, composing the DBRs mirrors are [77]:

$$T_a = \begin{bmatrix} cos(k_a a) & \frac{i}{n_a} sin(k_a a) \\ i n_a sin(k_a a) & cos(k_a a) \end{bmatrix}, \quad T_b = \begin{bmatrix} cos(k_b b) & \frac{i}{n_b} sin(k_b b) \\ i n_b sin(k_b b) & cos(k_b b) \end{bmatrix} \tag{B.1}$$

where $k_{a(b)} = \frac{\omega}{c} n_{a(b)}$ is the wave vector of propagating light in the medium a(b). The transfer matrix of a single QW of width L_w, placed at the center of the cavity, for the two polarization $\alpha = L, T$ is [90]:

$$T_{QW} = \frac{1}{\Delta_\alpha} \begin{bmatrix} e^{ik_z L_w}(\Delta_\alpha - i\Gamma_\alpha) & -i\Gamma_\alpha \\ i\Gamma_\alpha & e^{-ik_z L_w}(\Delta_\alpha + i\Gamma_\alpha) \end{bmatrix} \tag{B.2}$$

where $k_z = \sqrt{\epsilon_{cav} \frac{\omega^2}{c^2} - k_x^2}$ is the wave vector along the growth direction (z) of the microcavity and $\epsilon_{cav} = n^2$ the dielectric constant of the cavity, $\Delta_\alpha = \omega - \omega_{ex} + i\gamma$ is the detuning between the cavity (ω) and exciton ($\omega_e x$) resonance, where γ is the nonradiative exciton broadening, $\Gamma_T \cong \Gamma_0 \frac{k_0}{k_x}$ is the radiative width of the T (y-polarized) mode, $\Gamma_L \cong \Gamma_0 \frac{k_z}{k_0}$ is the radiative width of the L (x-polarized) mode and $\Gamma_0 = \frac{1}{a\pi\epsilon_0} \frac{\pi}{n_c a v} \frac{e^2}{m_0 c} f_{xy}$ is the decay rate of the exciton amplitude at $k_x = 0$ in a single QW, with ϵ_0 being the dielectric constant of the medium, m_0 the free electron mass and f_{xy} the oscillator strength. At

normal incidence it can be assumed, for simplicity, that there is not difference between the longitudinal and transverse polarization mode, so that $\gamma_T = \gamma_L = \gamma_0$.

The transfer matrix of the whole structure is obtained by multiplying, from left to right, the matrices of the different m layers [77]:

$$\mathbf{T} = \prod_{i=m}^{1} T_i \tag{B.3}$$

where $\mathbf{T}_i$ is the transfer matrix across the ith layer. The reflection (r) and transmission (t) coefficients of a structure composed by m layers and sandwiched between two semi-infinite media with refractive index n_{left} and n_{right} before and after the structure [77]:

$$r = \frac{n_{right}t_{11} + n_{left}n_{right}t_{12} - t_{21} - n_{left}t_{22}}{t_{21} - n_{left}t_{22} - n_{right}t_{11} + n_{left}n_{right}t_{12}}, \tag{B.4}$$

$$t = 2n_{left}\frac{t_{12}t_{21} - t_{11}t_{22}}{t_{21} - n_{left}t_{22} - n_{right}t_{11} + n_{left}n_{right}t_{12}}. \tag{B.5}$$

The reflectivity (R) and transmittivity (T) are:

$$R = |r|^2, \quad T = |t|^2 \frac{n_{right}}{n_{left}} \tag{B.6}$$

The structure investigated is a SiO_2-Ta_2O_5 microcavity where the cavity medium is a AlAs cavity of thickness $\lambda/2n_{AlAs}$ (with $\lambda = 753\,\text{nm}$). In the center of the cavity there is a GaAs QW of thickness equal to 10 nm. The DBRs are composed by N_{top} (left DBR) and N_{bottom} (right DBR) periods. One period (d) of a DBR contains a layers of SiO_2 (n = 1.458) of thickness $\lambda/4n_{SiO_2}$ and a layer of Ta_2O_5 (n = 2.137) of thickness $\lambda/4n_{Ta_2O_5}$. Before (left) and after (right) the structure I put, respectively, a layer of air (n=1, thickness = 100 nm) and a substrate layer (n=1.5, thickness = 100 nm). I have used the structure above and equation B.6 to calculate the reflectivity spectra that have been shown in Fig.2.7 (DBR), Fig.2.8 (cavity) and Fig.2.10 (b,c) (microcavity with embedded quantum well).

B.2 Results

By studying the Rabi splitting [Fig.2.10 (b,c)] as function of the number of DBRs it turned out that when the number of DBRs is increased:

- the cavity mode becomes narrower, which corresponds, as expected, to an increases of the cavity Q-factor,
- while the Rabi splitting decreases.

The latter can be explained qualitatively with the increase of the effective length of the cavity (L_{eff}) and an increase of the light penetration depth into the DBR (L_{DBR}), when the number of DBRs is increased, i.e., $L_{eff} = L_{cavity} + L_{DBR}$, in agreement with the results obtained in Ref. [227]. In fact, in the strong coupling regime (described in section 2.4.2), the Rabi splitting is defined as [90]:

$$\Omega = 2\sqrt{|V|^2 - \frac{1}{4}(\gamma_c - \gamma)^2} \tag{B.7}$$

where γ_c is the the FWHM of the cavity mode, γ is the non-radiative broadening and V represents the coupling between the exciton and the cavity mode [90]:

$$V = \sqrt{\frac{1+\sqrt{R}}{\sqrt{R}} \frac{c\Gamma_0}{n_{cav} L_{eff}}} \tag{B.8}$$

From equations B.7 and B.8, it follows that $\Omega \propto \frac{1}{L_{eff}}$, justifying the results obtained.

B.3 Igor Pro program codes

Authors: Caryl Richards & Pasquale Cilibrizzi

Main references: [90] and [77].

```
#pragma rtGlobals=1              // Use modern global access method.

Function CalcReflectivity()

Variable/G CavityLambda =752.7  //Wavelngth [nm]
Variable/G lmin=500     //Minimum wavelength
Variable/G lmax=1200                              //Maximum wavelength
```

```
Variable/G Delta=10000                  //Number of wavelength points i.e. resolution

Variable/G topperiods=8//Number of DBR periods
Variable/G botperiods=  topperiods      //Number of DBR periods equal in top/bottom DBRs
Variable/G LayerMax=5 + 2*topperiods + 2*botperiods

Variable/G qq=0
Variable/G wlen


Make/O/N=(Delta) Lambda
Make/O/N=(Delta) Reflectivity
Make/O/N=(Delta) Transmittance
Make/O/N=(Delta) Absorption

BuildDBR()

PauseUpdate; Silent 1

lambda[] = lmin + (lmax-lmin)*p/(Delta-1)                       //populates wave "lambda"
        do
        wlen = lambda[qq]
        TransferMatrix()//Calculates the transfer matrix for all layers at wavelength "wlen"
        qq+=1

        while (qq<Delta)

Display 'Reflectivity' vs 'Lambda'
Label left "Reflectivity  [%]";DelayUpdate
Label bottom "Wavelength [nm]"


//Display  'Transmittance' vs 'Lambda'
//Label left "Transmittance  [%]";DelayUpdate
//Label bottom "Wavelength [nm]"

//Display  'Absorption' vs 'Lambda'
//Label left "Absorption [%]";DelayUpdate
//Label bottom "Wavelength [nm]"

//RabiSplitting()
//Test()
//Test2()
End

////////////////////////////////////////////////////////////////////////////////

Function TransferMatrix()
```

```
Variable theta
Variable nref
Variable ii
Variable/C top,bot

Variable nright                 //substrate
Variable nleft                  //surface

Wave thick, refindex
Wave Reflectivity, Transmittance, Absorption
NVar  CavityLambda, LayerMax, wlen, qq , nAlAs, aaQW

////////////// Quantum Well Savona-Andreani \citep{Savona_1995}  //////////////

Variable/C      ArgumentOfe=cmplx (0, aaQW*nAlAs*2*pi/(2.99*10^17*wlen))//10^17speedOfLight[nm]
Variable/C      exponential = exp(ArgumentOfe)
Variable/C      NonRadiative = cmplx(0,10^-3/(6.852*10^-16))//excit. broadening 1meV in [nm]
Variable/G      detuning=  (2*pi/wlen) - (2*pi/765) + NonRadiative //omega - omega_exc
Variable/G      exdecay=(pi/nAlAs)*(2.818*10^-6)*(2.99*10^17)*(4/10^18)
//Exc.decayRate=(pi/n_cav)*(electron radius[nm])*(speedOfLight[nm/s])*(osc.strength per u.area)

////////////// Quantum Well Kavokin \citep{kavokin_microcavities_2007} //////////////

//      Variable/G      exdecay=(pi/nAlAs)*(2.818*10^-6)*(2.99*10^17)*(0.5/10^15)
//      Variable/C      C_exdecay= cmplx(0, exdecay)
//      Variable/C      NonRadiative = cmplx(0 , 1024*10^3)
//      Variable/C      gam0= cmplx(0, NonRadiative + exdecay)
//      Variable/C      r= C_exdecay/((2*pi/750) - (2*pi/wlen) - gam0)
//      Variable/C      t=1 + r

////////////////////////////////////////////////////////////////////////////////

Make/O/C/N=(2,2) tt //transfer matrix for layer ii
Make/O/C/N=(2,2) pp //total product transfer matrix for all layers for wavelength 'wlen'

pp[0][0] = cmplx(1,0)
pp[0][1] = cmplx(0,0)
pp[1][0] = cmplx(0,0)
pp[1][1] = cmplx(1,0)

for (ii=0; ii<(LayerMax-1); ii+=1)      // left --> right               Andreani
//for (ii=LayerMax-2; ii>-1; ii -=1)    // left <-- right                       Kavokin

        nref = refindex[ii]
        theta = nref*thick[ii]*2*pi/wlen

        if (ii !=(LayerMax+1)/2)
                tt[0][0] = cmplx(cos(theta), 0)
```

```
                tt[0][1] = cmplx(0,sin(theta))/nref
                tt[1][0] = cmplx(0,sin(theta))*nref
                tt[1][1] =  tt[0][0]

//print (LayerMax+1)/2

////////////////////ANDREANI QW MATRIX2//////////////////////////////

Variable/C      C_exdecay= cmplx(0, exdecay)
Variable/C      exponential2= exp(-ArgumentOfe)

else
                tt[0][0] = (detuning - exdecay)*(exponential/detuning)
                tt[0][1] =      - C_exdecay/detuning
                tt[1][0] =      C_exdecay/detuning
                tt[1][1] =      (detuning + exdecay)*(exponential2/detuning)

        endif

////////////////KAVOKIN QW MATRIX ////////////////////////////////////
//      else
//              tt[0][0] = 1
//              tt[0][1] = 0
//              tt[1][0] = -2*nAlAs*(r/t)
//              tt[1][1] = 1
//
//      endif
////////////////////////////////////////////////////////////////////////////////

\\ Multiply all the matrix composing the structure (equation B3)

        MatrixMultiply pp,tt
        wave/c Mproduct = M_product
        pp = Mproduct

//print pp[0][0]
endfor

nleft=refindex[0]
nright=refindex[(Layermax-1)]

top = nright*pp[0][0] + nleft*nright*pp[0][1] - pp[1][0] - nleft*pp[1][1]
bot = pp[1][0] - nleft*pp[1][1] - nright*pp[0][0] + nleft*nright*pp[0][1]


Reflectivity[qq] =  magsqr(top)/magsqr(bot)
Transmittance[qq] = (nleft/nright) / magsqr(bot)
Absorption[qq] = 1 - Reflectivity[qq]   - Transmittance[qq]
```

```
Return (1)
End

////////////////////////////////////////////////////////////////////////////////

//Build whole structure:
//Air + [DBR1 (Si/Tantalum) + Cavity (AlAs) + QW(GaAs) + DBR2(Tantalum/Si)] + Substrate

Function BuildDBR()

Variable/G nAir=1                                        //refractive index of air
Variable/G nSilica = 1.458                        //1.458 //refractive index of SiO2
Variable/G nTantalum = 2.3              //2.137 //refractive index of Ta2O5
Variable/G nAlAs=3.15833                         // refractive index of Empty cavity
Variable/G nGaAs=3.41917                //  refractive index of QW
Variable/G nSubstrate = 1.5             //refractive index of glass

Variable/G nn =0                                 // counts n layers // Layermax
Variable aa1, aa2                        //alternate thicknesses of DBR's layers
Variable/G aa3, aaQW            //thicknesses of Empty cavity region & QuantumWell

NVar  Cavitylambda, LayerMax, aa3 , aaQW
//see above --> LayerMax=5 + 2*topperiods + 2*botperiods

Variable/G repeats =(LayerMax-5)/2
// repeats= numero di layers in ciascuna DBR// (LayerMax-5)/4


Make/O/N=(LayerMax) thick,refindex

aa1 = Cavitylambda/4/nSilica
aa2 = Cavitylambda/4/nTantalum
aa3 = Cavitylambda/nAlAs/2
aaQW =10 //nm


Air()
        DBRtop(repeats, aa1,aa2)
                AlAs(aa3)
                        GaAs(aaQW)
                AlAs(aa3)
        DBRbot(repeats, aa1, aa2)
Substrate()

Variable Lcav=aa3
Variable Ldbr=(CavityLambda/2)*(nSilica*nTantalum/(nAlAs*(nTantalum - nSilica))
//see Ref.[83] eq.6
```

```
Variable Leff = Lcav + Ldbr

Print "Lcav=",Lcav, "Ldbr=",Ldbr , "Leff=",Leff


End

////////////////////////////////////////////////////////////////////////////////
//Includes 'air' superstrate in the top layer of the structure
Function Air()
Wave thick, refindex
NVar nn, nAir
        thick[nn]=100;refindex[nn]=nAir; nn+=1 //nn-=1
End

////////////////////////////////////////////////////////////////////////////////
//Glass substrate
Function Substrate()
Wave thick, refindex
NVar nn, nSubstrate
        thick[nn]=100;refindex[nn]=nSubstrate; nn+=1 //nn-=1
End

////////////////////////////////////////////////////////////////////////////////
//DBR layers, function populates the geometric thickness and respective refractive index
//in each DBR period
Function DBRtop(rpts,th1,th2)// (periods, aa1, aa2)
Variable rpts, th1,th2
Variable jj
Wave thick, refindex
NVar nn, nSilica, nTantalum
        for (jj=1;jj<=rpts/2;jj+=1)
        thick[nn]=th1; refindex[nn]=nSilica; nn+=1 //nn-=1
        thick[nn]=th2; refindex[nn]=nTantalum; nn+=1//nn-=1
        endfor
End

////////////////////////////////////////////////////////////////////////////////
//AlAs Empty region

Function AlAs(th1)
Variable th1
Wave thick, refindex
NVar nn, CavityLayer
Nvar nAlAs
thick[nn]=th1; refindex[nn]=nAlAs; nn+=1 //nn-=1
End
```

```
////////////////////////////////////////////////////////////////////////////////
// GaAs Quantum Well

Function GaAs(th1)
Variable th1
Wave thick, refindex
NVar nn,QWlayer
Nvar nGaAs
thick[nn]=th1; refindex[nn]=nGaAs;nn+=1  //nn-=1
End

 ////////////////////////////////////////////////////////////////////////////////
 //DBR layers, function populates the geometric thickness and respective refractive index
//in each DBR period

Function DBRbot(rpts,  th1,th2)// (periods, aa1, aa2)
Variable rpts, th1,th2
Variable jj
Wave thick, refindex
NVar nn, nSilica, nTantalum
        for (jj=1;jj<=rpts/2;jj+=1)
        thick[nn]=th2; refindex[nn]=nTantalum;nn+=1// nn-=1
        thick[nn]=th1; refindex[nn]=nSilica; nn+=1//nn-=1
        endfor
End
```

Bibliography

[1] Peter Y. Yu and Manuel Cardona. *Fundamentals of Semiconductors: Physics And Materials Properties*. Springer Science & Business Media, January 2005. ISBN 9783540254706.

[2] James R. Chelikowsky and Marvin L. Cohen. Nonlocal pseudopotential calculations for the electronic structure of eleven diamond and zinc-blende semiconductors. *Phys. Rev. B*, 14(2):556–582, July 1976. doi: 10.1103/PhysRevB.14.556. URL http://link.aps.org/doi/10.1103/PhysRevB.14.556.

[3] S.V. Gaponenko. *Optical Properties of Semiconductor Nanocrystals*. Cambridge University Press, October 1998. ISBN 9780521582414.

[4] W. Y. Liang. Excitons. *Phys. Educ.*, 5(4):226, July 1970. ISSN 0031-9120. doi: 10.1088/0031-9120/5/4/003. URL http://iopscience.iop.org/0031-9120/5/4/003.

[5] Mark Fox and Radu Ispasoiu. Quantum wells, superlattices, and band-gap engineering. In Safa Kasap Prof and Peter Capper Dr, editors, *Springer Handbook of Electronic and Photonic Materials*, pages 1021–1040. Springer US, 2006. ISBN 978-0-387-26059-4, 978-0-387-29185-7. URL http://link.springer.com/referenceworkentry/10.1007/978-0-387-29185-7_42.

[6] D. a. B. Miller, D. S. Chemla, D. J. Eilenberger, P. W. Smith, A. C. Gossard, and W. T. Tsang. Large roomtemperature optical nonlinearity in GaAs/Ga1x AlxAs multiple quantum well structures. *Applied Physics Letters*, 41(8):679–681, October 1982. ISSN 0003-6951, 1077-3118. doi: 10.1063/1.93648. URL http://scitation.aip.org/content/aip/journal/apl/41/8/10.1063/1.93648.

[7] C. Weisbuch, M. Nishioka, A. Ishikawa, and Y. Arakawa. Observation of the coupled exciton-photon mode splitting in a semiconductor quantum microcavity. *Phys. Rev. Lett.*, 69:3314–3317, Dec 1992. doi: 10.1103/PhysRevLett.69.3314. URL http://link.aps.org/doi/10.1103/PhysRevLett.69.3314.

[8] A. I. Tartakovskii, M. S. Skolnick, D. N. Krizhanovskii, V. D. Kulakovskii, R. M. Stevenson, R. Butt, J. J. Baumberg, D. M. Whittaker, and J. S. Roberts. Stimulated Polariton Scattering in Semiconductor Microcavities: New Physics and Potential Applications. *Adv. Mater.*, 13(22):1725–1730, November 2001. ISSN 1521-4095. doi: 10.1002/1521-4095(200111)13:22⟨1725::AID-ADMA1725⟩3.0.CO;2-Z. URL http://onlinelibrary.wiley.com/doi/10.1002/1521-4095(200111)13:22%3C1725::AID-ADMA1725%3E3.0.CO;2-Z/abstract.

[9] Tim Byrnes, Na Young Kim, and Yoshihisa Yamamoto. Exciton-polariton condensates. *Nat Phys*, 10(11):803–813, November 2014. ISSN 1745-2473. URL http://dx.doi.org/10.1038/nphys3143.

[10] Hui Deng, Gregor Weihs, David Snoke, Jacqueline Bloch, and Yoshihisa Yamamoto. Polariton lasing vs. photon lasing in a semiconductor microcavity. *PNAS*, 100(26):15318–15323, December 2003. ISSN 0027-8424, 1091-6490. doi: 10.1073/pnas.2634328100. URL http://www.pnas.org/content/100/26/15318.

[11] J. Kasprzak, M. Richard, S. Kundermann, A. Baas, P. Jeambrun, J. M. J. Keeling, F. M. Marchetti, M. H. Szymaska, R. Andr, J. L. Staehli, V. Savona, P. B. Littlewood, B. Deveaud, and Le Si Dang. BoseEinstein condensation of exciton polaritons. *Nature*, 443(7110):409–414, September 2006. ISSN 0028-0836. doi: 10.1038/nature05131. URL http://www.nature.com/nature/journal/v443/n7110/abs/nature05131.html.

[12] T. W. Neely, E. C. Samson, A. S. Bradley, M. J. Davis, and B. P. Anderson. Observation of vortex dipoles in an oblate bose-einstein condensate. *Phys. Rev. Lett.*, 104:160401, Apr 2010. doi: 10.1103/PhysRevLett.104.160401. URL http://link.aps.org/doi/10.1103/PhysRevLett.104.160401.

[13] I. Carusotto, S. X. Hu, L. A. Collins, and A. Smerzi. Bogoliubov-Čerenkov radiation in a bose-einstein condensate flowing against an obstacle. *Phys. Rev.*

Lett., 97:260403, Dec 2006. doi: 10.1103/PhysRevLett.97.260403. URL http://link.aps.org/doi/10.1103/PhysRevLett.97.260403.

[14] M.F. Shih, M. Segev, G.C. Valley, G. Salamo, B. Crosignani, and P. Di Porto. Observation of two-dimensional steady-state photorefractive screening solitons. *Electronics Letters*, 31:826–827(1), May 1995. ISSN 0013-5194. URL http://digital-library.theiet.org/content/journals/10.1049/el_19950570.

[15] George I. Stegeman and Mordechai Segev. Optical spatial solitons and their interactions: Universality and diversity. *Science*, 286(5444):1518–1523, November 1999. ISSN 0036-8075, 1095-9203. doi: 10.1126/science.286.5444.1518. URL http://www.sciencemag.org/content/286/5444/1518.

[16] J. Denschlag, J. E. Simsarian, D. L. Feder, Charles W. Clark, L. A. Collins, J. Cubizolles, L. Deng, E. W. Hagley, K. Helmerson, W. P. Reinhardt, S. L. Rolston, B. I. Schneider, and W. D. Phillips. Generating Solitons by Phase Engineering of a Bose-Einstein Condensate. *Science*, 287(5450):97–101, January 2000. ISSN 0036-8075, 1095-9203. doi: 10.1126/science.287.5450.97. URL http://www.sciencemag.org/content/287/5450/97.

[17] S. Pigeon, I. Carusotto, and C. Ciuti. Hydrodynamic nucleation of vortices and solitons in a resonantly excited polariton superfluid. *Phys. Rev. B*, 83(14):144513, April 2011. doi: 10.1103/PhysRevB.83.144513. URL http://link.aps.org/doi/10.1103/PhysRevB.83.144513.

[18] A. Amo, S. Pigeon, D. Sanvitto, V. G. Sala, R. Hivet, I. Carusotto, F. Pisanello, G. Lemnager, R. Houdr, E. Giacobino, C. Ciuti, and A. Bramati. Polariton superfluids reveal quantum hydrodynamic solitons. *Science*, 332(6034):1167–1170, June 2011. ISSN 0036-8075, 1095-9203. doi: 10.1126/science.1202307. URL http://www.sciencemag.org/content/332/6034/1167.

[19] G. Grosso, G. Nardin, F. Morier-Genoud, Y. Léger, and B. Deveaud-Plédran. Soliton instabilities and vortex street formation in a polariton quantum fluid. *Phys. Rev. Lett.*, 107:245301, Dec 2011. doi: 10.1103/PhysRevLett.107.245301. URL http://link.aps.org/doi/10.1103/PhysRevLett.107.245301.

[20] G. Grosso, G. Nardin, F. Morier-Genoud, Y. Léger, and B. Deveaud-Plédran. Dynamics of dark-soliton formation in a polariton quantum fluid. *Phys. Rev. B*,

86:020509, Jul 2012. doi: 10.1103/PhysRevB.86.020509. URL http://link.aps.org/doi/10.1103/PhysRevB.86.020509.

[21] Benoit Deveaud, Gael Nardin, Gabriele Grosso, and Yoan Lger. Dynamics of vortices and dark solitons in polariton superfluids. In Alberto Bramati and Michele Modugno, editors, *Physics of Quantum Fluids*, volume 177 of *Springer Series in Solid-State Sciences*, pages 99–126. Springer Berlin Heidelberg, 2013. ISBN 978-3-642-37568-2. doi: 10.1007/978-3-642-37569-9_6. URL http://dx.doi.org/10.1007/978-3-642-37569-9_6.

[22] R. Hivet, H. Flayac, D. D. Solnyshkov, D. Tanese, T. Boulier, D. Andreoli, E. Giacobino, J. Bloch, A. Bramati, G. Malpuech, and A. Amo. Half-solitons in a polariton quantum fluid behave like magnetic monopoles. *Nature Physics*, 8(10):724–728, 2012. ISSN 1745-2473. doi: 10.1038/nphys2406. URL http://www.nature.com/nphys/journal/v8/n10/full/nphys2406.html.

[23] O. A. Egorov, D. V. Skryabin, A. V. Yulin, and F. Lederer. Bright cavity polariton solitons. *Phys. Rev. Lett.*, 102:153904, Apr 2009. doi: 10.1103/PhysRevLett.102.153904. URL http://link.aps.org/doi/10.1103/PhysRevLett.102.153904.

[24] M. Sich, D. N. Krizhanovskii, M. S. Skolnick, A. V. Gorbach, R. Hartley, D. V. Skryabin, E. A. Cerda-Mndez, K. Biermann, R. Hey, and P. V. Santos. Observation of bright polariton solitons in a semiconductor microcavity. *Nat Photon*, 6(1):50–55, January 2012. ISSN 1749-4885. doi: 10.1038/nphoton.2011.267. URL http://www.nature.com/nphoton/journal/v6/n1/full/nphoton.2011.267.html.

[25] Joanna M. Zajac, Wolfgang Langbein, Maxime Hugues, and Mark Hopkinson. Polariton states bound to defects in gaas/alas planar microcavities. *Phys. Rev. B*, 85:165309, Apr 2012. doi: 10.1103/PhysRevB.85.165309. URL http://link.aps.org/doi/10.1103/PhysRevB.85.165309.

[26] Joanna M. Zajac and Wolfgang Langbein. Structure and zero-dimensional polariton spectrum of natural defects in gaas/alas microcavities. *Phys. Rev. B*, 86:195401, Nov 2012. doi: 10.1103/PhysRevB.86.195401. URL http://link.aps.org/doi/10.1103/PhysRevB.86.195401.

[27] Alexey Kavokin, Guillaume Malpuech, and Mikhail Glazov. Optical spin hall effect. *Phys. Rev. Lett.*, 95(13):136601, 2005. doi: 10.1103/PhysRevLett.95.136601. URL http://link.aps.org/doi/10.1103/PhysRevLett.95.136601.

[28] H. Flayac, D. D. Solnyshkov, I. A. Shelykh, and G. Malpuech. Transmutation of skyrmions to half-solitons driven by the nonlinear optical spin hall effect. *Phys. Rev. Lett.*, 110(1):016404, January 2013. doi: 10.1103/PhysRevLett.110.016404. URL http://link.aps.org/doi/10.1103/PhysRevLett.110.016404.

[29] MBE Group Website – University of Maryland. Molecular beam epitaxy, 2015. URL http://www.lps.umd.edu/MBEGroup/MBEHomePage.htm.

[30] Hui Deng, Hartmut Haug, and Yoshihisa Yamamoto. Exciton-polariton bose-einstein condensation. *Rev. Mod. Phys.*, 82:1489–1537, May 2010. doi: 10.1103/RevModPhys.82.1489. URL http://link.aps.org/doi/10.1103/RevModPhys.82.1489.

[31] P. Cilibrizzi, H. Ohadi, T. Ostatnicky, A. Askitopoulos, W. Langbein, and P. Lagoudakis. Linear wave dynamics explains observations attributed to dark solitons in a polariton quantum fluid. *Phys. Rev. Lett.*, 113(10):103901, September 2014. doi: 10.1103/PhysRevLett.113.103901. URL http://link.aps.org/doi/10.1103/PhysRevLett.113.103901.

[32] E. Kammann, T. C. H. Liew, H. Ohadi, P. Cilibrizzi, P. Tsotsis, Z. Hatzopoulos, P. G. Savvidis, A. V. Kavokin, and P. G. Lagoudakis. Nonlinear optical spin hall effect and long-range spin transport in polariton lasers. *Phys. Rev. Lett.*, 109(3):036404, July 2012. doi: 10.1103/PhysRevLett.109.036404. URL http://link.aps.org/doi/10.1103/PhysRevLett.109.036404.

[33] Pasquale Cilibrizzi, Alexis Askitopoulos, Matteo Silva, Faebian Bastiman, Edmund Clarke, Joanna M. Zajac, Wolfgang Langbein, and Pavlos G. Lagoudakis. Polariton condensation in a strain-compensated planar microcavity with InGaAs quantum wells. *Applied Physics Letters*, 105(19):191118, November 2014. ISSN 0003-6951, 1077-3118. doi: 10.1063/1.4901814. URL http://scitation.aip.org/content/aip/journal/apl/105/19/10.1063/1.4901814.

[34] A. Einstein. ber einen die Erzeugung und Verwandlung des Lichtes betreffenden heuristischen Gesichtspunkt [AdP 17, 132 (1905)]. *Ann. Phys.*, 14(S1):164–181,

February 2005. ISSN 1521-3889. doi: 10.1002/andp.200590004. URL http://onlinelibrary.wiley.com/doi/10.1002/andp.200590004/abstract.

[35] Albert Einstein. Strahlungs-Emission und Absorption nach der Quantentheorie. *Deutsche Physikalische Gesellschaft*, 18:318–323, 1916. URL http://adsabs.harvard.edu/abs/1916DPhyG..18..318E.

[36] M. S. Skolnick, T. A. Fisher, and D. M. Whittaker. Strong coupling phenomena in quantum microcavity structures. *Semicond. Sci. Technol.*, 13(7):645, July 1998. ISSN 0268-1242. doi: 10.1088/0268-1242/13/7/003. URL http://iopscience.iop.org/0268-1242/13/7/003.

[37] A. Imamoglu, R. J. Ram, S. Pau, and Y. Yamamoto. Nonequilibrium condensates and lasers without inversion: Exciton-polariton lasers. *Phys. Rev. A*, 53(6):4250–4253, June 1996. doi: 10.1103/PhysRevA.53.4250. URL http://link.aps.org/doi/10.1103/PhysRevA.53.4250.

[38] Alexey Kavokin. Exciton-polaritons in microcavities: Recent discoveries and perspectives. *physica status solidi (b)*, 247(8):1898–1906, 2010. ISSN 1521-3951. doi: 10.1002/pssb.200983955. URL http://dx.doi.org/10.1002/pssb.200983955.

[39] Le Si Dang, D. Heger, R. André, F. Bœuf, and R. Romestain. Stimulation of polariton photoluminescence in semiconductor microcavity. *Phys. Rev. Lett.*, 81:3920–3923, Nov 1998. doi: 10.1103/PhysRevLett.81.3920. URL http://link.aps.org/doi/10.1103/PhysRevLett.81.3920.

[40] P. Senellart and J. Bloch. Nonlinear emission of microcavity polaritons in the low density regime. *Phys. Rev. Lett.*, 82:1233–1236, Feb 1999. doi: 10.1103/PhysRevLett.82.1233. URL http://link.aps.org/doi/10.1103/PhysRevLett.82.1233.

[41] P. G. Savvidis, J. J. Baumberg, R. M. Stevenson, M. S. Skolnick, D. M. Whittaker, and J. S. Roberts. Angle-resonant stimulated polariton amplifier. *Phys. Rev. Lett.*, 84:1547–1550, Feb 2000. doi: 10.1103/PhysRevLett.84.1547. URL http://link.aps.org/doi/10.1103/PhysRevLett.84.1547.

[42] S. Christopoulos, G. Baldassarri Höger von Högersthal, A. J. D. Grundy, P. G. Lagoudakis, A. V. Kavokin, J. J. Baumberg, G. Christmann, R. Butté,

E. Feltin, J.-F. Carlin, and N. Grandjean. Room-temperature polariton lasing in semiconductor microcavities. *Phys. Rev. Lett.*, 98:126405, Mar 2007. doi: 10.1103/PhysRevLett.98.126405. URL http://link.aps.org/doi/10.1103/PhysRevLett.98.126405.

[43] Feng Li, L. Orosz, O. Kamoun, S. Bouchoule, C. Brimont, P. Disseix, T. Guillet, X. Lafosse, M. Leroux, J. Leymarie, M. Mexis, M. Mihailovic, G. Patriarche, F. Réveret, D. Solnyshkov, J. Zuniga-Perez, and G. Malpuech. From excitonic to photonic polariton condensate in a zno-based microcavity. *Phys. Rev. Lett.*, 110: 196406, May 2013. doi: 10.1103/PhysRevLett.110.196406. URL http://link.aps.org/doi/10.1103/PhysRevLett.110.196406.

[44] K. S. Daskalakis, S. A. Maier, R. Murray, and S. Kna-Cohen. Nonlinear interactions in an organic polariton condensate. *Nat Mater*, 13(3):271–278, March 2014. ISSN 1476-1122. doi: 10.1038/nmat3874. URL http://www.nature.com/nmat/journal/v13/n3/full/nmat3874.html.

[45] Johannes D. Plumhof, Thilo Stferle, Lijian Mai, Ullrich Scherf, and Rainer F. Mahrt. Room-temperature BoseEinstein condensation of cavity excitonpolaritons in a polymer. *Nat Mater*, 13(3):247–252, March 2014. ISSN 1476-1122. doi: 10.1038/nmat3825. URL http://www.nature.com/nmat/journal/v13/n3/full/nmat3825.html.

[46] Leonid V. Butov. Solid-state physics: A polariton laser. *Nature*, 447(7144): 540–541, May 2007. ISSN 0028-0836. doi: 10.1038/447540a. URL http://www.nature.com/nature/journal/v447/n7144/full/447540a.html.

[47] L. V. Butov and A. V. Kavokin. The behaviour of exciton-polaritons. *Nat Photon*, 6(1):2–2, January 2012. ISSN 1749-4885. doi: 10.1038/nphoton.2011.325. URL http://www.nature.com/nphoton/journal/v6/n1/full/nphoton.2011.325.html.

[48] Benot Deveaud-Pldran. The behaviour of exciton-polaritons. *Nat Photon*, 6(4): 205–205, April 2012. ISSN 1749-4885. doi: 10.1038/nphoton.2012.52. URL http://www.nature.com/nphoton/journal/v6/n4/full/nphoton.2012.52.html.

[49] Michiel Wouters and Iacopo Carusotto. Excitations in a nonequilibrium bose-einstein condensate of exciton polaritons. *Phys. Rev. Lett.*, 99:140402, Oct

2007. doi: 10.1103/PhysRevLett.99.140402. URL http://link.aps.org/doi/10.1103/PhysRevLett.99.140402.

[50] Hui Deng, Gregor Weihs, Charles Santori, Jacqueline Bloch, and Yoshihisa Yamamoto. Condensation of Semiconductor Microcavity Exciton Polaritons. *Science*, 298(5591):199–202, October 2002. ISSN 0036-8075, 1095-9203. doi: 10.1126/science.1074464. URL http://www.sciencemag.org/content/298/5591/199.

[51] Esther Wertz, Lydie Ferrier, Dmitry D. Solnyshkov, Pascale Senellart, Daniele Bajoni, Audrey Miard, Aristide Lematre, Guillaume Malpuech, and Jacqueline Bloch. Spontaneous formation of a polariton condensate in a planar GaAs microcavity. *Applied Physics Letters*, 95(5):051108, August 2009. ISSN 0003-6951, 1077-3118. doi: 10.1063/1.3192408. URL http://scitation.aip.org/content/aip/journal/apl/95/5/10.1063/1.3192408.

[52] Christian Schneider, Arash Rahimi-Iman, Na Young Kim, Julian Fischer, Ivan G. Savenko, Matthias Amthor, Matthias Lermer, Adriana Wolf, Lukas Worschech, Vladimir D. Kulakovskii, Ivan A. Shelykh, Martin Kamp, Stephan Reitzenstein, Alfred Forchel, Yoshihisa Yamamoto, and Sven Hfling. An electrically pumped polariton laser. *Nature*, 497(7449):348–352, May 2013. ISSN 0028-0836. doi: 10.1038/nature12036. URL http://www.nature.com/nature/journal/v497/n7449/full/nature12036.html.

[53] Pallab Bhattacharya, Thomas Frost, Saniya Deshpande, Md Zunaid Baten, Arnab Hazari, and Ayan Das. Room temperature electrically injected polariton laser. *Phys. Rev. Lett.*, 112:236802, Jun 2014. doi: 10.1103/PhysRevLett.112.236802. URL http://link.aps.org/doi/10.1103/PhysRevLett.112.236802.

[54] Gretchen K. Campbell. Quantum gases: Superfluidity goes 2d. *Nat Phys*, 8 (9):643–644, September 2012. ISSN 1745-2473. doi: 10.1038/nphys2395. URL http://www.nature.com/nphys/journal/v8/n9/full/nphys2395.html.

[55] D. A. Butts and D. S. Rokhsar. Predicted signatures of rotating Bose-Einstein condensates. *Nature*, 397(6717):327–329, January 1999. ISSN 0028-0836. doi: 10.1038/16865. URL http://dx.doi.org/10.1038/16865.

[56] K. W. Madison, F. Chevy, W. Wohlleben, and J. Dalibard. Vortex formation in a stirred bose-einstein condensate. *Phys. Rev. Lett.*, 84:806–809, Jan 2000.

doi: 10.1103/PhysRevLett.84.806. URL http://link.aps.org/doi/10.1103/PhysRevLett.84.806.

[57] Alberto Amo, Jrme Lefrre, Simon Pigeon, Claire Adrados, Cristiano Ciuti, Iacopo Carusotto, Romuald Houdr, Elisabeth Giacobino, and Alberto Bramati. Superfluidity of polaritons in semiconductor microcavities. *Nat Phys*, 5(11): 805–810, November 2009. ISSN 1745-2473. doi: 10.1038/nphys1364. URL http://www.nature.com/nphys/journal/v5/n11/abs/nphys1364.html.

[58] A. Amo, D. Sanvitto, F. P. Laussy, D. Ballarini, E. del Valle, M. D. Martin, A. Lematre, J. Bloch, D. N. Krizhanovskii, M. S. Skolnick, C. Tejedor, and L. Via. Collective fluid dynamics of a polariton condensate in a semiconductor microcavity. *Nature*, 457(7227):291–295, January 2009. ISSN 0028-0836. doi: 10.1038/nature07640. URL http://www.nature.com/nature/journal/v457/n7227/full/nature07640.html.

[59] K. G. Lagoudakis, M. Wouters, M. Richard, A. Baas, I. Carusotto, R. Andr, Le Si Dang, and B. Deveaud-Pldran. Quantized vortices in an excitonpolariton condensate. *Nat Phys*, 4(9):706–710, September 2008. ISSN 1745-2473. doi: 10.1038/nphys1051. URL http://www.nature.com/nphys/journal/v4/n9/full/nphys1051.html#B9.

[60] K. G. Lagoudakis, T. Ostatnick, A. V. Kavokin, Y. G. Rubo, R. Andr, and B. Deveaud-Pldran. Observation of Half-Quantum Vortices in an Exciton-Polariton Condensate. *Science*, 326(5955):974–976, November 2009. ISSN 0036-8075, 1095-9203. doi: 10.1126/science.1177980. URL http://www.sciencemag.org/content/326/5955/974.

[61] D. Sanvitto, F. M. Marchetti, M. H. Szymaska, G. Tosi, M. Baudisch, F. P. Laussy, D. N. Krizhanovskii, M. S. Skolnick, L. Marrucci, A. Lematre, J. Bloch, C. Tejedor, and L. Via. Persistent currents and quantized vortices in a polariton superfluid. *Nat Phys*, 6(7):527–533, July 2010. ISSN 1745-2473. doi: 10.1038/nphys1668. URL http://www.nature.com/nphys/journal/v6/n7/abs/nphys1668.html.

[62] Georgios Roumpos, Michael D. Fraser, Andreas Lffler, Sven Hfling, Alfred Forchel, and Yoshihisa Yamamoto. Single vortex-antivortex pair in an exciton-polariton condensate. *Nat Phys*, 7(2):129–133, February 2011. ISSN 1745-2473.

doi: 10.1038/nphys1841. URL http://www.nature.com/nphys/journal/v7/n2/full/nphys1841.html.

[63] Sunil Vyas P. Senthilkumaran. Two dimensional vortex lattices from pure wavefront tilts. *Opt Commun*, 283:2767–2771, 2010. URL http://202.114.89.42/resource/pdf/5496.pdf.

[64] Gary Ruben and David M. Paganin. Phase vortices from a youngs three-pinhole interferometer. *Phys. Rev. E*, 75(6):066613, June 2007. doi: 10.1103/PhysRevE.75.066613. URL http://link.aps.org/doi/10.1103/PhysRevE.75.066613.

[65] G. A. El, A. Gammal, and A. M. Kamchatnov. Oblique dark solitons in supersonic flow of a bose-einstein condensate. *Phys. Rev. Lett.*, 97:180405, Nov 2006. doi: 10.1103/PhysRevLett.97.180405. URL http://link.aps.org/doi/10.1103/PhysRevLett.97.180405.

[66] K. V. Kavokin, I. A. Shelykh, A. V. Kavokin, G. Malpuech, and P. Bigenwald. Quantum theory of spin dynamics of exciton-polaritons in microcavities. *Phys. Rev. Lett.*, 92(1):017401, January 2004. doi: 10.1103/PhysRevLett.92.017401. URL http://link.aps.org/doi/10.1103/PhysRevLett.92.017401.

[67] I. Shelykh, K. V. Kavokin, A. V. Kavokin, G. Malpuech, P. Bigenwald, H. Deng, G. Weihs, and Y. Yamamoto. Semiconductor microcavity as a spin-dependent optoelectronic device. *Phys. Rev. B*, 70(3):035320, July 2004. doi: 10.1103/PhysRevB.70.035320. URL http://link.aps.org/doi/10.1103/PhysRevB.70.035320.

[68] I. A. Shelykh, A. V. Kavokin, and G. Malpuech. Spin dynamics of exciton polaritons in microcavities. *phys. stat. sol. (b)*, 242(11):2271–2289, September 2005. ISSN 1521-3951. doi: 10.1002/pssb.200560965. URL http://onlinelibrary.wiley.com/doi/10.1002/pssb.200560965/abstract.

[69] I. A. Shelykh, T. C. H. Liew, and A. V. Kavokin. Spin rings in semiconductor microcavities. *Phys. Rev. Lett.*, 100(11):116401, March 2008. doi: 10.1103/PhysRevLett.100.116401. URL http://link.aps.org/doi/10.1103/PhysRevLett.100.116401.

[70] T. C. H. Liew, A. V. Kavokin, and I. A. Shelykh. Optical circuits based on polariton neurons in semiconductor microcavities. *Phys. Rev. Lett.*, 101(1):016402,

July 2008. doi: 10.1103/PhysRevLett.101.016402. URL http://link.aps.org/doi/10.1103/PhysRevLett.101.016402.

[71] A. Amo, T. C. H. Liew, C. Adrados, R. Houdr, E. Giacobino, A. V. Kavokin, and A. Bramati. Excitonpolariton spin switches. *Nature Photon.*, 4(6):361–366, 2010. ISSN 1749-4885. doi: 10.1038/nphoton.2010.79. URL http://www.nature.com/nphoton/journal/v4/n6/full/nphoton.2010.79.html.

[72] Alberto Bramati and Michele Modugno. *Physics of Quantum Fluids: New Trends and Hot Topics in Atomic and Polariton Condensates*. Springer Science & Business Media, July 2013. ISBN 9783642375699.

[73] Mark Steger, Gangqiang Liu, Bryan Nelsen, Chitra Gautham, David W. Snoke, Ryan Balili, Loren Pfeiffer, and Ken West. Long-range ballistic motion and coherent flow of long-lifetime polaritons. *Phys. Rev. B*, 88(23):235314, December 2013. doi: 10.1103/PhysRevB.88.235314. URL http://link.aps.org/doi/10.1103/PhysRevB.88.235314.

[74] Daniele Bajoni, Pascale Senellart, Aristide Lemaitre, and Jacqueline Bloch. Photon lasing in gaas microcavity: Similarities with a polariton condensate. *Phys. Rev. B*, 76:201305, Nov 2007. doi: 10.1103/PhysRevB.76.201305. URL http://link.aps.org/doi/10.1103/PhysRevB.76.201305.

[75] Neil W. Ashcroft and N. David Mermin. *Solid State Physics*. Holt, Rinehart and Winston, 1976. ISBN 9780030839931.

[76] V.M. Agranovich and G.F. Bassani. *Electronic Excitations in Organic Based Nanostructures*. Academic Press, November 2003. ISBN 9780080519210.

[77] Alexey Kavokin, Jeremy J. Baumberg, Guillaume Malpuech, and Fabrice P. Laussy. *Microcavities*. Series on Semiconductor Science and Technology 16, December 2007. ISBN 978-0-19-922894-2.

[78] Efthimios Kaxiras. *Atomic and Electronic Structure of Solids*. Cambridge University Press, January 2003. ISBN 9780521523394.

[79] Nigel E. Hussey. Strongly correlated electrons: Landau theory takes a pounding. *Nat Phys*, 3(7):445–446, July 2007. ISSN 1745-2473. doi: 10.1038/nphys666. URL http://www.nature.com/nphys/journal/v3/n7/full/nphys666.html.

[80] J. Frenkel. On the transformation of light into heat in solids. II. *Phys. Rev.*, 37 (10):1276–1294, May 1931. doi: 10.1103/PhysRev.37.1276. URL http://link.aps.org/doi/10.1103/PhysRev.37.1276.

[81] Gregory H. Wannier. The structure of electronic excitation levels in insulating crystals. *Phys. Rev.*, 52(3):191–197, August 1937. doi: 10.1103/PhysRev.52.191. URL http://link.aps.org/doi/10.1103/PhysRev.52.191.

[82] N. F. Mott. Conduction in polar crystals. II. the conduction band and ultra-violet absorption of alkali-halide crystals. *Trans. Faraday Soc.*, 34(0):500–506, January 1938. ISSN 0014-7672. doi: 10.1039/TF9383400500. URL http://pubs.rsc.org/en/content/articlelanding/1938/tf/tf9383400500.

[83] Svtoslav Anatol'evi Moskalenko and D. W. Snoke. *Bose-Einstein Condensation of Excitons and Biexcitons: And Coherent Nonlinear Optics with Excitons*. Cambridge University Press, February 2000. ISBN 9780521580991.

[84] Fedor T. Vasko and Alex V. Kuznetsov. *Electronic States and Optical Transitions in Semiconductor Heterostructures*. Springer Science & Business Media, January 1999. ISBN 9780387985671.

[85] T. Kazimierczuk, D. Frohlich, S. Scheel, H. Stolz, and M. Bayer. Giant rydberg excitons in the copper oxide cu2o. *Nature*, 514(7522):343–347, October 2014. ISSN 0028-0836. URL http://dx.doi.org/10.1038/nature13832.

[86] Sven Hofling and Alexey Kavokin. Solid-state physics: A historic experiment redesigned. *Nature*, 514(7522):313–314, October 2014. ISSN 0028-0836. URL http://dx.doi.org/10.1038/514313a.

[87] M. Bugajski and K. Regiski. Optical properties of semiconductor quantum wells. *Opto-electronics Review*, 1996(3-4):83–100, 1996. URL http://www.scopus.com/inward/record.url?eid=2-s2.0-3142563149&partnerID=40&md5=553c0f9ce44b4cc03605d18839838ff7. cited By 1.

[88] Alexey Kavokin, Jeremy J. Baumberg, Guillaume Malpuech, and Fabrice P. Laussy. *Microcavities*. Oxford University Press, May 2011. ISBN 9780199602278.

[89] Kerry J. Vahala. Optical microcavities. *Nature*, 424(6950):839–846, August 2003. ISSN 0028-0836. doi: 10.1038/nature01939. URL http://www.nature.com/nature/journal/v424/n6950/abs/nature01939.html.

[90] V. Savona, L.C. Andreani, P. Schwendimann, and A. Quattropani. Quantum well excitons in semiconductor microcavities: Unified treatment of weak and strong coupling regimes. *Solid State Communications*, 93(9):733 – 739, 1995. ISSN 0038-1098. doi: http://dx.doi.org/10.1016/0038-1098(94)00865-5. URL http://www.sciencedirect.com/science/article/pii/0038109894008655.

[91] D. M. Whittaker, P. Kinsler, T. A. Fisher, M. S. Skolnick, A. Armitage, A. M. Afshar, M. D. Sturge, and J. S. Roberts. Motional narrowing in semiconductor microcavities. *Phys. Rev. Lett.*, 77:4792–4795, Dec 1996. doi: 10.1103/PhysRevLett.77.4792. URL http://link.aps.org/doi/10.1103/PhysRevLett.77.4792.

[92] Jonathan R. Tischler, M. Scott Bradley, Qiang Zhang, Tolga Atay, Arto Nurmikko, and Vladimir Bulovi. Solid state cavity QED: Strong coupling in organic thin films. *Organic Electronics*, 8(23):94–113, April 2007. ISSN 1566-1199. doi: 10.1016/j.orgel.2007.01.008. URL http://www.sciencedirect.com/science/article/pii/S1566119907000079.

[93] Y. Yamamoto, F. Tassone, and H. Cao. *Semiconductor Cavity Quantum Electrodynamics*. Springer Science & Business Media, September 2000. ISBN 9783540675204.

[94] P. Trm and W. L. Barnes. Strong coupling between surface plasmon polaritons and emitters: a review. *Rep. Prog. Phys.*, 78(1):013901, January 2015. ISSN 0034-4885. doi: 10.1088/0034-4885/78/1/013901. URL http://iopscience.iop.org/0034-4885/78/1/013901.

[95] V. Savona, C. Piermarocchi, A. Quattropani, P. Schwendimann, and F. Tassone. Optical properties of microcavity polaritons. *Phase Transit.*, 68(1):169–279, 1999. ISSN 0141-1594. doi: 10.1080/01411599908224518. WOS:000079806400007.

[96] Robert Johne. *Strong light matter coupling in semiconductor nanostructures. Nonlinear effects and applications*. Phd thesis, Université Blaise Pascal - Clermont-Ferrand II, September 2009. URL https://tel.archives-ouvertes.fr/tel-00725283.

[97] J. J. Hopfield. Theory of the contribution of excitons to the complex dielectric constant of crystals. *Phys. Rev.*, 112:1555–1567, Dec 1958. doi: 10.1103/PhysRev.112.1555. URL http://link.aps.org/doi/10.1103/PhysRev.112.1555.

[98] Alexey Kavokin and Guillaume Malpuech. *Cavity Polaritons*. Academic Press, November 2003. ISBN 9780080481371.

[99] C. Piermarocchi, F. Tassone, V. Savona, A. Quattropani, and P. Schwendimann. Exciton formation rates in gaas/al$_x$ga$_{1-x}$as quantum wells. *Phys. Rev. B*, 55:1333–1336, Jan 1997. doi: 10.1103/PhysRevB.55.1333. URL http://link.aps.org/doi/10.1103/PhysRevB.55.1333.

[100] M. Umlauff, J. Hoffmann, H. Kalt, W. Langbein, J. M. Hvam, M. Scholl, J. Söllner, M. Heuken, B. Jobst, and D. Hommel. Direct observation of free-exciton thermalization in quantum-well structures. *Phys. Rev. B*, 57:1390–1393, Jan 1998. doi: 10.1103/PhysRevB.57.1390. URL http://link.aps.org/doi/10.1103/PhysRevB.57.1390.

[101] F. Tassone, C. Piermarocchi, V. Savona, A. Quattropani, and P. Schwendimann. Bottleneck effects in the relaxation and photoluminescence of microcavity polaritons. *Phys. Rev. B*, 56:7554–7563, Sep 1997. doi: 10.1103/PhysRevB.56.7554. URL http://link.aps.org/doi/10.1103/PhysRevB.56.7554.

[102] Gabriela Slavcheva and Philippe Roussignol. *Optical Generation and Control of Quantum Coherence in Semiconductor Nanostructures*. Springer Science & Business Media, June 2010. ISBN 9783642124914.

[103] F. Tassone and Y. Yamamoto. Exciton-exciton scattering dynamics in a semiconductor microcavity and stimulated scattering into polaritons. *Phys. Rev. B*, 59:10830–10842, Apr 1999. doi: 10.1103/PhysRevB.59.10830. URL http://link.aps.org/doi/10.1103/PhysRevB.59.10830.

[104] D. Porras, C. Ciuti, J. J. Baumberg, and C. Tejedor. Polariton dynamics and bose-einstein condensation in semiconductor microcavities. *Phys. Rev. B*, 66:085304, Aug 2002. doi: 10.1103/PhysRevB.66.085304. URL http://link.aps.org/doi/10.1103/PhysRevB.66.085304.

[105] M. S Skolnick, R. M Stevenson, A. I Tartakovskii, R Butt, M Emam-Ismail, D. M Whittaker, P. G Savvidis, J. J Baumberg, A Lematre, V. N Astratov,

and J. S Roberts. Polaritonpolariton interactions and stimulated scattering in semiconductor microcavities. *Materials Science and Engineering: C*, 19(12):407–416, January 2002. ISSN 0928-4931. doi: 10.1016/S0928-4931(01)00433-7. URL http://www.sciencedirect.com/science/article/pii/S0928493101004337.

[106] H.-J. Miesner, D. M. Stamper-Kurn, M. R. Andrews, D. S. Durfee, S. Inouye, and W. Ketterle. Bosonic Stimulation in the Formation of a Bose-Einstein Condensate. *Science*, 279(5353):1005–1007, February 1998. ISSN 0036-8075, 1095-9203. doi: 10.1126/science.279.5353.1005. URL http://www.sciencemag.org/content/279/5353/1005.

[107] I. A. Shelykh, A. V. Kavokin, Yuri G. Rubo, T. C. H. Liew, and G. Malpuech. Polariton polarization-sensitive phenomena in planar semiconductor microcavities. *Semicond. Sci. Technol.*, 25(1):013001, January 2010. ISSN 0268-1242. doi: 10.1088/0268-1242/25/1/013001. URL http://iopscience.iop.org/0268-1242/25/1/013001.

[108] Mikhail I. Dyakonov. *Spin Physics in Semiconductors*. Springer Science & Business Media, July 2008. ISBN 9783540788201.

[109] M. M. Glazov, M. A. Semina, E. Ya. Sherman, and A. V. Kavokin. Spin noise of exciton polaritons in microcavities. *Phys. Rev. B*, 88:041309, Jul 2013. doi: 10.1103/PhysRevB.88.041309. URL http://link.aps.org/doi/10.1103/PhysRevB.88.041309.

[110] K. V. Kavokin, I. A. Shelykh, A. V. Kavokin, G. Malpuech, and P. Bigenwald. Quantum theory of spin dynamics of exciton-polaritons in microcavities. *Phys. Rev. Lett.*, 92:017401, Jan 2004. doi: 10.1103/PhysRevLett.92.017401. URL http://link.aps.org/doi/10.1103/PhysRevLett.92.017401.

[111] Bose. Plancks Gesetz und Lichtquantenhypothese. *Z. Physik*, 26(1):178–181, December 1924. ISSN 0044-3328. doi: 10.1007/BF01327326. URL http://link.springer.com/article/10.1007/BF01327326.

[112] Einstein. Quantentheorie des einatomigen idealen gases. *Sitzungsberichte der Preussischen Akademie der Wissenschaften, Physikalisch-mathematische Klasse*, K1(1):261–267, 1924. URL http://echo.mpiwg-berlin.mpg.de/ECHOdocuView?url=/permanent/echo/einstein/sitzungsberichte/PG8B073X/index.meta.

[113] M. H. Anderson, J. R. Ensher, M. R. Matthews, C. E. Wieman, and E. A. Cornell. Observation of Bose-Einstein Condensation in a Dilute Atomic Vapor. *Science*, 269(5221):198–201, July 1995. ISSN 0036-8075, 1095-9203. doi: 10.1126/science.269.5221.198. URL http://www.sciencemag.org/content/269/5221/198.

[114] *Notes from the course 'Complements of Structure of Matter' - Prof. Matteo Ferrari.*, 2009.

[115] Mark Fox. *Quantum Optics : An Introduction: An Introduction*. Oxford University Press, April 2006. ISBN 9780191524257.

[116] Lev P. Pitaevskii and Sandro Stringari. *Bose-Einstein Condensation*. Clarendon Press | International Series of Monographs on Physics 116, April 2003. ISBN 978-0-19-850719-2.

[117] Vincenzo Savona and Davide Sarchi. BoseEinstein condensation of microcavity polaritons. *phys. stat. sol. (b)*, 242(11):2290–2301, September 2005. ISSN 1521-3951. doi: 10.1002/pssb.200560964. URL http://onlinelibrary.wiley.com/doi/10.1002/pssb.200560964/abstract.

[118] W. Ketterle, D. S Durfee, and D. M Stamper-Kurn. Making, probing and understanding Bose-Einstein condensates. *cond-mat/9904034*, April 1999. URL http://arxiv.org/abs/cond-mat/9904034.

[119] J. Kasprzak, D. D. Solnyshkov, R. André, Le Si Dang, and G. Malpuech. Formation of an exciton polariton condensate: Thermodynamic versus kinetic regimes. *Phys. Rev. Lett.*, 101:146404, Oct 2008. doi: 10.1103/PhysRevLett.101.146404. URL http://link.aps.org/doi/10.1103/PhysRevLett.101.146404.

[120] Benot Deveaud, Antonio Quattropani, and Paolo Schwendimann. *Quantum Coherence in Solid State Systems*. IOS Press, January 2009. ISBN 9781607500391.

[121] Michiel Wouters, Iacopo Carusotto, and Cristiano Ciuti. Spatial and spectral shape of inhomogeneous nonequilibrium exciton-polariton condensates. *Phys. Rev. B*, 77:115340, Mar 2008. doi: 10.1103/PhysRevB.77.115340. URL http://link.aps.org/doi/10.1103/PhysRevB.77.115340.

[122] Iacopo Carusotto and Cristiano Ciuti. Quantum fluids of light. *Rev. Mod. Phys.*, 85(1):299–366, February 2013. doi: 10.1103/RevModPhys.85.299. URL http://link.aps.org/doi/10.1103/RevModPhys.85.299.

[123] Franco Dalfovo, Stefano Giorgini, Lev P. Pitaevskii, and Sandro Stringari. Theory of bose-einstein condensation in trapped gases. *Rev. Mod. Phys.*, 71:463–512, Apr 1999. doi: 10.1103/RevModPhys.71.463. URL http://link.aps.org/doi/10.1103/RevModPhys.71.463.

[124] P. G. Kevrekidis, D. J. Frantzeskakis, and R. Carretero-Gonzlez. Basic Mean-Field Theory for Bose-Einstein Condensates. In Professor Panayotis G. Kevrekidis, Professor Dimitri J. Frantzeskakis, and Professor Ricardo Carretero-Gonzlez, editors, *Emergent Nonlinear Phenomena in Bose-Einstein Condensates*, number 45 in Atomic, Optical, and Plasma Physics, pages 3–21. Springer Berlin Heidelberg, 2008. ISBN 978-3-540-73590-8, 978-3-540-73591-5. URL http://link.springer.com/chapter/10.1007/978-3-540-73591-5_1.

[125] R.N. Silver. Superfluid helium and neutron scattering, a new chapter in the condensate saga. *Los Almos Scienc*, 19:158–179, Jul 1990. doi: 0. URL https://library.lanl.gov/cgi-bin/getfile?19-11.pdf.

[126] P. Kapitza. Viscosity of Liquid Helium below the -Point. *Nature*, 141:74–74, January 1938. doi: 10.1038/141074a0. URL http://www.nature.com/nature/journal/v141/n3558/abs/141074a0.html.

[127] J.F. Allen and A.D. Misener. Flow of Liquid Helium II. *Nature*, 141:75–75, January 1938. doi: 10.1038/141075a0. URL http://www.nature.com/nature/journal/v141/n3558/abs/141075a0.html.

[128] F. London. The -Phenomenon of Liquid Helium and the Bose-Einstein Degeneracy : Abstract : Nature. *Nature*, 141:643–644, April 1938. doi: 10.1038/141643a0. URL http://www.nature.com/nature/journal/v141/n3571/abs/141643a0.html.

[129] Jean Dalibard, Bertrand Duplantier, and Vincent Rivasseau. *Poincare Seminar 2003*. Springer Science & Business Media, May 2004. ISBN 9783764371067.

[130] LD Landau. The theory of superfluidity of helium ii. *J. Phys*, 5(1):71–90, 1941. URL http://www.ufn.ru/dates/pdf/j_phys_ussr/j_phys_ussr_1947_11_1/12_landau_j_phys_ussr_1947_11_1_91.pdf.

[131] Allan Griffin, D. W Snoke, and S Stringari. *Bose-Einstein condensation*. Cambridge University Press, Cambridge; New York, 1995. ISBN 0521464730 9780521464734 0521589908 9780521589901.

[132] C. Raman, M. Khl, R. Onofrio, D. S. Durfee, C. E. Kuklewicz, Z. Hadzibabic, and W. Ketterle. Evidence for a Critical Velocity in a Bose-Einstein Condensed Gas. *Phys. Rev. Lett.*, 83(13):2502–2505, September 1999. doi: 10.1103/PhysRevLett.83.2502. URL http://link.aps.org/doi/10.1103/PhysRevLett.83.2502.

[133] A. P. Chikkatur, A. Görlitz, D. M. Stamper-Kurn, S. Inouye, S. Gupta, and W. Ketterle. Suppression and enhancement of impurity scattering in a bose-einstein condensate. *Phys. Rev. Lett.*, 85:483–486, Jul 2000. doi: 10.1103/PhysRevLett.85.483. URL http://link.aps.org/doi/10.1103/PhysRevLett.85.483.

[134] Wolfgang Ketterle and N. J. van Druten. Bose-einstein condensation of a finite number of particles trapped in one or three dimensions. *Phys. Rev. A*, 54:656–660, Jul 1996. doi: 10.1103/PhysRevA.54.656. URL http://link.aps.org/doi/10.1103/PhysRevA.54.656.

[135] N. D. Mermin and H. Wagner. Absence of ferromagnetism or antiferromagnetism in one- or two-dimensional isotropic heisenberg models. *Phys. Rev. Lett.*, 17:1133–1136, Nov 1966. doi: 10.1103/PhysRevLett.17.1133. URL http://link.aps.org/doi/10.1103/PhysRevLett.17.1133.

[136] D. J. Bishop and J. D. Reppy. Study of the superfluid transition in two-dimensional ^{4}He films. *Phys. Rev. Lett.*, 40:1727–1730, Jun 1978. doi: 10.1103/PhysRevLett.40.1727. URL http://link.aps.org/doi/10.1103/PhysRevLett.40.1727.

[137] Rmi Desbuquois, Lauriane Chomaz, Tarik Yefsah, Julian Lonard, Jrme Beugnon, Christof Weitenberg, and Jean Dalibard. Superfluid behaviour of a two-dimensional Bose gas. *Nat Phys*, 8(9):645–648, September 2012. ISSN 1745-2473. doi: 10.1038/nphys2378. URL http://www.nature.com/nphys/journal/v8/n9/full/nphys2378.html#ref3.

[138] Georgios Roumpos, Michael Lohse, Wolfgang H. Nitsche, Jonathan Keeling, Marzena Hanna Szymaska, Peter B. Littlewood, Andreas Lffler, Sven Hfling, Lukas Worschech, Alfred Forchel, and Yoshihisa Yamamoto. Power-law decay of the spatial correlation function in exciton-polariton condensates. *PNAS*, 109(17):6467–6472, April 2012. ISSN 0027-8424, 1091-6490. doi: 10.1073/pnas.1107970109. URL http://www.pnas.org/content/109/17/6467.

[139] R. Balili, V. Hartwell, D. Snoke, L. Pfeiffer, and K. West. Bose-Einstein Condensation of Microcavity Polaritons in a Trap. *Science*, 316(5827):1007–1010, May 2007. ISSN 0036-8075, 1095-9203. doi: 10.1126/science.1140990. URL http://www.sciencemag.org/content/316/5827/1007.

[140] M. Maragkou, A. J. D. Grundy, E. Wertz, A. Lemaître, I. Sagnes, P. Senellart, J. Bloch, and P. G. Lagoudakis. Spontaneous nonground state polariton condensation in pillar microcavities. *Phys. Rev. B*, 81:081307, Feb 2010. doi: 10.1103/PhysRevB.81.081307. URL http://link.aps.org/doi/10.1103/PhysRevB.81.081307.

[141] Gal Nardin, Gabriele Grosso, Yoan Lger, Barbara Pitka, Franois Morier-Genoud, and Benot Deveaud-Pldran. Hydrodynamic nucleation of quantized vortex pairs in a polariton quantum fluid. *Nat Phys*, 7(8):635–641, August 2011. ISSN 1745-2473. doi: 10.1038/nphys1959. URL http://www.nature.com/nphys/journal/v7/n8/full/nphys1959.html.

[142] M. R. Matthews, B. P. Anderson, P. C. Haljan, D. S. Hall, C. E. Wieman, and E. A. Cornell. Vortices in a bose-einstein condensate. *Phys. Rev. Lett.*, 83:2498–2501, Sep 1999. doi: 10.1103/PhysRevLett.83.2498. URL http://link.aps.org/doi/10.1103/PhysRevLett.83.2498.

[143] E. J. Yarmchuk, M. J. V. Gordon, and R. E. Packard. Observation of stationary vortex arrays in rotating superfluid helium. *Phys. Rev. Lett.*, 43:214–217, Jul 1979. doi: 10.1103/PhysRevLett.43.214. URL http://link.aps.org/doi/10.1103/PhysRevLett.43.214.

[144] C. A. M. Castelijns, K. F. Coates, A. M. Guénault, S. G. Mussett, and G. R. Pickett. Landau critical velocity for a macroscopic object moving in superfluid ^3B: Evidence for gap suppression at a moving surface. *Phys. Rev. Lett.*, 56:69–72,

Jan 1986. doi: 10.1103/PhysRevLett.56.69. URL http://link.aps.org/doi/10.1103/PhysRevLett.56.69.

[145] Lothar Meyer and F. Reif. Ion motion in superfluid liquid helium under pressure. *Phys. Rev.*, 123:727–731, Aug 1961. doi: 10.1103/PhysRev.123.727. URL http://link.aps.org/doi/10.1103/PhysRev.123.727.

[146] T. Winiecki, J. F. McCann, and C. S. Adams. Pressure drag in linear and nonlinear quantum fluids. *Phys. Rev. Lett.*, 82:5186–5189, Jun 1999. doi: 10.1103/PhysRevLett.82.5186. URL http://link.aps.org/doi/10.1103/PhysRevLett.82.5186.

[147] T. Frisch, Y. Pomeau, and S. Rica. Transition to dissipation in a model of superflow. *Phys. Rev. Lett.*, 69:1644–1647, Sep 1992. doi: 10.1103/PhysRevLett.69.1644. URL http://link.aps.org/doi/10.1103/PhysRevLett.69.1644.

[148] A. M. Kamchatnov and S. V. Korneev. Oblique solitons generated by the flow of a polariton condensate past an obstacle. *J. Exp. Theor. Phys.*, 115(4):579–585, November 2012. ISSN 1063-7761, 1090-6509. doi: 10.1134/S1063776112080080. URL http://link.springer.com/article/10.1134/S1063776112080080.

[149] Yu. G. Gladush, G. A. El, A. Gammal, and A. M. Kamchatnov. Radiation of linear waves in the stationary flow of a bose-einstein condensate past an obstacle. *Phys. Rev. A*, 75:033619, Mar 2007. doi: 10.1103/PhysRevA.75.033619. URL http://link.aps.org/doi/10.1103/PhysRevA.75.033619.

[150] Mordechai Segev and George Stegeman. Self-trapping of optical beams: Spatial solitons. *Physics Today*, 51(8):42–48, 1998. doi: 10.1063/1.882370. URL http://link.aip.org/link/?PTO/51/42/1.

[151] Zhigang Chen, Mordechai Segev, and Demetrios N Christodoulides. Optical spatial solitons: historical overview and recent advances. *New J. Phys.*, 75(8):086401, August 2012. ISSN 0034-4885, 1361-6633. doi: 10.1088/0034-4885/75/8/086401. URL http://iopscience.iop.org/0034-4885/75/8/086401.

[152] M Hercher. Laser-induced damage in transparent media. *J. Opt. Soc. Am.*, 54: 563, 1964.

[153] Mordechai Segev, Bruno Crosignani, Amnon Yariv, and Baruch Fischer. Spatial solitons in photorefractive media. *Phys. Rev. Lett.*, 68(7):923–926, February 1992. doi: 10.1103/PhysRevLett.68.923. URL http://link.aps.org/doi/10.1103/PhysRevLett.68.923.

[154] K. Hayata and M. Koshiba. Multidimensional solitons in quadratic nonlinear media. *Phys. Rev. Lett.*, 71(20):3275–3278, November 1993. doi: 10.1103/PhysRevLett.71.3275. URL http://link.aps.org/doi/10.1103/PhysRevLett.71.3275.

[155] M. Nakazawa and K. Suzuki. 10 gbit/s pseudorandom dark soliton data transmission over 1200 km. *Electronics Letters*, 31(13):1076–1077, 1995. ISSN 0013-5194. doi: 10.1049/el:19950701.

[156] P. D. Miller. Zero-crosstalk junctions made from dark solitons. *Phys. Rev. E*, 53: 4137–4142, Apr 1996. doi: 10.1103/PhysRevE.53.4137. URL http://link.aps.org/doi/10.1103/PhysRevE.53.4137.

[157] Toshio Tsuzuki. Nonlinear waves in the pitaevskii-gross equation. *J. Low Temp. Phys.*, 4(4):441–457, 1971. ISSN 0022-2291. doi: 10.1007/BF00628744. URL http://www.springerlink.com/content/w576565460h03131/abstract/.

[158] Y.S. Kivshar. Dark solitons in nonlinear optics. *J. Quantum. Electron.*, 29(1):250–264, January 1993. ISSN 0018-9197. doi: 10.1109/3.199266.

[159] A. D. Jackson, G. M. Kavoulakis, and C. J. Pethick. Solitary waves in clouds of bose-einstein condensed atoms. *Phys. Rev. A*, 58:2417–2422, Sep 1998. doi: 10.1103/PhysRevA.58.2417. URL http://link.aps.org/doi/10.1103/PhysRevA.58.2417.

[160] N.N. Bogoliubov. On the theory of superfluidity. *Journal of Physics*, 0:23–32, May 1947. ISSN 0. URL http://ufn.ru/dates/pdf/j_phys_ussr/j_phys_ussr_1947_11_1/3_bogolubov_j_phys_ussr_1947_11_1_23.pdf.

[161] M. R. Andrews, D. M. Kurn, H.-J. Miesner, D. S. Durfee, C. G. Townsend, S. Inouye, and W. Ketterle. Propagation of sound in a bose-einstein condensate. *Phys. Rev. Lett.*, 79:553–556, Jul 1997. doi: 10.1103/PhysRevLett.79.553. URL http://link.aps.org/doi/10.1103/PhysRevLett.79.553.

[162] Iacopo Carusotto and Cristiano Ciuti. Probing microcavity polariton superfluidity through resonant rayleigh scattering. *Phys. Rev. Lett.*, 93:166401, Oct 2004. doi: 10.1103/PhysRevLett.93.166401. URL http://link.aps.org/doi/10.1103/PhysRevLett.93.166401.

[163] Hugo Flayac, Dmitry Solnyshkov, and Guillaume Malpuech. Oblique half-solitons and their generation in exciton-polariton condensates. *Phys. Rev. B*, March 2011. doi: 10.1103/PhysRevB.83.193305. URL http://arxiv.org/abs/1103.4516. H. Flayac, D. D. Solnyshkov, and G. Malpuech, Phys. Rev. B 83, 193305 (2011).

[164] Maxime Richard, Jacek Kasprzak, Robert Romestain, Régis André, and Le Si Dang. Spontaneous coherent phase transition of polaritons in cdte microcavities. *Phys. Rev. Lett.*, 94:187401, May 2005. doi: 10.1103/PhysRevLett.94.187401. URL http://link.aps.org/doi/10.1103/PhysRevLett.94.187401.

[165] Eugene Hecht. *Optics*. Addison-Wesley, 2002. ISBN 9780805385663.

[166] P. Tsotsis, P. S. Eldridge, T. Gao, S. I. Tsintzos, Z. Hatzopoulos, and P. G. Savvidis. Lasing threshold doubling at the crossover from strong to weak coupling regime in GaAs microcavity. *New J. Phys.*, 14(2):023060, February 2012. ISSN 1367-2630. doi: 10.1088/1367-2630/14/2/023060. URL http://iopscience.iop.org/1367-2630/14/2/023060.

[167] J. Fischer, G. Savenko, I. D. Fraser, M. S. Holzinger, S. Brodbeck, M. Kamp, A. Shelykh, I. C. Schneider, and S. Höfling. Spatial coherence properties of one dimensional exciton-polariton condensates. *Phys. Rev. Lett.*, 113:203902, Nov 2014. doi: 10.1103/PhysRevLett.113.203902. URL http://link.aps.org/doi/10.1103/PhysRevLett.113.203902.

[168] M. Gurioli, F. Bogani, D. S. Wiersma, Ph. Roussignol, G. Cassabois, G. Khitrova, and H. Gibbs. Experimental study of disorder in a semiconductor microcavity. *Phys. Rev. B*, 64:165309, Oct 2001. doi: 10.1103/PhysRevB.64.165309. URL http://link.aps.org/doi/10.1103/PhysRevB.64.165309.

[169] Wolfgang Langbein and Jørn M. Hvam. Elastic scattering dynamics of cavity polaritons: Evidence for time-energy uncertainty and polariton localization. *Phys. Rev. Lett.*, 88:047401, Jan 2002. doi: 10.1103/PhysRevLett.88.047401. URL http://link.aps.org/doi/10.1103/PhysRevLett.88.047401.

[170] Wolfgang Langbein. Energy and momentum broadening of planar microcavity polaritons measured by resonant light scattering. *J. Phys.: Condens. Matter*, 16 (35):S3645, September 2004. ISSN 0953-8984. doi: 10.1088/0953-8984/16/35/006. URL http://iopscience.iop.org/0953-8984/16/35/006.

[171] Marco Abbarchi, Carole Diederichs, Ludovic Largeau, Vincenzo Ardizzone, Olivia Mauguin, Timothee Lecomte, Aristide Lemaitre, Jacqueline Bloch, Philippe Roussignol, and Jerome Tignon. Discretized disorder in planar semiconductor microcavities: Mosaicity effect on resonant rayleigh scattering and optical parametric oscillation. *Phys. Rev. B*, 85:045316, Jan 2012. doi: 10.1103/PhysRevB.85.045316. URL http://link.aps.org/doi/10.1103/PhysRevB.85.045316.

[172] Joanna M. Zajac, Edmund Clarke, and Wolfgang Langbein. Suppression of cross-hatched polariton disorder in GaAs/AlAs microcavities by strain compensation. *Applied Physics Letters*, 101(4):041114, July 2012. ISSN 0003-6951, 1077-3118. doi: 10.1063/1.4739245. URL http://scitation.aip.org/content/aip/journal/apl/101/4/10.1063/1.4739245.

[173] R. Houdré, J. L. Gibernon, P. Pellandini, R. P. Stanley, U. Oesterle, C. Weisbuch, J. O'Gorman, B. Roycroft, and M. Ilegems. Saturation of the strong-coupling regime in a semiconductor microcavity: Free-carrier bleaching of cavity polaritons. *Phys. Rev. B*, 52:7810–7813, Sep 1995. doi: 10.1103/PhysRevB.52.7810. URL http://link.aps.org/doi/10.1103/PhysRevB.52.7810.

[174] K. Fujiwara, K. Kanamoto, Y.N. Ohta, Y. Tokuda, and T. Nakayama. Classification and origins of GaAs oval defects grown by molecular beam epitaxy. *Journal of Crystal Growth*, 80(1):104–112, January 1987. ISSN 0022-0248. doi: 10.1016/0022-0248(87)90529-X. URL http://www.sciencedirect.com/science/article/pii/002202488790529X.

[175] Naresh Chand and S.N.G. Chu. A comprehensive study and methods of elimination of oval defects in MBE-GaAs. *Journal of Crystal Growth*, 104(2):485–497, July 1990. ISSN 0022-0248. doi: 10.1016/0022-0248(90)90151-A. URL http://www.sciencedirect.com/science/article/pii/002202489090151A.

[176] A. M. Kamchatnov and L. P. Pitaevskii. Stabilization of solitons generated by a supersonic flow of bose-einstein condensate past an obstacle. *Phys. Rev. Lett.*,

100:160402, Apr 2008. doi: 10.1103/PhysRevLett.100.160402. URL http://link.aps.org/doi/10.1103/PhysRevLett.100.160402.

[177] G. Grosso, G. Nardin, F. Morier-Genoud, Y. Lger, and B. Deveaud-Pldran. Dynamics of dark-soliton formation in a polariton quantum fluid. *Phys. Rev. B*, 86(2):020509, July 2012. doi: 10.1103/PhysRevB.86.020509. URL http://link.aps.org/doi/10.1103/PhysRevB.86.020509.

[178] Wolfgang Langbein. Spontaneous parametric scattering of microcavity polaritons in momentum space. *Phys. Rev. B*, 70:205301, Nov 2004. doi: 10.1103/PhysRevB.70.205301. URL http://link.aps.org/doi/10.1103/PhysRevB.70.205301.

[179] M. V. Berry. *Rays, wavefronts and phase: a picture book of cusps*. Elsevier Science Publishers B.V., Amsterdam, 1992 edition, 1992. URL http://www.phy.bris.ac.uk/people/berry_mv/the_papers/Berry228.pdf.

[180] M. V. Berry, J. F. Nye, and F. J. Wright. The elliptic umbilic diffraction catastrophe. *Philosophical Transactions of the Royal Society of London. Series A, Mathematical and Physical Sciences*, 291(1382):453–484, April 1979. ISSN 0080-4614. doi: 10.2307/75150. URL http://www.jstor.org/stable/75150. ArticleType: research-article / Full publication date: Apr. 12, 1979 / Copyright 1979 The Royal Society.

[181] Joanna Zajac and Wolfgang Langbein. Structure and zero-dimensional polariton spectrum of natural defects in GaAs/AlAs microcavities. *Phys. Rev. B*, 86(19), 2012. doi: 10.1103/PhysRevB.86.195401.

[182] E. Hecht and A. Zajac. *Optics*. Addison-Wesley, 1982.

[183] A. W. Snyder and Love J. D. *Optical Waveguide Theory*. Chapman and Hall, 1983.

[184] G. Tosi, G. Christmann, N. G. Berloff, P. Tsotsis, T. Gao, Z. Hatzopoulos, P. G. Savvidis, and J. J. Baumberg. Sculpting oscillators with light within a nonlinear quantum fluid. *Nat Phys*, 8:190–194, Mar 2012. doi: 10.1038/nphys2182. URL http://dx.doi.org/10.1038/nphys2182.

[185] Mordechai Segev. From the guest editor–solitons: A universal phenomenon of self-trapped wave packets. *Opt. Photon. News*, 13(2):27, Feb 2002. doi: 10.1364/OPN.13.2.000027. URL http://www.osa-opn.org/abstract.cfm?URI=opn-13-2-27.

[186] Giovanna Panzarini, Lucio Claudio Andreani, A. Armitage, D. Baxter, M. S. Skolnick, V. N. Astratov, J. S. Roberts, Alexey V. Kavokin, Maria R. Vladimirova, and M. A. Kaliteevski. Exciton-light coupling in single and coupled semiconductor microcavities: Polariton dispersion and polarization splitting. *Phys. Rev. B*, 59(7):5082–5089, February 1999. doi: 10.1103/PhysRevB.59.5082. URL http://link.aps.org/doi/10.1103/PhysRevB.59.5082.

[187] C. Leyder, M. Romanelli, J. Ph Karr, E. Giacobino, T. C. H. Liew, M. M. Glazov, A. V. Kavokin, G. Malpuech, and A. Bramati. Observation of the optical spin hall effect. *Nature Physics*, 3(9):628–631, 2007. ISSN 1745-2473. doi: 10.1038/nphys676. URL http://www.nature.com/nphys/journal/v3/n9/full/nphys676.html.

[188] Maria Maragkou, Caryl E. Richards, Tomas Ostatnick, Alastair J. D. Grundy, Joanna Zajac, Maxime Hugues, Wolfgang Langbein, and Pavlos G. Lagoudakis. Optical analogue of the spin hall effect in a photonic cavity. *Opt. Lett.*, 36(7):1095–1097, April 2011. doi: 10.1364/OL.36.001095. URL http://ol.osa.org/abstract.cfm?URI=ol-36-7-1095.

[189] Usama Al Khawaja and Henk Stoof. Skyrmions in a ferromagnetic bose-einstein condensate. *Nature*, 411(6840):918–920, June 2001. ISSN 0028-0836. doi: 10.1038/35082010. URL http://www.nature.com/nature/journal/v411/n6840/abs/411918a0.html.

[190] C. Adrados, A. Amo, T. C. H. Liew, R. Hivet, R. Houdr, E. Giacobino, A. V. Kavokin, and A. Bramati. Spin rings in bistable planar semiconductor microcavities. *Phys. Rev. Lett.*, 105(21):216403, November 2010. doi: 10.1103/PhysRevLett.105.216403. URL http://link.aps.org/doi/10.1103/PhysRevLett.105.216403.

[191] A. V. Sekretenko, S. S. Gavrilov, S. I. Novikov, V. D. Kulakovskii, S. Hfling, C. Schneider, M. Kamp, and A. Forchel. Spin and density patterns of polariton condensates resonantly excited in strained planar microcavities with a nonuniform potential landscape. *Phys. Rev. B*, 88(20):205302, November 2013. doi: 10.1103/

PhysRevB.88.205302. URL http://link.aps.org/doi/10.1103/PhysRevB.88.205302.

[192] P. G. Lagoudakis, P. G. Savvidis, J. J. Baumberg, D. M. Whittaker, P. R. Eastham, M. S. Skolnick, and J. S. Roberts. Stimulated spin dynamics of polaritons in semiconductor microcavities. *Phys. Rev. B*, 65(16):161310, April 2002. doi: 10.1103/PhysRevB.65.161310. URL http://link.aps.org/doi/10.1103/PhysRevB.65.161310.

[193] Michiel Wouters, Iacopo Carusotto, and Cristiano Ciuti. Spatial and spectral shape of inhomogeneous nonequilibrium exciton-polariton condensates. *Phys. Rev. B*, 77(11):115340, March 2008. doi: 10.1103/PhysRevB.77.115340. URL http://link.aps.org/doi/10.1103/PhysRevB.77.115340.

[194] E. Wertz, L. Ferrier, D. D. Solnyshkov, R. Johne, D. Sanvitto, A. Lematre, I. Sagnes, R. Grousson, A. V. Kavokin, P. Senellart, G. Malpuech, and J. Bloch. Spontaneous formation and optical manipulation of extended polariton condensates. *Nature Phys.*, 6(11):860–864, 2010. ISSN 1745-2473. doi: 10.1038/nphys1750. URL http://www.nature.com/nphys/journal/v6/n11/full/nphys1750.html.

[195] M. Z. Maialle, E. A. de Andrada e Silva, and L. J. Sham. Exciton spin dynamics in quantum wells. *Phys. Rev. B*, 47(23):15776–15788, June 1993. doi: 10.1103/PhysRevB.47.15776. URL http://link.aps.org/doi/10.1103/PhysRevB.47.15776.

[196] Elena Kammann. *On the dynamics of spinor condensates in microcavities*. Phd thesis, University of Southampton, January 2013. URL http://eprints.soton.ac.uk/347528/.

[197] M. Vladimirova, S. Cronenberger, D. Scalbert, K. V. Kavokin, A. Miard, A. Lemaitre, J. Bloch, D. Solnyshkov, G. Malpuech, and A. V. Kavokin. Polariton-polariton interaction constants in microcavities. *Phys. Rev. B*, 82:075301, Aug 2010. doi: 10.1103/PhysRevB.82.075301. URL http://link.aps.org/doi/10.1103/PhysRevB.82.075301.

[198] N. Takemura, S. Trebaol, M. Wouters, M. T. Portella-Oberli, and B. Deveaud. Heterodyne spectroscopy of polariton spinor interactions. *Phys. Rev. B*, 90:195307,

Nov 2014. doi: 10.1103/PhysRevB.90.195307. URL http://link.aps.org/doi/10.1103/PhysRevB.90.195307.

[199] H. Ohadi, E. Kammann, T. C. H. Liew, K. G. Lagoudakis, A. V. Kavokin, and P. G. Lagoudakis. Spontaneous symmetry breaking in a polariton and photon laser. *Phys. Rev. Lett.*, 109:016404, Jul 2012. doi: 10.1103/PhysRevLett.109.016404. URL http://link.aps.org/doi/10.1103/PhysRevLett.109.016404.

[200] W. Langbein, I. Shelykh, D. Solnyshkov, G. Malpuech, Yu. Rubo, and A. Kavokin. Polarization beats in ballistic propagation of exciton-polaritons in microcavities. *Phys. Rev. B*, 75(7):075323, February 2007. doi: 10.1103/PhysRevB.75.075323. URL http://link.aps.org/doi/10.1103/PhysRevB.75.075323.

[201] Shuichi Murakami, Naoto Nagaosa, and Shou-Cheng Zhang. Dissipationless quantum spin current at room temperature. *Science*, 301(5638):1348–1351, September 2003. ISSN 0036-8075, 1095-9203. doi: 10.1126/science.1087128. URL http://www.sciencemag.org/content/301/5638/1348.

[202] Wolfgang Langbein and Jørn M. Hvam. Elastic scattering dynamics of cavity polaritons: Evidence for time-energy uncertainty and polariton localization. *Phys. Rev. Lett.*, 88:047401, Jan 2002. doi: 10.1103/PhysRevLett.88.047401. URL http://link.aps.org/doi/10.1103/PhysRevLett.88.047401.

[203] B. Richards and E. Wolf. Electromagnetic Diffraction in Optical Systems. II. Structure of the Image Field in an Aplanatic System. *Proceedings of the Royal Society of London A: Mathematical, Physical and Engineering Sciences*, 253(1274): 358–379, December 1959. ISSN 0080-4630. doi: 10.1098/rspa.1959.0200. URL http://rspa.royalsocietypublishing.org/content/253/1274/358.

[204] John Lekner. Polarization of tightly focused laser beams. *J. Opt. A: Pure Appl. Opt.*, 5(1):6, January 2003. ISSN 1464-4258. doi: 10.1088/1464-4258/5/1/302. URL http://iopscience.iop.org/1464-4258/5/1/302.

[205] Ralf Dorn, Susanne Quabis, and Gerd Leuchs. The focus of lightlinear polarization breaks the rotational symmetry of the focal spot. *Journal of Modern Optics*, 50 (12):1917–1926, August 2003. ISSN 0950-0340. doi: 10.1080/09500340308235246. URL http://dx.doi.org/10.1080/09500340308235246.

[206] Ziyang Chen, Limin Hua, and Jixiong Pu. Chapter 4 - Tight Focusing of Light Beams: Effect of Polarization, Phase, and Coherence. In Emil Wolf, editor, *Progress in Optics*, volume 57 of *Progress in Optics*, pages 219–260. Elsevier, 2012. URL http://www.sciencedirect.com/science/article/pii/B9780444594228000047.

[207] C. Antón, T. C. H. Liew, G. Tosi, M. D. Martín, T. Gao, Z. Hatzopoulos, P. S. Eldridge, P. G. Savvidis, and L. Viña. Energy relaxation of exciton-polariton condensates in quasi-one-dimensional microcavities. *Phys. Rev. B*, 88:035313, Jul 2013. doi: 10.1103/PhysRevB.88.035313. URL http://link.aps.org/doi/10.1103/PhysRevB.88.035313.

[208] P. Renucci, T. Amand, X. Marie, P. Senellart, J. Bloch, B. Sermage, and K. V. Kavokin. Microcavity polariton spin quantum beats without a magnetic field: A manifestation of coulomb exchange in dense and polarized polariton systems. *Phys. Rev. B*, 72:075317, Aug 2005. doi: 10.1103/PhysRevB.72.075317. URL http://link.aps.org/doi/10.1103/PhysRevB.72.075317.

[209] M. D. Martin, G. Aichmayr, L. Viña, and R. Andr. Polarization control of the nonlinear emission of semiconductor microcavities. *Phys. Rev. Lett.*, 89:077402, Jul 2002. doi: 10.1103/PhysRevLett.89.077402. URL http://link.aps.org/doi/10.1103/PhysRevLett.89.077402.

[210] Hiroki Saito, Yuki Kawaguchi, and Masahito Ueda. Breaking of chiral symmetry and spontaneous rotation in a spinor bose-einstein condensate. *Phys. Rev. Lett.*, 96:065302, Feb 2006. doi: 10.1103/PhysRevLett.96.065302. URL http://link.aps.org/doi/10.1103/PhysRevLett.96.065302.

[211] A. Amo, T. C. H. Liew, C. Adrados, E. Giacobino, A. V. Kavokin, and A. Bramati. Anisotropic optical spin hall effect in semiconductor microcavities. *Phys. Rev. B*, 80:165325, Oct 2009. doi: 10.1103/PhysRevB.80.165325. URL http://link.aps.org/doi/10.1103/PhysRevB.80.165325.

[212] A. A. High, A. T. Hammack, J. R. Leonard, Sen Yang, L. V. Butov, T. Ostatnický, M. Vladimirova, A. V. Kavokin, T. C. H. Liew, K. L. Campman, and A. C. Gossard. Spin currents in a coherent exciton gas. *Phys. Rev. Lett.*, 110:246403,

Jun 2013. doi: 10.1103/PhysRevLett.110.246403. URL http://link.aps.org/doi/10.1103/PhysRevLett.110.246403.

[213] D. Sanvitto, S. Pigeon, A. Amo, D. Ballarini, M. De Giorgi, I. Carusotto, R. Hivet, F. Pisanello, V. G. Sala, P. S. S. Guimaraes, R. Houdr, E. Giacobino, C. Ciuti, A. Bramati, and G. Gigli. All-optical control of the quantum flow of a polariton condensate. *Nat Photon*, 5(10):610–614, October 2011. ISSN 1749-4885. doi: 10.1038/nphoton.2011.211. URL http://www.nature.com/nphoton/journal/v5/n10/full/nphoton.2011.211.html.

[214] A. Askitopoulos, H. Ohadi, A. V. Kavokin, Z. Hatzopoulos, P. G. Savvidis, and P. G. Lagoudakis. Polariton condensation in an optically induced two-dimensional potential. *Phys. Rev. B*, 88(4):041308, July 2013. doi: 10.1103/PhysRevB.88.041308. URL http://link.aps.org/doi/10.1103/PhysRevB.88.041308.

[215] Elena Kammann, Hamid Ohadi, Maria Maragkou, Alexey V. Kavokin, and Pavlos G. Lagoudakis. Crossover from photon to exciton-polariton lasing. *New J. Phys.*, 14(10):105003, October 2012. ISSN 1367-2630. doi: 10.1088/1367-2630/14/10/105003. URL http://iopscience.iop.org/1367-2630/14/10/105003.

[216] Maurice G. A. Bernard and Georges Duraffourg. Laser Conditions in Semiconductors. *phys. stat. sol. (b)*, 1(7):699–703, January 1961. ISSN 1521-3951. doi: 10.1002/pssb.19610010703. URL http://onlinelibrary.wiley.com/doi/10.1002/pssb.19610010703/abstract.

[217] D. Ballarini, M. De Giorgi, E. Cancellieri, R. Houdr, E. Giacobino, R. Cingolani, A. Bramati, G. Gigli, and D. Sanvitto. All-optical polariton transistor. *Nat Commun*, 4:1778, April 2013. doi: 10.1038/ncomms2734. URL http://www.nature.com/ncomms/journal/v4/n4/full/ncomms2734.html.

[218] R. Cerna, Y. Lger, T. K. Paraso, M. Wouters, F. Morier-Genoud, M. T. Portella-Oberli, and B. Deveaud. Ultrafast tristable spin memory of a coherent polariton gas. *Nat Commun*, 4, June 2013. doi: 10.1038/ncomms3008. URL http://www.nature.com/ncomms/2013/130613/ncomms3008/full/ncomms3008.html.

[219] C. Antón, S. Morina, T. Gao, P. S. Eldridge, T. C. H. Liew, M. D. Martín, Z. Hatzopoulos, P. G. Savvidis, I. A. Shelykh, and L. Viña. Optical control of spin textures in quasi-one-dimensional polariton condensates. *Phys. Rev. B*, 91:075305,

Feb 2015. doi: 10.1103/PhysRevB.91.075305. URL http://link.aps.org/doi/10.1103/PhysRevB.91.075305.

[220] Liesbeth Venema. Silicon electronics and beyond. *Nature*, 479(7373):309–309, November 2011. ISSN 0028-0836. doi: 10.1038/479309a. URL http://www.nature.com/nature/journal/v479/n7373/full/479309a.html.

[221] H. Ohadi, R. L. Gregory, T. Freegarde, Y. G. Rubo, A. V. Kavokin, and P. G. Lagoudakis. Dissipative phase locking of exciton-polariton condensates. *arXiv:1406.6377 [cond-mat]*, June 2014. URL http://arxiv.org/abs/1406.6377. arXiv: 1406.6377.

[222] David Snoke. Polariton condensates: A feature rather than a bug. *Nat Phys*, 4 (9):673–673, September 2008. ISSN 1745-2473. doi: 10.1038/nphys1064. URL http://www.nature.com/nphys/journal/v4/n9/full/nphys1064.html.

[223] I. M. Georgescu, S. Ashhab, and Franco Nori. Quantum simulation. *Rev. Mod. Phys.*, 86:153–185, Mar 2014. doi: 10.1103/RevModPhys.86.153. URL http://link.aps.org/doi/10.1103/RevModPhys.86.153.

[224] Richard P. Feynman. Simulating physics with computers. *Int J Theor Phys*, 21 (6-7):467–488, June 1982. ISSN 0020-7748, 1572-9575. doi: 10.1007/BF02650179. URL http://link.springer.com/article/10.1007/BF02650179.

[225] R. Dingle, W. Wiegmann, and C. H. Henry. Quantum states of confined carriers in very thin al$_x$ga$_{1-x}$As-gaas-al$_x$ga$_{1-x}$As heterostructures. *Phys. Rev. Lett.*, 33: 827–830, Sep 1974. doi: 10.1103/PhysRevLett.33.827. URL http://link.aps.org/doi/10.1103/PhysRevLett.33.827.

[226] D. A. B. Miller. Optical physics of quantum wells. In *Quantum Dynamics of Simple Systems*, pages 239–266. CRC Press, g. -l. oppo, s. m. barnett, e. riis, and m. wilkinson (institute of physics, london, 1996) edition, 1996.

[227] F. Rveret, P. Disseix, J. Leymarie, A. Vasson, F. Semond, M. Leroux, and J. Massies. Influence of the mirrors on the strong coupling regime in planar GaN microcavities. *Phys. Rev. B*, 77(19):195303, May 2008. doi: 10.1103/PhysRevB.77.195303. URL http://link.aps.org/doi/10.1103/PhysRevB.77.195303.